DISSERTATION

ANALYTICAL SPECTROSCOPY METHOD DEVELOPMENT TO STUDY MECHANISMS OF ALZHEIMER'S AND TUBERCULOSIS DISEASES

Submitted by

Cheryle Nicole Beuning

Department of Chemistry

In partial fulfillment of the requirements

For the Degree of Doctor of Philosophy

Colorado State University

Fort Collins, Colorado

Spring 2020

Doctoral Committee:

Advisor: Debbie C. Crans

Nancy E. Levinger
George Barisas
Ellen R. Fisher
Mark Zabel

ABSTRACT

ANALYTICAL SPECTROSCOPY METHOD DEVELOPMENT TO STUDY MECHANISMS OF ALZHEIMER'S AND TUBERCULOSIS DISEASES

This dissertation covers the analytical method development created to study and enhance the knowledge of two specific disease mechanisms important to Alzheimer's disease and *Mycobacterium tuberculosis*. There are two parts in this dissertation where Part 1 is entitled *Measurement of The Kinetic Rate Constants of Interpeptidic Divalent Transition Metal Ion Exchange in Neurodegenerative Disease.* Part 2 is entitled *The Electrochemistry of Truncated Menaquinone Electron Transporters with Saturated Isoprene Side Chains Important in Tuberculosis.* These diseases appear on the World Health Organization's top 10 leading causes of death worldwide. The amyloid-beta (Aβ) peptides are associated with Alzheimer's disease, where neurodegeneration is caused by the aggregation of the peptide into senile plaques within neuronal synaptic cleft spaces. Alzheimer's disease currently has no cure due to its multi-causative pathology. One disease mechanism is the coordination of divalent metal ions to the peptide. Specifically, Aβ coordinates Cu(II) and Zn(II) ions that can enhance the aggregation of Aβ into plaques. These metal ions are highly regulated within the human body and are usually found bound to peptides and not as free ions. Therefore, the Aβ must sequester the metals from other proteins and peptides.

The primary research in this dissertation advances fluorescence method development to measure interpeptidic Cu(II) exchange kinetics to be able to measure this type of disease mechanism. The small peptides GHK (Gly – His – Lys) and DAHK (Asp – Ala – His – Lys) both chelate Cu(II) with nM affinity, have biological relevance as they are motifs found in human blood like Aβ, and chelate Cu(II) with similar nitrogen-rich binding ligands as Aβ. By substituting non-coordinating lysine residues with fluorescent tryptophan, the interpeptidic exchange rates can be measured since tryptophan fluorescence is statically quenched when within 14 angstroms of a paramagnetic bound Cu(II). Thus Cu(II) transfer from Cu(H$_{-1}$GHW) to either GHK or DAHK can be monitored by recovered GHW fluorescence as the Cu(II) is exchanged and second-order kinetic rate constants were determined. This methodology was then used to monitor the Cu(II) exchange from truncated Cu(Aβ$_{1-16}$) and Cu(Aβ$_{1-28}$) complexes to GHW and DAHW,

where second-order reaction kinetic rate constants were determined. While in the exchanges between Cu(H_{-1}GHW) with GHK/DAHK the second-order rate constants were on the magnitude of 10^2 or 10^1 $M^{-1}s^{-1}$, respectively, the exchanges from Cu(Aβ) complexes were 2-3 orders of magnitude larger, 10^4 $M^{-1}s^{-1}$ (to GHW and DAHW). These differences in rate constant magnitude arise from the fact that the affinity of GHW (K_A = 10^{13} M^{-1}) for Cu(II) is larger than Aβ (K_A =10^{10} M^{-1}). This method development is an important step to an accurate measurement of the interpeptidic exchange between Aβ peptides, including in their fibril and plaque formations.

Since senile plaques are found in synaptic cleft spaces with nanometer distances between neurons, a model system was generated to study coordination reactions at the nanoscale. In order to do this, the metal ion would need to be released in a controlled manner. Studies of metal ion burst reactions through the use of photocages can simulate bursts of ions like those seen in the synaptic cleft. Zn(II) is often released in its ionic form within the synapse in its function as a neurotransmitter, so we simulated a burst of Zn(II) ions by using a photocage, $[Zn(NTAdeCage)]^-$ which releases Zn(II) when irradiated with light. The photocage was irradiated to release Zn(II) then we followed its reaction progress with an *in situ* chelator, Zincon, in reverse micelles and in bulk aqueous buffer. The coordination reaction was 1.4 times faster in an aqueous buffer than in reverse micelles, despite the Zn(II) and Zincon being closer in the nanoparticle. These observations suggested that there is an impact on coordination reactivity within a highly heterogeneous environment with a cell-like membrane, which is due to the partitioning of each ligand. We observe that the photocage stays in the water pool of the reverse micelle and the Zincon partitions into the membrane interface. Thus, the coordination reactivity is diminished, likely due to the need for Zn(II) to diffuse to the Zincon, crossing a highly organized Stern layer to encounter the Zincon. Whereas in aqueous buffer, these are free to encounter each other despite being hundreds of nanometers apart. These proof of concept studies are integral to studying initial binding dynamics of metal ions with peptides at the nanoscale present in cells and neuronal synapses.

Tuberculosis is a pathogenic bacterium which despite having a curable medication, can be drug-resistant. Menaquinone (MK) analogs with regiospecific partial saturation in their isoprenyl side chain, such as MK-9(II-H_2), are found in many types of bacteria, including pathogenic *Mycobacterium tuberculosis* and function as electron transport lipids cycling between quinone and quinol forms within the electron transport

system. While the function of MK is well established, the role of regiospecific partial saturation in the isoprenyl side chain on MK remains unclear and may be related to the redox function. Recently, an enzyme in *M. tuberculosis* called MenJ was shown to selectively saturate the second isoprene unit of MK-9 to MK-9(II-H_2). The knockout expression of this enzyme was shown to be essential to the survival of the bacterium. A series of synthesized truncated MK-n analogs were investigated using a systematic statistical approach to test the effects of regiospecific saturation on the redox potentials. Using principal component analysis on the experimental redox potentials, the effects of saturation of the isoprene tail on the redox potentials were identified. The partial saturation of the second isoprene unit resulted in more positive redox potentials, requiring less energy to reduce the quinone. While full saturation of the isoprene tail resulted in the most negative potentials measured, requiring more energy to reduce the quinone. These observations give insight into why these partially saturated menaquinones are conserved in nature.

ACKNOWLEDGEMENTS

First, I want to thank my husband, Mr. Jason Brian Beuning, who has always been supportive of my academic career, goals, and dreams. You are my foundation, without which none of this was possible. So thank you for your love and always being a constant in my life, I love you. I want to thank my mother, Mrs. Bonnie Sue Raney, for her support, love, always believing in me, listening to me when graduate school was rough, helping me in my endeavors both financially and emotionally, and being a wonderful and kind mother. To my husband's parents, Brian and Karen Beuning, thank you for all your support over the years in both my undergraduate and graduate studies. To Dan E. Gilmore, Stan Raney, and Mary A. Cox, and the rest of my family and friends, I thank you for your encouragement and love.

I would like to acknowledge and thank my mentor Debbie C. Crans for her support, understanding, fierce backing, and mentorship in my graduate career. Thank you for helping me become a better chemist. Similarly, I would also like to thank Nancy E. Levinger and Christelle Hureau for their mentorship on collaborative research projects. I would like to thank our other collaborators Shawn Burdette and Dean Crick. For my co-workers Jordan T. Koehn, Kaitlin A. Doucette, and all the others in the Crans group, I thank you for your collaborations, friendships, and support over the years. Thank you to my committee members for their support and advisement. I also thank the CSU Chemistry Department for everything they have done for me, including family medical leave support during my father's illness and death. I would like to thank the Chateaubriand STEM Fellowship program for the funds to perform research in Toulouse, France, under the advisement of Christelle Hureau, I am truly grateful for the time I spent in your country, it was a fantastic experience and one I cherish.

Lastly, I would like to acknowledge my undergraduate mentees, Noah Barkley, Luca Zocchi, and Molly Hartman, for their hard work in helping collect data for my research projects. Thank you for your contributions to my research. I learned much from being your mentor as I hope you learned from me, good luck to you all in your future academic endeavors.

DEDICATION

My dissertation is dedicated to my late father, David Lee Cox, who passed away on April 18, 2018, at the age of 58, from lung cancer during my 5th year of graduate school. Though I only had 20 years with you, I am forever grateful I was able to meet you when I was 17 and be your daughter for the time we had. I wish you could have seen me walk at graduation, first in the family to be called Doctor. We may not come from much, but I know with finishing my Ph.D. in Chemistry, I made you proud. You always let me know that. I love you, I miss you every day, and I wish you were still with us. May you rest in peace and be free of the pain you endured from cancer, which took your life much too soon.

TABLE OF CONTENTS

LIST OF TABLES

LIST OF FIGURES

LIST OF EQUATIONS

CHAPTER 1: INTRODUCTION AND SPECTROSCOPY BACKGROUNDS

1.1 Introduction to the research projects and their significance

In this dissertation, the primary research goals were to use analytical spectroscopic method development to understand, measure, and/or quantify the mechanisms, physical and/or chemical properties of molecules and their reactions associated with two diseases, Alzheimer's disease (AD) and tuberculosis disease (TB). In 2016, according to the World Health Organization (WHO), listed the top 10 leading causes of death in the world where AD was #5 and TB was #10.[1] The characterization of biological molecules and their reactions associated with a disease is often a very arduous task, involving many iterations until a reproducible assay is developed. These mechanisms can then be the targets for drug development, especially for those reaction mechanisms that are essential for disease progression. There are two primary research projects described in this dissertation. The first, Part 1, is concerned with the measurement of kinetic constants in the interpeptidic Cu(II) exchange of peptides associated with AD and is discussed in Chapters 2 and 3. The second, Part 2, is concerned with the differences in electrochemical redox potentials of a series of truncated regiospecifically saturated menaquinones (MK), which are essential electron transporters in *Mycobacterium tuberculosis* (*M. tuberculosis*) and are discussed in Chapter 5.

Unfortunately, no cure exists for AD despite three decades of continued research since the amyloid-beta peptide (Aβ) was first associated with the senile plaques that cause brain atrophy.[2-3] The senile plaques are found in the synaptic cleft space between neurons and lead to their atrophy since the neurons can no longer signal to each other. Thus, the symptoms of dementia and memory loss occur, and eventually, death as the brain can no longer work properly. The Aβ peptide forms aggregates which accumulate into these senile plaques, where many aggregation mechanisms exist, for a complete background see Chapter 3 section 3.1. AD has a multi-causative pathology and is one reason why there is no cure. In 2019, the Alzheimer's Association reported that AD currently affects 5.8 million Americans, costs $290 billion in only the treatment of symptoms, is the 6th leading cause of death in the United States, and every 65 seconds a person is diagnosed with the disease.[4] As the world's population increases and ages, these numbers are expected to rise until the cost of treatment surpasses a trillion dollars by 2050, with 14 million Americans affected.[4] Despite all the research, no definitive cure or vaccine has been found.

Although, with the arrival of advanced gene therapy technologies like CRISPR, some hope is on the horizon. In a recent 2018 study, gene therapy was used to target specific genes that seem to play a harmful role in AD progressions like the allele APOE4 (*apolipoprotein* E) and swap in genes that play a protective role like the APOE2 allele.[5] But these types of therapies are still in their infancy.

Part 1 of the dissertation includes the analytical method development to monitor and measure the kinetics of divalent metal ion exchange using optical spectroscopy. The divalent transition metal ions Cu(II) and Zn(II) are essential for all biological life, including humans, bacteria, fungi, and animals.[6-17] Their presence is important for the structural and functional roles of many metalloproteins and biological processes. For example, Cu(II) is essential metal for proteins like ceruloplasmin, is a redox-active metal ion that participates in oxidative phosphorylation for mitochondrial energy production, and is an indispensable co-factor in some oxidases and peroxidases.[7, 11, 13, 18-20] Zn(II) is an essential co-factor in metalloproteins like metallothioneins, it is the second most abundant transition metal that is vital to good health, and can be found in its ionic form in labile pools for its function as a neurotransmitter.[6, 14, 16-17, 21-24] Both metals are considered essential in embryonic development, especially within the brain. Transition metals have an unfriendly biological history due to their inherent toxicity. However, the misconceptions about the roles of transition metals in biology are beginning to be considered. Their prevalence in disease mechanisms, including neurodegenerative disease, is becoming more widely understood as proteins associated with the diseases have many sites that these metals can bind to. The delicate balance of metal ion homeostasis in the body is important to both health and disease mechanisms.

The primary research project concerns the method development to measure the interpeptidic exchange rate constants of Cu(II) in small peptide motifs found in human blood and associated with neurodegenerative diseases like AD.[25] Within the human blood and serum, GHK (Gly-His-Lys) is associated with human growth factor and is found intact as a tripeptide, and DAHK (Asp-Ala-His-Lys) is the N-terminus sequence of human serum albumin (HSA).[19, 26-27] The amyloid-beta peptides (Aβ) are associated with AD where the full-length Aβ peptide can have 39 – 42 amino acid residues, and truncated forms also exist, see Chapter 3 section 3.1 for a complete background. Both Cu(II) and Zn(II) are found in 0.5 – 1.0 mM concentrations in the senile plaques associated with AD due to their complexation with the Aβ peptide.[28] The complexation of Cu(II), Zn(II), and Fe(II) to the Aβ peptide has been shown to enhance the propensity

of the peptides to aggregate into the plaques and is one of the many pathologies of AD. Therefore, understanding the kinetics of exchange in these peptides with themselves or other biological peptide motifs will help to create drugs that can stop the exchange, sequester the metals from aggregates, or target the initial binding. Some drugs like clioquinol were developed to target the metal ion binding pathology of AD by trying to actively sequester Cu(II) and Zn(II) from Aβ complexes.[28-30]

There is a minor research project in Part 1 that concerns the light-induced photolytic release of Zn(II) at the nanoscale present in reverse micelles using photocaged complexes and monitoring of Zn(II) coordination with a ligand *in situ*.[31] The ability to mimic metal ion bursts on the nanoscale can help to develop methods to monitor reactions at the cellular scale through the use of model membrane systems like reverse micelles or liposomes. The method of generating metal ion burst reactions in reverse micelles was developed for collaboration in the Crans and Levinger research groups to eventually study interpeptidic exchange or the initial binding dynamics of metal ions to Aβ peptides at the same scale found in the neuronal synaptic cleft, where senile plaques are found. Unfortunately, this extension from the proof-of-concept methodology presented in Chapter 4 has not been implemented to that goal yet, but is an important step to be able to monitor fast metal ion complexation at the nanoscale, and where mixing apparatus is too slow to measure sub-millisecond time-scale complexation mechanisms.

Part 2 of this dissertation includes the non-aqueous electrochemistry and spectroelectrochemistry method development to study certain menaquinone (MK, MK-*n*, *n* = number of isoprene units) electron transporters found in many pathogenic bacteria, such as *M. tuberculosis*. TB infects about a quarter of the world's population, according to the WHO.[32] Although in 2017, only about 10 million people fell ill, where about 1.6 million of those perished.[32] TB is epidemic in first and third world countries alike. While TB is curable through many first- and second-line medications, since it is a bacteria, it is prone to drug-resistance. Over 500 thousand cases of first-line drug rifampicin resistivity were reported in 2017, with some strains having multi-drug and extensive-drug resistivity.[32] As the bacteria can have multi-drug resistivity, new disease mechanisms must be identified as drug targets. Other diseases like AIDS can complicate the progression of TB and lead to death. In the 1.6 million deaths associated with the disease in 2017, 0.3 million of those were people infected with HIV/AIDS.[32] TB is the leading cause of death in those afflicted with HIV/AIDS (other than AIDS itself).

The partial regiospecific saturation of the second isoprene unit of the MK isoprenyl side chain is conserved in many pathogenic bacteria, including *Mycobacterium*, *Corynebacterium*, *Halobacterium*, and *Brevibacterium* families.[33-36] An enzyme called MenJ is responsible for the regiospecific partial saturation of MK-9 to MK-9(II-H_2) in TB.[37-38] The prevalence of these beta-saturated MK analogs in so many bacteria may have to do with its redox function. A systematic statistical approach was used to determine the effects of isoprenyl side chain saturation on the redox reactivity of a series of unsaturated, partially saturated, and fully saturated truncated MK analogs.[39] The truncated MK analogs we have studied have side chains with 1 – 3 isoprene units, which were synthesized by a colleague in the Crans laboratory, Dr. Jordan T. Koehn.

The following sections will introduce the relevant spectroscopy background for each instrumentation or method used for the characterization of the research projects described within. There is a section on the kinetic treatment of fluorimetry data. Real experimental examples are provided, where appropriate, to show how these approaches or methods were used within the research projects described herein. Each of the four major research projects has its own chapter. Lastly, an appendix is provided at the end for contributions to projects that are not discussed in the body of the dissertation, or those which were only co-authored contributions.

1.2 Absorption and fluorescence spectroscopy

Fluorescence is the measurement of the emission of light by a fluorophore upon absorption of light at a specific wavelength. Absorption is the measurement of the amount of light absorbed by the fluorophore. The absorption of light promotes electrons from the highest occupied molecular orbital (HOMO) ground state, S_o, to the lowest unoccupied molecular orbital (LUMO) excited state, S_1, **Figure 1.1**. After excitation, the fluorophore will return to the ground state by releasing the absorbed energy, which is called emission or radiative decay. This emission of absorbed energy is called fluorescence when it is from a singlet excited state (S_1), or phosphorescence if from a triplet excited state (T_1). The two states depend on the direction of the spin of the excited electron and are radiative releases of energy, which can be measured using fluorimetry spectrometers. The Stokes Shift arises from the fact that emission light always has a longer wavelength (lower energy) than the absorbed light, so the absorption spectrum is always at a shorter wavelength (higher energy) than the emission spectrum of the fluorophore. In **Figure 1.1,** the absorption

and fluorescence of the fluorescent tryptophan tripeptide, GHW (Gly-His-Trp), is shown, where the absorption maximum is 280 nm, and the emission maximum is 365 nm.

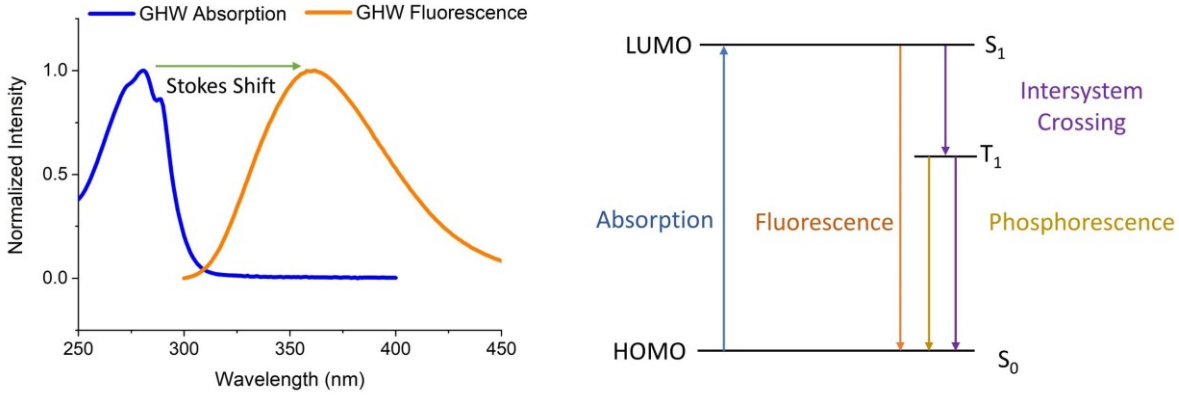

Figure 1.1 *Left* Normalized intensity of the absorption and fluorescence spectrums of a tryptophan containing tripeptide GHW. *Right* Schematic of absorption and emission in the HOMO to LUMO optical gap. Fluorescence is the radiative decay from $S_1 \rightarrow S_0$ and phosphorescence is the radiative decay from $T_1 \rightarrow S_0$. Intersystem crossing is the non-radiative deactivation from $S_1 \rightarrow T_1$ then $T_1 \rightarrow S_0$ and can happen in the presence of heavy atoms with paramagnetic electrons.

In absorption and emission spectroscopy, the Beer-Lambert law is expressed differently. For absorption spectroscopy, **Eq. 1.1** shows that absorbance (A) is linearly proportional to the product of molar absorptivity (ε), concentration (C), and cuvette pathlength (ℓ). Similarly, in emission spectroscopy, **Eq. 1.2** shows that fluorescence intensity (I_F) is linearly proportional to the product of molar absorptivity (ε), concentration (C), and cuvette pathlength (ℓ), as well as the excitation source intensity (I_o) and the quantum yield of the fluorophore (ϕ_f). Due to the dependence on excitation source intensity and quantum yield of a fluorophore, fluorescence spectroscopy often requires less concentrated solutions than absorbance spectroscopy and is much more sensitive. As a result, there is a maximum concentration where fluorescence intensity is still linearly proportional, **Eq. 1.3**.

(**Eq. 1.1**) $A = \varepsilon C \ell$

(**Eq. 1.2**) $I_F = I_o (2.303 \varepsilon C \ell) \phi_f$

(**Eq 1.3**) $C_{max} = 0.05 * (\varepsilon \ell)^{-1}$

(**Eq 1.4**) $(I^0_F / I_Q) = 1 + \tau_f k_q [Q]$

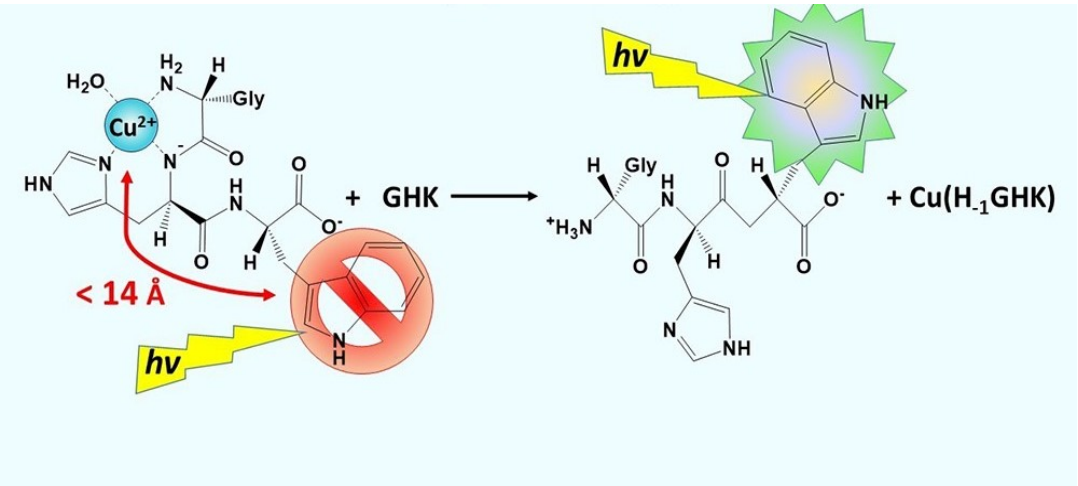

Figure 1.2 Cartoon schematic of the static tryptophan fluorescence quenching in inter-peptidic Cu(II) exchange between Cu(H_{-1}GHW) and GHK.

Fluorescence quenching is a signal response that follows the Stern-Volmer equation, which relates a fluorophore with its quencher, **Eq. 1.4**, where the ratio of the fluorescence intensity without a quencher present (I^0_F) to the fluorescence intensity with a quencher present (I_Q) is equal to 1 plus the product of the lifetime of the emission excited state of only the fluorophore (τ_f), the quencher rate coefficient (k_q) and the concentration of quencher ([Q]). In the system described below, the fluorophore is tryptophan, and the quencher is a bound paramagnetic Cu(II). The Cu(II) quenches the fluorescence of tryptophan by a relaxation mechanism called the external heavy atom effect. When the Cu(II) is within 14 Å of the tryptophan, the paramagnetic electron from Cu(II) interferes with the intersystem crossing of the fluorophore, **Figures 1.1, 1.2**. The intersystem crossing is the rate of change between singlet S_1 and triplet T_1 excited states, which is usually extremely slow. The presence of a paramagnetic electron from a heavy atom greatly enhances this rate to a point where the emission of absorbed light is deactivated. Specifically, the non-radiative deactivation due to the increase in the rate of intersystem crossing results in no light to be emitted, and thus the fluorescence is quenched. As seen in **Figure 1.3**, as Cu(II) is added to a solution of GHW (pH 7.4, 0.1 M HEPES), the fluorescence intensity decreases. This is a static fluorescence quenching as the Cu(II) must be bound to the peptide for this to occur and does not occur if the Cu(II), which may be bound to another ligand in solution, collides with the tryptophan, as in other types quenching mechanisms.

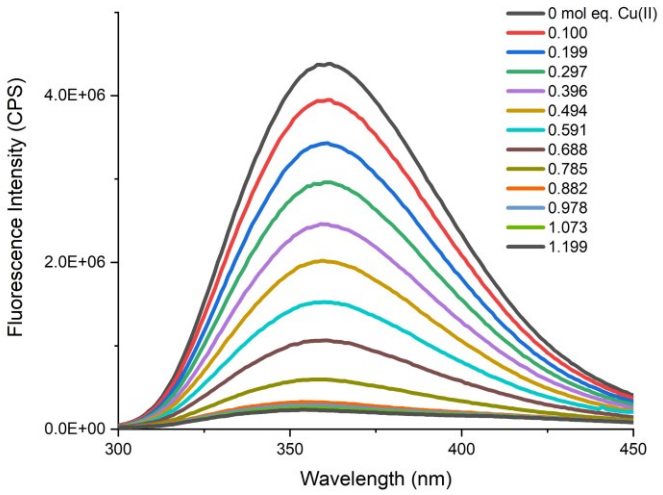

Figure 1.3 The fluorescence intensity of GHW being quenched by addition of mol equivalence of Cu(II).

Tryptophan absorbance and fluorescence are extremely sensitive to the surrounding chemical environment due to two anisotropic perpendicular electronic transitions present in the indole fluorophore, **Figure 1.4**. These two anisotropic states are denoted as ^1L_a and ^1L_b electronic transitions. While both absorb light at 280 nm, when excitation light of 290 nm is used, the ^1L_a electronic transition is favored for emission fluorescence. Absorption is associated more with the ^1L_b electronic transition, and emission from this transition is rare. The source of environmental sensitivity due to the ^1L_a transition state arises from the creation of a large dipole, where the pyrrole ring is partially positively charged, as compared to the ^1L_b transition. Changes in the solvent environment can affect the dipole of the ^1L_a transition state by interactions such as hydrogen bonding to the nitrogen's hydrogen or changes in pH. These effects make tryptophan's fluorescence extremely sensitive to its solvent environment.

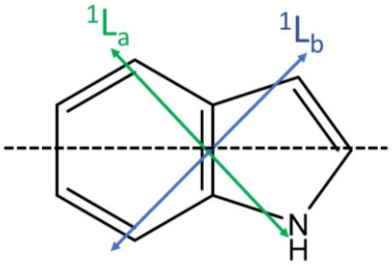

Figure 1.4 The anisotropic electronic transition states of the indole chromophore of tryptophan.

Calibration curves are performed whenever a set of fluorimetry data is acquired to be able to convert tryptophan fluorescence intensity (counts per second, CPS) to concentration. As tryptophan is extremely sensitive to its surrounding environment, calibrations must be performed in the same conditions as the kinetic experiments with the same instrument parameters such as slit width, excitation ($\lambda_{excitation}$), and emission ($\lambda_{emission}$) wavelengths. A blank measurement without any fluorescent peptide is taken and subtracted out from all data points. An example of a calibration curve for GHW is given in **Figure 1.5**. The concentration of GHW peptide is determined through absorption measurements of the stock solutions, where an average and standard deviation is obtained. Then the error is propagated from the volumes of pipettes used to make working solutions and calibrator additions in the fluorescence calibration curve, **Table 1.1**. The calibration is repeated three times, and the error in fluorescence intensity is a standard deviation of those three runs, **Table 1.1**. The error in concentration, as well as the error in fluorescence intensity CPS, is considered by using OriginPro (student versions, 2018b and 2019b) software by using the instrumental error weighting option, **Figure 1.5**. In 0.1 M HEPES at pH 7.40, the GHW fluorescence is linearly proportional to concentration, where the slope and y-intercept are used to determine the concentration in the experimental kinetic data.

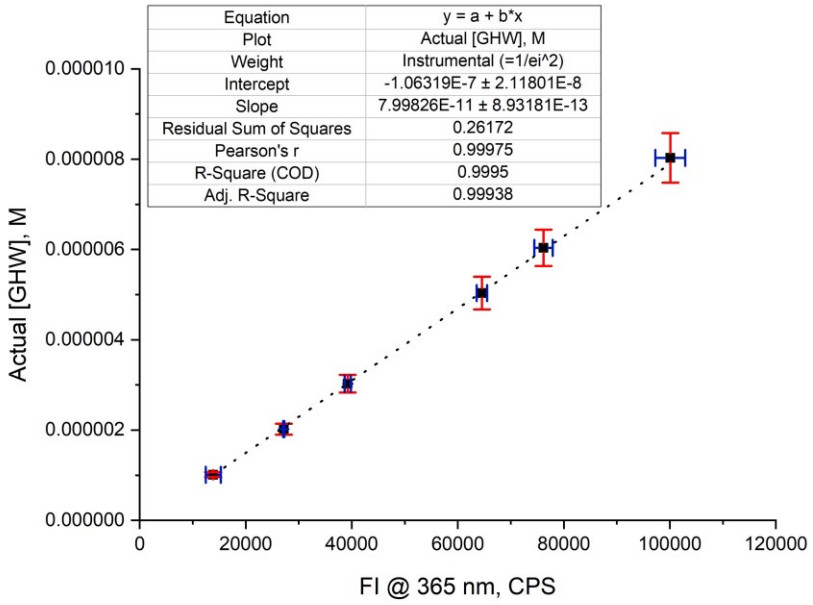

Figure 1.5: An example of a calibration curve created for GHW (0.1 M HEPES, pH 7.40) using the data in **Table 1.1** and analyzed in OriginPro software. Instrumental error weighting is used, the error in [GHW] are the red error bars and the error in fluorescence intensity are the blue error bars. Instrumental parameters include, 1.5 nm slit width, $\lambda_{excitation}$ = 290 nm, and $\lambda_{emission.}$ = 365 nm.

Table 1.1: Example of experimental calibration curve data taken for GHW in 0.1 M HEPES at pH 7.40 shown in **Figure 1.5**.

Actual [GHW], M	Error [GHW], M	I_F @ 365 nm, CPS	Error I_F @ 365 nm, CPS
1.01E-06	5.36E-08	13863	1414
2.02E-06	1.20E-07	27180	135
3.03E-06	1.97E-07	39247	586
5.03E-06	3.62E-07	64543	975
6.03E-06	4.03E-07	76157	1726
8.03E-06	5.49E-07	100080	2834

1.3 Kinetic treatment of fluorescence data

Two approaches were used to determine the second-order kinetic rate constants of the interpeptidic exchange of Cu(II). The first approach uses the method of initial rates to determine reaction orders and the rate constant for the Cu(II) exchange in the small peptides (GHK, DAHK, etc.). This approach was used in the exchange of Cu(II) from Cu(H_{-1}GHW) to GHK or DAHK or the reverse exchange of Cu(H_{-1}GHK) to GHW, described in Chapter 2. The second approach uses second-order fitting of the kinetic data in the exchange of Cu(II) from truncated Cu($A\beta_{1-16}$) and Cu($A\beta_{1-28}$) complexes to GHW, DAHW, or GGW, found in Chapter 3. These exchanges were much faster than the exchanges examined previously, and the method of initial rates could not be consistently employed.

The method of initial rates can determine rate law, reaction orders, and rate constants of a reaction and is a very straightforward kinetic treatment of data. Because these peptide complexes can have different coordination chemistry when the metal ion complex and peptide are in excessive concentrations, a pseudo-first-order approach cannot be used. Often, kinetic measurements are made in pseudo-first-order conditions where one reactant is in large excess compared to another reactant. This can induce other complexes to form, such as Cu($H_{-2}(GHW)_2$). To avoid this, we used very similar concentration profiles in the exchanges, careful to not put any one reactant in a large excess of the other.

In a very simple A + B → C + D reaction with a rate law, rate = $k\,[A]^m\,[B]^n$, the method of initial rates requires two sets of kinetic data to be acquired. In one set of data, the concentration of B is held constant while the concentration of A is varied in at least four different experimental conditions to determine the order *m* of reactant A. Similarly, to determine the order *n* of reactant B, the concentration of A is held constant

while the concentration of B is varied in at least four different experimental conditions. For example, **Table 1.2** lists the experimental conditions used to determine the orders in the exchange of Cu(H_{-1}GHW) to GHK or DAHK, where reactant A is Cu(H_{-1}GHW), and reactant B is GHK or DAHK. The rate is determined in M/s using an Excel 2016 slope function of the data points in that region, **Figure 1.6,** as tryptophan fluorescence is recovered. Then the slope of log rate versus log [peptide] plots determines the order for that reactant, **Figure 1.7**, where all reaction orders were determined to be one. Finally, the rate law is determined as the orders of reactants are known, and the rate constant can be found **Eq. 1.5**.

(**Eq. 1.5**) rate = k [Cu(H_{-1}GHW)] [GHK]

Table 1.2: Example of the approximate concentration profiles used in the method of initial rates for the Cu(H_{-1}GHW) to GHK/DAHK exchanges.

	$[Cu(H_{-1}GHW)]_{initial}$, μM	$[GHK]/[DAHK]_{initial}$, μM
Exp A	10	5
	10	10
	10	15
	10	20
Exp B	3	5
	5	5
	8	5
	10	5

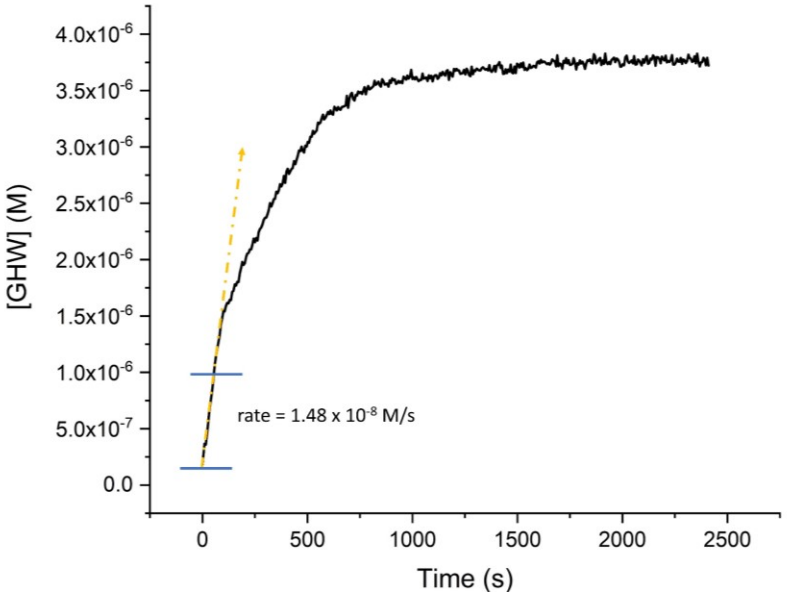

Figure 1.6: The kinetic trace of an equimolar exchange of 10 μM Cu(H_{-1}GHW) + 10 μM GHK. The yellow dotted line is a tangent to visualize the initial rate of the exchange. The data within the two blue horizontal lines was used to determine the rate in M/s using the slope function in Excel 2016.

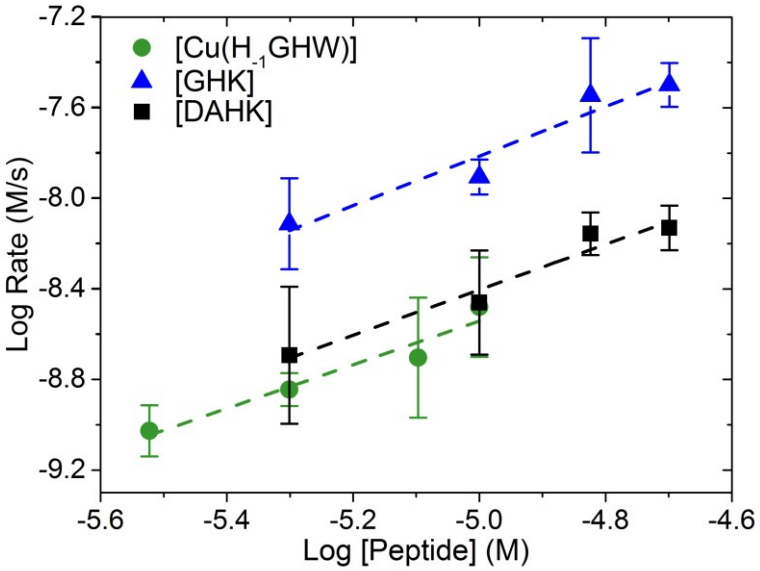

Figure 1.7: For order analysis of Cu(H_{-1}GHW) (green circle, m = 0.966 ± 0.168, R^2 = 0.91), a constant 5 μM GHK was used, for that of GHK (blue triangle, m = 1.09 ± 0.19, R^2 = 0.91), a constant 10 μM Cu(H_{-1}GHW) was used, and for that of DAHK (black square, m = 1.00 ± 0.15, R^2 = 0.94), a constant 10 μM Cu(H_{-1}GHW) was used. Error bars indicate two to three replicates.

The fitting approach used in the exchanges of truncated Cu(Aβ) complexes to the fluorescent GHW, DAHW, or GGW followed **Eq. 1.6**. In **Eq. 1.6**, the initial concentrations at t = 0 of $[Cu(A\beta)]_0$ and $[GHW]_0$ are known, while the $[GHW]_t$ is determined from the fluorescence at each data point at a time, *t*. The kinetic data was gathered in a similar fashion as the previous work; reactant concentrations were kept close to each other, calibration curves generated each time a set of data was gathered, and fluorescence intensity data were converted to concentration before analysis using calibration curves. Since this approach is looking at a decrease in tryptophan rather than a recovery of fluorescence like in our previous experiments, a smaller slit width was used to discourage an inner filter effect (IFE). IFE happens when some of the emitted light is reabsorbed by the fluorophore. Thus a decrease in fluorescence is observed but may not be due to the exchange. In order to determine a slit width that does not lead to an IFE, the fluorescence of the tryptophan peptides was monitored over the time frame of the kinetic experiment, and 1.5 nm was chosen as no decreases in fluorescence CPS was observed. As these exchanges were much faster than the previous work, the method of initial rates did not produce reliable rate constants or orders, due to the inability to get data points within the linear portion of the kinetic curve. We must manually add the reactants

due to the lack of any stopped-flow apparatus, which usually takes about four to five seconds. Within that 4 – 5 seconds in these exchanges, a large decrease in fluorescence was observed, see *inset* **Figure 1.8**. Therefore, second-order fitting of the data using **Eq. 1.6** allowed for the determination of rate constants by using the first 10 - 40 seconds of kinetic data (depending on the exchange examined), setting the y-intercept to zero, and graphing the left side of the equation versus time, where the slope of the line is the second-order rate constant. These data were graphed, and their slopes determined in OriginPro 2019b (student version), then the slopes can be averaged and 95% confidence levels obtained. **Figure 1.8** shows an example of graphing the transformed kinetic data to determine the rate constant from the slope of the line, where the *y*-axis is the left side of **Eq. 1.6**.

$$\textbf{(Eq. 1.6)}\ \frac{1}{[Cu(A\beta)]_0 - [GHW]_0} * \ln\left(\frac{[GHW]_0 * ([Cu(A\beta)]_0 - ([GHW]_0 - [GHW]_t))}{[Cu(A\beta)]_0 [GHW]_t}\right) = k * t$$

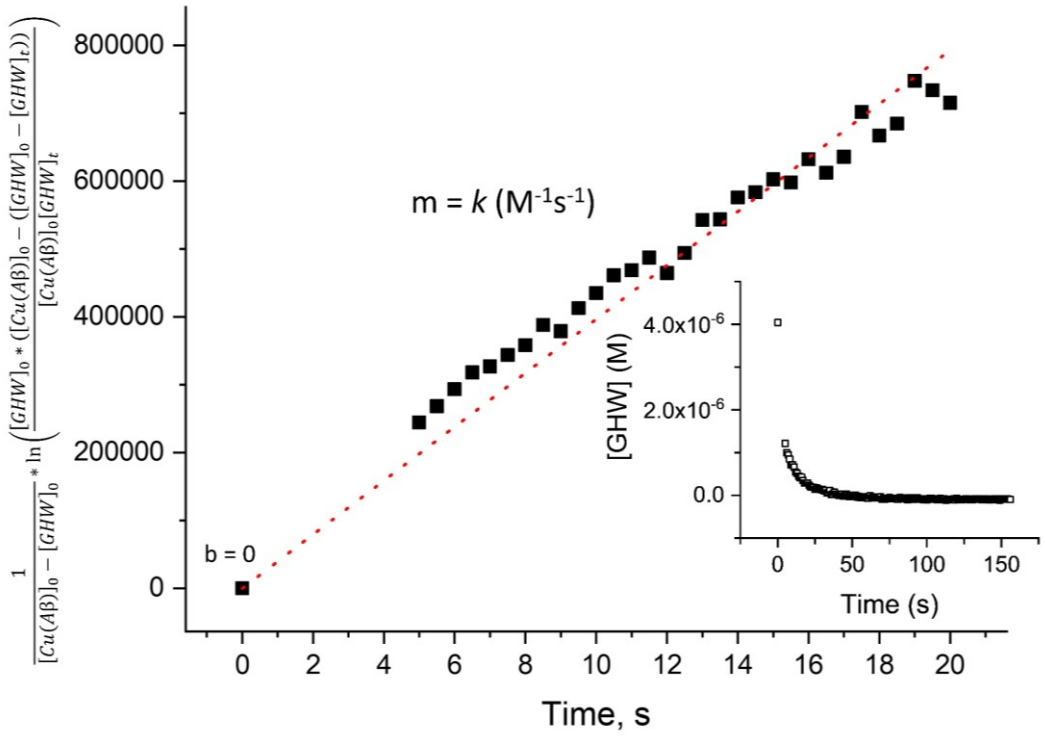

Figure 1.8: Example of the second-order fitting performed on the kinetic data in the interpeptidic exchanges involving Cu(Aβ) complexes. The exchange shown here is 4 μM GHW + 5 μM Cu(Aβ$_{1\text{-}16}$) at pH 7.40 in 0.1 M HEPES. The first 20 s of data are used. The slope is determined by setting the y-intercept to zero. *Inset* is the kinetic concentration versus time data.

1.4 Nuclear magnetic resonance

Nuclear magnetic resonance, NMR, is an atomic level absorption spectroscopy which gives structural and environmental information about a molecule and its atoms through the absorption of radio waves under an applied magnetic field. Historically, it is used to elucidate the structures and purity of natural and synthesized molecules as well as interpretation of how the chemical environment can alter the chemical shifts in an NMR spectrum. In cartesian *xyz* coordinates, spin (angular momentum) is along the *z*-axis, where the magnetic quantum number, m_S, is spin-up or spin-down, and where the number of angular momentum states is equal to 2S + 1. When an external magnetic field is applied to an atom with a non-zero spin number, an induced splitting of the spin states occurs when irradiated with an appropriate radio frequency, *v*, and an energy difference between the two states is generated, **Figure 1.9.** This promotion of atoms to higher energy states is called resonance. The population of atoms in each energy state is denoted as N_α (lower energy state) and N_β (higher energy state), and there is always a slight excess of population in the lower energy state, $N_\alpha > N_\beta$, following the Boltzmann distribution. In the absence of an applied magnetic field, the spin states are degenerate, or at the same energy. The energy difference, ΔE, arises

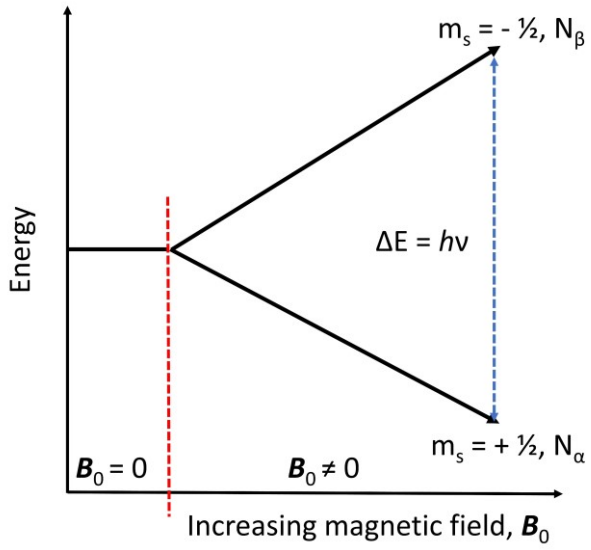

Figure 1.9: The energy diagram of the simplest half-integer spin, *I* = 1/2 resulting in two energy states N_α/N_β, with opposing spins m_s = +1/2 (aligned with $\boldsymbol{B}_0$) or -1/2 (aligned against $\boldsymbol{B}_0$). For larger values of *I*, more states exist.

from the different alignment of the spin in either the same (N_α, m_s = + 1/2) or opposite (N_β, m_s = - 1/2) direction as the applied magnetic field, $\boldsymbol{B}_0$, which is always situated along the z-axis, **Eq. 1.7**, where h is Plank's constant, and γ is the magnetogyric ratio. Each atom has a nuclear constant called the magnetogyric ratio, γ, which determines the radio frequency at a given magnetic field strength needed to make the atom resonate and is based on the magnetic moment, μ, and the spin number, I, **Eq. 1.8**.

(**Eq. 1.7**) $\Delta E = h\nu = \boldsymbol{B}_0 h\gamma/2\pi$

(**Eq. 1.8**) $\gamma = 2\pi\mu/hI$

NMR spectroscopy involves basic 1-dimensional (1-D) techniques that focus on a single nuclei type such as ^{1}H or ^{13}C NMR. These experiments give structural and chemical environment information about the molecule of interest. In 1-D NMR, the spectrum is taken by putting the sample in a constant magnetic field, where the field strength of a magnet is given in MHz and is based on the frequency needed for a proton to resonate. For instance, a 500 MHz NMR is at about 117,500 Gauss or 11.75 Tesla. Once in the constant magnetic field aligned along the ***z***-axis, an appropriate radio frequency is pulsed for the atom of interest along the *x*-axis (a common pulse is at 90°, or π/2), the pulsed frequency must be large enough to capture the entire frequency range for that nuclei. Once irradiated, the atoms in the sample are excited to the higher state, and a free induction decay (FID) is recorded as the nuclei relax back down to the ground state and release their absorbed energy. The FID can be mathematically transformed by a technique called Fourier transformation (FT), and the NMR spectrum is produced.

Deuterated solvents are very important in NMR as most instruments use the deuterium (^{2}H) signal to stabilize the magnetic field and make it homogeneous. This is achieved by locking the $\boldsymbol{B}_0$ to the frequency of the deuterated solvent. Luckily, deuterium does not show up in the NMR spectrum. This is very important as most solvents have hydrogen atoms, thus would completely dominate the NMR spectrum due to the large intensity. The concentration of the solvent is always much greater than the analyte dissolved in the solvent; thus, deuterated solvents are extremely important to use. Inhomogeneity in the magnetic field leads to extreme signal broadenings, like that seen with ferromagnetic materials like iron or paramagnetic metals like copper. Shimming by small magnets helps to keep the magnetic field stable and homogeneous in the sample volume.

When the sample is pulsed by a radio frequency along the *x*-axis, the magnetic vector aligned along the *z*-axis is tipped to the *y*-axis by 90°. The vector then processes back to the *z*-axis in a relaxation mechanism and is a measure of time. The T_1 is called longitudinal relaxation, which is the transfer of energy from excited nuclei to neighboring processing nuclei. When T_1 is short, then the intensity of the NMR peak is related to the number of that type of nuclei. For example, in ^{1}H NMR, the integration of the area under the peak is proportional to the number of hydrogen atoms (protons). The T_2 is called transverse relaxation, which is the transfer of energy from processing nuclei to each other. This type of relaxation causes line broadening and signal loss in the NMR spectrum and is usually due to the fanning out of the effective net magnetization along the *xy* plane.

The NMR spectrum contains signals at very particular chemical shifts, δ (ppm), which give detail about the structure and chemical environment felt by the atom. The value ppm is determined from the frequency of the signal in Hz divided by the frequency range of the spectrometer in MHz, for example, if a ^{1}H NMR signal is at 7 ppm on a 300 MHz instrument, the signal was at a frequency of 2100 Hz. Chemical shifts are reported as ppm, as these values do not change, given the instrument MHz value. Whereas if the chemical shift was given in Hz, the values would be different depending on the instrument used and would be difficult to compare chemical shifts across different instruments. Like infrared spectroscopy, in ^{1}H NMR, functional groups tend to have select regions of chemical shift ppm that the peaks show up at. For example, aromatic protons are often in the range of 6 - 9 ppm (downfield), while aliphatic protons are often in the range of 0 – 4 ppm (upfield). The chemical shifts of atoms are very predictable and can be projected using software like ChemDraw but are dependent on the solvent environment. For example, a chemical shift of a proton in a molecule will be different in aqueous solutions than in organic solvents. Even partitioning effects of a molecule within a membrane, like those in reverse micelles, will exhibit differences in the chemical shift of a proton, depending on its localized chemical environment. Similarly, when a metal ion binds to a ligand, the signals of the ligand's protons near to the bound metal will shift from the unbound state.

In addition to the chemical shift, the splitting patterns and the integration give a great deal of information about the structure and chemical environment felt by the atoms in the molecule. For instance, integration of ^{1}H NMR peaks will give the number of protons of that type there are in the molecule and is an effect of the T_1 relaxation. A summation over all the integration for all signals should give the total number

of hydrogen atoms in the molecule, and deviations from the expected number can indicate purity issues or contamination. The phenomenon known as spin coupling allows us to determine which protons are near each other in a molecule based on how much splitting of the peak is visible and the distance in Hz between them, known as coupling constants. Spin coupling arises from the coupling of the spin of the nuclei with other nearby bound nuclei through their bonded electrons following the Pauli principle that paired spins are antiparallel, and thus energy stable. This often only works when the coupled protons are 1 - 3 bonds away from each other, except in cases of aromaticity or conjugation, or a specific 4 bond coupling known simply as W coupling. If there are no coupled protons, a simple singlet (s) peak shows up on the NMR spectrum. If there is one coupled proton, a doublet (d) shows up on the NMR spectrum. If there are two coupled protons, a triplet (t) shows up on the NMR spectrum. Thus, the extent of splitting is equal to n + 1, where n is the number of coupled protons, and the distance between the peaks is the coupling constant, J, which does not exceed 20 Hz. The values of J are predictable and are different depending on the structure in the molecule. Many complex systems can arise, for example, such as doublets of doublets (dd) or a doublet of triplets (dt), which are due to coupled protons with different coupling constants.

Correlation NMR spectrometry is the collection of 2-D NMR techniques, which are valuable as they give information which is not otherwise obtainable using the 1-D NMR spectrum. All 2-D techniques are comprised of similar 1-D spectra, which have been plotted using a *xy* fashion, but often have more complex pulse sequences than the 1-D NMR. The pulse sequence in 2-D NMR techniques often involves multiple pulses and a time delay between them, or a mixing time. This allows for interaction by the coupled technique, so correlations form. Correlations are often found as cross-peaks with diagonals if the two nuclei are the same, as in $^{1}H^{1}H$ COSY (correlation spectroscopy) NMR, which gives information about which protons are next to each other in a molecular structure. Contour peaks in the 2-D spectrum are those that line up with two individual signals from the spectra of different atoms, as in $^{1}H^{13}C$ HSQC (heteronuclear single quantum coherence spectroscopy) NMR, which gives information about which protons are attached to which carbon atoms. There are many 2-D NMR techniques that can tell you different structural information, like which H atoms are bound to which C atoms, or if two C or H atoms are near in space.

1.5 Electron paramagnetic resonance

Electron paramagnetic resonance (EPR) is very similar to NMR, in which a magnetic field and radio wave irradiation are used to generate an energy difference that can be measured. However, this technique uses the unpaired electron in paramagnetic or radical molecules or metals like Cu(II). Just like how nuclei have spin which generates a magnetic field, an isolated unpaired electron has a charge and spin, which can also generate a magnetic field. The interaction of the unpaired electron with an externally applied magnetic field is theoretically like how NMR induces a spin state energy difference. In EPR, this is called the Zeeman effect **Figure 1.10**, which follows **Eq. 1.9**, where g_e is the g-factor of an isolated electron ($g_e = 2.0023192778$), and β is the Bohr magneton. The unpaired electron has a particle spin of ½, so it has two spin states, m_s = ± ½ . Since electrons are parts of nuclei and are subject to orbital momentum, the experimental g-factor always deviates from the ideal g_e and are denoted as g. For experimental values of g, **Eq. 1.10** is followed, where the frequency (in MHz) is a constant value, and the magnetic field (in Gauss) is determined experimentally. Unlike NMR, the radio frequency is held constant, in the GHz range, while the magnetic field is varied.

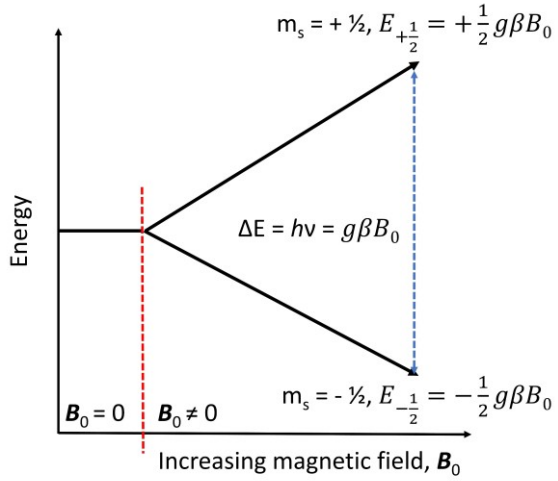

Figure 1.10: Induced energy difference of the spin states within a magnetic field for a paramagnetic electron with ms = ± ½ which either aligns with or against the magnetic field.

(**Eq. 1.9**) $\Delta E = E_{+\frac{1}{2}} - E_{-\frac{1}{2}} = g_e \beta \boldsymbol{B}_0$

(**Eq. 1.10**) $g = h\nu/\beta \boldsymbol{B}_0$

(**Eq 1.11**) $A = g \mu_e \Delta \boldsymbol{B}_0/h$

Since the g-factor has directional anisotropic contributions in the *xyz* Cartesian coordinates (g_x, g_y, g_z) a low temperature or "powder" spectrum is often taken. Especially for EPR involving Cu(II), without freezing the sample, all the directional vectors would cancel each other out due to their ability to freely move, and no spectrum would be recorded. In a frozen sample, there is a net summation of all possible orientations since they are fixed in space, and a spectrum can be recorded. An EPR spectrum is often either plotted with the magnetic field or, more commonly, the g-factor (referenced axis) as the *x*-axis with absorption derivative as intensity on the *y*-axis. With the g-factor as the *x*-axis, measurements can be directly compared over differing days or instruments since the frequency and magnetic field are already accounted for by **Eq. 1.10**. With Cu(II), there is a parallel ($g_{||}$) and perpendicular ($g_{\perp}$) region of the spectrum, which is a result of axial anisotropy. Axial anisotropy means that one axis is different than the other two, $g_{||} = g_z$ and $g_{\perp} = g_x = g_y$. These regions can overlap, especially in Cu(II) EPR. The g-factor is often a fingerprint value for Cu(II) complexes.

For the Cu(H-1GHW) complex, a powder EPR spectrum is given in **Figure 1.11A,** which shows the parallel and perpendicular regions and their overlap. The parallel region's peaks are called hyperfine interactions, which arise from the coupling of the paramagnetic electron to the Cu(II) nucleus. In the perpendicular region, these are called superhyperfine interactions and arise from the coupling of the paramagnetic electron to the ligand nuclei. These are both perturbations of the energy differences observed in the Zeeman effect and are like the proton coupling observed in NMR. The coupling leads to complexity in the spectrum, just like in NMR. The $g_{||}$ and $g_{\perp}$ values can be interpolated from the EPR spectrum as the midpoint in the range of the region. So, for the 4 peaks of Cu(II) in the $g_{||}$ region, the g-factor value is the midpoint of the parallel range. Similarly, the $g_{\perp}$ is taken as the midpoint of the perpendicular range. The hyperfine ($A_{||}$) coupling constants are determined by the width in Tesla ($\Delta \boldsymbol{B}_0$) between the two peaks, **Figure 1.11B** and follows **Eq. 1.11**, where μ_e is the magnetic moment of an electron. The number of peaks in the parallel region follows the 2S + 1 rule, where for Cu(II), both ^{63}Cu and ^{65}Cu have nuclear spins of 3/2, and 4 peaks are often observed (**Figure 1.11A** 1-4). The parallel peaks can merge into the perpendicular

region, as seen in **Figure 1.11A** and **B**, where three peaks are very clear in the parallel region, and the fourth is within the perpendicular region. When this type of overlap happens, it can significantly alter the perpendicular region's peaks, as seen in the zoomed images of the perpendicular region below each spectrum. The superhyperfine coupling in the perpendicular region is sensitive to bound ligand nuclei. The splitting patterns here follow the $2nI + 1$ rule, where n is the number of identical nuclei, and I is the spin number for that nuclei. For Cu(H$_{-1}$GHW), there are three nitrogen ligands and one oxygen ligand (3N + 1O) bound to the Cu(II). Therefore, there should be 7 superhyperfine peaks. However, when the paramagnetic electron is not coupled to the same ligand type all the time, as in the case with a bound water molecule in the Cu(H$_{-1}$GHW) complex, the intensity is diminished, and the peaks are less defined, see zoomed perpendicular region **Figure 1.11A**. When the electron is in the same ligand environment, as in a 4N binding like a Cu(H$_{-2}$(GHK)$_2$) complex, 9 superhyperfine coupling peaks are clearly defined, see zoomed perpendicular region **Figure 1.11B**.

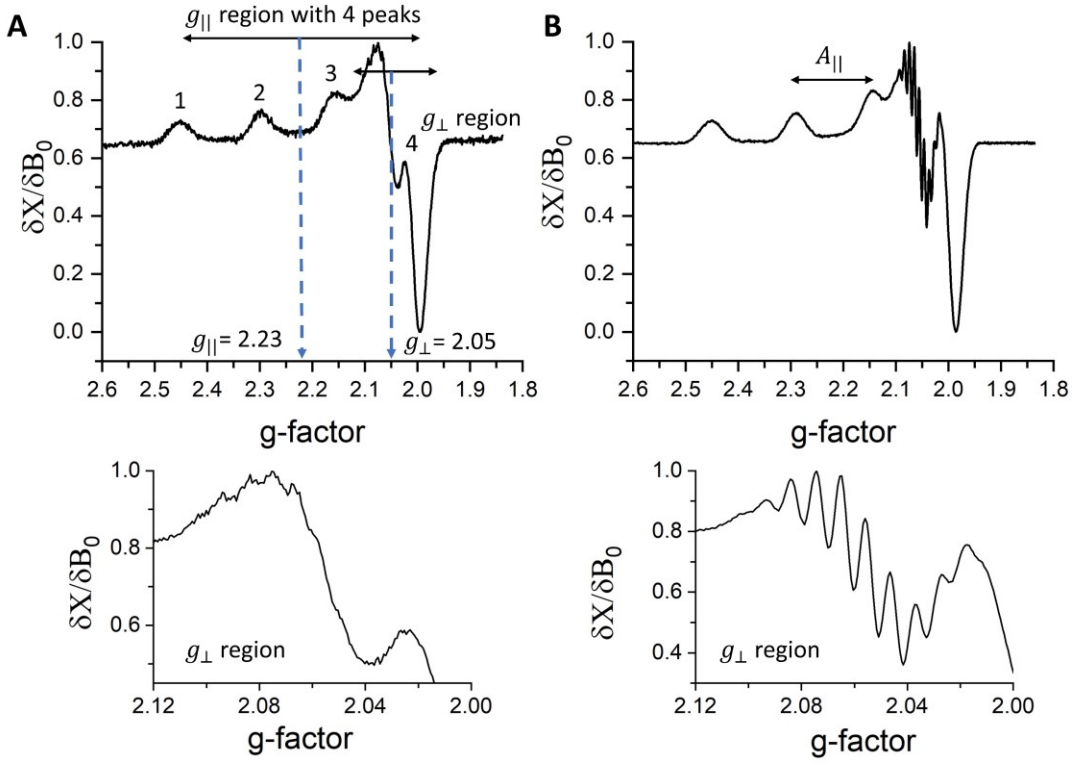

Figure 1.11: The powder EPR spectrum of Cu(H$_{-1}$GHW) (A) and of Cu(H$_{-2}$(GHK)$_2$) (B). Samples were frozen with liquid N_2, then run at low temperature at v = 9.5 GHz. The perpendicular region is highlighted below each spectrum to show superhyperfine coupling between the paramagnetic electron and its ligand environment.

1.6 Electrochemistry and cyclic voltammetry

Electrochemistry is the study of redox-active compounds and their ability to transfer electrons to generate or store energy. One of the most common electrochemical techniques is cyclic voltammetry, which has robust methods that can determine the physical and chemical properties of a redox-active system. Cyclic voltammetry is a potential sweep method in which the applied potential is scanned from some initial potential to a vertex potential, and then back to the initial potential. During the cyclic voltammetry experiment, information can be obtained about both the oxidized and reduced species, **Figure 1.12**. The half-wave potential, $E_{1/2}$, is the midpoint between the cathodic and anodic peak potentials, E_{pc} and E_{pa}, respectively, **Eq. 1.12**. The cathodic and anodic peak currents, i_{pc} and i_{pa}, are measured considering the double-layer capacitance (horizontal dotted lines) to determine the amount of current passed at the peak potential (vertical dotted lines).

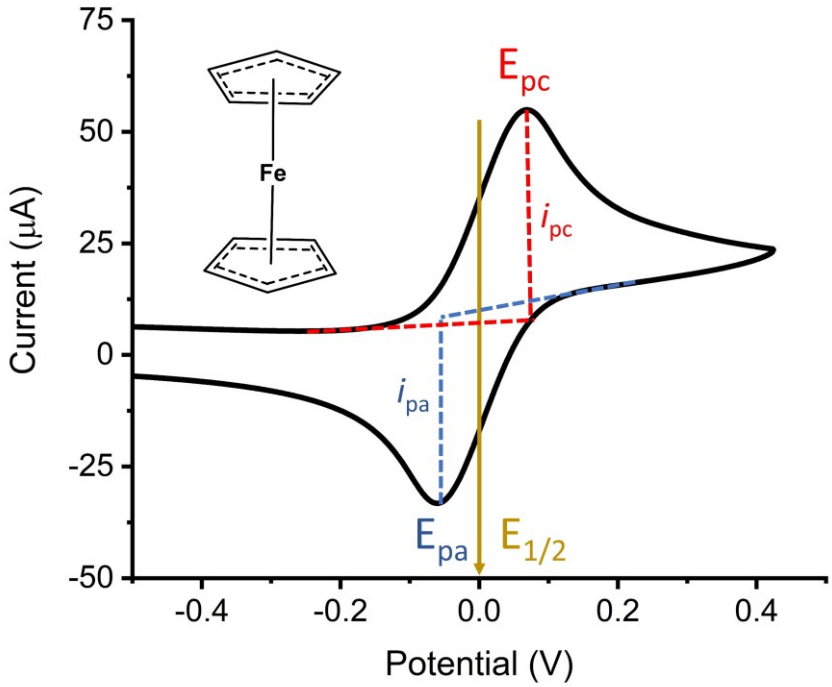

Figure 1.12: A cyclic voltammogram of 2 mM ferrocene (structure in the top left) in acetonitrile, using a glassy carbon working electrode, a platinum wire auxiliary electrode, and a Ag^+/Ag non-aqueous reference electrode (0.1 M $AgNO_3$ in MeCN with 0.1 M tetrabutylammonium perchlorate) with at a scan rate of 100 mV/s. The Fc^+/Fc couple redox potential is set to 0 V as an internal standard in electrochemical studies, which the *x*-axis is Potential vs Fc^+/Fc. The cathodic (red) and anodic (blue) peak potentials (E_{pc}, E_{pa}) and peak currents (i_{pc}, i_{pa}) are shown. The redox potential, or half-wave potential ($E_{1/2}$) is shown in yellow.

(**Eq. 1.12**) $E_{1/2} = \frac{1}{2}(E_{pc} + E_{pa})$

Since potential sweep methods involve a potential that is always changing, a charging current, i_c, is always present at the electrode surface. In **Figure 1.12**, the tangential lines that are drawn (horizontal dotted lines) are the baseline charging current for that scan rate and concentration of the analyte, as shown in **Eq. 1.13**, where C_d is the differential capacitance of the double layer (shown in the second equation), D_O is the diffusion coefficient, *n* is the number of electrons in the redox process, C_O^* is the bulk concentration of species, and *v* is the scan rate. In cyclic voltammograms, the double-layer capacitance can usually be manually inspected by hand (as shown in **Figure 1.12**) or by some electrochemistry software programs and usually doesn't need to be quantified, just subtracted from the actual current passed.

(**Eq. 1.13**) $\frac{|i_C|}{i_p} = \frac{C_d\, v^{1/2}\,(10^{-5})}{2.69\, n^{3/2}\, D_O^{1/2}\, C_O^*}$, $i = v\, C_d \left[1 - e^{-\frac{t}{R_s C_d}}\right]$

When the scan rate is very high, or the concentration of an analyte is very low, the resulting linear sweep voltammetry can be highly distorted. Therefore, cyclic voltammetry often requires effective concentration ranges where scan rates are limited. A common scan rate used is 100 mV/s and a concentration of 1 - 3 mM. The resulting vertical dotted lines for i_{pc} and i_{pa} in **Figure 1.12** are the amount of current passed due to the ferrocene being reduced or oxidized, with double-layer capacitance omitted. The ratio of peak currents, **Eq. 1.14**, is used as an indication of the reversibility of the redox process. When the ratio of peak currents approaches unity, then the system is considered completely reversible, while deviations from unity indicate quasi-reversibility or irreversibility. Importantly, the peak current can be used to determine the diffusion coefficients, D_o, of redox-active species by using the Randles-Sevcik equation, **Eq. 1.15**, where the constant 2.69 x 10^5 is determined by Faraday's constant, temperature, and the gas constant at standard temperature and pressure (STP) conditions, i_p is peak current measured, *n* is the number of electrons in the redox process, C_O^* is the bulk concentration of species, *A* is the area of the working electrode, and *v* is the scan rate. The diffusion coefficient is an indication of how well the species will move to and from the electrode surface and can be used to determine the thickness of the diffusion layer. Lastly, to determine the number of electrons in the redox process, the potential width between the

peaks is used, **Eq. 1.16**. In aqueous solution, a general rule is that a ΔE_p of 59 mV means one electron is in the redox process. In aprotic solutions, due to ohmic drop (high resistivity, IR drop), this can deviate from 59 mV. Thus, a factor of *x* was determined by setting the ferrocene *n* to 1 (as this is known), and determining the measured ΔE_p, then *x* is calculated for that solvent., **Eq. 1.17**.

(**Eq. 1.14**) $\frac{i_{pc}}{i_{pa}} = 1$, for reversible

(**Eq. 1.15**) $D_O = \left(\frac{i_p}{2.69x10^5\, n^{\frac{3}{2}}\, A\, C_O^*\, v^{\frac{1}{2}}}\right)^2$

(**Eq. 1.16**) $\Delta E_p = \left|E_{pc} - E_{pa}\right|$

(**Eq. 1.17**) $n = x\left(\frac{(59\,mV)}{(\Delta E_p)}\right)$

In cyclic voltammetry, a classical three-electrode system is used. As shown in **Figure 1.13**, there is a glassy carbon working electrode (WE), a platinum wire auxiliary electrode (AE), and a refillable $Ag/AgNO_3$ reference electrode (RE). In order for the RE to keep its constant potential, as is required for any RE, all current must be passed through the WE and AE. To do this, the WE and AE must be physically closer than the WE and RE. The electrodes are situated like in the photo in Figure 1.13. The solution is put into the vial, and Argon gas is bubbled through to desolvate O_2 gas before performing the experiment.

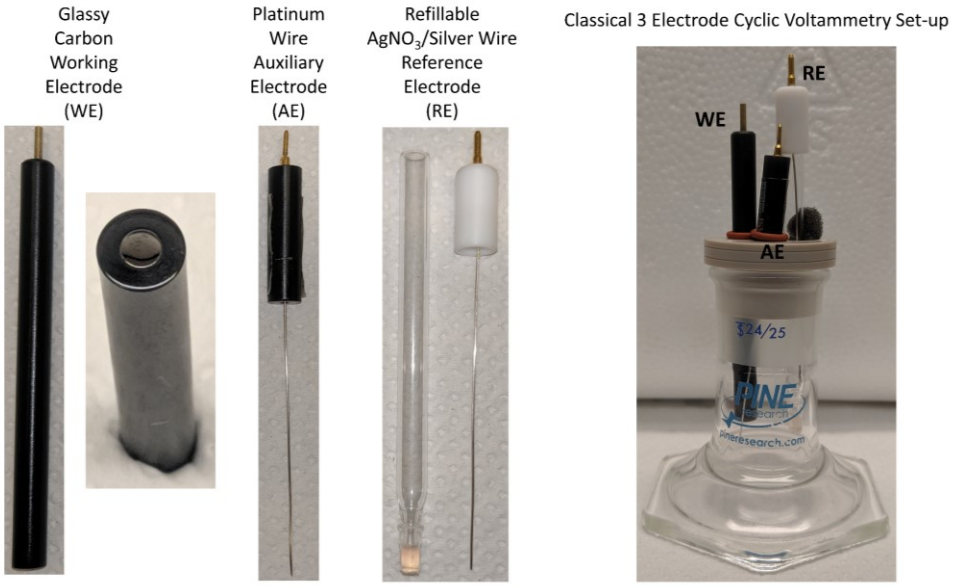

Figure 1.13: Pictures of a glassy carbon working electrode (WE), a platinum wire auxiliary electrode (AE), a refillable $Ag/AgNO_3$ reference electrode (RE), and their cyclic voltammetry setup.

1.7 Spectroelectrochemistry

Spectroelectrochemistry is the combination of both optical spectroscopy and electrochemistry. We can use specialized instrumentation that can hold a solution at a certain potential while its absorption spectroscopy is obtained. First, the potentials of each redox process are determined by conventional cyclic voltammetry. Then these values can be used to hold the potential constant while the absorption spectroscopy is obtained. **Figure 1.14** shows the Pine Research Honeycomb electrode plate that has both platinum WE and AE on the plate, where the WE is in the Honeycomb portion of the plate, and the AE runs around the edge.

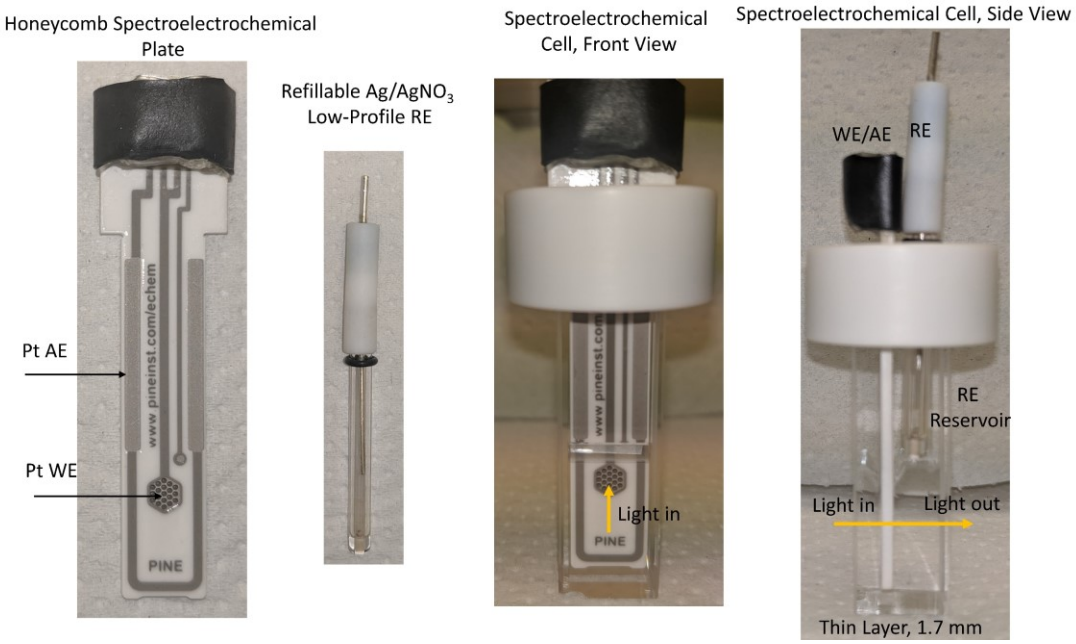

Figure 1.14: Spectroelectrochemical cell kit from Pine Research. The WE/AE plate and the low-profile refillable $Ag/AgNO_3$ RE are shown. A front and side view of the spectroelectrochemical cell kit show how the plate and RE fit into the thin layer quartz cuvette. There is a reservoir where the RE can contact the solution. The light in is always situated toward the front of the plate.

The location of the WE allows for quick equilibration of the solution to the applied potential. This is inserted in a thin layer quartz cuvette with a pathlength of ℓ = 1.7 mm. The electrode plate is connected via a USB port to the Wavedriver 20 instrument. The electrochemical cell can then be placed in a cuvette holder attached to a detector (Avantes AvaSpec 2048) and lamp source (Avantes AvaLight Dual DHc halogen-deuterium lamp) with fiber optic cables. The height of the beam of light is situated directly in the Honeycomb holes and is much more effective at the light being able to pass through than mesh electrode assemblies.

A low profile non-aqueous refillable $Ag/AgNO_3$ reference electrode is used and fits in the reservoir behind the plate. The UV-vis spectrum is taken while the instrument holds the potential at preset parameters. The Pine Research AfterMath software can simultaneously control both the potentiostat and the spectroscopy.

CHAPTER 1 REFERENCES

1. WorldHealthOrganization The Top 10 Causes of Death. https://www.who.int/news-room/fact-sheets/detail/the-top-10-causes-of-death (accessed 11/11/19).

2. Glenner, G. G.; Wong, C. W., Alzheimer's Disease: Initial Report of the Purification and Characterization of a Novel Cerebrovascular Amyloid Protein. *Biochem. Biophys. Res. Commun.* **1984,** *120* (3), 885-890.

3. Wong, C. W.; Quaranta, V.; Glenner, G. G., Neuritic Plaques and Cerebrovascular Amyloid in Alzheimer Disease are Antigenically Related. *Proc. Natl. Acad. Sci. U. S. A.* **1985,** *82* (24), 8729-8732.

4. Alzheimer'sAssociation Facts and Figures. https://www.alz.org/alzheimers-dementia/facts-figures (accessed 11/11/19).

5. Rosenberg, J. B.; Kaplitt, M. G.; De, B. P.; Chen, A.; Flagiello, T.; Salami, C.; Pey, E.; Zhao, L.; Ricart Arbona, R. J.; Monette, S.; Dyke, J. P.; Ballon, D. J.; Kaminsky, S. M.; Sondhi, D.; Petsko, G. A.; Paul, S. M.; Crystal, R. G., AAVrh.10-Mediated APOE2 Central Nervous System Gene Therapy for APOE4-Associated Alzheimer's Disease. *Hum Gene Ther Clin Dev* **2018,** *29* (1), 24-47.

6. Cuajungco, M. P.; Lees, G. J., Zinc metabolism in the Brain: Relevance to Human Neurodegenerative Disorders. *Neurobiol. Dis.* **1997,** *4* (3-4), 137-169.

7. Festa, R. A.; Thiele, D. J., Copper: An Essential Metal in Biology. *Curr. Biol.* **2011,** *21* (21), R877-R883.

8. Franz, K. J.; Metzler-Nolte, N., Introduction: Metals in Medicine. *Chem. Rev.* **2019,** *119* (2), 727-729.

9. Haas, K. L.; Franz, K. J., Application of Metal Coordination Chemistry To Explore and Manipulate Cell Biology. *Chem. Rev.* **2009,** *109* (10), 4921-4960.

10. Kiss, T.; Odani, A., Demonstration of the Importance of Metal Ion Speciation in Bioactive Systems. *Bull. Chem. Soc. Jpn.* **2007,** *80* (9), 1691-1702.

11. Kozlowski, H.; Janicka-Klos, A.; Brasun, J.; Gaggelli, E.; Valensin, D.; Valensin, G., Copper, Iron, and Zinc ions Homeostasis and Their Role in Neurodegenerative Disorders (Metal Uptake, Transport, Distribution and Regulation). *Coord. Chem. Rev.* **2009,** *253* (21), 2665-2685.

12. Kozlowski, H.; Luczkowski, M.; Remelli, M.; Valensin, D., Copper, Zinc and Iron in Neurodegenerative Diseases (Alzheimer's, Parkinson's and Prion Diseases). *Coord. Chem. Rev.* **2012,** *256* (19), 2129-2141.

13. Maret, W., Metalloproteomics, Metalloproteomes, and the Annotation of Metalloproteins. *Metallomics* **2010,** *2* (2), 117-125.

14. Maret, W., Zinc and Zinc Ions in Biological Systems. In *Encyclopedia of Metalloproteins*, Kretsinger, R. H.; Uversky, V. N.; Permyakov, E. A., Eds. Springer New York: New York, NY, 2013; pp 2396-2400.

15. Sigel, A. S., H. Sigel R. , *Interrelations Between Essential Metal Ions and Human Diseases*. Springer: Dordrecht, The Netherlands, 2013; Vol. 13, p 1-29, 229-286, 359-381, 389-409.

16. Tapiero, H.; Tew, K. D., Trace Elements in Human Physiology and Pathology: Zinc and Metallothioneins. *Biomed. Pharmacother.* **2003,** *57* (9), 399-411.

17. Yamasaki, S.; Sakata-Sogawa, K.; Hasegawa, A.; Suzuki, T.; Kabu, K.; Sato, E.; Kurosaki, T.; Yamashita, S.; Tokunaga, M.; Nishida, K.; Hirano, T., Zinc is a Novel Intracellular Second Messenger. *J. Cell Biol.* **2007,** *177* (4), 637-645.

18. Linder, M. C., Lomeli, N.A., Donley, S., Mehrbod, P.C, Cotton, S., Wooten, L., Copper Transport in Mammals. *Adv. Exp. Med. Biol.* **1999,** *448*, 1-16.

19. Pickart, L.; Freedman, J. H.; Loker, W. J.; Peisach, J.; Perkins, C. M.; Stenkamp, R. E.; Weinstein, B., Growth-modulating Plasma Tripeptide may Function by Facilitating Copper Uptake into Cells. *Nature* **1980,** *288* (5792), 715-717.

20. Rubino, J. T.; Franz, K. J., Coordination Chemistry of Copper Proteins: How Nature Handles a Toxic Cargo for Essential Function. *J. Inorg. Biochem.* **2012,** *107* (1), 129-143.

21. Kambe, T.; Tsuji, T.; Hashimoto, A.; Itsumura, N., The Physiological, Biochemical, and Molecular Roles of Zinc Transporters in Zinc Homeostasis and Metabolism. *Physiol. Rev.* **2015,** *95* (3), 749-784.

22. Krężel, A.; Maret, W., The Biological Inorganic Chemistry of Zinc Ions. *Arch. Biochem. Biophys.* **2016,** *611*, 3-19.

23. Que, E. L.; Bleher, R.; Duncan, F. E.; Kong, B. Y.; Gleber, S. C.; Vogt, S.; Chen, S.; Garwin, S. A.; Bayer, A. R.; Dravid, V. P.; Woodruff, T. K.; O'Halloran, T. V., Quantitative Mapping of Zinc Fluxes in the Mammalian Egg Reveals the Origin of Fertilization-induced Zinc Sparks. *Nat. Chem.* **2014,** *7*, 130.

24. Que, E. L.; Domaille, D. W.; Chang, C. J., Metals in Neurobiology: Probing Their Chemistry and Biology with Molecular Imaging. *Chem. Rev.* **2008,** *108* (5), 1517-1549.

25. Beuning, C. N.; Mestre-Voegtlé, B.; Faller, P.; Hureau, C.; Crans, D. C., Measurement of Interpeptidic Cu(II) Exchange Rate Constants by Static Fluorescence Quenching of Tryptophan. *Inorg. Chem.* **2018,** *57* (9), 4791-4794.

26. Meloun, B.; Morávek, L.; Kostka, V., Complete Amino Acid Sequence of Human Serum Albumin. *FEBS Letters* **1975,** *58* (1-2), 134-137.

27. Rózga, M.; Sokołowska, M.; Protas, A. M.; Bal, W., Human Serum Albumin Coordinates Cu(II) at its N-terminal Binding Site with 1 pM Affinity. *J. Biol. Inorg. Chem.* **2007,** *12* (6), 913-918.

28. Nguyen, M.; Robert, A.; Sournia-Saquet, A.; Vendier, L.; Meunier, B., Characterization of New Specific Copper Chelators as Potential Drugs for the Treatment of Alzheimer's Disease. *Chemistry – A European Journal* **2014,** *20* (22), 6771-6785.

29. Cherny, R. A.; Atwood, C. S.; Xilinas, M. E.; Gray, D. N.; Jones, W. D.; McLean, C. A.; Barnham, K. J.; Volitakis, I.; Fraser, F. W.; Kim, Y.-S.; Huang, X.; Goldstein, L. E.; Moir, R. D.; Lim, J. T.; Beyreuther, K.; Zheng, H.; Tanzi, R. E.; Masters, C. L.; Bush, A. I., Treatment with a Copper-Zinc Chelator Markedly and Rapidly Inhibits β-Amyloid Accumulation in Alzheimer's Disease Transgenic Mice. *Neuron* **2001,** *30* (3), 665-676.

30. Mital, M.; Zawisza, I. A.; Wiloch, M. Z.; Wawrzyniak, U. E.; Kenche, V.; Wróblewski, W.; Bal, W.; Drew, S. C., Copper Exchange and Redox Activity of a Prototypical 8-Hydroxyquinoline: Implications for Therapeutic Chelation. *Inorg. Chem.* **2016,** *55* (15), 7317-7319.

31. Beuning, C. N.; Barkley, N. E.; Basa, P. N.; Burdette, S. C.; Levinger, N. E.; Crans, D. C., Coordination Chemistry of a Controlled Burst of Zn^{2+} in Bulk Aqueous and Nanosized Water Droplets with a Zincon Chelator. *Inorg. Chem.* **2019,** *Published ASAP Dec. 6 2019* DOI: 10.1021/acs.inorgchem.9b02848.

32. WorldHealthOrganization 10 Facts on Tuberculosis. https://www.who.int/features/factfiles/tuberculosis/en/ (accessed 11/11/19).

33. Azerad, R.; Cyrot, M. O.; Lederer, E. L., Structure of the Dihydromenaquinone-9 of *Mycobacterium phlei*. *Biochem. Biophys. Res. Commun.* **1967,** *27* (2), 249-252.

34. Azerad, R.; Cyrot-Pelletier, M.-O., Structure and Configuration of the Polyprenoid Side Chain of Dihydromenaquinones from Myco- and Corynebacteria. *Biochim.* **1973,** *55* (5), 591-603.

35. Collins, M. D.; Jones, D., Distribution of Isoprenoid Quinone Structural Types in Bacteria and Their Taxonomic Implication. *Microbiol. rev.* **1981,** *45* (2), 316-354.

36. Collins, M. D.; Pirouz, T.; Goodfellow, M.; Minnikin, D. E., Distribution Of Menaquinones In Actinomycetes and Corynebacteria *J. Gen. Microbiol.* **1977,** *100* (JUN), 221-230.

37. Upadhyay, A.; Fontes, F. L.; Gonzalez-Juarrero, M.; McNeil, M. R.; Crans, D. C.; Jackson, M.; Crick, D. C., Partial Saturation of Menaquinone in Mycobacterium tuberculosis: Function and Essentiality of a Novel Reductase, MenJ. *ACS Cent. Sci.* **2015,** *1* (6), 292-302.

38. Upadhyay, A.; Kumar, S.; Rooker, S. A.; Koehn, J. T.; Crans, D. C.; McNeil, M. R.; Lott, J. S.; Crick, D. C., Mycobacterial MenJ: An Oxidoreductase Involved in Menaquinone Biosynthesis. *ACS Chem. Biol.* **2018,** *13* (9), 2498-2507.

39. Beuning, C. N.; Koehn, J. T.; Crick, D. C.; Crans, D. C., Redox Potentials of Truncated Menaquinone Analogs in Aprotic Solvents are Sensitive to Saturation in the Isoprene Side Chain. **2020,** *Submitted*.

PART 1) MEASUREMENT OF THE KINETIC RATE CONSTANTS OF INTERPEPTIDIC DIVALENT TRANSITION METAL ION EXCHANGE IN NEURODEGENERATIVE DISEASE

CHAPTER 2: MEASUREMENT OF INTERPEPTIDIC CU(II) EXCHANGE RATE CONSTANTS BY STATIC FLUORESCENCE QUENCHING OF TYRPTOPHAN[1]

2.1 Summary

The interpeptidic exchange of Cu(II) between biologically relevant peptides like Gly-His-Lys (GHK) was measured through proximity static fluorescence quenching of a noncoordinating tryptophan residue by Cu(II). The inability to spectrally distinguish between starting and final $Cu(H_{-1}GHK)^{+}$ complexes by the current methods was solved by the replacement of noncoordinating lysine for tryptophan in the starting complex, $Cu(H_{-1}GHW)$. Because the apoGHW is the only fluorescent species, the recovered fluorescence is directly proportional to the $[Cu(II)]_{exchanged}$ between GHW and GHK. The apparent second-order rate constants of the exchanges from $Cu(H_{-1}GHW)$ to GHK and DAHK are 1.6 (±0.2) × 10^2 and 5.0 (±0.7) × 10^1 $M^{-1}s^{-1}$, respectively. The easy-to-implement kinetic fluorescent method described here for Cu(II) interpeptidic exchange can be expanded to other biological systems.

2.2 Introduction to interpeptidic exchange kinetics using tryptophan fluorescence quenching and small Cu(II) tri- and tetra-peptide complexes

The role of interpeptidic metal ion exchange in disease is becoming of increasing importance and beginning to be addressed in a range of biological systems including neurodegenerative illnesses like Alzheimer's disease.[3-12] Specifically, Cu(II) coordinates in structural or functional sites in proteins like amyloid-beta (Aβ) the primary protein associated with Alzheimer's disease, human serum albumin (HSA), ceruloplasmin, tau and prions where the binding ligands are mainly nitrogen (N) sites like the amine terminus (NH_2), histidine (N_{im}), and deprotonated amide backbone (N^-).[3-4, 13-17] Since GHK (Gly-His-Lys) is associated with cell growth factor, and DAHK (Asp-Ala-His-Lys) is the N-terminal sequence of HSA, investigation of the homo- or hetero-inter-peptidic Cu(II) exchange between GHK and DAHK binding sites is important as these two motifs co-exist in the serum.[16-19] The GHK and DAHK peptides readily form metal

[1] Beuning, C. N.; Mestre-Voegtlé, B.; Faller, P.; Hureau, C.; Crans, D. C., Measurement of Interpeptidic Cu(II) Exchange Rate Constants by Static Fluorescence Quenching of Tryptophan. *Inorg. Chem.* **2018,** *57* (9), 4791-4794. DOI: 10.1021/acs.inorgchem.8b00182

coordination complexes in the presence of Cu(II) ions, **Figure 2.1**, and their structures and stoichiometry have been determined by electron paramagnetic resonance (EPR), UV-Vis spectrometry, isothermal titration calorimetry (ITC), and Job Plots.[20-21] Despite the limitations of comparing the behavior of short peptide complexes to large protein complexes, the similar Cu(II) coordination sites of the chosen model peptides are suitable for use in the proof of concept studies to determine inter-peptidic Cu(II) exchange rate constants by static fluorescence quenching of tryptophan.[3-4, 6-10, 12, 22-25]

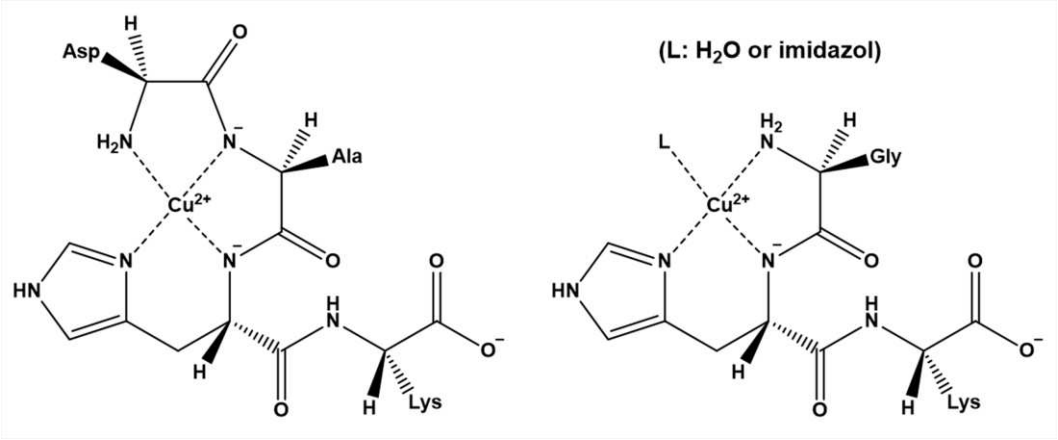

Figure 2.1 Solution structures of Cu(II) bound to DAHK (left, Lys = Trp for DAHW) and GHK (right, Lys = Trp for GHW, L = H_2O) in 0.1 M HEPES at pH 7.4. The L = H_2O in the Cu(H_{-1}GHW) complex can be readily exchanged by an incoming imidazole ligand (L = N_{im}) from a second added peptide, forming Cu(H_{-1}GHW)(GHK/DAHK), a 1:2 ternary complex. The overall charges on the peptides were omitted for clarity.

Previous studies of Cu(II) exchange from short peptide complexes were performed with free amino acids, EDTA, and nitrogen-rich ligands like the ethylenediamine family as their initial, ternary, and final complexes can be spectrally distinguished by stopped-flow absorbance, see selected systems in **Table 2.1**.[2, 26-37] We have designed a fluorescence experiment by replacing non-coordinating lysine (K, Lys) with tryptophan (W, Trp) and using proximity static fluorescence quenching of GHW by paramagnetic Cu(II). The critical energy transfer distance between Cu(II) and GHW must be within a maximum of 14 Å for greater than 90% quenching, where greater distances provide less or no quenching.[38] Cu(II) quenching of GHW residues has been extensively used to examine metal-binding domains of proteins and so peptides containing W within the metal-binding site are probes to measure inter-peptidic processes.[38-39]

Table 2.1: Cu(II) exchange rate constants of some selected systems.

Initial Cu (II) Complex + Ligand → Final Cu(II) Complex	Ligand Donors of Initial Complex	Ligand Donors of Final Complex	Rate Constant, k $M^{-1}s^{-1}$, for Initial to Final Complex	pH	Ref.
$Cu(H_{-2}GGG)^{-}$ + HCys → $Cu(H_{-1}GGG)(Cys^{-})$	NH_2, 2 N^{-}, OH_2	2 NH_2, N^{-}, S^{-}	> x 10^6	8.7	2
$Cu(H_{-1}GGG)(Cys^{-})$ + HCys → $Cu(Cys^{-})_2$	2 NH_2, N^{-}, S^{-}	2 NH_2, 2 S^{-}	3.3 x 10^3	8.7	2
$Cu(H_{-1}HGG)(Cys^{-})$ + HCys → $Cu(Cys^{-})_2$	2 NH_2, N_{im}, S-	2 NH_2, 2 S^{-}	> x 10^6	8.7	2
$Cu(H_{-1}LGG)(Cys^{-})$ + HCys → $Cu(Cys^{-})_2$	2 NH_2, N^{-}, S^{-}	2 NH_2, 2 S^{-}	9 x 10^2	8.7	2
$Cu(H_{-3}GGGG)^{2-}$ + Gly^{-} → $Cu(H_{-2}GGGG)(Gly^{-})$	NH_2, 3 N^{-}	2 NH_2, 2 N^{-}	7.8 x 10^5	9-10	26
$Cu(H_{-2}GGHG)^{-}$ + Pes → $Cu(H_{-1}GGHG)(Pes^{-})$	NH_2, 2 N^{-}, N_{im}	2 NH_2, N^{-}, S-	1.8	7.5	30
$Cu(H_{-2}GGHG)^{-}$ + Pes → $Cu(H_{-1}GGHG)(Pes^{-})$	NH_2, 2 N^{-}, N_{im}	2 NH_2, N^{-}, S-	4.1	8.5	30
$Cu(H_{-1}GGGGG)(Pes^{-})$ + Pes → $Cu(Pes^{-})_2$	2 NH_2, N^{-}, S^{-}	2 NH_2, 2 S^{-}	3.6 x 10^1	7.5	30
$Cu(H_{-1}GGGGG)(Pes^{-})$+ Pes → $Cu(Pes^{-})_2$	2 NH_2, N^{-}, S^{-}	2 NH_2, 2 S^{-}	1.1 x 10^2	8.5	30
$Cu(_L\text{-His})_2$ + HSA → $Cu(HSA)(_L\text{-His})$	2 NH_2, N_{im}, COO^{-} (or 2 N_{im})	NH_2, 2 N^{-}, N_{im}	4.85 x 10^2	7.5	16
$Cu(_L\text{-His})_2$ + GGH → $Cu(H_{-1}GGH)(_L\text{-His})$	2 NH_2, N_{im}, COO^{-} (or 2 N_{im})	2 NH_2, N^{-}, N_{im}	1.21 x 10^2	7.5	16
$Cu(H_{-2}GGG)^{-}$ + trien → $Cu(trien)^{2+}$	NH_2, 2 N^{-}, OH_2	Amine N	1.1 x 10^7	8.4	37
$Cu(H_{-2}GGH)^{-}$ + trien → $Cu(trien)^{2+}$	NH_2, 2 N^{-}, N_{im}	Amine N	5 x 10^{-1}	uk	28
$Cu(H_{-1}GHG)$ + HCys → $Cu(H_{-1}GHG)(Cys^{-})$	NH_2, OH_2 N^{-}, N_{im}	2 NH_2, N^{-}, S^{-}	> x 10^6	8.7	29
$Cu(H_{-2}GGH)^{-}$ + HCys → $Cu(H_{-1}GGH)(Cys^{-})$	NH_2, 2 N^{-}, N_{im}	2 NH_2, N^{-}, S^{-}	4 x 10^1	8.7	29
$Cu(H_{-1}GHG)(Cys^{-})$ + HCys → $Cu(Cys^{-})_2$	2 NH_2, N^{-}, S^{-}	2 NH_2, 2 S^{-}	6.9 x 10^3	8.7	29
$Cu(H_{-1}GGH)(Cys^{-})$ + HCys → $Cu(Cys^{-})_2$	2 NH_2, N^{-}, S^{-}	2 NH_2, 2 S^{-}	3-4 x 10^3	8.7	29
$Cu(H_{-1}GHW)$ + GHK^{+}→ $Cu(H_{-1}GHK)^{+}$	NH_2, OH_2, N^{-}, N_{im}	NH_2, OH_2, N^{-}, N_{im}	1.56 (± 0.16) x 10^2	7.4	1
$Cu(H_{-1}GHK)^{+}$ + GHW→ $Cu(H_{-1}GHW)$	NH_2, OH_2, N^{-}, N_{im}	NH_2, OH_2, N^{-}, N_{im}	4.26 (± 0.31) x 10^2	7.4	UP
$Cu(H_{-1}GHW)$ + DAHK → $Cu(H_{-2}DAHK)^{-}$	NH_2, OH_2, N^{-}, N_{im}	NH_2, 2 N^{-}, N_{im}	5.0 (± 0.7) x 10^1	7.4	1
$Cu(H_{-2}DAHW)^{2-}$ + GHK^{+}→ $Cu(H_{-1}GHK)^{+}$	NH_2, 2 N^{-}, N_{im}	NH_2, OH_2, N^{-}, N_{im}	Very slow	7.4	1
$Cu(H_{-2}DAHW)^{2-}$ + DAHK → $Cu(H_{-2}DAHK)^{-}$	NH_2, 2 N^{-}, N_{im}	NH_2, 2 N^{-}, N_{im}	Very slow	7.4	1

*Abbreviations: Gly = Glycine, Cys = Cysteine, His = Histidine, Pes = Penicillamine, HSA = human serum albumin, trien = triethylenetetraamine, UP = unpublished

According to **Eq. 2.1**, the Cu(II) complexes are characterized as $Cu(H_{-n}P)^{(m-n+1)}$ where m is the overall charge of apoP (where P = GHK or DAHK), and n reflects the number of N^{-} donor ligands in the complex. In our system, when P = GHK then m = 1, n = 1 and when P = DAHK then m = 0, n = 2. The apoGHW peptide is fluorescent, and the $Cu(H_{-1}GHW)$ complex is non-fluorescent; thus, stoichiometric amounts of apoGHW are produced when the non-fluorescent GHK (homo-inter-peptidic exchange) or

DAHK (hetero-inter-peptidic exchange) peptides are added, **Eq. 2.1**. When complex equilibria reactions exist, non-pseudo first-order kinetic approaches to determine rate constants are necessary. For example, a large excess of one reagent in **Eq. 2.1** leads to different complex speciation, specifically 1:1 versus 1:2 (Cu:P) complexes. The conditions under which the correct speciation is present must be identified before the kinetics can be measured. In this case, all kinetic measurements for the Cu(H_{-1}GHW) exchanges were performed under specific pH, relative concentrations, and buffer conditions to obtain the 1:1 speciation.

$$(\textbf{Eq. 2.1})\ Cu(H_{-n}GHW) + P^{m} \underset{\rightleftharpoons}{k_{obsP}} Cu(H_{-n}P)^{(m-n+1)} + GHW + (n\text{-}1)H^{+}$$

2.3 Experimental methods

2.3.1 Materials

The GHW (99.73% pure), GHK (99.73%), DAHW (96.89%), and DAHK (98.64%) peptides used were purchased from GeneCust (Luxembourg). The source of Cu(II) ions was $CuSO_4 \bullet 5H_20$ purchased from Aldrich. Buffer chemicals HEPES (99.5%) and NaOH (97.0%) were purchased from Sigma. All water used was purified by a Milli-Q purification system to 17-18 MΩ•cm resistivity.

2.3.2 Instrumentation and software

The UV-vis experiments were performed on a BMG LabTech SpectroStar Nano or a Perkin-Elmer Lambda 25 spectrophotometer. Fluorescence experiments were performed on a Fluorolog-3 or Fluorolog-4 Horiba Fluorimeter or BMG ClarioStar Fluorimeter. Electron paramagnetic resonance (EPR) experiments were performed on a Bruker spectrometer Elexys E500 instrument. Quartz or glass cuvettes with a 1 cm path length were used. Where applicable well plates used had 200 µL volumes and were treated not to absorb UV light used to excite in fluorescence experiments. All data were analyzed in OriginPro 2017b-2019b (student version) or Excel 2016.

2.3.3 UV-vis spectroscopy

The UV-vis samples were designed so that the addition of Cu(II) titrant volume did not significantly affect peptide concentration by dilution. Stock peptides were diluted to approximately 1 mM with 0.1 M HEPES buffer at pH 7.40 in the cuvette before titration with Cu(II) – for detailed concentration determination, see section 1.3.6. Samples were mixed upon each aliquot of Cu(II) added (0.1 to 0.2 mol equivalence) before a spectrum was taken. The tryptophan-containing peptides were directly measured through their

tryptophan absorbance, λ_{max} = 280 nm and ε = 5690 $M^{-1}cm^{-1}$. Using Beer's law, **Eq. 1.1**, concentration and absorbance can be directly related. The $Cu(H_{-1}GHK)^{+}$ and $Cu(H_{-1}GHW)$ have λ_{max} = 600 nm and ε = 50 $M^{-1}cm^{-1}$ while the $Cu(H_{-2}DAHK)^{-}$ and $Cu(H_{-2}DAHW)^{2-}$ have λ_{max} = 525 nm and ε = 100 $M^{-1}cm^{-1}$, **Figure 2.2**. The HEPES buffer, apoGHK, and apoDAHK have no absorbance where the Cu(II) complexes form, 400 – 800 nm, **Figure 2.3**. The apoGHW and apoDAHW both absorb at 280 nm (ε = 5690 $M^{-1}cm^{-1}$) and within the 400 – 800 nm have little absorbance, **Figure 2.3**. The UV-Vis instrument (Perkin-Elmer Lambda 25) is equipped with two cuvette holders, one for the sample and the other for the background, in this case, is 0.1 M HEPES. Thus, the data taken these figures are background corrected at the time of acquisition.

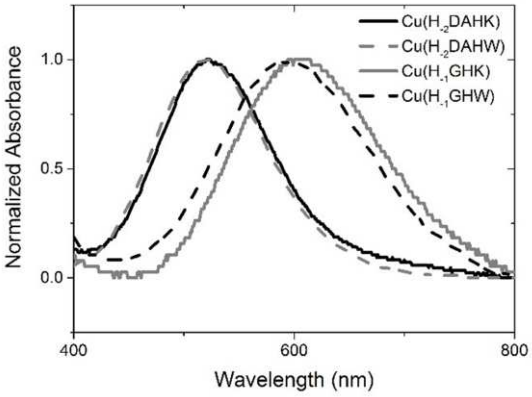

Figure 2.2 The $Cu(H_{-1}GHK)^{+}$ and $Cu(H_{-2}DAHK)^{-}$ complexes have a λ_{max} = 600 nm (ε = 50 $M^{-1}cm^{-1}$) and 525 nm (ε = 100 $M^{-1}cm^{-1}$), respectively.[1-2] Normalized UV-Vis spectra for all four complexes (in 0.1 M HEPES, pH 7.4) are shown to confirm they have identical maximum wavelengths. The GHW complex is slightly shifted as compared to the GHK complex and could be due to slight variations of pH.

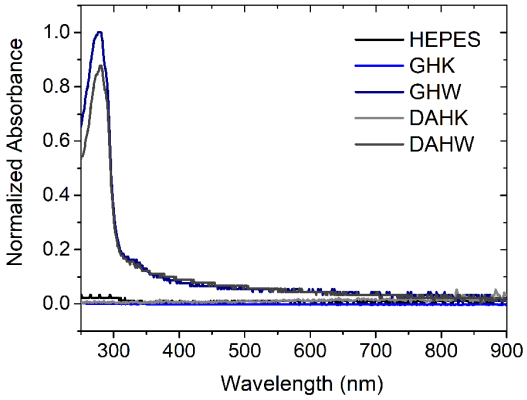

Figure 2.3 The normalized control UV-Vis spectra show no absorbance of HEPES buffer, apoGHK, and apoDAHK between 400 – 800 nm and little absorbance of apoGHW and apoDAHW between 400 – 800 nm, while the tryptophan absorbance is seen at λ_{max} = 280 nm (ε = 5690 $M^{-1}cm^{-1}$).

2.3.4 Fluorescence spectroscopy and sample preparation

Kinetic measurements were designed to take advantage of paramagnetic fluorescence static quenching of tryptophan by Cu(II) proximity to the fluorophore. Upon the Cu(II) exchange, the fluorescence recovery of the unbound tryptophan peptide's (apoGHW) fluorescence recovery was monitored with time. The method of initial rates was used for rate law determination and rate constant calculation. Since, at such low concentrations, the fluorescence intensity (I_F) is linearly proportional to concentration following **Eq. 1.2**,

the apo[GHW] can be determined from the experimental data by calibration curves taken before kinetic measurements. Therefore, the maximum concentration whose fluorescence signal is linearly proportional is determined by **Eq. 1.3**. As all Cu(H_{-1}GHW) fluorescence is quenched, the amount of recovered apo[GHW] observed is also equal to the concentration of Cu(II) exchanged since it is a 1:1 complex in these conditions. Thus the $[Cu(II)]_{exchanged}$ can be measured with time to determine a rate of Cu(II) exchange. The rate constants were determined at 95% confidence intervals with 17 and 14 degrees of freedom for the Cu(H_{-1}GHW) to GHK and DAHK exchanges, respectively. For Cu(H_{-1}GHW) measurements in the Fluorolog-3 or Fluorolog-4 Horiba Fluorimeters the following parameters were used; a quartz or glass cell of 1 cm path length, $\lambda_{excitation}$ = 290 nm, $\lambda_{emission}$ = 365 nm, an emission and excitation slit width of 5 nm, and 1000-2000 µL total sample volume.

Samples were prepared so that the added Cu(II) ions and incoming peptide GHK/DAHK were 1-5 µL of the total volume to minimize any dilution effects or changes in pH. For DAHW measurements in the BMG ClarioStar Fluorimeter, a 290 ± 10 nm excitation filter and a $\lambda_{emission}$ = 352 nm were used along with 200 µL UV treated well plates. All kinetic experiments for GHW exchanges were performed under conditions where there was no large excess of GHK/DAHK. This could induce preferential 1:2 Cu:P complexes. The kinetic experiment concentrations were chosen in the range where the ratio of [Cu(H_{-1}GHW)]/[GHK] (or [DAHK]) versus rate was linear, which resulted in the second-order kinetic rate constants.

2.3.5 Electron paramagnetic resonance spectroscopy and sample preparation

All spectra are normalized in both the derivative of the signal (*y*-axis) and the g factor (*x*-axis), where the g factor is a dimensionless value and is determined by the EPR equation (**Eq. 2.2**) where *h* = 6.626 x 10^{-34} J·s (Plank's constant), *v* is the constant frequency of the experiment in Hz, β = 9.274 x 10^{-28} $J \cdot G^{-1}$ (Bohr magneton), and B_o is the value of the varied magnetic field in Gauss. For experiments run on different days, which may have differences in the frequency, plotting the EPR spectra with these axes allows for direct spectral comparison. The $A_{//}$ (hyperfine coupling constants) values are determined by using the spectra and determining the frequency window between peaks.

(**Eq. 2.2**) $g = (hv)^*(\beta B_o)^{-1}$

The 1:1 Cu(II): GHW and Cu(II):DAHW samples were prepared at [Cu(II)-Peptide] = 0.5 mM in 0.1 M HEPES at pH 7.40. The samples were approximately 200 µL in which 40 µL was a 50/50 Glycerol/Water

mixture to give an 80:20 HEPES-Water : Glycerol ratio. The samples were vortexed to ensure complete mixing, transferred to an EPR tube, left uncapped, and then frozen with liquid N_2 within 2 minutes of preparation (frozen to ensure capture of ternary species). The samples were then run on the EPR instrument at approximately 9.5 GHz (exact frequencies GHK – 9.437358 GHz, GHW – 9.516630 GHz, DAHK – 9.531073 GHz, and DAHW – 9.511427 GHz). The 1:2 Cu(II):GHK samples run at 0.10, 0.20, 0.50, and 1.0 mM Cu(II) (double these concentrations for GHK) were prepared and ran in the same fashion as described above. The concentration range for the EPR study was chosen as this is a working range for EPR experiments.

2.3.6 Stock peptide preparation and concentration determination

Peptide stock solutions of approximately 50 mM in DI water were prepared given that trifluoroacetic acid (TFA) anions co-precipitate during peptide synthesis on cationic peptide sites. The molecular mass of these co-precipitated peptides is larger than the peptides alone where GHW, GHK, DAHW, and DAHK have molecular masses of 398.42, 340.38, 527.53, and 469.49 g/mol, respectively, but have apparent molecular masses of 626.16, 682.16, 755.20, and 811.21 g/mol, respectively, when TFA anions are regarded. To determine the actual concentration of the stock peptide solutions of a known concentration of Cu(II) ions (from $CuSO_4$•$5H_20$ in DI H_2O with 0.5151 M concentration was determined by absorbance ε = 12 $M^{-1}cm^{-1}$ at 800 nm and titration by Zincon monosodium salt before dilution) were titrated into a peptide solution of approximately 1 mM. All four peptides chelate Cu(II) in a 1:1 mole ratio with high affinity and have UV-Vis d→d transition maxima at 525 or 600 nm for DAHK/W and GHK/W, respectively, **Figure 2.2**.

A Job Plot of net absorbance (Abs λ_{max} – Abs_{400nm}) vs µL Cu(II) titrated was used to calculate the peptide concentration by using the maximum volume of Cu(II) and calculating peptide concentration assuming a 1:1 molar ratio, **Figure 2.4, Eq. 2.3**. The gain in absorbance near 400 nm is due to the growth of a charge transfer band when $Cu(H_{-1}GHK)^+$ is created in high concentrations, e.g., toward the end of the titration. **Figure 2.4** shows an example of this type of plot for determination of GHK stock concentration, where the left panel is the absorbance growth of $Cu(H_{-1}GHK)^+$ as Cu(II) is titrated into a solution of GHK (for this example it was 20 µL stock in 1000 µL HEPES) and the right panel is the Job Plot showing the apex at approximately 1 mol equivalence near 16 uL of Cu(II) added. The Job Plots of all four peptides showed a 1 mole equivalence of Cu(II) ions were needed to completely titrate the peptides, indicating the

1:1 coordination ratio in the experimental conditions. These titrations, in combination with both the EPR and UV-Vis spectroscopy, indicate the 1:1 coordination ratio. Actual peptide concentrations are approximately 10-20% lower than the apparent molecular mass calculated concentration with TFA anions. All stock solutions were prepared in Milli-Q water and stored in the freezer. The UV-Vis working peptide solutions were prepared in 0.1 M HEPES at pH 7.40 (pH increased with NaOH) to promote the correct Cu(II) speciation.

(**Eq. 2.3**) [GHK] = L Cu(II) * mol/L Cu(II) * 1 mol GHK/1 mol Cu(II) * 1/L GHK

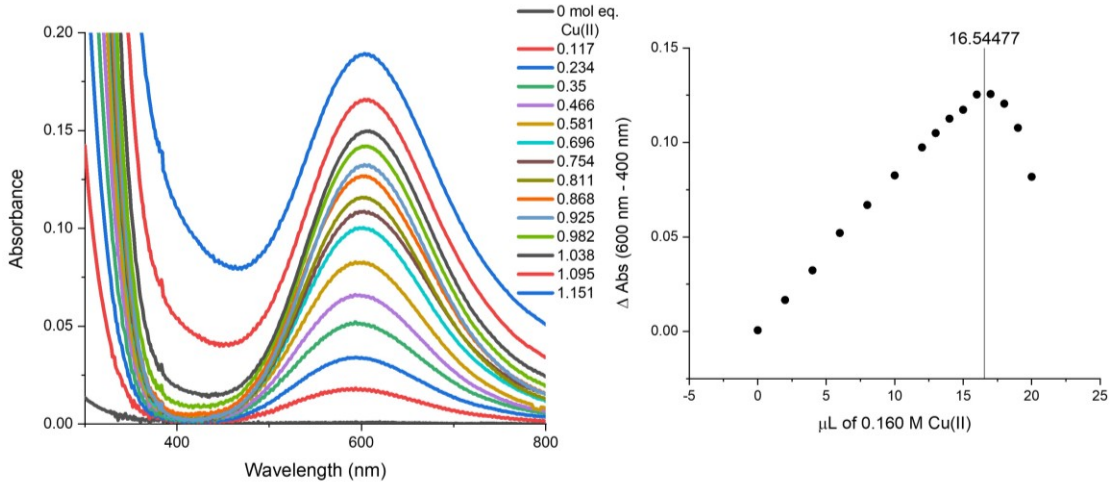

Figure 2.4 *Left* Absorbance of $Cu(H_{-1}GHK)^+$ as GHK is titrated with Cu(II). The large increases at 600 nm are due to charge transfer bands of the complex and indicate when the titration is complete. Cu(II) volumes added were, 0, 2, 4, 6, 8, 10, 12, 13, 14, 15, 16, 17, 18, 19, and 20 µL, the mol equivalence were determined by mol Cu(II)/mol GHK after determining the GHK concentration. *Right* Job Plot of the ΔAbsorbance (600 nm – 400 nm) versus the volume of a known [Cu(II)] added. At the apex, all GHK is titrated by Cu(II) in a 1:1 ratio, so the stock concentration of GHK can be determined by dimensional analysis, given that [Cu(II)] is known and the stock GHK volume that was diluted is known (in this case the aliquot used was 20 uL of stock GHK).

2.4 Results and discussion

To demonstrate that the replacement of the basic and aliphatic K for the neutral and aromatic W did not impact the Cu(II) coordination chemistry, the solution structures of the W peptide complexes were examined by both EPR and UV-Vis spectroscopies. The N atoms of K or W residues are not likely candidates for Cu(II) coordination as NH_2, N^-, and N_{im} sites are heavily preferred for these peptides at physiological pH.[34, 40] The solution Cu(II) coordination environments of the DAHK/DAHW complexes are 4N binding in the equatorial plane (NH_2, 2 N^-, and N_{im}) and of the GHK/GHW complexes are 3N+1O binding

in the equatorial plane (NH_2, N^-, N_{im}, and OH_2), **Figure 2.1**.[20] The low-temperature EPR spectra for all four complexes are given in **Figure 2.5,** where the lysine containing peptide complexes were previously reported.[20] The EPR hyperfine coupling constants and g factors were determined for the W containing peptides for the parallel and/or perpendicular EPR regions; Cu(H_{-1}GHW) has $g_{//}$ = 2.23, $A_{//}$ (^{63}Cu) = 560 MHz, and $g_{\perp}$ of 2.05, identical to those previously reported for Cu(H_{-1}GHK)$^+$.[20] Cu(H_{-2}DAHW)$^{-2}$ has $g_{//}$ of 2.19, $A_{//}$ (^{63}Cu) = 596 MHz, and $g_{\perp}$ of 2.04, identical to those previously reported for Cu(H_{-2}DAHK)$^-$.[20] The UV-Vis spectra of all four Cu(II)-peptide complexes were measured and their maximum wavelengths were determined to be λ = 525 nm (ε = 100 $M^{-1}cm^{-1}$) for DAHK/DAHW and λ = 600 nm (ε = 50 $M^{-1}cm^{-1}$) for GHK/GHW for the d→d transition of the coordinated Cu(II), **Figure 2.2**.[20-21] Therefore, the UV-Vis and EPR spectroscopic signatures of the Cu(II) complexes of W and K peptides document the identical equatorial plane Cu(II) coordination environment.

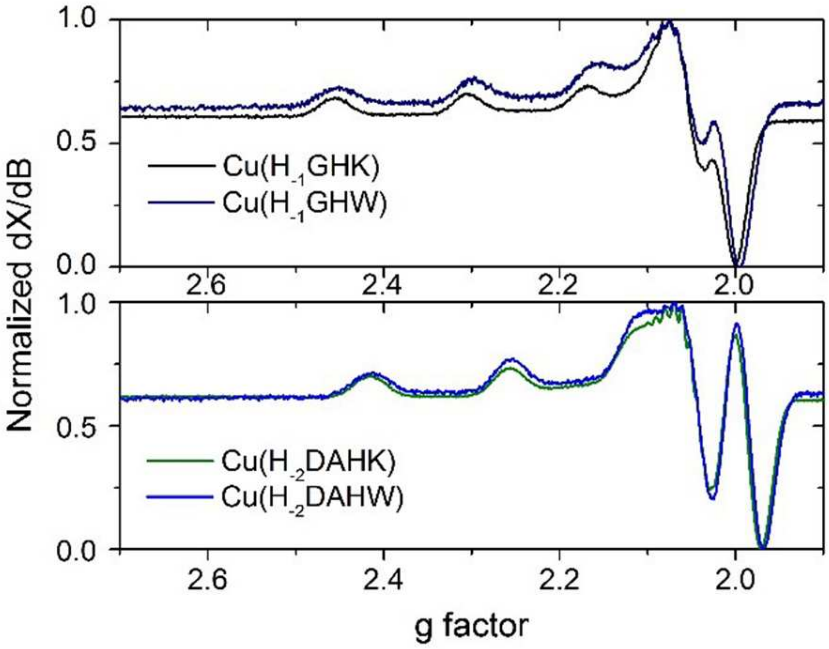

Figure 2.5 Frozen EPR spectra (v ≈ 9.5 GHz – see section 1.3.5 for exact values) of all four peptide complexes are shown, 0.5 mM, 0.1 M HEPES pH 7.4, 10 % (v/v) glycerol, frozen with liquid N_2, T = 100 *K*, and under non-saturating conditions.

(**Eq. 2.4**) $$\frac{d[GHW]_{recovered}}{dt} = \frac{d[Cu(II)]_{exchanged}}{dt} = k_{obsP}\,[Cu(H_{-1}GHW)][P]$$

The forward rate laws of the exchange reactions in **Eq. 2.1** were determined experimentally with the method of initial rates. The Log Rate versus Log [Peptide] graph in **Figure 2.6** shows slopes equal to one for all reactants, which defined each reactant as first order and resulted in an overall second-order rate law, **Eq. 2.4**, see **Tables 2.2** (GHK) and **2.3** (DAHK) for all concentration profiles used for the exchange kinetics for each peptide as well as the kinetic constants determined.

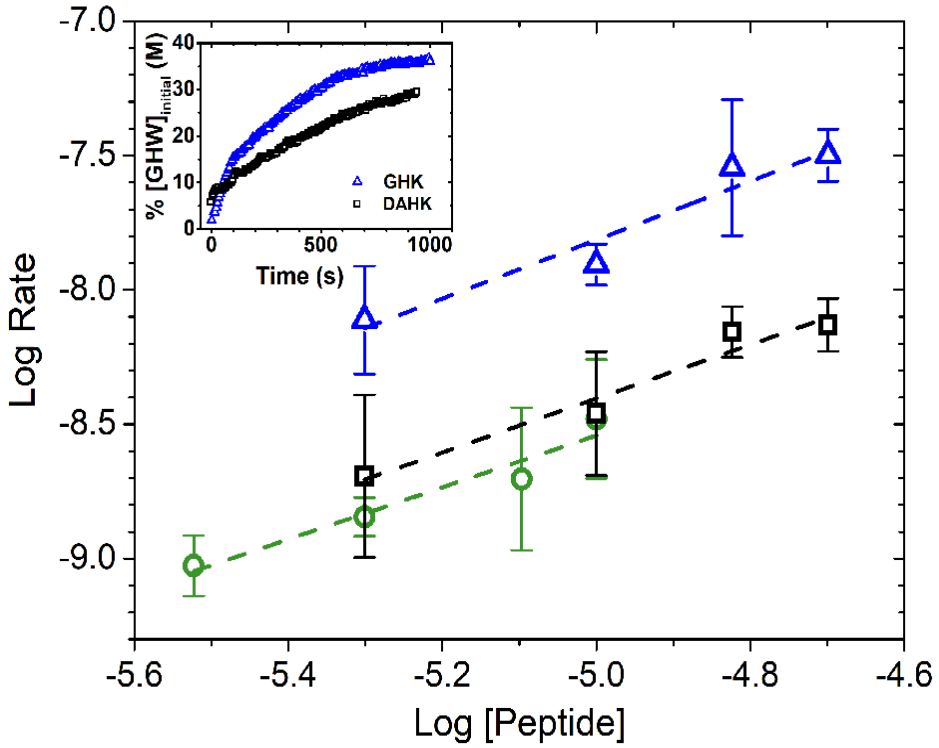

Figure 2.6 The Log Rate versus Log [Peptide] graph determined the orders of the reactants by their slopes (m). All reactants were experimentally determined as first order. Original values of [Peptide] were in M and Rate in M/s. For order analysis of Cu(H_{-1}GHW) (green circle, m = 0.966 ± 0.168, R^2 = 0.91) a constant 5 μM GHK was used, of GHK (blue triangle, m = 1.09 ± 0.19, R^2 = 0.91) a constant 10 μM Cu(H_{-1}GHW) was used, and of DAHK (black square, m = 1.00 ± 0.15, R^2 = 0.94) a constant 10 μM Cu(H_{-1}GHW) was used. Error bars indicate 2-3 replicates. *Inset* The crude kinetic data of the 10 μM Cu(H_{-1}GHW) + 10 μM GHK or 10 μM DAHK exchanges.

Generally, most kinetics is studied under pseudo-first-order conditions by using at least a 10-fold excess of one of the reactants. However, due to the limit of the quantifiable apo[GHW] (μM) and formation of 1:2 Cu:P complexes in a large excess of one reactant, it was not possible to obtain reproducible rate constants under pseudo-first-order conditions. As a result, concentrations of each reactant were adjusted to ensure 1:1 speciation, and only initial linear data points under 10% release of apo[GHW] were utilized to

measure rate, inset **Figure 2.6**. The inset shows the crude kinetic data of recovered W fluorescence in the 10 μM Cu(H_{-1}GHW) to 10 μM GHK or DAHK exchange. The W parameters of Cu(H_{-1}GHW) exchanges included fluorescence cuvettes of 1 cm path length, ε = 5690 $M^{-1}cm^{-1}$, $\lambda_{excitation}$ = 290 nm, $\lambda_{emission}$ = 365 nm, and 5 nm excitation and emission slit widths. In the Cu(H_{-1}GHW) exchanges the conditional second-order (pH 7.4, 0.1 M HEPES) Cu(II) exchange rate constants were determined to be k_{obs}GHK = 1.6 (± 0.2) x 10^2 $M^{-1}s^{-1}$ (n=18, 95%) and k_{obs}DAHK = 5.0 (± 0.7) x 10^1 $M^{-1}s^{-1}$ (n=15, 95%). We attempted to measure the Cu(II) exchange from Cu(H_{-2}DAHW)$^{-2}$ to GHK and DAHK, but the exchange was too slow with very low fluorescence recovery to yield reliable rate constants even in conditions of excess added peptide, **Figure 2.7**.

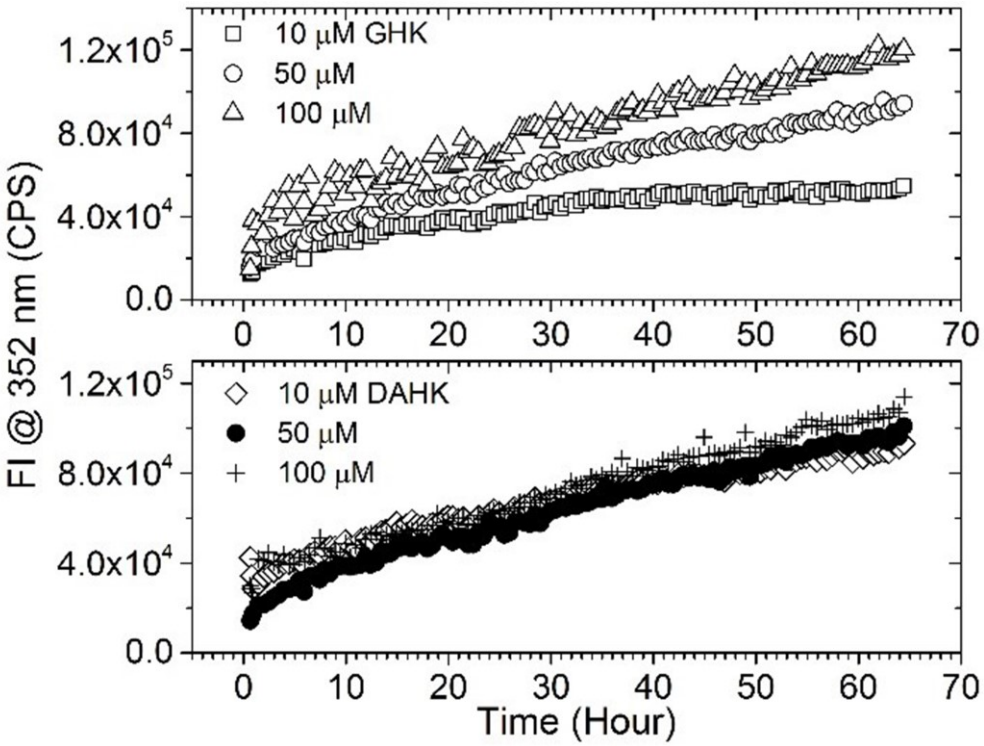

Figure 2.7 The kinetic curves obtained for the Cu(H_{-2}DAHW)$^{2-}$ to GHK or DAHK exchange. The slow kinetics resulted in little fluorecence recovery of DAHW over the course of 3 days even at very large concentration differences. The data shown here is used qualitatively to compare this slow exchange to the fast exchange in the Cu(H_{-1}GHW) exchanges.

Table 2.2: Kinetic data for the Cu(H_{-1}GHW) to GHK exchanges (T= 22 ± 1 °C). The 95% confidence level was taken at 17 degrees of freedom where t = 1.74, s = 38 $M^{-1}s^{-1}$ and n = 18 measurements (E = x 10^).

$[Cu(H_{-1}GHW)]_i$, M	$[GHK]_i$, M	Rate, M/s	k, $M^{-1}s^{-1}$
1.00E-05	5.00E-06	7.98E-09	160
1.00E-05	1.00E-05	1.48E-08	148
1.00E-05	2.00E-05	2.40E-08	120
1.00E-05	5.00E-06	7.68E-09	154
1.00E-05	5.00E-06	1.09E-08	217
1.00E-05	1.00E-05	1.23E-08	123
1.00E-05	1.50E-05	2.83E-08	189
1.00E-05	2.00E-05	3.15E-08	157
1.00E-05	2.00E-05	2.14E-08	107
1.00E-05	2.00E-05	2.14E-08	107
1.00E-05	5.00E-06	7.68E-09	154
1.00E-05	5.00E-06	1.09E-08	217
8.00E-06	5.00E-06	5.42E-09	135
5.00E-06	5.00E-06	4.42E-09	177
5.00E-06	5.00E-06	5.96E-09	238
3.00E-06	5.00E-06	1.99E-09	133
3.00E-06	5.00E-06	1.92E-09	128
3.00E-06	5.00E-06	2.15E-09	144

Table 2.3: Kinetic data for the Cu(H_{-1}GHW) to DAHK exchanges (T=22 ± 1 °C). The 95% confidence level was taken at 14 degrees of freedom where t = 1.76, s = 16 $M^{-1}s^{-1}$ and n = 15 measurements (E = x 10^).

$[Cu(H_{-1}GHW)]_i$, M	$[DAHK]_i$, M	Rate, M/s	k, $M^{-1}s^{-1}$
3.00E-06	5.00E-06	7.83E-10	52.20
3.00E-06	5.00E-06	1.13E-09	75.40
5.00E-06	5.00E-06	1.27E-09	50.89
5.00E-06	5.00E-06	1.61E-09	64.39
8.00E-06	5.00E-06	1.28E-09	32.10
8.00E-06	5.00E-06	3.05E-09	76.14
1.00E-05	5.00E-06	1.24E-09	24.77
1.00E-05	5.00E-06	3.31E-09	66.23
1.00E-05	1.00E-05	3.72E-09	37.17
1.00E-05	1.00E-05	5.63E-09	56.34
1.00E-05	1.50E-05	8.68E-09	57.84
1.00E-05	1.50E-05	5.63E-09	37.55
1.00E-05	1.50E-05	6.87E-09	45.80
1.00E-05	2.00E-05	6.28E-09	31.40
1.00E-05	2.00E-05	8.65E-09	43.26

Approximately 40% of the $[GHW]_{initial}$ (from $[Cu(H_{-1}GHW)]$) was recovered for the equimolar GHK exchange, which indicates the Cu(II) binding affinities of GHK and GHW are on the same order of magnitude. Less fluorescence was recovered at equilibrium in the DAHK exchange despite the fact that DAHK has a slightly larger affinity for Cu(II).[20] The slower rate observed for DAHK as the entering ligand is in line with an extra amide N-H group which must be deprotonated to allow for Cu(II) coordination, which is sluggish at physiological pH.[34] The differences in exchange rates between $Cu(H_{-1}GHW)$ or $Cu(H_{-2}DAHW)^{-2}$ to GHK or DAHK are proposed to arise from the ease of formation of an intermediate ternary species, $Cu(H_{-1}GHW)(P)$ or $Cu(H_{-2}DAHW)(P)$. These ternary species are not fluorescent as the W residue is still near the Cu(II). The faster kinetics observed for $Cu(H_{-1}GHW)$ exchanges are linked to the labile water, which allows for fast exchange with N_{im} ligand of the entering GHK/DAHK histidine residue, **Figure 2.1**. The N_{im} binding has previously been discussed by EPR labeling of $^{15}N_{im}$ for $Cu(GHK)_2$ complexes.[20] The GHK/DAHK peptides are initially coordinated in a monodentate manner through the N_{im}, then through chelate effects sequesters the Cu(II) forming the final 1:1 complexes of $Cu(H_{-1}GHK)^+$ or $Cu(H_{-2}DAHK)^-$ and releases the apoGHW.[34]

To characterize the relative amount of ternary species, the low-temperature EPR spectra of a range of concentrations from 0.1 to 1.0 mM with the ratio of 1:2 Cu(II):GHK were compared to the 1:1 $Cu(H_{-1}GHW)$ complex, **Figure 2.8**. The hyperfine coupling constants and g-values suggest a concentration-dependent formation of the ternary species. When super-hyperfine lines are well-resolved, the perpendicular region of a Cu(II) EPR spectrum is very indicative of the ligands bound in the equatorial plane. For a 4N environment, with equivalent N atoms, 9 lines are expected and observed for a 1:2 Cu(II):GHK stoichiometry. The $g_{//}$ minima observed between g = 2.0 to 1.98 corresponds to the 4th parallel resonance and is dependent on the amount of ternary species formed. Change in position of this minimum toward that of the $Cu(H_{-1}GHK)^+$ species with decreasing [Cu(II)] mirrors the decrease in the concentration of ternary species. From the correlation between the g-values and the amount of ternary species (inset **Figure 2.8**), it can be estimated that in the equimolar exchange experiment at 10 μM, <10 % are ternary species. These studies are in line with the formation of a ternary species in solution when the starting species is $Cu(H_{-1}GHW)$.

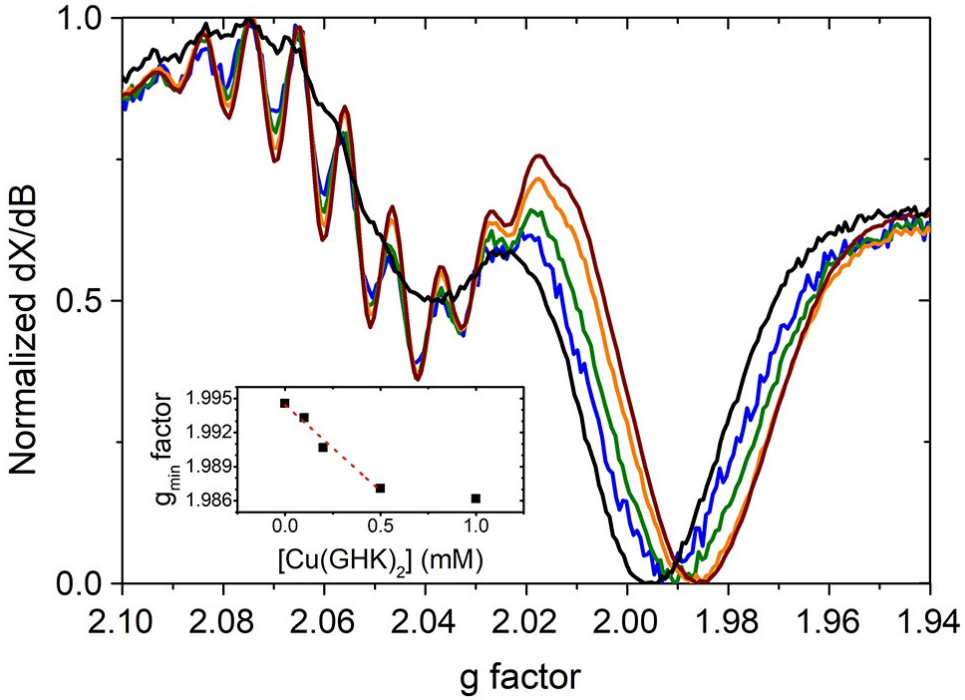

Figure 2.8 Low temperature EPR spectra of the 1:2 Cu(II):GHK complex at: 0.1 (blue), 0.2 (green), 0.5 (orange), and 1.0 mM (red) for [Cu(II)] (where [GHK] = 2[Cu(II)]). The Cu(H_{-1}GHW) complex was measured at 0.5 mM (black) for comparison of a pure binary complex. The perpendicular region is shown (ν = 9.5 GHz, 0.1 M HEPES pH 7.4, 10% (v/v) glycerol, T = 100 K, and under non-saturating conditions). *Inset* The g_{min} factor values as function of the concentration of ternary $Cu(GHK)_2$, indicating the portion of ternary species formed.

The rate constants listed in **Table 2.1** depend on the location of the His residue, pH, sequence length, or available N donor ligands.[16, 26, 28-30, 37] Some general trends can be deduced that are of interest to the current study. First, the highest rate constants are observed when the starting complex has an exchangeable water ligand, as exemplified by the k = 1.1 x 10^7 $M^{-1}s^{-1}$ value when starting from Cu(H_{-2}GGG)$^-$ exchanged to triethylenetetramine (trien) or the ternary species formation of Cu(H_{-1}GHG)(Cys^-) with k > 1 x 10^6 $M^{-1}s^{-1}$, **Table 2.1**.[29, 37] Second, the position of His is crucial and in the third position on the starting complex leads to a very slow reaction and may be due to a dual effect of having no labile water and creating the very stable ATCUN (Amino Terminus Cu and Ni binding) motif. For example, the Cu(II) exchange rate constant to trien from Cu(H_{-2}GGG)$^-$ is eight orders of magnitude larger than from Cu(H_{-2}GGH)$^-$, **Table 2.1**.[28, 37] Our observations correlate with reported data that when the starting complex has an ATCUN motif, the rate is much slower. Third, the nature of the entering ligand impacts the rate constant, with ligands offering

a higher chelate effect leading to faster exchange rates as exemplified by the four orders of magnitude larger Cu(II) exchange rate from $Cu(H_{-2}GGG)^-$ to trien versus HCys, **Table 2.1**. The determined $Cu(H_{-1}GHW)$ Cu(II) exchange rate constant is an order of magnitude faster for GHK than DAHK which may be due to multiple factors including that the DAHK N-terminus has a negatively charged acidic residue, that there is one more amide N-H to be deprotonated in DAHK, and that a smaller metallocycle is formed between the N-terminal amine and the anchoring N_{im} in GHK (9 membered) versus DAHK (12 membered).

2.5 Conclusions

In conclusion, we have determined the inter-peptidic Cu(II) exchange rate constants with fluorescence spectroscopy. We demonstrated that: (i) replacing lysine with tryptophan in the peptide sequence was a successful approach for investigating Cu(II) inter-peptidic metal ion transfer as both residues are non-coordinating and do not change the Cu(II) coordination, (ii) when tryptophan is within 14 Å of the Cu(II) binding site it can be used as an indicator to measure inter- and intra-peptidic Cu(II) exchange rate constants via stoichiometric static fluorescence quenching, (iii) when the initial Cu(II)-tripeptide complex had histidine in the second position as in GHK/GHW, a coordinated water is readily exchangeable with the incoming peptide and the Cu(II) exchange rate constants can be measured by the fluorescence method described, (iv) when the initial Cu(II)-tetrapeptide complex had histidine in the third position as in DAHK/DAHW, the Cu(II) exchange rate constants were too slow to be measured by the method described, and (v) the measured inter-peptidic Cu(II) exchange rate constants from an initial $Cu(H_{-1}GHW)$ complex to GHK or DAHK were k_{obs}GHK = 1.6 (± 0.2) x 10^2 $M^{-1}s^{-1}$ and k_{obs}DAHK = 5.0 (± 0.7) x 10^1 $M^{-1}s^{-1}$.

2.6 Unpublished work on the reverse exchange of Cu(H$_{-1}$GHK) + GHW

We were able to measure a reverse rate constant for the $Cu(H_{-1}GHK)^+ + GHW \rightarrow Cu(H_{-1}GHW) + GHK^+$ exchange. To prevent an inner filter effect (IFE), we reduced the slit width to 1.5 nm, and all other parameters used were the same, see section 2.3.4. The interpeptidic Cu(II) exchange rate constant determined by the method of initial rates for this exchange was k = 4.26 (±0.31) x 10^2 $M^{-1}s^{-1}$ (95% confidence, n = 24, t = 2.069, σ = 73 $M^{-1}s^{-1}$). We postulated in the published work that since only about 40% of the $[GHW]_{intial}$ was recovered that these complexes would have similar affinities on the same order of magnitude. We observe that in the reverse exchange, the rate constant is slightly faster and on the same order of magnitude, which is consistent with our initial findings.

CHAPTER 2 REFERENCES

1. Beuning, C. N.; Mestre-Voegtlé, B.; Faller, P.; Hureau, C.; Crans, D. C., Measurement of Interpeptidic Cu(II) Exchange Rate Constants by Static Fluorescence Quenching of Tryptophan. *Inorg. Chem.* **2018,** *57* (9), 4791-4794.

2. Hanaki, A.; Hiraoka, M.; Abe, T.; Funahashi, Y.; Odani, A., Stopped-Flow Spectroscopic Studies on the Ligand-Exchange Reaction of Cu–(Glycine-Peptide) Complexes, Cu(H−iL), with Cysteine. Cu(II) Transport and Characterization of the Intermediate Ternary Complexes Cu(H−1L)(Cys−); L = Glycylglycine (i = 1), Triglycine (i = 2), Tetraglycine (i = 2 or 3), and Pentaglycine (i = 2 or 3). *Bull. Chem. Soc. Jpn.* **2003,** *76* (9), 1747-1755.

3. Alies, B.; Hureau, C.; Faller, P., The Role of Metal Ions in Amyloid Formation: General Principles from Model Peptides. *Metallomics* **2013,** *5* (3), 183-192.

4. Faller, P.; Hureau, C.; Berthoumieu, O., Role of Metal Ions in the Self-assembly of the Alzheimer's Amyloid-β Peptide. *Inorg. Chem.* **2013,** *52* (21), 12193-12206.

5. Pedersen, J. T.; Hureau, C.; Hemmingsen, L.; Heegaard, N. H. H.; Østergaard, J.; Vašák, M.; Faller, P., Rapid Exchange of Metal between Zn7–Metallothionein-3 and Amyloid-β Peptide Promotes Amyloid-Related Structural Changes. *Biochemistry* **2012,** *51* (8), 1697-1706.

6. Jiang, D.; Zhang, L.; Grant, G. P. G.; Dudzik, C. G.; Chen, S.; Patel, S.; Hao, Y.; Millhauser, G. L.; Zhou, F., The Elevated Copper Binding Strength of Amyloid-β Aggregates Allows the Sequestration of Copper from Albumin: A Pathway to Accumulation of Copper in Senile Plaques. *Biochemistry* **2013,** *52* (3), 547-556.

7. Kepp, K. P., Alzheimer's Disease: How Metal Ions Define β-amyloid Function. *Coord. Chem. Rev.* **2017,** *351* (Supplement C), 127-159.

8. Kozlowski, H.; Luczkowski, M.; Remelli, M.; Valensin, D., Copper, Zinc and Iron in Neurodegenerative Diseases (Alzheimer's, Parkinson's and Prion Diseases). *Coord. Chem. Rev.* **2012,** *256* (19), 2129-2141.

9. Lovell, M. A.; Robertson, J. D.; Teesdale, W. J.; Campbell, J. L.; Markesbery, W. R., Copper, Iron and Zinc in Alzheimer's Disease Senile Plaques. *J. Neurol. Sci.* **1998,** *158* (1), 47-52.

10. Mital, M.; Zawisza, I. A.; Wiloch, M. Z.; Wawrzyniak, U. E.; Kenche, V.; Wróblewski, W.; Bal, W.; Drew, S. C., Copper Exchange and Redox Activity of a Prototypical 8-Hydroxyquinoline: Implications for Therapeutic Chelation. *Inorg. Chem.* **2016,** *55* (15), 7317-7319.

11. Pizzanelli, S.; Forte, C.; Pinzino, C.; Magri, A.; La Mendola, D., Copper(ii) Complexes with Peptides Based on the Second Cell Binding Site of Fibronectin: Metal Coordination and Ligand Exchange Kinetics. *Phys. Chem. Chem. Phys.* **2016,** *18* (5), 3982-3994.

12. Waggoner, D. J.; Bartnikas, T. B.; Gitlin, J. D., The Role of Copper in Neurodegenerative Disease. *Neurobiol. Dis.* **1999,** *6* (4), 221-230.

13. Maret, W., Metalloproteomics, Metalloproteomes, and the Annotation of Metalloproteins. *Metallomics* **2010,** *2* (2), 117-125.

14. Viles, J. H.; Cohen, F. E.; Prusiner, S. B.; Goodin, D. B.; Wright, P. E.; Dyson, H. J., Copper Binding to the Prion Protein: Structural Implications of Four Identical Cooperative Binding Sites. *Proc. Natl. Acad. Sci.* **1999,** *96* (5), 2042-2047.

15. Zgirski, A.; Frieden, E., Binding of Cu(II) to Non-prosthetic Sites in Ceruloplasmin and Bovine Serum Albumin. *J. Inorg. Biochem.* **1990,** *39* (2), 137-148.

16. Lau, S.-J.; Sarkar, B., Ternary Coordination Complex between Human Serum Albumin, Copper (II), and l-Histidine. *J. Biol. Chem.* **1971,** *246* (19), 5938-5943.

17. Rózga, M.; Sokołowska, M.; Protas, A. M.; Bal, W., Human Serum Albumin Coordinates Cu(II) at its N-terminal Binding Site with 1 pM Affinity. *J. Biol. Inorg. Chem.* **2007,** *12* (6), 913-918.

18. Meloun, B.; Morávek, L.; Kostka, V., Complete Amino Acid Sequence of Human Serum Albumin. *FEBS Letters* **1975,** *58* (1-2), 134-137.

19. Pickart, L.; Freedman, J. H.; Loker, W. J.; Peisach, J.; Perkins, C. M.; Stenkamp, R. E.; Weinstein, B., Growth-modulating Plasma Tripeptide may Function by Facilitating Copper Uptake into Cells. *Nature* **1980,** *288* (5792), 715-717.

20. Hureau, C.; Eury, H.; Guillot, R.; Bijani, C.; Sayen, S.; Solari, P.-L.; Guillon, E.; Faller, P.; Dorlet, P., X-ray and Solution Structures of CuIIGHK and CuIIDAHK Complexes: Influence on Their Redox Properties. *Chem. - Eur. J.* **2011,** *17* (36), 10151-10160.

21. Trapaidze, A.; Hureau, C.; Bal, W.; Winterhalter, M.; Faller, P., Thermodynamic Study of Cu2+ Binding to the DAHK and GHK Peptides by Isothermal Titration Calorimetry (ITC) with the Weaker Competitor Glycine. *J. Biol. Inorg. Chem.* **2012,** *17* (1), 37-47.

22. Deibel, M. A.; Ehmann, W. D.; Markesbery, W. R., Copper, Iron, and Zinc Imbalances in Severely Degenerated Brain Regions in Alzheimer's Disease: Possible Relation to Oxidative Stress. *J. Neurol. Sci.* **1996,** *143* (1–2), 137-142.

23. Barritt, J. D.; Viles, J. H., Truncated Amyloid-β(11–40/42) from Alzheimer Disease Binds Cu2+ with a Femtomolar Affinity and Influences Fiber Assembly. *J. Biol. Chem.* **2015,** *290* (46), 27791-27802.

24. Borghesani, V.; Alies, B.; Hureau, C., CuII Binding to Various Forms of Amyloid-β Peptides: Are They Friends or Foes? *Eur. J. Inorg. Chem.* **2018,** *2018* (1), 7-15.

25. Faller, P., Gonzalez, P. , Bossak, K. , Stefaniak, E. , Hureau, C. , Raibaut, L. and Bal, W., N-terminal Cu Binding Motifs Xxx-Zzz-His (ATCUN) and Xxx-His and their derivatives: Chemistry, Biology and Medicinal Applications. *Chem. - Eur. J.* **2018,** *in press*.

26. Dukes, G. R.; Margerum, D. W., Amino Acid Catalysis of the Transfer of Copper(II) from Oligopeptide Complexes to Ethylenediaminetetraacetate. *Inorg. Chem.* **1972,** *11* (12), 2952-2959.

27. Dukes, G. R.; Pagenkopf, G. K.; Margerum, D. W., Triglycine Autocatalysis of the Reaction Between Copper-triglycine and Ethylenediaminetetraacetate Ion. *Inorg. Chem.* **1971,** *10* (11), 2419-2424.

28. Fields, T. R., Kropp, P.J., Ligand Displacement of Glycylglycyl-L-histidine from its Cu(II) Complex. A Proton-assisted Mechanism Initiated at a Nonterminal Position. *J. Am. Chem. Soc.* **1974,** *96* (24), 7560-7562.

29. Hanaki, A.; Ikota, N.; Ueda, J.-i.; Ozawa, T.; Odani, A., Transport of the Cu(II) Bound with Histidine-Containing Tripeptides to Cysteine. Coordination Mode and Exchangeability of Cu(II) in the Complexes. *Bull. Chem. Soc. Jpn.* **2003,** *76* (11), 2143-2150.

30. Hanaki, A.; Odani, A., Transport of Cu(II) from an Albumin Mimic Peptide, GlyGlyHisGly, to Histidine and Penicillamine. *J. Inorg. Biochem.* **2007,** *101* (10), 1428-1437.

31. Hauer, H.; Billo, E. J.; Margerum, D. W., Ethylenediamine and Diethylenetriamine Reactions with Copper(II)-triglycine. *J. Am. Chem. Soc.* **1971,** *93* (17), 4173-4178.

32. Hauer, H.; Dukes, G. R.; Margerum, D. W., Peptide Steric Effects on the Kinetics of Copper(II)-tripeptide Reactions. *J. Am. Chem. Soc.* **1973,** *95* (11), 3515-3522.

33. Linder, M. C., Lomeli, N.A., Donley, S., Mehrbod, P.C, Cotton, S., Wooten, L., Copper Transport in Mammals. *Adv. Exp. Med. Biol.* **1999,** *448*, 1-16.

34. Margerum, D. W., Dukes, G. R. , Kinetics and Mechanisms of Metal-ion and Proton-transfer Reactions of Oligopeptide Complexes. *Met. Ions Biol. Syst.* **1974,** *1*, 157-207.

35. Hanaki, A.; Funahashi, Y.; Odani, A., Ternary Cu(II) Complexes, Cu(H−1L)(ACys−) and Cu(H−2L)(ACys−); L = peptides, ACys− = N-acetyl-cysteinate. Analogous Complexes to the Intermediates in the Transport of Cu(II) from Cu(H−2L) to Cysteine. *J. Inorg. Biochem.* **2006,** *100* (3), 305-315.

36. Hanaki, A.; Ueda, J.-i.; Ikota, N., Ternary Complexes from Cu(II)–Oligopeptide and N-Acetyl-L-histidine, as Studied by Circular Dichroism Spectroscopy. *Bull. Chem. Soc. Jpn.* **2004,** *77* (8), 1475-1477.

37. Pagenkopf, G. K.; Margerum, D. W., Steric Factors in the Kinetics of Ligand Exchange with Copper(II)-triglycine (CuH-2L-). *J. Am. Chem. Soc.* **1970,** *92* (9), 2683-2686.

38. Lehrer, S. S., Fluorescence and Absorption Studies of the Binding of Copper and Iron to Transferrin. *J. Biol. Chem.* **1969,** *244* (13), 3613-3617.

39. Ghisaidoobe, A.; Chung, S., Intrinsic Tryptophan Fluorescence in the Detection and Analysis of Proteins: A Focus on Förster Resonance Energy Transfer Techniques. *Int. J. Mol. Sci.* **2014,** *15* (12), 22518.

40. Harford, C.; Sarkar, B., Amino Terminal Cu(II)- and Ni(II)-Binding (ATCUN) Motif of Proteins and Peptides: Metal Binding, DNA Cleavage, and Other Properties. *Acc. Chem. Res.* **1997,** *30* (3), 123-130.

CHAPTER 3: MEASUREMENT OF INTERPEPTIDIC CU(II) EXCHANGE RATE CONSTANTS FROM TRUNCATED CU(II) – AMYLOID-BETA COMPLEXES TO SMALL PEPTIDE MOTIFS BY TRYPTOPHAN FLUORESCENCE QUENCHING

3.1 Summary

The interpeptidic Cu(II) exchange rate constants were measured for two truncated amyloid-beta Cu(Aβ) complexes, Cu($Aβ_{1-16}$) and Cu($Aβ_{1-28}$), to fluorescent peptides GHW, DAHW, and GGW using our previously reported tryptophan fluorescence quenching methodology. These second-order rate constants were determined at three pHs (pH – 6.8, 7.4, and 8.7) important to the Cu(Aβ) complex coordination. The interpeptidic Cu(II) exchange rate constants vary in their order of magnitudes from 10^3 to 10^4 $M^{-1}s^{-1}$ depending on a number of variables; including the pH, the length of the amyloid-beta peptide, whether the tryptophan peptide contained a histidine ligand, the number of amide deprotonations needed in the tryptophan peptide to coordinate the Cu(II), and the extent of the created tryptophan peptide metallocycle. As peptides like GHK and DAHK are important motifs found in the blood and serum, their ability to sequester Cu(II) ions from Cu(Aβ) complexes may be an important mechanism in the treatment of Alzheimer's disease. Thus, their kinetic Cu(II) interpeptidic exchange rate constants are important chemical constants that can aid in the development of drug treatment.

3.2 Introduction to the amyloid-beta peptide, Alzheimer's disease, and the interpeptidic Cu(II) exchange of Cu(Aβ) complexes with tryptophan-containing small tri- and tetra-peptides

The amyloid-beta (Aβ) peptide was first sequenced in 1984 by Glenner and Wong after its purification from brain tissue in post-mortem patients suffering from Alzheimer's disease (AD).[1] In the following year, they identified Aβ as a major component in the senile plaques observed in AD, which was the first report of the possible link of Aβ in the pathology of AD.[2] In the three decades since Aβ's connection to AD, it has been the object of extensive research concerning neurodegenerative disease. The prevalence of the Aβ peptide in neurodegenerative disease is not confined to just AD, but also prion, Huntington's and Parkinson's diseases. The human amyloid precursor protein (APP) is cleaved by α-, β-, and γ-secretases into both non-amyloidogenic and amyloidogenic peptides, which have many essential biological functions

in both neuron and synapse (space between neurons) development and repair, signaling, and even iron transport.[3] There are mixed reports of the actual biological function of Aβ, which is one of the amyloidogenic peptides created by the β- and γ- secretase cleavage of APP. For example, neuronal survival may be connected to Aβ as neuronal cell death was reported in studies performed with secretase inhibited Aβ production, and the addition of exogenous $A\beta_{1-40}$ could restore viability.[4]

What is known about the Aβ peptide in the pathology of AD is multifaceted. The Aβ peptide can form innocuous soluble monomers, which do not seem to contribute to disease mechanisms. However, it can form toxic oligomeric species, large unorganized aggregates, highly organized beta-sheet fibrils, neurofibrillary tangles, and metal ion complexes all of which can eventually amass into the senile plaques which are a hallmark of AD.[3, 5-13] Indeed, pathogenic Aβ is on a spectrum, where toxicity is due to mechanisms which increase Aβ production as compared to normal healthy levels and not all people will experience AD or have senile plaques even though they create the peptide. Similarly, some toxicity of the Aβ peptide has been in its ability to form ion channels in membranes, which can alter K^+ and Ca^{2+} homeostasis in cells.[14-15] The buildup of the precipitated peptide in the space between neurons, called the synaptic cleft space, results in less communication between the neurons as they can no longer signal to each other. Over time, this leads to atrophy of the neurons since they can no longer communicate, and this eventually manifests as the symptoms of dementia and memory loss. In fact, the brain of a person with advanced late-stage AD can be significantly smaller than a healthy brain, due to the atrophy of the neurons. The Aβ peptide is not purely localized to the brain but is found in cerebrospinal fluid (CSF), plasma, and interstitial fluid. Correlation of plasma and CSF ratios of the common isoforms of the Aβ peptide and tau proteins have been reported to give an indication of early-onset AD by decreased amounts of $A\beta_{1-42}$ peptide in these fluids due to their precipitation into plaques.[16-17] However, CSF biomarkers have given more consistent results according to a recent meta-data analysis.[18]

The transition metals Zn(II), Fe(II), and Cu(II) are all essential biological metals, are highly regulated in the body, and the disruption of the homeostasis of these metals usually results in disease where neurodegenerative diseases as the most prominent, since these metals have functions in the brain.[10, 19-24] One type of Aβ aggregation is the chelation of Cu(II), Zn(II), and Fe(II) ions in the brain within the synaptic cleft space, and concentrations up to 400, 950, and 1100 μM [25], respectively, have been found in AD

plaques.[5-6, 8-11, 21] The coordination of these metals to the Aβ peptide has shown an increase in the propensity of it to aggregate and precipitate into senile plaques. These metals have a high affinity for the Aβ peptides, with association constants on the orders of 10^{10} M^{-1} for Cu(II) and 10^{6} M^{-1} for Zn(II).[5, 26] The redox-active Cu(II) and Fe(II) also form complexes that can generate reactive oxygen species (ROS), where oligomeric species cause the most ROS damage as they are most available for the metals to participate in oxidative stress. When the metal is confined to the plaques, it is less likely to be involved in ROS generation. Cu(II) is a particularly interesting metal as it is involved in many biologically essential cellular processes like red blood cell formation, has many redox functions such as for mitochondrial oxidative phosphorylation within the brain, and is essential in healthy fetal brain development.[19, 27] We have focused on Cu(II) binding to the Aβ peptide due to some of these issues, such as ROS generation. While Zn(Aβ) complexes also precipitate into plaques, some mechanisms such as metallothionein exchanging their bound Zn(II) for Cu(II) from Cu(Aβ) complexes to generate Zn(Aβ) complexes may be in direct response to the ROS generation pathology.[28] Hypoxia due to increased mitochondrial ROS generation up-regulates APP expression which creates more Aβ peptide which can lead to the development of AD.[29]

The Aβ peptide has many isoforms, including the most well-known lengths that are most associated with aggregation mechanisms, $Aβ_{1-40}$ (major form) and $Aβ_{1-42}$ (minor form), and the sequence is shown in **Figure 3.1**. The $Aβ_{1-42}$ isoform is much more prone to aggregate than $Aβ_{1-40}$.[30] The cleavage of the APP is not highly specific, and small truncated isoforms like $Aβ_{1-16}$ and $Aβ_{1-28}$ are also observed. The Aβ peptide has a well-known metal-binding domain in the first 16 amino acid residues rich with nitrogen-donor ligands, including deprotonated amide N^-, imidazole histidine N_{im}, and terminal NH_2, as well as oxygen-donor ligands like amide C=O and terminal COO^- binding sites. For Cu(Aβ) complexes, two major components are in equilibrium at physiological pH, **Figure 3.1**, and exhibit different binding.[5-6, 8-9] Component I, which is predominant at pH 6.8, has terminal NH_2, amide C=O, and two histidine N_{im} Cu(II) binding sites in the equatorial plane and the terminus COO^- in the axial plane. The histidine contributions for Component I are from His6 and His13/14 (which are in equilibrium). Component II which is predominant at pH 8.7, has terminal NH_2, amide N^-, amide C=O, one histidine N_{im} Cu(II) binding sites in the equatorial plane, and the terminus COO^- in the axial plane. The histidine ligand in Component II can be either His6, His13, or His14,

where all three residues equally contribute (are in equilibrium). The binding affinity of Cu(II) to Aβ has been measured at 1 x 10^{10} M^{-1} and encompasses all forms.[26]

Aβ - DAEFRHDSGY[10]EVHHQK[16]LVFFAEDVGSNK[28]GAIIGLMVGGVV[40]IA[42]

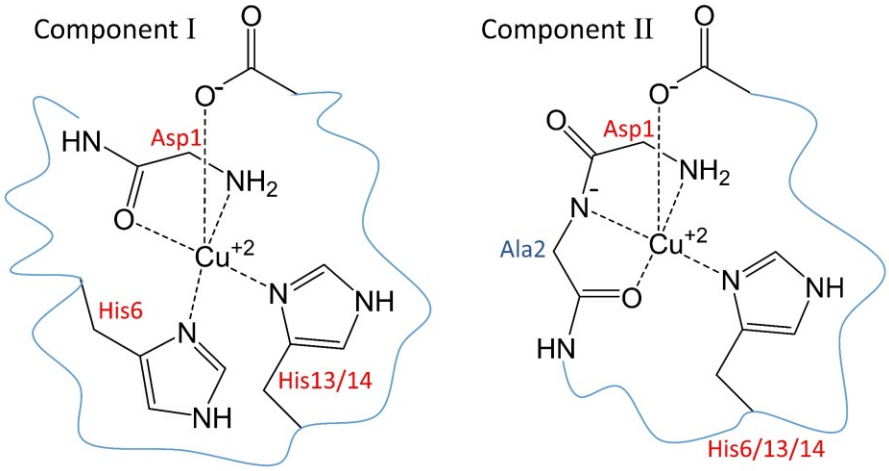

Figure 3.1: Cartoon schematic of the two components of Cu(Aβ) complexes. The full sequence is given, with primary metal binding sites in red and secondary in blue. In the structures, the blue lines represent the continuing peptide chain and are drawn to show a simplistic representation of the equatorial binding ligands to Cu(II). An apical oxygen is shown and is the terminal COO^-. Component I is predominant at pH 6.8, Component II is predominant at pH 8.7, and at physiological pH 7.4 both complexes exist in equilibrium.

Since the Cu(Aβ) complex has a predominant form at pH 6.8 (component I) and 8.7 (component II), which are in equilibrium at pH 7.4, we measured the interpeptidic Cu(II) exchanges at all three pH's relevant to the complex. For Cu(Aβ), there are four possible complexes based on the pH of the solution. At pH 6.8, $Cu(A\beta_{1\text{-}16})^-$ and $Cu(A\beta_{1\text{-}28})^{2-}$ are the predominant complexes that have no deprotonated amide nitrogen. At pH 8.7, $Cu(H_{-1}A\beta_{1\text{-}16})^{2-}$ and $Cu(H_{-1}A\beta_{1\text{-}28})^{3-}$ are the predominant complexes that have one deprotonated amide nitrogen. At pH 7.4, these respective truncated complexes are in equilibrium with each other. For example, both $Cu(A\beta_{1\text{-}16})^-$ and $Cu(H_{-1}A\beta_{1\text{-}16})^{2-}$ are present at pH 7.4, and there is no way to distinguish which complex the Cu(II) is being exchanged from. The assumption is that both components have an equal binding affinity, so one could assume they are taken from both in equal measure. Therefore, in the following discussion, the two truncated forms will simply be referred to as $Cu(A\beta_{1\text{-}16})$ and $Cu(A\beta_{1\text{-}28})$, with their charges omitted for the sake of clarity.

The short peptides GHK (Gly-His-Lys) and DAHK (Asp-Ala-His-Lys) are two motifs found in the blood. GHK is associated with the human growth factor, while DAHK is the N-terminus sequence of human serum albumin (HSA) that also binds Cu(II). We were also interested in a peptide which had no histidine residues for comparisons, so we used a simple tripeptide GGW (Gly-Gly-Trp). These peptides coordinate Cu(II) with the same types of binding sites as Aβ, **Figure 3.2**. The three complexes which are created are denoted as $Cu(H_{-n}P)^{m-n+1}$ where *n* is the number of deprotonated amide N^- and *m* is the overall charge of the unbound zwitterion peptide. The three complexes which are formed upon the exchange from Cu(Aβ) complexes are $Cu(H_{-1}GHW)$, $Cu(H_{-2}DAHW)^{2-}$, and $Cu(H_{-2}GGW)^-$. The Cu(II) binding affinities of these small peptides are much greater than for Aβ, where the lysine containing peptides were measured at 1.4 x 10^{13} M^{-1} for $Cu(H_{-1}GHK)^+$ and 3.9 x 10^{13} M^{-1} for $Cu(H_{-2}DAHK)^-$. This is a result of the very stable formation of small 5 or 6 membered rings, which result in the formation of large 9 to 12 membered metallocycles. Therefore, the dissociation of Cu(II) from these complexes is not favored and is very slow as these structures are highly stable. For the $Cu(H_{-2}GGW)^-$ complex, the structure was determined from a reported structure for $Cu(H_{-2}GGG)^-$ coordination, and is confirmed by both EPR and UV-vis spectroscopy.[31]

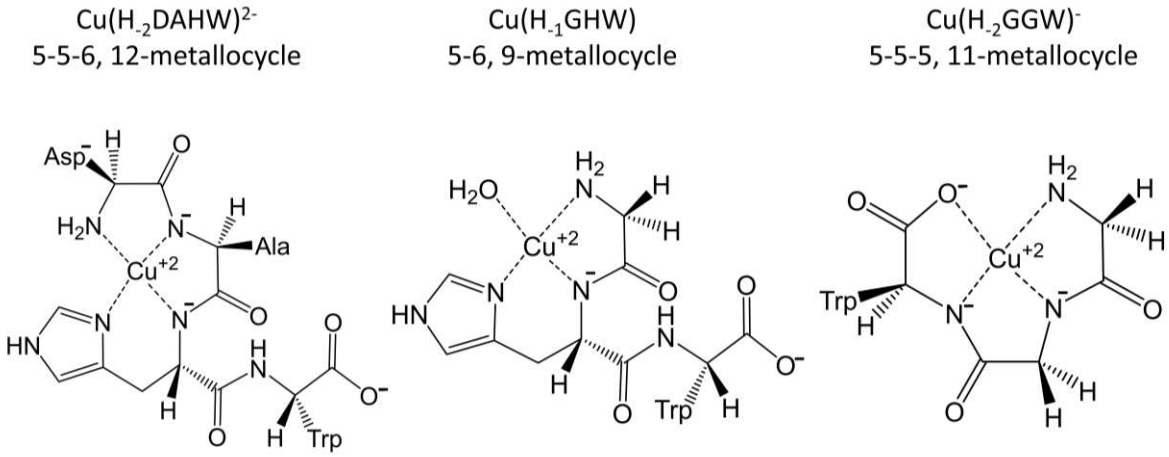

Figure 3.2: The solution structures of the $Cu(H_{-1}GHW)$, $Cu(H_{-2}DAHW)^{2-}$, and $Cu(H_{-2}GGW)^-$ complexes created upon interpeptidic exchange from Cu(Aβ).

Using this same fluorimetry methodology described in Chapters 1 and 2,[32] we monitored the exchange of Cu(II) from two different truncated isoforms, $Cu(Aβ_{1-16})$ and $Cu(Aβ_{1-28})$ to GHW, DAHW, or GGW following **Eq. 3.1**, where a is the charge of the free Aβ peptide, b is the number of deprotonated amide N^- in the Cu(Aβ) complex, m is the charge of the free tryptophan-containing peptide (P), and n is the

number of deprotonated amide N^- in the Cu(P) complex. See **Table 3.1** for all values of a, b, m, and n. The charge of the free ligand is determined by the zwitterion where the N-terminus is NH_3^+, and the C-terminus is COO^-, the amino acids Arg (R) and Lys (K) are NH_3^+, and Asp (D) and Glu (E) are COO^-. To coordinate Cu(II), the N-terminus must be deprotonated to NH_2. We measured the simple GGW peptide to observe differences in Cu(II) exchange when there is no histidine in the sequence, which is a strong Cu(II) ligand and important in the creation of stable Cu(II)-peptide complexes.[33]

(**Eq. 3.1**) $$Cu(H_{-b}A\beta)^{a-b+1} + P^m \longrightarrow Cu(H_{-n}P)^{m-n+1} + A\beta^a + (n-b)H^+$$

Table 3.1: Values of a, b, m, and n for all complexes in this work for use in **Eq. 3.1**.

Complex	Charge free ligand m (P) or a (Aβ)	# N^- in complex n (Cu(P)) or b (Cu(Aβ))
$Cu(H_{-1}GHW)$	0	1
$Cu(H_{-2}DAHW)^{2-}$	-1	2
$Cu(H_{-2}GGW)^-$	0	2
$Cu(A\beta_{1-16})^-$	-2	0
$Cu(H_{-1}A\beta_{1-16})^{2-}$	-2	1
$Cu(A\beta_{1-28})^{2-}$	-3	0
$Cu(H_{-1}A\beta_{1-28})^{3-}$	-3	1

The kinetic data were fit using a second-order approach following **Eq. 3.2**. Since there is no way to measure the variable $[Cu(A\beta)]_t$, we must estimate it since we know how much Cu(II) has been exchanged, and we know the initial Cu(Aβ) concentration. Therefore **Eq. 3.3** shows that the concentration of Cu(Aβ) at any time, $[Cu(A\beta)]_t$, must equal the initial concentration of Cu(Aβ) minus the change in concentration of the fluorescent peptide, as one Cu(II) is exchanged for every Cu(Aβ) dissociated, since all peptides coordinate in a 1:1 mol ratio. Therefore, **Eq. 1.6** is the final form of the second-order fitting used to transform the data to determine rate constants, which was discussed in Chapter 1, section 1.3. These exchanges go to completion (or very close to completion) in the GHW and DAHW exchanges due to their three orders of magnitude larger association constants, while in the GGW exchange are likely an equilibrium mechanism.

(**Eq. 3.2**) $$\frac{1}{[Cu(A\beta)]_0 - [GHW]_0} * \ln\left(\frac{[GHW]_0 * [Cu(A\beta)]_t}{[Cu(A\beta)]_0 [GHW]_t}\right) = k * t$$

(**Eq. 3.3**) $$[Cu(A\beta)]_t = [Cu(A\beta)]_0 - ([GHW]_0 - [GHW]_t)$$

(**Eq. 1.6**) $$\frac{1}{[Cu(A\beta)]_0 - [GHW]_0} * \ln\left(\frac{[GHW]_0 * ([Cu(A\beta)]_0 - ([GHW]_0 - [GHW]_t))}{[Cu(A\beta)]_0 [GHW]_t}\right) = k * t$$

These studies are an important step to determine the interpeptidic exchange of Cu(II) between full-length Aβ isoforms in both their soluble monomeric, aggregate, and fibril formations. The full-length Aβ peptides are significantly more difficult to work with due to their hydrophobic residues, which predominate in the 17 – 42 amino acid region and their aggregation mechanisms. The $A\beta_{1-16}$ isoform does not aggregate like the full-length $A\beta_{1-40/42}$, which is an important variable in the current studies, and this isoform is often used to study Cu(II) binding.

3.3 Experimental methods

3.3.1 Materials

All peptides were used as purchased from the manufacturer. The GHW (99.73% pure), DAHW (96.89%), and GGW (98.64%) peptides used were purchased from GeneCust (Luxembourg). The truncated Aβ peptides were purchased from Synpeptide Co., Ltd (China) in the with the following lengths $A\beta_{1-16}$ (> 95%) and $A\beta_{1-28}$ (> 95%). The source of Cu(II) ions was $CuSO_4 \bullet 5H_20$ and was purchased from Aldrich. Buffer chemicals HEPES (99.5%) and NaOH (97.0%) were purchased from Sigma. All water used was purified by a Synergy Milli-Q purification system to 19 MΩ•cm resistivity. Quartz cuvettes were used in all absorption and emission spectroscopy with 1 cm path-lengths. All solid peptides were stored in a -20 C freezer.

3.3.2 Instrumentation

Fluorimetry measurements were performed on a Horiba Jobin-Yvon FluoroLog-3 spectrofluorometer. Fluorimetry parameters included a 1.5 nm slit width, an excitation wavelength of 290 nm, an emission wavelength of 365 nm, and a 0.25 s time interval with quartz cuvettes ℓ = 1.0 cm. Absorption measurements were performed with an AvaLight DHc dual deuterium-halogen lamps light source for spectroscopy in the 200 – 2500 nm range and AvaSpec-2048 detector. The cuvette holder was attached to the light source and the detector by fiber optic cables. Parameters included a boxcar width of 5 and an average of 100 scans per capture. A thin layer, ℓ = 1.7 mm, quartz cuvettes were used. EPR spectra were taken on a Bruker 9.4 GHz ELEXSYS spectrometer with 1 Gauss resolution, 2500 G to 3700 G, 0.5 mT amplitude modulation, approximately 9.4 GHz (see figure captions for exact values), and at 150 K.

3.3.3 Determination of stock peptide concentrations.

About 50.0 – 70.0 mg of tryptophan-containing peptides GHW, DAHW, and GGW were dissolved in 1.00 mL of DI H_2O and were kept stored in a -20 C freezer and only thawed when needed. To determine the stock concentration of the tryptophan peptides, they were diluted to approximately 1 mM in 0.1 M HEPES at pH 7.40 in a quartz cuvette and the absorbance at 280 nm (ε = 5690 $M^{-1}cm^{-1}$ for tryptophan absorption) was measured. This was repeated six times for each peptide. Between 2.0 – 6.0 mg of $A\beta_{1-16}$ or $A\beta_{1-28}$ peptide was added to 2.00 mL of 0.1 M HEPES at pH 7.40 and lightly vortexed until completely dissolved. These stock solutions were approximately 1 mM. To determine the stock concentration of the Aβ peptides, they were diluted to about 0.1 mM, and the absorbance at 274 nm (ε = 1280 $M^{-1}cm^{-1}$ for tyrosine absorption) was measured and repeated six times for each peptide.

3.3.4 Creation of Cu(Aβ) complexes

Once the stock concentrations of Aβ were known, a mole equivalence of Cu(II) from a 0.5151 M $CuSO_4 \cdot 5H_20$ stock solution, ε = 12 $M^{-1}cm^{-1}$ at 800 nm, was added and the resulting solution was clear and light blue in color.

3.3.5 Fluorimetry sample preparation

To create samples for fluorescence measurement of kinetics, a large aliquot of HEPES buffer at the appropriate pH was added to the cuvette (between 994 – 995 µL) using a calibrated 1000 µL pipette and the fluorescence was measured. This blank HEPES fluorescence is subtracted from sample fluorescence intensity. Then 5 - 7 µL of approximately 1.0 mM GHW, DAHW, or GGW peptide was added to the HEPES, mixed, and then its fluorescence intensity was measured. This measurement was always the initial tryptophan peptide concentration used in the second-order transformation of data. Lastly, 5 - 7 µL of approximately 1.0 mM Cu(Aβ) was added to the cuvette, the cuvette was simply flicked to slightly mix, then added to the cuvette holder, and the kinetic experiment started, the time to add the aliquot was manually measured between 4-5 seconds, recorded, and added to the time data.

3.3.6 *EPR sample preparation*

Cu(H_{-2}GGW) samples were prepared at 3.73 mM (the UV-vis spectrum was taken before freezing) and frozen in an EPR tube with dry ice and acetone. For creation of the ternary species, approximately 8-10 µL of 78 mM GHW was added to the bottom of an EPR tube, then a about 300 - 400 µL of 1.0 mM

Cu($A\beta_{1-16}$) in 0.1 M HEPES was added the same EPR tube and then immediately frozen in the dry ice and acetone mixture.

3.3.7 Software

Kinetic fluorescence data was gathered, and then a calibration curve was obtained using OriginPro student version (2019b or 2018b), and then the signal was converted to concentration in Microsoft Excel 2016. The second-order transformation of data was performed in Microsoft Excel 2016, and then linear regression analysis was performed in OriginPro 2019b for the first 20 – 40 s of data depending on the exchange being analyzed where the y-intercept was manually set to zero. The slopes of these lines are the second-order rate constant in $M^{-1}s^{-1}$, each exchange has 12 – 15 runs, which are then averaged, and the confidence level obtained. Any outliers were determined by a Grubb's test.

3.4 Results and discussion

First, we could confirm the coordination of Cu(H_{-2}GGW) by EPR and UV-vis spectroscopies. The maximum wavelength of the Cu(H_{-2}GGW) is 546 nm and agrees with the reported value for the Cu(H_{-2}GGG) complex at 552 nm[34], **Figure 3.3**. This would indicate that the tryptophan is not coordinated to the Cu(II) as in the case with GHW and DAHW. The Cu(H_{-2}GGW) complex has a g factor values of $g_{//}$ = 2.22 and a $g_{\perp}$ = 2.01, with a hyperfine coupling constant of $A_{//}(^{63}Cu)$= 500 MHz. The lack of any clearly defined superhyperfine coupling is expected with 3N + 1O binding, however, seven peaks can be observed in some cases.

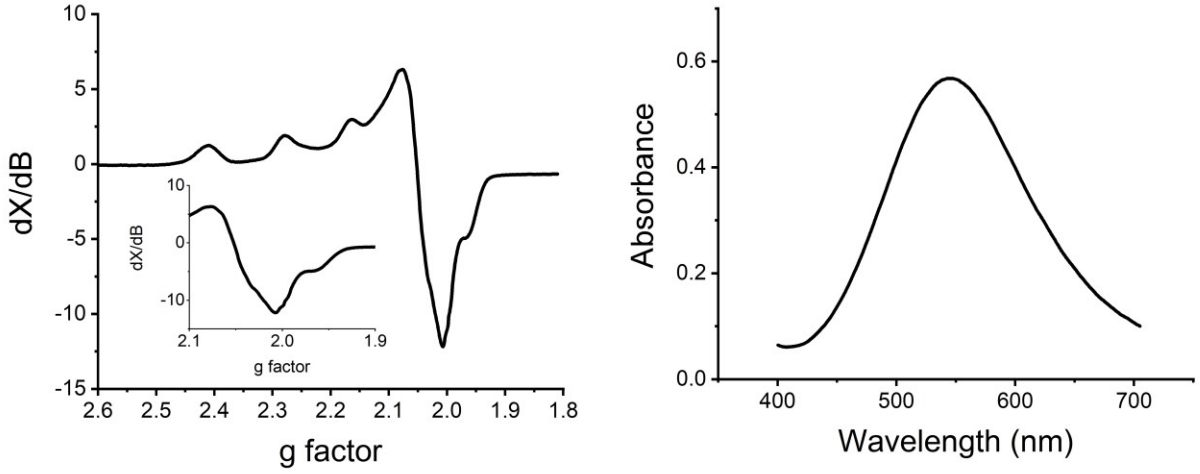

Figure 3.3: Low-temperature EPR (left) and UV-vis spectrums (right, LMCT) of the Cu(H_{-2}GGW) complex. Samples were taken at T = 150 K at 9.369992 GHz and at 3.73 mM.

The interpeptidic Cu(II) exchange from Cu($A\beta_{1-16}$) and Cu($A\beta_{1-28}$) to GHW, DAHW, and GGW was monitored using the previously reported fluorimetry method.[32] These exchanges were monitored at three different pH 6.83, 7.40, and 8.70 in 0.1 M HEPES. The measurement of kinetic rate constants is usually performed under pseudo-first-order conditions where one reactant is in a large excess of the other. With metal ion peptide complexes having such conditions can induce higher-order complexes to form, where there are multiple peptides per metal ion. In order to avoid this, concentrations of reactants in the interpeptidic exchange of Cu(II) are similar, with no excess of one reactant over another. Specifically, the reaction concentrations were within 1 mM of each other, such as 4 μM GHW + 5 μM Cu($A\beta_{1-16}$), where the tryptophan peptides ranged from 4 – 6 μM and the Cu(Aβ) complexes ranged from 4 – 7 μM. Actual initial concentrations for the tryptophan peptides were determined through the fluorescence data, while the initial concentrations for the Cu(Aβ) complexes were determined from their tyrosine absorption and amount of Cu(II) ions added, but the approximate values are given in **Table 3.2**.

Table 3.2: Approximate concentration profiles used in the interpeptidic exchanges. Actual concentrations vary as described.

$[Peptide]_0$, mM	$[Cu(A\beta)]_0$, mM
5	4
5	5
5	6
4	5
6	5
6	7

We used a second-order fitting approach to determine the rate constants in these exchanges, **Eqs. 3.2,** and **1.6**. Previously, we used the method of initial rates to determine the rate constants, which worked well because the peptides all had similar association constants on the order of 10^{13} M^{-1}, which resulted in slower rates of exchange. The current exchanges studied were much faster, which resulted in fewer data points in the linear portion of the kinetic traces and is due to the weaker Cu(II) association constants for the Aβ peptides, on the order of 10^{10} M^{-1}, compared to the tryptophan-containing peptides. Therefore, the second-order fitting approach was used, especially since our current instrumentation does not have stopped-flow capabilities, which would have given data in the 4-5 seconds it takes to manually add solutions together and start a kinetic measurement. A typical kinetic trace (*inset*) and second-order fit of the data

which has been transformed using **Eq 1.6** is shown in **Figure 3.4** (GHW), **Figure 3.5** (DAHW), and **Figure 3.6** (GGW) for each exchange at the approximate 4 μM P + 5 μM Cu(Aβ) concentration profile at all three pH conditions. The kinetic data were manually inspected to determine what time the plots began to plateau, so depending on the exchange, the data used to determine the rate constant is anywhere from the first 10 - 40 seconds. Each concentration profile in **Table 3.2** is run in triplicate so that 12 -15 rate constants were measured for each exchange. These second-order rate constants were then averaged, and their 95 % confidence levels determined and are reported in **Table 3.3**.

Table 3.3: Conditional second-order rate constants between P + Cu(Aβ) exchanges at the given pH in 0.1 M HEPES.

k_P , $M^{-1}s^{-1}$	pH 6.8	pH 7.4	pH 8.7
k_{GHW} - Cu($Aβ_{1-16}$)	4.1 (± 0.3) x 10^4	4.1 (± 0.4) x 10^4	2.9 (± 0.3) x 10^4
k_{GHW} - Cu($Aβ_{1-28}$)	1.44 (± 0.07) x 10^4	2.48 (± 0.17) x 10^4	1.09 (± 0.14) x 10^4
k_{DAHW} - Cu($Aβ_{1-16}$)	1.04 (± 0.11) x 10^4	2.16 (± 0.13) x 10^4	2.18 (± 0.17) x 10^4
k_{DAHW} - Cu($Aβ_{1-28}$)	6.8 (± 0.6) x 10^3	1.33 (± 0.10) x 10^4	1.26 (± 0.15) x 10^4
k_{GGW} - Cu($Aβ_{1-16}$)	----	1.12 (± 0.09) x 10^3	1.58 (± 0.12) x 10^3
k_{GGW} - Cu($Aβ_{1-28}$)	----	1.07 (± 0.18) x 10^3	1.03 (± 0.11) x 10^3

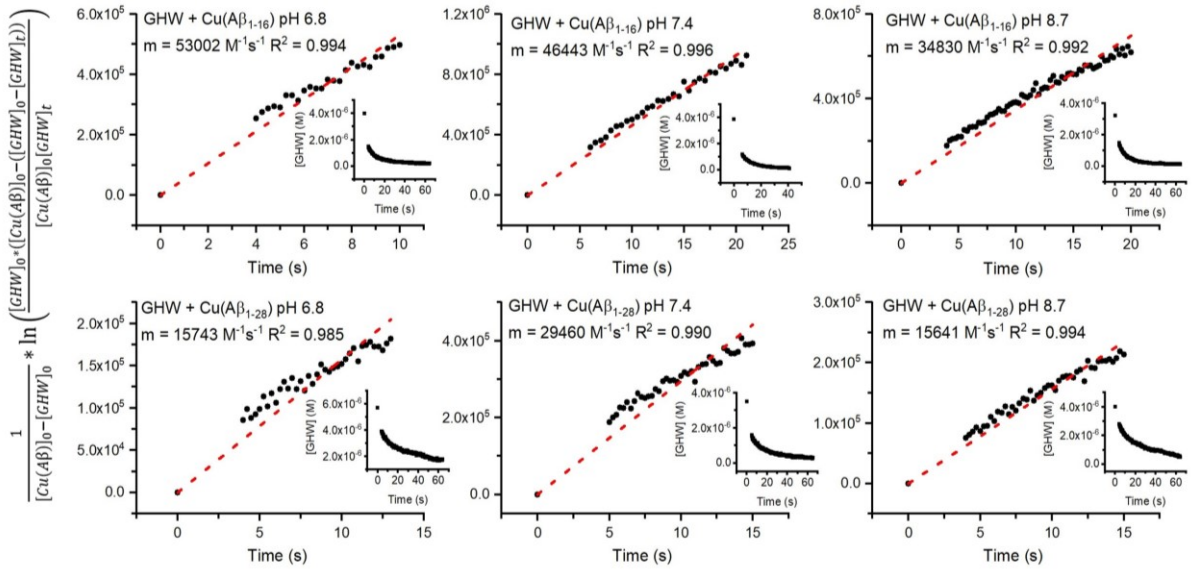

Figure 3.4: The GHW + Cu(Aβ) exchanges where $[GHW]_0$ and $[GHW]_t$ are determined by fluorescence data and $[Cu(Aβ_{1-16})]_0$ = 5.47 mM and $[Cu(Aβ_{1-28})]_0$ = 5.40 mM. Insets are the kinetic concentration versus time graphs.

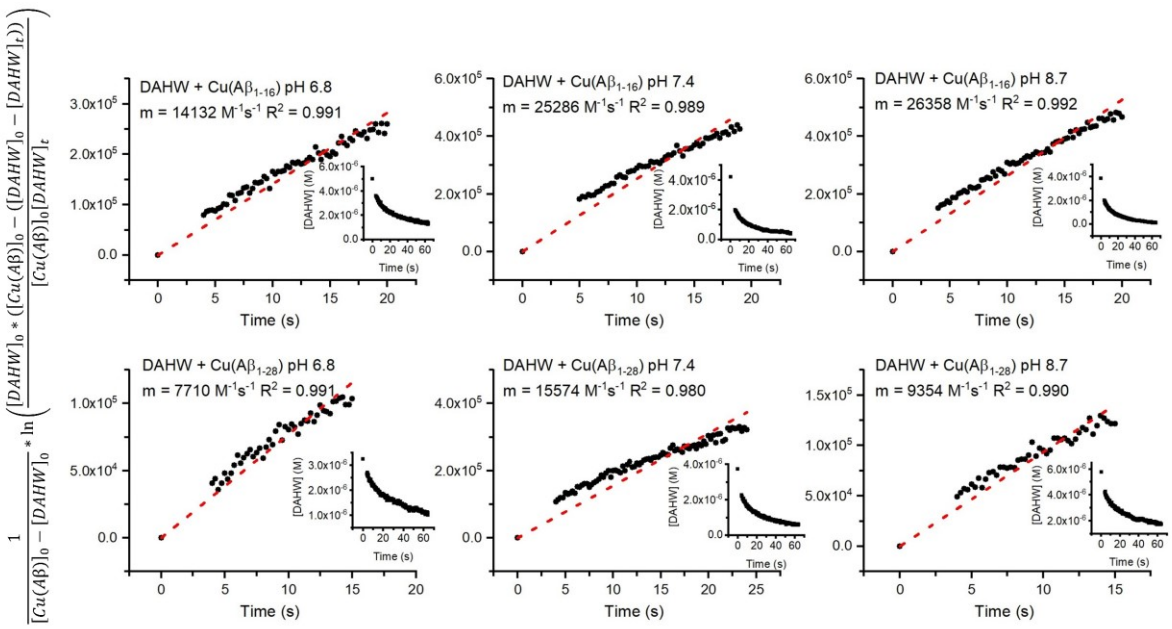

Figure 3.5: The DAHW + Cu(Aβ) exchanges where $[DAHW]_0$ and $[DAHW]_t$ are determined by fluorescence data and $[Cu(A\beta_{1\text{-}16})]_0$ = 5.47 mM and $[Cu(A\beta_{1\text{-}28})]_0$ = 5.40 mM. Insets are the kinetic concentration versus time graphs.

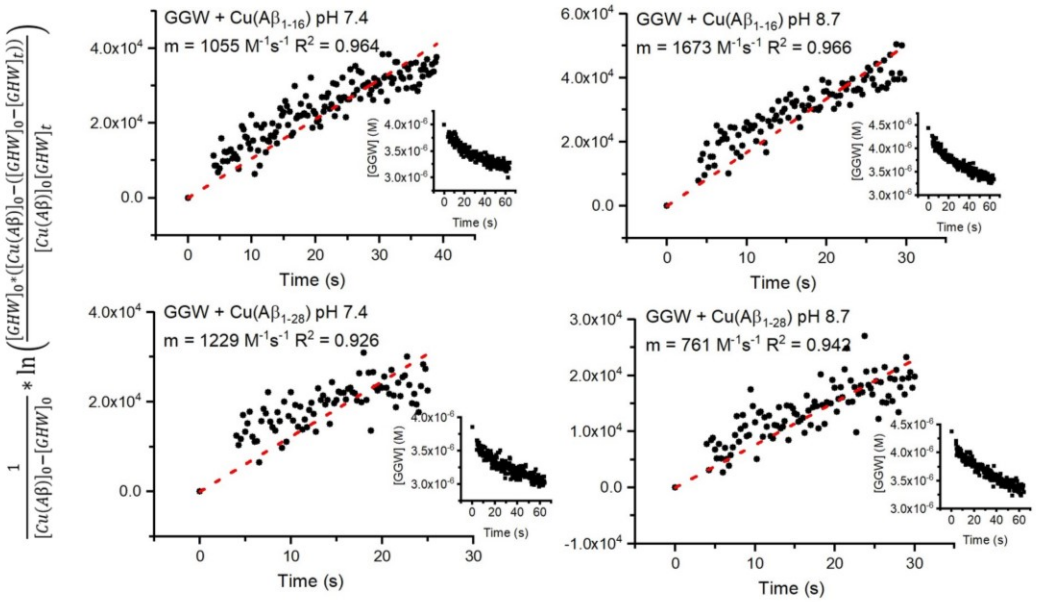

Figure 3.6: The GGW + Cu(Aβ) exchanges where $[GGW]_0$ and $[GGW]_t$ are determined by fluorescence data and $[Cu(A\beta_{1\text{-}16})]_0$ = 5.47 mM and $[Cu(A\beta_{1\text{-}28})]_0$ = 5.40 mM. Insets are the kinetic concentration versus time graphs.

There are some trends that can be observed in the conditional second-order rate constants that are reported in **Table 3.3**. First, the GHW exchanges are always faster than the DAHW exchanges, except with Cu(Aβ_{1-28}) at pH 8.7, where they are more similar. This trend is likely due to the combination of effects where the Cu(H$_{-1}$GHW) complex has only one amide deprotonation, a smaller metallocycle is formed, and has a coordinated water molecule. In comparison, the Cu(H$_{-2}$DAHW)$^{2-}$ complex requires two amide deprotonations, forms a larger metallocycle, has no coordinated water, and has an anionically charged N-terminus residue. Since the pKa of amide nitrogen protons are near 9, at the higher the pH, it becomes easier to deprotonate these binding sites to accommodate the Cu(II). However, chelate effects do effectively lower the pKa of these motifs.[33] Chelate effects are a phenomenon where once the metal has attached, the subsequent anchoring is favored and the effective pH needed to deprotonate the amide nitrogen is lowered.[33] Similarly, the smaller metallocycle formed in the GHK complex may also contribute to these effects. Lastly, the presence of an anionically charged and bulky residue at the N-terminus may deter Cu(II) binding at the N-terminus as compared to just hydrogen in the glycine residue. The N-terminus binding is especially important in the ATCUN (amino terminus copper and nickel) motifs. While the DAHK peptide has a slightly larger affinity for Cu(II) than GHK, the combination of these effects is probably the reason why the GHW exchanges are much faster than the DAHW exchanges.

In our previous work described in Chapter 2, the exchanges of Cu(II) from Cu(H$_{-1}$GHW) to GHK and DAHK peptides depended on the formation of a ternary complex. We attributed the faster rate constants of the GHK peptides to the ability of the coordinated water to dissociate, which allowed for faster ternary complex formation, and ultimately a faster exchange rate. Similarly, a ternary complex must initially form between the Cu(Aβ) complex and the incoming tryptophan peptide. As shown in **Figure 3.7**, we were able to capture the GHW-Cu(Aβ_{1-16}) ternary complex by low-temperature EPR spectroscopy. Since both the Cu(Aβ_{1-16}) and Cu(H$_{-1}$GHW) complexes have 3N + 1O binding in the equatorial plane when the Cu(II) is bound only to one of the peptides, the $g_{\perp}$ region would not have distinct and clear superhyperfine coupling. However, distinct superhyperfine coupling is observed in the EPR spectrum in **Figure 3.7**. Since the superhyperfine coupling is only clearly defined like this when the paramagnetic electron is in the same ligand environment, as in a 4N binding, we are observing the ternary species created, GHW-Cu(Aβ_{1-16}).

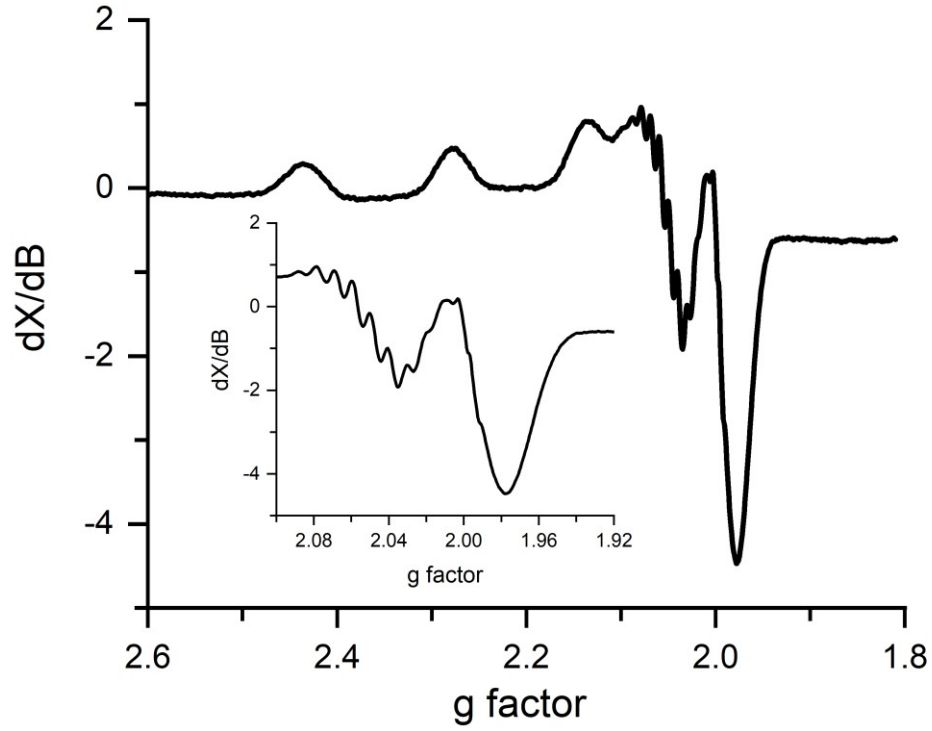

Figure 3.7: Low-temperature EPR of ternary complex formation GHW-Cu($A\beta_{1-16}$). Samples were taken at T = 150 K at 9.370512 GHz.

Since the larger Aβ peptide has more residues that surround the Cu(II) coordination sphere, this presents a barrier to the initial Cu(II) coordination by the tryptophan peptide to create the ternary complex. This would result in a slower ternary complex formation in the longer Aβ peptide than in the shorter length. Indeed, the Cu($A\beta_{1-16}$) exchanges to GHW and DAHW had faster rate constants than the corresponding Cu($A\beta_{1-28}$) exchanges. Interestingly, this does not seem to be the case in the GGW exchanges at pH 7.4, where both rate constants are essentially the same, but does agree at pH 8.7 where they are statistically different. This may be an indication of a hypothesis in our previous paper, that the initial binding in the ternary complex is the histidine residue and not the N-terminus.[32] The lack of a His residue in GGW and the slow exchange displayed by these exchanges would indicate that there is a difference between the ternary complex formation that is exhibited by GHW and DAHW. Since the only structural difference is the lack of a His residue, and since we have an indication that the His ligand may be the initial binding site in ternary complex formation from previous work in the Hureau group[35], this result seems to agree with our previous statements that the His residue is the likely first chelation site by the GHW and DAHW peptides in the ternary complex formation.

All of the measurable exchanges for the GGW peptide (at pH 6.8, these were too slow and not reported here as the fitting process was not reliable) were considerably slower than either GHW or DAHW. This was an expected result as there is no histidine ligand present in GGW. The effect of histidine in the second and third positions of small peptide sequences has been shown to create very stable complexes.[33, 35-36] Therefore, the lack of any histidine residues in the peptide resulted in a much slower exchange by at least one order of magnitude. One reason is that when histidine binds the Cu(II), a very stable 6 membered ring forms between the amide nitrogen and the histidine nitrogen. When no histidine is present, only a 5 membered ring forms between the backbone amide or N-terminus nitrogens, see structures in **Figure 3.2**. These 6 membered rings are inherently more stable than 5 membered rings.

Lastly, the pH of the solution does seem to affect the rate constant, as would be indicated by the mechanism given in **Eq. 3.1**, where a net number of protons can be generated as a product in the exchange. For the GHW + Cu($A\beta_{1-16}$) exchange, the rate constant is the same at pH 6.8 and 7.4 but is slower at pH 8.7. In **Eq 3.1**, a net of 1 H^+ is generated in the GHW + Cu($A\beta_{1-16}$) exchange when the complex is Cu($A\beta_{1-16}$)$^-$ which is predominant at pH 6.8. No net H^+ is generated by the Cu($H_{-1}A\beta_{1-16}$)$^{2-}$ complex, predominant at pH 8.7. Therefore, the exchange is faster for GHW when protons are generated as a product. Conversely, for the DAHW + Cu($A\beta_{1-16}$) exchange, the rate constant is the same at pH 7.4 and 8.7 and slower at pH 6.8. A net 2 H^+ is generated at the lower pH where the Cu($A\beta_{1-16}$)$^-$ complex is predominant than the net 1 H^+, which is generated at the higher pH where the Cu($H_{-1}A\beta_{1-16}$)$^{2-}$ is predominant. Therefore, the exchange is faster for DAHW when less H^+ is generated as products. Due to the nature of these peptides, as pH decreases, they have a harder time deprotonating the amide and N-terminus protons to allow for Cu(II) complexation. So for DAHW, which has 3 of these types of binding sites, the exchanges are faster at the higher pHs where fewer protons are generated in the exchange, which decreases the pH less as time progresses. While for GHW, which only has two of these types of binding sites, is less dependent on the generation of additional protons. In the DAHW exchange with Cu($A\beta_{1-28}$) this trend is conserved, whereas for GHW it is not. We measured the GHW + Cu($A\beta_{1-28}$) exchanges at pH 6.8 a second time and found no difference in the rate constant. Thus, the trend is lost upon lengthening of the amyloid peptide, which may have implications in the ternary species formation.

3.5 Conclusions

We have extended our previous methodology to measure interpeptidic Cu(II) exchange rate constants in truncated amyloid-beta peptides to the tryptophan-containing GHW, DAHW, and GGW. The interpeptidic Cu(II) exchange rate constants vary in their order of magnitudes from 10^3 to 10^4 $M^{-1}s^{-1}$ depending on a number of variables; including the pH, the length of the amyloid-beta peptide, whether the tryptophan peptide contained a histidine ligand, the number of amide deprotonations needed in the tryptophan peptide to coordinate the Cu(II), and the extent of the created tryptophan peptide metallocycle. We found that almost all of the GHW exchanges were faster than the DAHW exchanges except in one case. These observations were attributed to the fact that GHW creates a smaller metallocycle and requires fewer deprotonations to accommodate Cu(II) coordination. Similarly, all GHW and DAHW exchanges were faster than the corresponding GGW exchanges, which is due to the lack of a histidine residue in the GGW peptide. The longer Aβ peptide complexes present a barrier for the ternary complex formation. Thus, all exchanges from the Cu($A\beta_{1-16}$) complexes are faster than from Cu($A\beta_{1-28}$), which is most likely due to faster ternary species formation in the shorter peptide .

CHAPTER 3 REFERENCES

1. Glenner, G. G.; Wong, C. W., Alzheimer's Disease: Initial Report of the Purification and Characterization of a Novel Cerebrovascular Amyloid Protein. *Biochem. Biophys. Res. Commun.* **1984,** *120* (3), 885-890.

2. Wong, C. W.; Quaranta, V.; Glenner, G. G., Neuritic Plaques and Cerebrovascular Amyloid in Alzheimer Disease are Antigenically Related. *Proc. Natl. Acad. Sci. U. S. A.* **1985,** *82* (24), 8729-8732.

3. Chen, G.-f.; Xu, T.-h.; Yan, Y.; Zhou, Y.-r.; Jiang, Y.; Melcher, K.; Xu, H. E., Amyloid Beta: Structure, Biology and Structure-based Therapeutic Development. *Acta Pharmacol. Sin.* **2017,** *38* (9), 1205-1235.

4. Plant, L. D.; Boyle, J. P.; Smith, I. F.; Peers, C.; Pearson, H. A., The Production of Amyloid β Peptide Is a Critical Requirement for the Viability of Central Neurons. *J. Neurosci.* **2003,** *23* (13), 5531-5535.

5. Alies, B.; Hureau, C.; Faller, P., The Role of Metal Ions in Amyloid Formation: General Principles from Model Peptides. *Metallomics* **2013,** *5* (3), 183-192.

6. Faller, P.; Hureau, C.; Berthoumieu, O., Role of Metal Ions in the Self-assembly of the Alzheimer's Amyloid-β Peptide. *Inorg. Chem.* **2013,** *52* (21), 12193-12206.

7. Greenwald, J.; Riek, R., Biology of Amyloid: Structure, Function, and Regulation. *Structure* **2010,** *18* (10), 1244-1260.

8. Hureau, C., Coordination of redox active metal ions to the amyloid precursor protein and to amyloid-β peptides involved in Alzheimer disease. Part 1: An overview. *Coordination Chemistry Reviews* **2012,** *256* (19–20), 2164-2174.

9. Hureau, C.; Dorlet, P., Coordination of redox active metal ions to the amyloid precursor protein and to amyloid-β peptides involved in Alzheimer disease. Part 2: Dependence of Cu(II) binding sites with Aβ sequences. *Coordination Chemistry Reviews* **2012,** *256* (19–20), 2175-2187.

10. Kepp, K. P., Alzheimer's Disease: How Metal Ions Define β-amyloid Function. *Coord. Chem. Rev.* **2017,** *351* (Supplement C), 127-159.

11. Lovell, M. A.; Robertson, J. D.; Teesdale, W. J.; Campbell, J. L.; Markesbery, W. R., Copper, Iron and Zinc in Alzheimer's Disease Senile Plaques. *J. Neurol. Sci.* **1998,** *158* (1), 47-52.

12. Miura, T.; Suzuki, K.; Kohata, N.; Takeuchi, H., Metal Binding Modes of Alzheimer's Amyloid β-Peptide in Insoluble Aggregates and Soluble Complexes. *Biochemistry* **2000,** *39* (23), 7024-7031.

13. Parthasarathy, S.; Long, F.; Miller, Y.; Xiao, Y.; McElheny, D.; Thurber, K.; Ma, B.; Nussinov, R.; Ishii, Y., Molecular-Level Examination of Cu2+ Binding Structure for Amyloid Fibrils of 40-Residue Alzheimer's β by Solid-State NMR Spectroscopy. *Journal of the American Chemical Society* **2011,** *133* (10), 3390-3400.

14. Wilcock, D. M.; Vitek, M. P.; Colton, C. A., Vascular Amyloid Alters Astrocytic Water and Potassium Channels in Mouse Models and Humans with Alzheimer's Disease. *Neuroscience* **2009,** *159* (3), 1055-1069.

15. Demuro, A.; Parker, I.; Stutzmann, G. E., Calcium Signaling and Amyloid Toxicity in Alzheimer Disease. *J. of Biol. Chem.* **2010,** *285* (17), 12463-12468.

16. Hansson, O.; Zetterberg, H.; Buchhave, P.; Londos, E.; Blennow, K.; Minthon, L., Association Between CSF Biomarkers and Incipient Alzheimer's Disease in Patients with Mild Cognitive Impairment: A Follow-up Study. *Lancet Neurol.* **2006,** *5* (3), 228-234.

17. Blennow, K.; Hampel, H.; Weiner, M.; Zetterberg, H., Cerebrospinal Fluid and Plasma Biomarkers in Alzheimer Disease. *Nat. Rev. Neurol.* **2010,** *6* (3), 131-144.

18. Olsson, B.; Lautner, R.; Andreasson, U.; Öhrfelt, A.; Portelius, E.; Bjerke, M.; Hölttä, M.; Rosén, C.; Olsson, C.; Strobel, G.; Wu, E.; Dakin, K.; Petzold, M.; Blennow, K.; Zetterberg, H., CSF and Blood Biomarkers for the Diagnosis of Alzheimer's Disease: A Systematic Review and Meta-analysis. *Lancet Neurol.* **2016,** *15* (7), 673-684.

19. Festa, R. A.; Thiele, D. J., Copper: An Essential Metal in Biology. *Curr Biol* **2011,** *21* (21), R877-R883.

20. Franz, K. J.; Metzler-Nolte, N., Introduction: Metals in Medicine. *Chem. Rev.* **2019,** *119* (2), 727-729.

21. Jomova, K.; Vondrakova, D.; Lawson, M.; Valko, M., Metals, Oxidative Stress and Neurodegenerative Disorders. *Mol. Cell. Biochem.* **2010,** *345* (1), 91-104.

22. Kozlowski, H.; Janicka-Klos, A.; Brasun, J.; Gaggelli, E.; Valensin, D.; Valensin, G., Copper, Iron, and Zinc ions Homeostasis and Their Role in Neurodegenerative Disorders (Metal Uptake, Transport, Distribution and Regulation). *Coord. Chem. Rev.* **2009,** *253* (21), 2665-2685.

23. Kozlowski, H.; Luczkowski, M.; Remelli, M.; Valensin, D., Copper, Zinc and Iron in Neurodegenerative Diseases (Alzheimer's, Parkinson's and Prion Diseases). *Coord. Chem. Rev.* **2012,** *256* (19), 2129-2141.

24. Maret, W., Zinc and Zinc Ions in Biological Systems. In *Encyclopedia of Metalloproteins*, Kretsinger, R. H.; Uversky, V. N.; Permyakov, E. A., Eds. Springer New York: New York, NY, 2013; pp 2396-2400.

25. Nguyen, M.; Robert, A.; Sournia-Saquet, A.; Vendier, L.; Meunier, B., Characterization of New Specific Copper Chelators as Potential Drugs for the Treatment of Alzheimer's Disease. *Chemistry – A European Journal* **2014,** *20* (22), 6771-6785.

26. Alies, B.; Renaglia, E.; Rózga, M.; Bal, W.; Faller, P.; Hureau, C., Cu(II) Affinity for the Alzheimer's Peptide: Tyrosine Fluorescence Studies Revisited. *Analytical Chemistry* **2013,** *85* (3), 1501-1508.

27. Linder, M. C., Lomeli, N.A., Donley, S., Mehrbod, P.C, Cotton, S., Wooten, L., Copper Transport in Mammals. *Adv. Exp. Med. Biol.* **1999,** *448*, 1-16.

28. Pedersen, J. T.; Hureau, C.; Hemmingsen, L.; Heegaard, N. H. H.; Østergaard, J.; Vašák, M.; Faller, P., Rapid Exchange of Metal between Zn7–Metallothionein-3 and Amyloid-β Peptide Promotes Amyloid-Related Structural Changes. *Biochemistry* **2012,** *51* (8), 1697-1706.

29. Pearson, H. A.; Peers, C., Physiological Roles for Amyloid β Peptides. *J. Physiol.* **2006,** *575* (1), 5-10.

30. Snyder, S. W.; Ladror, U. S.; Wade, W. S.; Wang, G. T.; Barrett, L. W.; Matayoshi, E. D.; Huffaker, H. J.; Krafft, G. A.; Holzman, T. F., Amyloid-beta Aggregation: Selective Inhibition of Aggregation in Mixtures of Amyloid with Different Chain Lengths. *Biophys. J.* **1994,** *67* (3), 1216-1228.

31. Hanaki, A.; Kawashima, T.; Konishi, T.; Takano, T.; Mabuchi, D.; Odani, A.; Yamauchi, O., Copper(II)–tripeptide complexes in aqueous solution. Effects of the C-terminal chelate ring size on the coordination structure of doubly deprotonated complex species. *Journal of Inorganic Biochemistry* **1999,** *77* (3–4), 147-155.

32. Beuning, C. N.; Mestre-Voegtlé, B.; Faller, P.; Hureau, C.; Crans, D. C., Measurement of Interpeptidic Cu(II) Exchange Rate Constants by Static Fluorescence Quenching of Tryptophan. *Inorg. Chem.* **2018,** *57* (9), 4791-4794.

33. Margerum, D. W., Dukes, G. R. , Kinetics and Mechanisms of Metal-ion and Proton-transfer Reactions of Oligopeptide Complexes. *Met. Ions Biol. Syst.* **1974,** *1*, 157-207.

34. Hanaki, A.; Ikota, N.; Ueda, J.-i.; Ozawa, T.; Odani, A., Transport of the Cu(II) Bound with Histidine-Containing Tripeptides to Cysteine. Coordination Mode and Exchangeability of Cu(II) in the Complexes. *Bull. Chem. Soc. Jpn.* **2003,** *76* (11), 2143-2150.

35. Wong, L. F.; Cooper, J. C.; Margerum, D. W., Kinetics of copper(II)-glycylglycyl-L-histidine reactions. Acid decomposition and proton-assisted nucleophilic displacement by triethylenetetramine. *Journal of the American Chemical Society* **1976,** *98* (23), 7268-7274.

36. Fields, T. R., Kropp, P.J., Ligand Displacement of Glycylglycyl-L-histidine from its Cu(II) Complex. A Proton-assisted Mechanism Initiated at a Nonterminal Position. *J. Am. Chem. Soc.* **1974,** *96* (24), 7560-7562.

CHAPTER 4: COORDINATION CHEMISTRY OF A CONTROLLED BURST OF Zn^{2+} IN BULK AQUEOUS AND NANOSIZED WATER DROPLETS WITH A ZINCON CHELATOR[1]

4.1 Summary

The light-induced photolysis of $[Zn(NTAdeCage)]^{1-}$ generates a temporally controlled burst of Zn^{2+}, which are rapidly chelated *in situ* by the free ligand, $Zincon^{2-}$. The $[Zn(Zincon)]^{2-}$ coordination progress is monitored using absorption spectroscopy in bulk aqueous buffer and reverse micelle environments. The $[Zn(NTAdeCage)]^{1-}$ photocage and free ligand $Zincon^{2-}$ have different reverse micelle locations that affect the $[Zn(Zincon)]^{2-}$ formation at the nanoscale as compared to the bulk aqueous buffer. The formation of $[Zn(Zincon)]^{2-}$ in bulk aqueous buffer is more efficient despite the released Zn^{2+} and $Zincon^{2-}$ being physically closer within reverse micelles. The observed reduction of complex formation is attributed to the interfacial partitioning of $Zincon^{2-}$, distinct from the Zn^{2+} photocage in the water pool, requiring diffusion for the species to meet to form $[Zn(Zincon)]^{2-}$. This work introduces a proof-of-concept methodology to experimentally measure fast chelation reactions in confined spaces and thus provides an approach to explore cellular responses.

4.2 Introduction to Zn^{2+} bursts by $[Zn(NTAdeCage)]^{1-}$ photolysis, reverse micelles, and Zincon

The diverse metabolite and metal ion homeostasis that exists in cells limits our ability to study metal ion processes in complex biological systems.[5-10] Zn^{2+} is the second most abundant transition metal within the brain and can be stored as bound to metalloproteins or as labile Zn^{2+} pools bound to metabolites, which has contributed to its role in neurodegenerative disease.[6, 9, 11-28] Zn^{2+} has many structural and catalytic roles as co-factors for metalloproteins and enzymes, but the release of Zn^{2+} in its ionic form is essential for its function as a neurotransmitter.[6, 11-14, 17-18, 29] As cells present a highly heterogeneous and crowded reaction environment, studying metal ion complexation reactions confined at the nanoscale in simpler systems like reverse micelles provides a fundamental characterization of such reactions.[6, 9-10, 14, 30-31] Methods to form

[1] Beuning, C. N.; Barkley, N. E.; Basa, P. N.; Burdette, S. C.; Levinger, N. E.; Crans, D. C., Coordination Chemistry of a Controlled Burst of Zn^{2+} in Bulk Aqueous and Nanosized Water Droplets with a Zincon Chelator. *Inorg. Chem.* **2019,** *Published ASAP Dec. 6 2019* DOI: 10.1021/acs.inorgchem.9b02848.

and control a burst of metal ions and follow their coordination reactions on a cellular scale promotes a better understanding of the functions that transition metals have in biology.

Photocaged metal complexes use light to release metal ions *in situ*, enabling controlled metal ion generation.[2, 10, 32-37] We demonstrate the photolysis of a metal-bound photocage, $[Zn(NTAdeCage)]^{1-}$, to generate a temporally controlled burst of Zn^{2+} in the nanosized reverse micelles. Upon release, the metal ion undergoes a complexation reaction with an *in situ* chelator ligand. The relative metal ion affinity of the photocage must be greater than the chelating agent so that any metal ions transferred arise from photolytic release and not sequestration. How this type of process proceeds when confined to a highly heterogeneous nanoscale environment, is not known.

In this work, a nitrilotriacetate decarboxylation photocage, $[Zn(NTAdeCage)]^{1-}$ (K_D = 1.0 x 10^{-13} M), released a burst of Zn^{2+} upon irradiation at 355 nm, **Figure 4.1a**.[2] The *in situ* chelating ligand, $Zincon^{2-}$ complexed to the released ions to form $[Zn(Zincon)]^{2-}$, **Figure 4.1b**.[3-4] We chose $Zincon^{2-}$ as the *in situ* ligand due to its commercial availability, its lower Zn^{2+} affinity (K_D = 2.09 x 10^{-6} M), and it has well-resolved absorption features of its bound and unbound states. The quantum yield of $[Zn(NTAdeCage)]^{1-}$ was previously reported near 30% in 40 mM HEPES, 100 mM KCl, pH 7.5, irradiation at 3 W and 365 nm. [2] At an average laser power of 0.133 W, the quantum yield was 16.7% in bulk aqueous buffer (40 mM HEPES, pH 7.4) or 17.4% in reverse micelles (same buffer and pH in 0.2 M AOT w_0 30) and does not contribute to the observed differences in reaction progress discussed. We followed the complexation reaction progress within reverse micelles because they present a simple self-assembling nanoscale system which can be used to characterize how the presence of an interface and nanoconfinement affects molecules and their reactions, **Figure 4.1c**.[37-47] A common self-assembling surfactant is sodium bis(2-ethylhexyl) sulfosuccinate (AOT), which is dissolved in an organic solvent like 2,2,4-trimethyl pentane (isooctane). When small volumes of water are added to AOT/isooctane solutions, isolated nanosized water droplets form surrounded by a monolayer of surfactant molecules. We characterize reverse micelle size by w_0 = [water]/[AOT].[48] The nanoscopic reverse micelle provides various sub-environments where encapsulated molecules can partition to upon confinement, **Figure 4.1c**. These include a bulk-like (for larger w_0 sizes) water pool interior (A), a highly organized interfacial Stern layer where water interacts strongly with the anionic AOT sulfonate headgroups and Na^+ counterions (B), aliphatic surfactant tails (C), or the organic solvent (D). Considering

the number of micelles formed and the number of molecules of each species are known, the w_0 = 30 size and 32 μM species concentrations ensured a statistical distribution one $[Zn(NTAdeCage)]^{1-}$ and one $Zincon^{2-}$ per reverse micelle. Having both species in most of the reverse micelles meant that they did not have to exchange their contents for the reaction to proceed.

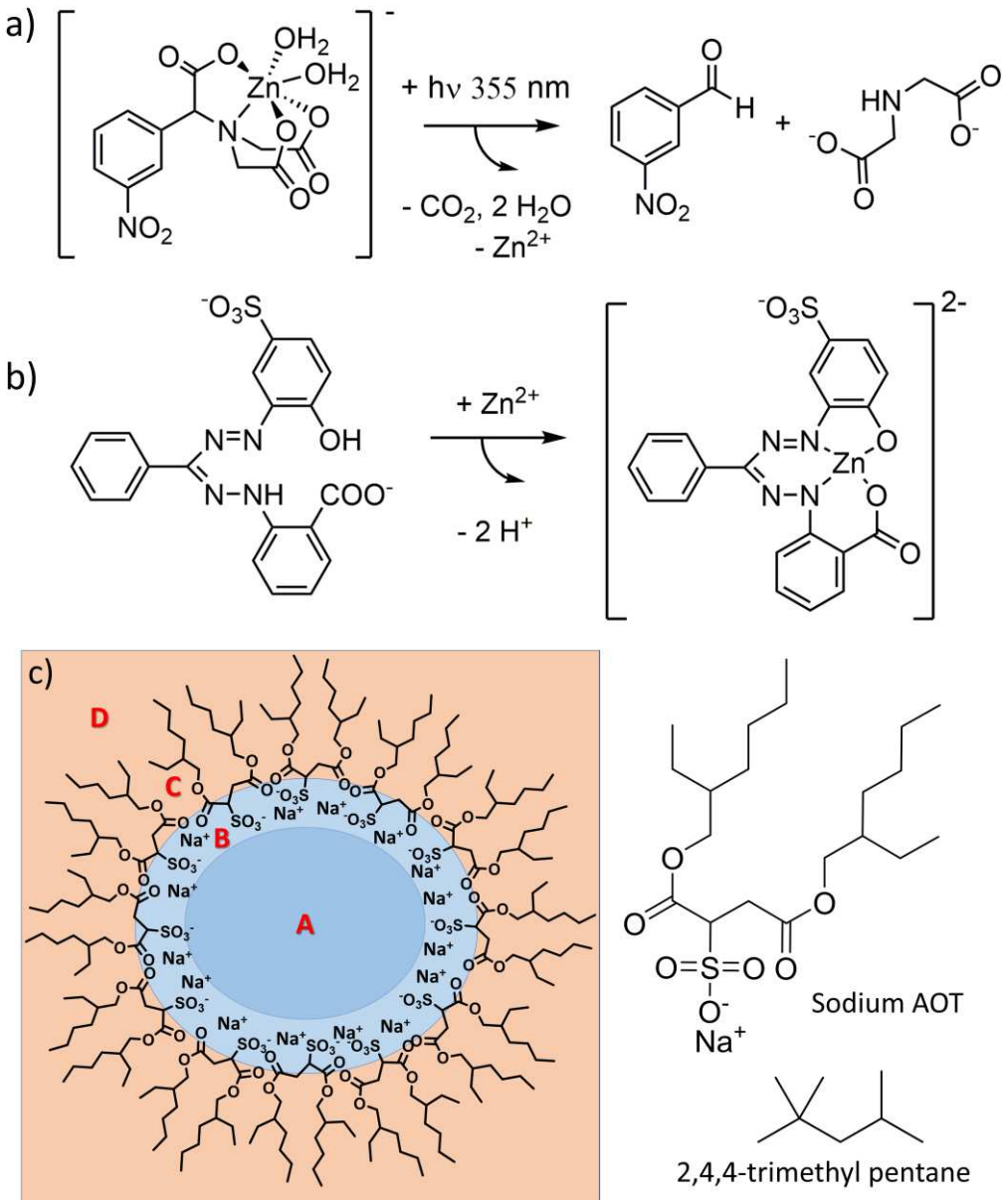

Figure 4.1: a) Scheme for the $[Zn(NTAdeCage)]^{1-}$ photolytic decarboxylation to form *m*-nitrobenzaldehyde and iminodiacetic acid.[2] b) Scheme for complexation reaction of Zn^{2+} with $Zincon^{2-}$ to form $[Zn(Zincon)]^{2-}$.[3-4] c) Cartoon representing the reverse micelle regions A: interior bulk-like water pool; B: interfacial Stern layer and AOT head groups; C) hydrophobic surfactant tails; D) nonpolar phase.

4.3 Experimental methods

4.3.1 Materials

The following chemicals were purchased from Sigma-Aldrich and used without purification, and all solvents are ACS reagent grade; [5-(hydroxy-5-sulfophenyl)-3-phenyl-1-formazyl] benzoic acid monosodium salt (Zincon^{2-}), $ZnSO_4 \bullet 7H_2O$, HCl, NaOH, acetone, dimethyl sulfoxide (DMSO), acetonitrile (ACN), ethyl acetate, 2,2,4-trimethyl pentane (isooctane), and (4-(2-hydroxyethyl)-1-piperazineethanesulfonic acid) (HEPES). Sodium bis(ethylhexyl) sulfosuccinate (AOT, Sigma, 97%) was further purified using a previously reported method.[42, 49-50] 2,2'-((carboxy(3-nitrophenyl)methyl)azanediyl)diacetic acid (NTAdeCage^{3-}) decarboxylation cage was synthesized by the Burdette group.[2] All aqueous solutions were prepared with high purity deionized (DI) water at 18.2 MΩ•cm resistivity from a Millipore or Nanopore system. Both light-sensitive materials, Zincon^{2-} and NTAdeCage^{3-}, were stored in the dark and under refrigeration.

4.3.2 Instrumentation

Absorption spectra were collected a Perkin Elmer Lambda 25 UV-vis spectrometer with 1500 µL quartz cuvettes with a 1 cm pathlength at room temperature, with a sample cuvette and background cuvette holder. Background spectra were automatically subtracted from sample absorption with a second paired cuvette with blank solutions. Photolysis experiments were performed with an OPOTEK Inc. Opolette 355 LD nanosecond laser with a pulse frequency at 20 Hz at 100 % efficiency, at 355 nm, with an average power of ~133 mW, at room temperature. All NMR studies were performed on an Agilent or Bruker 400 MHz instrument, with at least 256 scans with 8 transients, mixing times of 200 ms, pulse delay of 1.5 s, at 273 K, in ^{1}H NMR, COSY, and HSQC.

4.3.3 Preparation of stock NTAdeCage^{3-}, Zincon^{2-}, and Zn^{2+} solutions

The stock solution of 4.0 mM NTAdeCage^{3-} was created by dissolving in 40 mM HEPES at pH 7.4. The stock solution of 24.17 mM Zn^{2+} ions was created in DI water from $ZnSO_4 \bullet 7H_2O$. The stock solutions of 2.0 – 5.0 mM Zincon^{2-} were prepared by completely dissolving the powder in approximately 150-300 µL of 0.1 M NaOH then diluted to 1000 µL with 40 mM HEPES buffer solution. The Zincon^{2-} solubility in a basic solution (1.0 M NaOH) is much greater than at lower pH, and at 0.1 M NaOH, the solubility is 1 mg/mL or

about 2 mM.[51] If the pH dropped below 5, Zincon^{2-} precipitated out of solution. Aqueous stock solutions of all light-sensitive material were stored covered by foil in the refrigerator for up to one week. Both Zincon^{2-} and [Zn(NTAdeCage)]$^{1-}$ solutions were prepared freshly and used within a week of preparation.

4.3.4 Sample preparation for UV-vis spectroscopy and photolysis experiments

Samples were prepared at concentrations to ensure absorbances less than one in a 1 cm pathlength optical quartz micro cuvette. The molar absorptivity of Zincon^{2-} depends on buffer system, environment, and pH but is approximately 24,000 $M^{-1}cm^{-1}$ in the aqueous buffered solution and near 18,000 $M^{-1}cm^{-1}$ in the reverse micelles; the [Zn(Zincon)]$^{2-}$ is approximately 15,000 $M^{-1}cm^{-1}$.[3, 52] A 40 μM concentration of Zincon^{2-} in buffered aqueous solution gave an absorbance near 0.95. As all three species absorb in the 230-350 nm wavelength range (Figure 2), they can all absorb the laser photolysis radiation at 355 nm.

4.3.5 Aqueous sample preparation

Aliquots of stock solutions were pipetted directly into the optical quartz micro cuvette to create the final concentrations. Specifically, the 40 μM [Zn(NTAdeCage)]$^{1-}$ was first created by addition of a large aliquot of 40 mM HEPES into the cuvette, and then the volumes of Zn^{2+} and NTAdeCage^{3-} stocks were added to create 40 μM [Zn(NTAdeCage)]$^{1-}$ assuming a 1:1 chelation ratio and inverted at least three times to mix and ensure complexation. Then 10 μL aliquots (or less) were added of Zincon^{2-} so that the final Zincon^{2-} concentration in the cuvette volume was also 40 μM. This allowed for little concentration changes in the [Zn(NTAdeCage)]$^{1-}$ by adding small volumes of the second ligand. After all the species were added to the cuvettes, they were closed and inverted at least three times to ensure proper mixing.

4.3.6 Reverse micelle sample preparation

An aqueous solution of the [Zn(NTAdeCage)]$^{1-}$ complex was prepared in 40 mM HEPES, and then Zincon^{2-} was added. This solution was created at a higher concentration (331 μM) so that when diluted with a large aliquot of AOT-isooctane, the overall sample concentration was 32 μM for both species in the final sample volume. Then a calculated volume of the aqueous sample with both species was added to the appropriate volume of 0.2 M AOT in isooctane to create the appropriate w_0 value reverse micelle. The mixture was then vortexed until clear with a rose color (Zincon^{2-}) or a violet color ([Zn(Zincon)]$^{2-}$); hazy

samples were discarded and remade. All reverse micelles samples were prepared immediately before their spectroscopy was performed. The reverse micelle w_0 size ranged from 0 (no added water) up to 50, where larger w_0 values indicate larger water pools where bulk-like water properties can exist.[48, 53] The relationship w_0 = [H_2O]/[AOT] was used to find the respective volumes of aqueous and AOT-isooctane solutions required.[48] For example, a w_0 = 30 with 0.2 M AOT requires 107 µL of aqueous solution and 1000 µL of AOT-isooctane. The residual water content of the purified AOT was analyzed by NMR by a previous method and calculated at 0.33 H_2O molecule/AOT molecule. This value was considered in the w_0 calculation.[49-50] A reverse micelle size of w_0 = 30 was chosen to ensure a system that statistically had one [Zn(NTAdeCage)]$^{1-}$ and one Zincon^{2-} molecule in each reverse micelle at the 32 µM concentrations and still had the parameters required for UV-vis monitoring. Also, the interior of larger reverse micelles have more bulk-like water properties, and lower percentages of interfacial water, thus larger reverse micelle sizes enable direct comparison between the photolysis in reverse micelles to that of bulk water.[48, 53] Due to the volatility of isooctane, the AOT-isooctane solutions were prepared freshly, capped, and sealed with parafilm for up to two weeks to prevent concentrating the AOT from isooctane evaporation. The blank used in all reverse micelle UV-vis experiments was an empty (no analyte) reverse micelle of the w_0 as in the experiment. No difference of Zincon^{2-} absorption spectra were found in an aqueous solution of NaCl at high (1.0 M) concentrations, like that found at the reverse micelle interface.

4.3.7 Photolysis sample handling

All cuvette samples were prepared as described above and measured within 1 h of preparation. All samples were kept in the dark container between transport from the laser to the UV-vis spectrometer. The time between photolysis exposure was less than 10 min, which included taking the UV-vis absorption spectrum between exposures with completed photolysis within 60 min of initial sample preparation within the cuvette. All photolysis experiments in aqueous buffered solution and reverse micelles were performed in duplicate.

4.3.8 Photolysis experiment design

Photolysis samples were created freshly before each photolysis session; the photolysis was completed within an hour with an average laser power of 129 ± 4 mW for reverse micelles or 133± 4 mW

for aqueous buffered solutions with 100% efficiency, a frequency of 20 Hz, at a wavelength of 355 nm. Samples were exposed to the laser for a well-defined time period, after which they were transported in the dark from the laser to the UV-vis spectrometer to avoid any photolysis due to ambient light. Upon photolysis, the color of the solution gradually changed from rose/orange to violet/blue, indicating $Zincon^{2-}$ conversion to $[Zn(Zincon)]^{2-}$. Samples were kept in the dark at ambient room temperature between laser photolysis and absorbance measurements and inverted three times to mix after each laser exposure period.

4.3.9 NMR sample preparation

All reverse micelle solutions for NMR analysis were prepared with 0.75 M AOT in isooctane with 100 % D_2O instead of water for the NMR lock. The NMR studies required a higher concentration of AOT so that signals from Zincon, and $[Zn(Zincon)]^{2-}$ were above the sensitivity limit with 0.75 M AOT requiring an overall 1 mM $Zincon^{2-}$ concentration needed for measurable NMR signals. Because the aqueous solubility of $Zincon^{2-}$ is limited, larger volumes of water associated with larger AOT concentration facilitated the measurements. The high AOT concentration limited the size to $w_0 = 20$, and we attempted to prepare $w_0 = 30$ reverse micelles, but they were unstable due to their cloudy, phase-separated appearance. The CH_2 and CH_3 signals from the AOT and isooctane, which are not deuterated, are very intense and dominate the reverse micelle spectra leading to larger signal to noise ratios in the reverse micelle spectra. The pH of the D_2O was adjusted with DCl or NaOD to give a pD near 9, where pD = pH + 0.4.[54] A pH near 9 was chosen for NMR characterization of $Zincon^{2-}$ and $[Zn(Zincon)]^{2-}$ as this is the optimal pH for Zn^{2+} complexation to $Zincon^{2-}$ according to speciation charts, while a physiological pH was preferred for the photolysis experiments.[4, 55] For $Zincon^{2-}$ NMR in acetone, the addition of 7.7% D_2O immensely improved the solubility of $Zincon^{2-}$, and the NMR peaks in acetone alone were not as well resolved due to inhomogeneity in the sample of insoluble $Zincon^{2-}$.

4.3.10 Processing software used in analysis

OriginPro 2018b (student version) was used for all figure creation, and some data analysis, including Gaussian and linear fitting. Microsoft Excel 2016 was used to perform simple data analysis such as averages, standard deviations, or other simple calculations. ChemDraw Professional 16.0 was used to create chemical structures. MestReNova x64 was used to create NMR spectra, perform multiplet analysis,

and the stacking of NMR spectra. The resolution booster processing tool was used to determine isomer content in the aqueous ^{1}H NMR spectra of both Zincon^{2-} and [Zn(Zincon)]$^{2-}$.

4.4 Results and discussion

4.4.1 Aqueous and reverse micelle control experiments performed

To enable the interpretation of photolysis experiments of complex mixtures, we measured individual absorption spectra of the components. **Figure 4.2** displays the absorption spectra of each species, [Zn(NTAdeCage)]$^{1-}$, Zincon^{2-}, and [Zn(Zincon)]$^{2-}$, in aqueous buffered solution (panel a) and reverse micelles (panel b). The sole absorption feature displayed by [Zn(NTAdeCage)]$^{1-}$ appears at 270 nm in both aqueous and reverse micelles, which suggests that it resides in the water pool and maintains its hydrated coordination sphere. The [Zincon]$^{2-}$ maximum wavelength shifts 70 nm to 545 nm in reverse micelles from 475 nm in aqueous solution and displays a significantly altered peak shape, suggesting it embeds in the interface. The [Zn(Zincon)]$^{2-}$ spectrum displays a similar peak maximum and shape near 620 nm with increased intensity at the short wavelength side in the reverse micelles. This suggests [Zn(Zincon)]$^{2-}$ may interact with the interfacial water but is not as dramatic as the observed changes in the Zincon^{2-} spectrum.

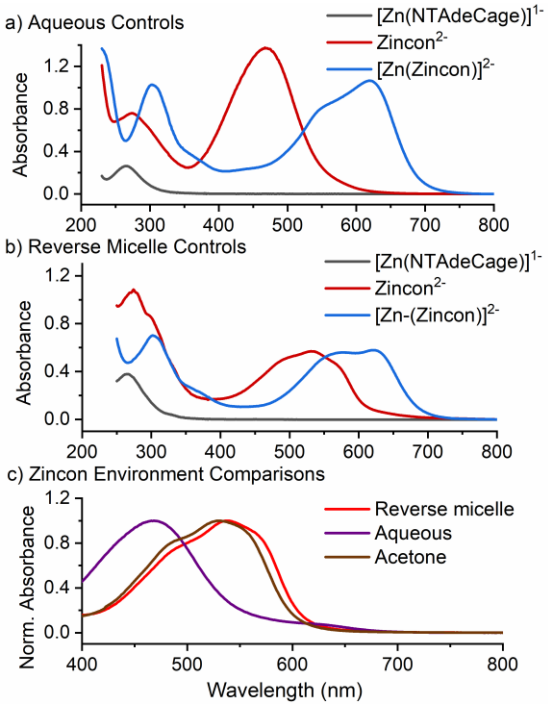

Figure 4.2: The UV-vis absorption spectra of a) [Zn(NTAdeCage)]$^{1-}$, Zincon^{2-}, and [Zn(Zincon)]$^{2-}$ in 40 mM HEPES at pH 7.40 (40 - 50 μM); b) 32 μM [Zn(NTAdeCage)]$^{1-}$, Zincon^{2-}, and [Zn(Zincon)]$^{2-}$ in 40 mM HEPES at pH 7.40 within w_0 = 30 reverse micelles (0.02 M AOT); c) Zincon^{2-} chemical environment comparisons of the aqueous, reverse micelle, and acetone normalized absorption spectra.

We also measured spectra for combinations of $[Zn(NTAdeCage)]^{1-}$ and $Zincon^{2-}$ to confirm that $[Zn(Zincon)]^{2-}$ complexation arises from the photolytic release of ions and not by the Zn^{2+} abstraction from intact photocages. **Figure 4.3** shows that when both $[Zn(NTAdeCage)]^{1-}$ and $Zincon^{2-}$ are present in solution, the $[Zn(NTAdeCage)]^{1-}$ remains largely intact, with about 5% of $[Zn^{2+}]_{total}$ bound to $Zincon^{2-}$. This also confirmed that the $NTAdeCage^{3-}$ photocage has a higher Zn^{2+} affinity than $Zincon^{2-}$. When Zn^{2+} is added to a solution of $NTAdeCage^{3-}$ and $Zincon^{2-}$, the Zn^{2+} preferentially binds to $NTAdeCage^{3-}$ with about 6% of $[Zn^{2+}]_{total}$ bound to $Zincon^{2-}$, **Figure 4.4**. When $NTAdeCage^{3-}$ is added to a solution of $[Zn(Zincon)]^{2-}$, it sequesters a stoichiometric amount of Zn^{2+} and no $[Zn(Zincon)]^{2-}$ peak remains, **Figure 4.5**. These experiments confirm that Zn^{2+} complexed by $Zincon^{2-}$ originates from the Zn^{2+} captured after photolysis of the $[Zn(NTAdeCage)]^{1-}$ and not by the Zn^{2+} abstraction from intact photocages.

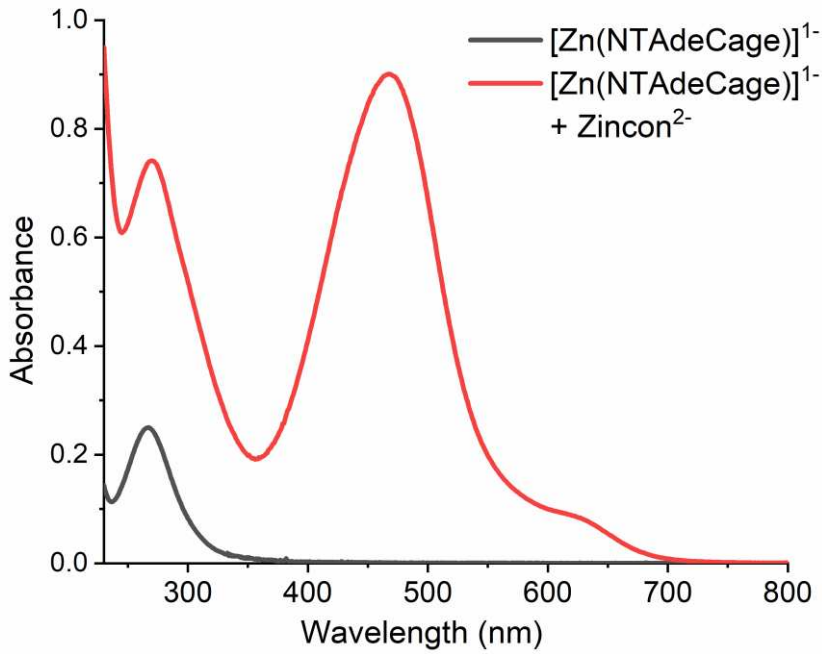

Figure 4.3: The spectra shown here are the control experiments to determine that $[Zn(NTAdeCage)]^{1-}$ remains intact in the presence of $Zincon^{2-}$. First, 40 μM $[Zn(NTAdeCage)]^{1-}$ was created (black line), and then 40 μM $Zincon^{2-}$ (red line) was added, and the spectra were taken 2 minutes after addition.

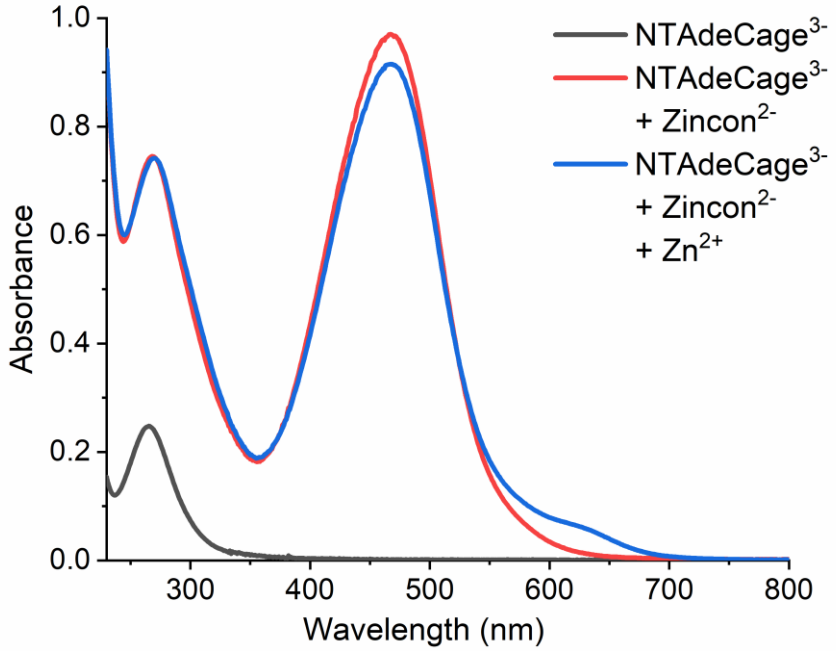

Figure 4.4: The spectra shown here are the control experiments to determine that Zn^{2+} preferentially binds to $NTAdeCage^{3-}$ in the presence of both ligands. First, 40 μM $NTAdeCage^{3-}$ is added (black line) and then 40 μM $Zincon^{2-}$ is added (red line). Once the $NTAdeCage^{3-}$ + $Zincon^{2-}$ solution was created, then 40 μM Zn^{2+} was added (blue line).

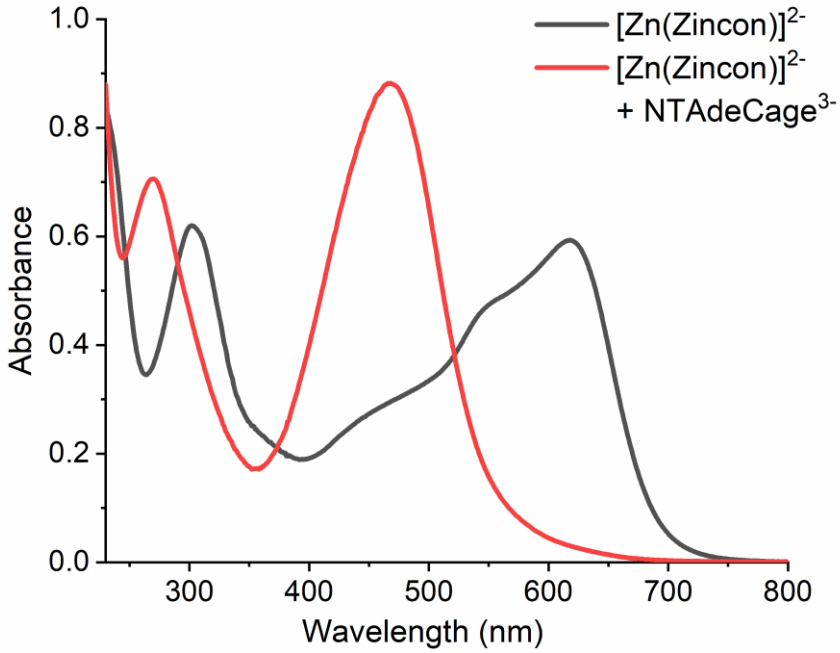

Figure 4.5: The spectra shown here are the control experiments that show $NTAdeCage^{3-}$ sequestered a stoichiometric amount Zn^{2+} from $[Zn(Zincon)]^{2-}$. First, 40 μM $[Zn(Zincon)]^{2-}$ is created (black line). When 40 μM $NTAdeCage^{3-}$ is added (red line) the unbound $Zincon^{2-}$ peak at 475 nm was generated.

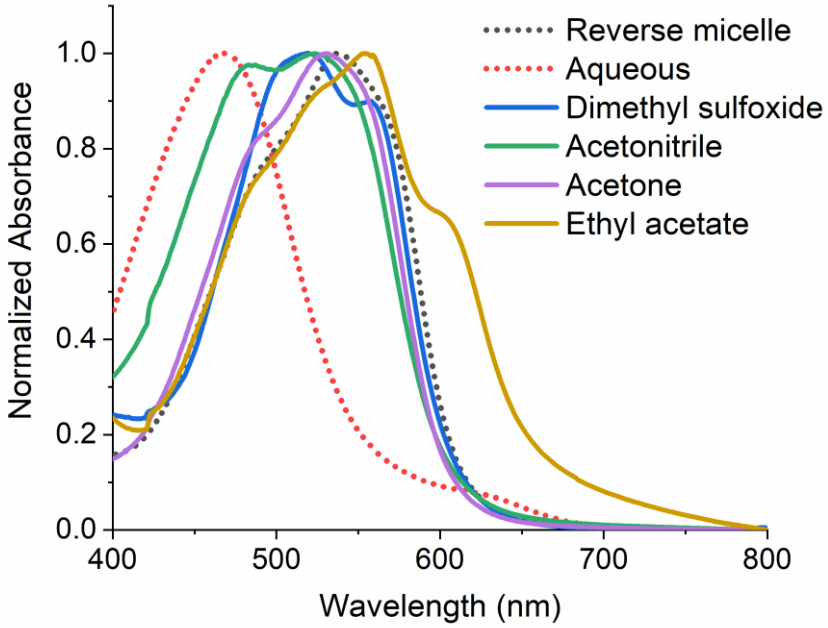

Figure 4.6: Comparison of spectra of 40 μM Zincon^{2-} in w_0 = 30 AOT reverse micelles, aqueous buffered solution, with Zincon^{1-} (COOH protonated in organic solvent) in dimethyl sulfoxide (DMSO), acetonitrile, acetone, and ethyl acetate. The spectra of Zincon^{2-} in reverse micelles (black) and Zincon^{-} in acetone (purple) share similar spectral shape and position.

Various properties of reverse micelles could affect the Zincon^{2-} absorption spectrum. The large 70 nm red-shift of the Zincon^{2-} absorption peak in reverse micelles suggests a distinct difference from the aqueous environment. To determine if the observed red-shift could be attributed to a hydrophobic environment, we measured the Zincon^{2-} absorption spectrum in several polar organic solvents, including acetone, dimethyl sulfoxide, ethyl acetate, and acetonitrile, **Figure 4.6**. The remarkable similarity between the Zincon^{2-} spectrum in acetone and in reverse micelles, **Figure 4.2c**, is consistent with Zincon^{2-} penetrating deeply into the interface where it interacts with the organic portion of the AOT surfactant. Molecules as large as Zincon^{2-} can sample multiple reverse micelle regions, potentially spanning a range of physical environments.[42] Selective solvation of different Zincon isomers may result in contributions with slightly different spectroscopic signatures that can coalesce in the same wavelength range and contribute to broadening in the UV-vis absorption spectrum.[39, 48, 50, 53] Indeed, the Zincon^{2-} spectrum in reverse micelles required four contributions in a sum of Gaussians fit, **Figure 4.7**, and **Table 4.1**. Experiments varying Zincon^{2-} concentration and reverse micelle size, w_0, show little effect on the peak position except for slight increases in the short wavelength shoulder, **Figure 4.8**.

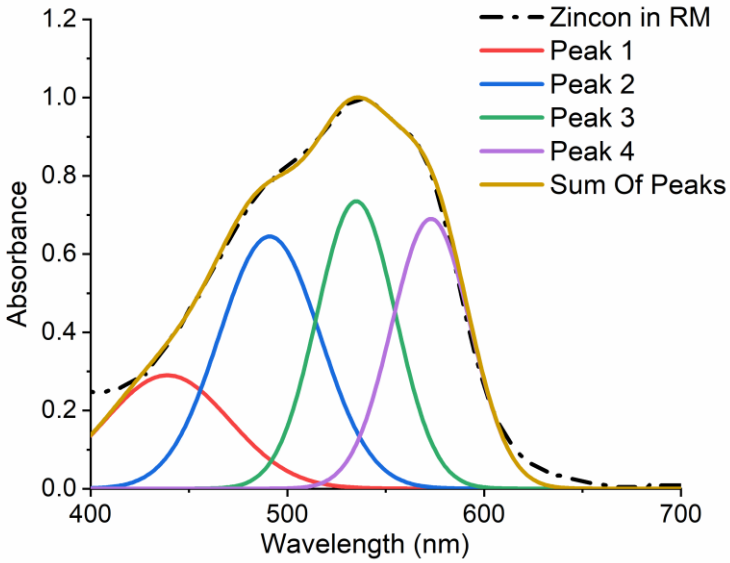

Table 4.1: The Gaussian fitting parameters for fit shown in **Figure 4.7** where λ is the central wavelength (nm), σ is the variance (nm), and A is the relative absorbance maximum for each peak.

	Peak 1	Peak 2	Peak 3	Peak 4
λ (nm)	439	491	535	573
σ (nm)	1000	660	400	400
A	0.29	0.65	0.74	0.69

Figure 4.7: The fit of the normalized absorption spectrum of 10 μM Zincon^{2-} in w_0 = 30 reverse micelles to a sum of Gaussian peaks. The experimentally acquired spectrum is shown with the black dotted line. There are four distinct peaks when summed together (yellow line) fit the experimental conditions. The Gaussian peak information is given in **Table S1**. These results suggest that as many as four peaks contribute to the reverse micelle experimental peak shape. These could be due to different isomers or different ways that the Zincon^{2-}associates with reverse micelle interface (see NMR analysis section for further discussion).

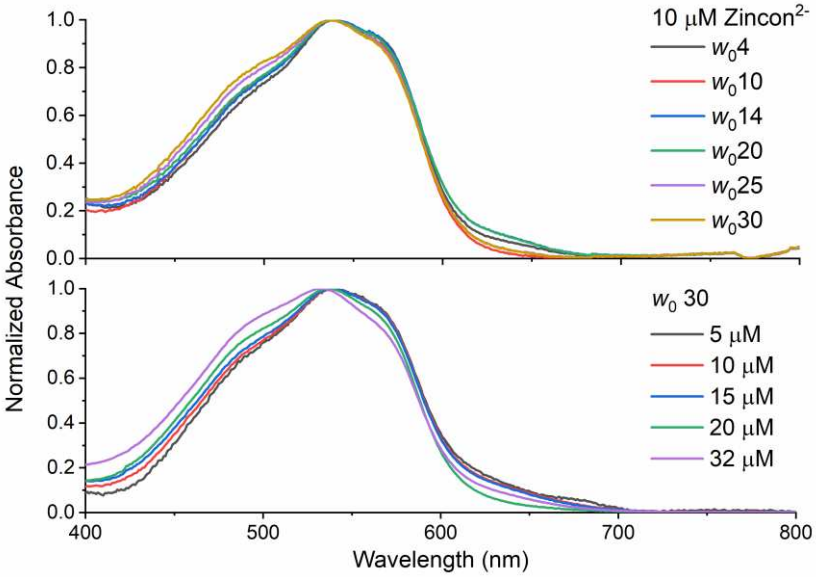

Figure 4.8: *Top* Normalized absorbance of 10 μM Zincon^{2-} (in 40 mM HEPES, pH 7.4) in varying reverse micelle sizes, w_0 = 4-30. We used 0.2 M AOT due to excellent solubility of solutes in all reverse micelle sizes. *Bottom* Normalized absorbance of a constant reverse micelle size w_0 = 30 (0.2 M AOT) with varying overall concentrations of Zincon^{2-} in 40 mM HEPES in the overall 1 mL reverse micelle sample. The spectral shapes are very similar with varying reverse micelle size or concentration, except slight increases on the short wavelength shoulder. This indicates that the Zincon^{2-} preferentially localizes in the interfacial location regardless of reverse micelle sizes or concentration.

4.4.2 Nuclear Magnetic Resonance analysis of Zincon^{2-} and [Zn(Zincon)]$^{2-}$ reverse micelle locations.

If the Zincon^{2-} and [Zn(Zincon)]$^{2-}$ interact with or embed in the interfacial Stern layer or AOT tails, as the UV-vis absorption spectroscopy suggests, it should severely impede their molecular motion. We test this hypothesis using NMR spectroscopy, whose chemical shifts and spectral peak widths are sensitive to molecular tumbling. Changes in NMR peak chemical shifts observed between aqueous buffered solution and reverse micelles has often been attributed to interfacial probe location. We used various NMR techniques to elucidate the extent of interfacial penetration by Zincon^{2-} or [Zn(Zincon)]$^{2-}$ in reverse micelles.[39, 41-43, 53, 56]

4.4.2.1 The NMR analysis of Zincon^{2-} in aqueous buffer, reverse micelles, and acetone chemical environments.

We focused on the ^{1}H NMR characterization of the Zincon^{2-} aromatic hydrogens (H_A – H_J **Figure 4.9**) in various conditions. **Figure 4.10** shows the aromatic region in the ^{1}H NMR spectra of the free Zincon^{2-} in D_2O, in 7.7% (v/v) D_2O in d_6-acetone, and in AOT reverse micelles prepared with D_2O. Peak labels, defined in **Figure 4.9**, are based on the hydrogen assignments derived from 1D ^{1}H NMR integration, splitting, as well as 2D ^{1}H^{1}H COSY cross-peaks, and/or ^{1}H^{13}C HSQC NMR, see **Figures 4.11** (^{1}H NMR in D_2O), **4.12** (^{1}H^{1}H COSY in D_2O), **4.13** (^{1}H NMR in d_6 acetone/7.7% D_2O), **4.14** (^{1}H^{1}H COSY in d_6 acetone/7.7% D_2O), **4.15** (^{1}H ^{13}C HSQC in d_6 acetone w/ 7.7% (v/v) D_2O) and **4.16** (^{1}H NMR in w_0 = 20, 0.75 M AOT). There are a few changes in [AOT], [Zincon^{2-}], pH, and w_0 size between NMR and UV-Vis spectroscopies, as discussed in the experimental section in the NMR sample preparation section.

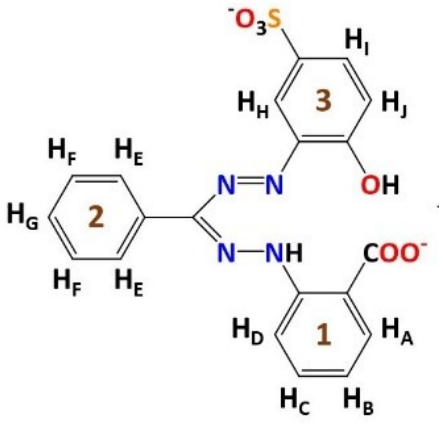

Figure 4.9: The structure of Zincon^{2-} in the deprotonated form found at pH 7.40. Aromatic hydrogens are labeled for identification in NMR analysis.

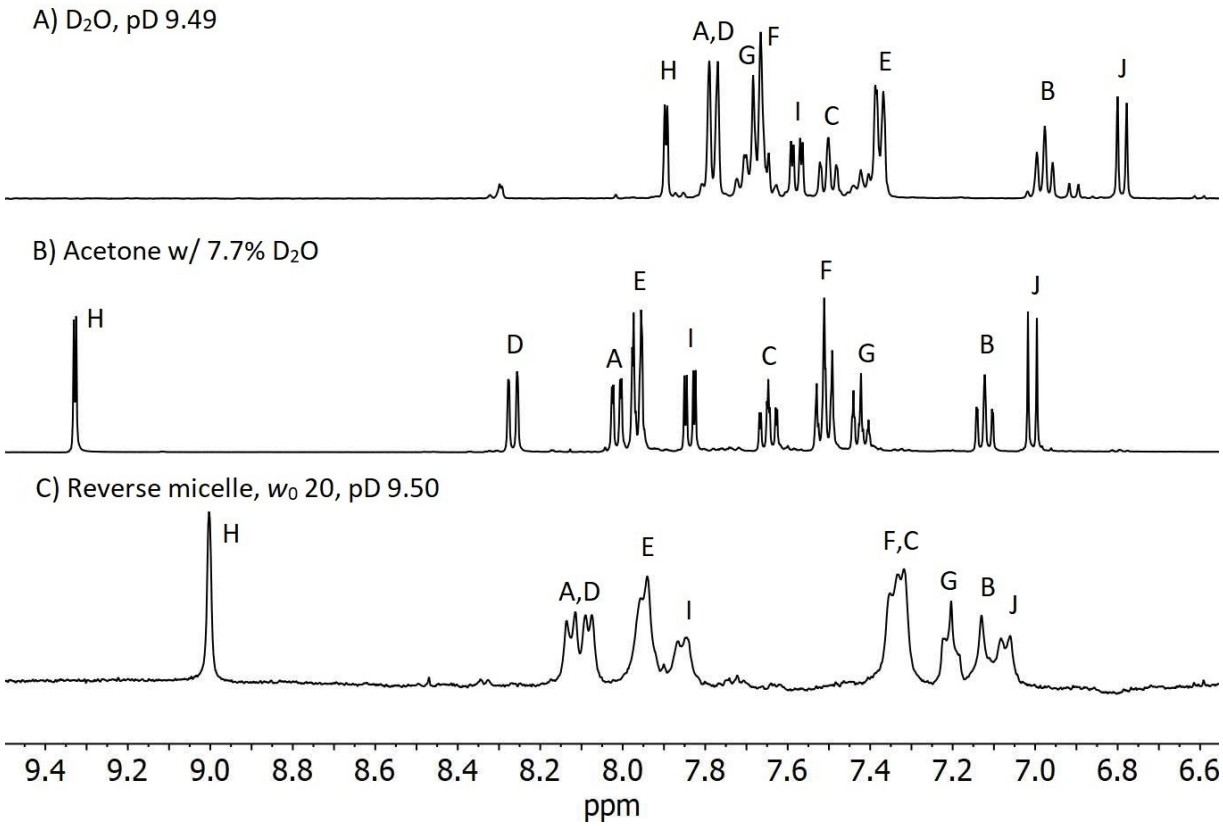

Figure 4.10: The stacked ^{1}H NMR spectra showing signals arising from aromatic region of the hydrogens of unbound Zincon^{2-} in *A:* D_2O pD = 9.49; *B:* d_6 acetone with 7.7% (v/v) D_2O; *C:* w_0 = 20 reverse micelle (0.75 M AOT, pD = 9.50). The aromatic hydrogens are labeled as assigned in **Figure 4.9**.

We make several general observations from these ^{1}H NMR spectra. First, the differences between the spectrum of Zincon^{2-} in aqueous and reverse micelle environments, **Figure 4.10** A and C, respectively, indicate that Zincon^{2-} does not reside in a bulk-like water environment when it is in the reverse micelles. Essentially all aromatic hydrogens display different chemical shifts in bulk aqueous versus reverse micellar environments, **Table 4.2**. The chemical shift range for Zincon^{2-} in reverse micelles extends further downfield, 7.07 – 9.00 ppm (reverse micelle) vs. 6.79 – 7.90 ppm (aqueous). Specifically, the Zincon^{2-} reverse micelle ^{1}H NMR signals experience both upfield and downfield shifting compared to the spectrum in D_2O, consistent with a heterogeneous chemical environment of the ligand, see **Table 4.2** for absolute changes in ppm (Δ ppm).[39, 56-57] Reports using 2D NMR have further examined locations of compounds in reverse micelles and found that such shifting is indicative of various types of interfacial interactions depending on the concentration, charge, shape, and hydrophobic/hydrophilic nature of the ligand.[39, 43, 56-57]

The upfield shift of hydrogens F and G along with the fact that phenyl ring 2 (**Figure 4.9**) is unsubstituted suggests that it points toward the AOT hydrocarbon tails, a hydrophobic chemical environment. Except for peaks F, G, and C, all other Zincon^{2-} peaks shift downfield compared to the aqueous environment. This suggests that most of the Zincon^{2-} aromatic hydrogens are situated within the interfacial region where the charged environment of the interface stabilizes the substituents on the phenyl rings 1 and 3 (**Figure 4.9**), that have charged species.

Table 4.2: Chemical shifts and changes of Zincon aromatic protons in aqueous, reverse micelle, and acetone-D_2O chemical environments. The change in proton chemical shift, Δ ppm, is listed in the header. A downfield shift is a positive number, while an upfield shift is a negative number.

Proton, H_i	Aqueous ppm	Reverse Micelle ppm	Acetone/7.7% D_2O ppm	Δ ppm Reverse Micelle – Aqueous	Δ ppm Acetone – Reverse Micelle	Δ ppm Acetone – Aqueous
A	7.78	8.10	8.01	0.32	-0.09	0.23
B	6.98	7.13	7.12	0.15	-0.01	0.14
C	7.50	7.33	7.65	-0.17	0.32	0.15
D	7.78	8.10	8.27	0.32	0.17	0.49
E	7.38	7.95	7.96	0.57	0.01	0.58
F	7.67	7.32	7.51	-0.35	0.19	-0.16
G	7.68	7.21	7.43	-0.47	0.22	-0.25
H	7.90	9.00	9.33	1.10	0.33	1.43
I	7.58	7.85	7.84	0.27	-0.01	0.26
J	6.79	7.07	7.01	0.28	-0.06	0.22

Second, the chemical shift range (7.01 – 9.33) and peak positions observed for Zincon^{2-} in d_6 acetone/D_2O bear a resemblance to the spectrum of Zincon^{2-} in reverse micelles. The chemical shifts of hydrogens are similar, and peak position changes, Δ ppm, from acetone to reverse micelles are small overall with about half of the signals appearing at essentially the same chemical shift, **Table 4.2**. The mixed solvent system appears to present an environment that closely resembles the AOT reverse micelle interfacial region, especially when considering that ~30% of the total water content in w_0 = 20 reverse micelles is interfacial water (~20% in w_0 = 30).[48] Indeed, when comparing peak positions between Zincon^{2-} in acetone – D_2O and reverse micelle – D_2O, many similarities arise, including similar chemical shift values and the direction of the shift (downfield *vs*. upfield) with the exception of proton C, **Table 4.2**.

Third, the Zincon^{2-} ^{1}H NMR peaks are much broader in reverse micelles than they are in aqueous or acetone solutions. We attribute the peak broadening to slowed molecular tumbling. If Zincon^{2-} molecules

reside embedded in the interface, the molecular tumbling can only occur on the time-scale for the entire reverse micelle tumbling, which is orders of magnitude slower than the individual molecules. Additionally, the rigidity of the interface can inhibit molecular motion precluding full relaxation back to the magnetic plane before the next NMR radiofrequency pulse arrives and therefore causing line broadening. Increasing the mixing time of the NMR experiment helps mitigate broadening due to incomplete relaxation. Taken together, the Zincon^{2-} UV-vis and NMR spectra indicate that Zincon^{2-} spans the reverse micelle interfacial Stern layer with the phenyl ring 2 with aromatic hydrogens F and G embedded in the AOT tails and phenyl rings 1 and 3 within the charged interfacial Stern layer.

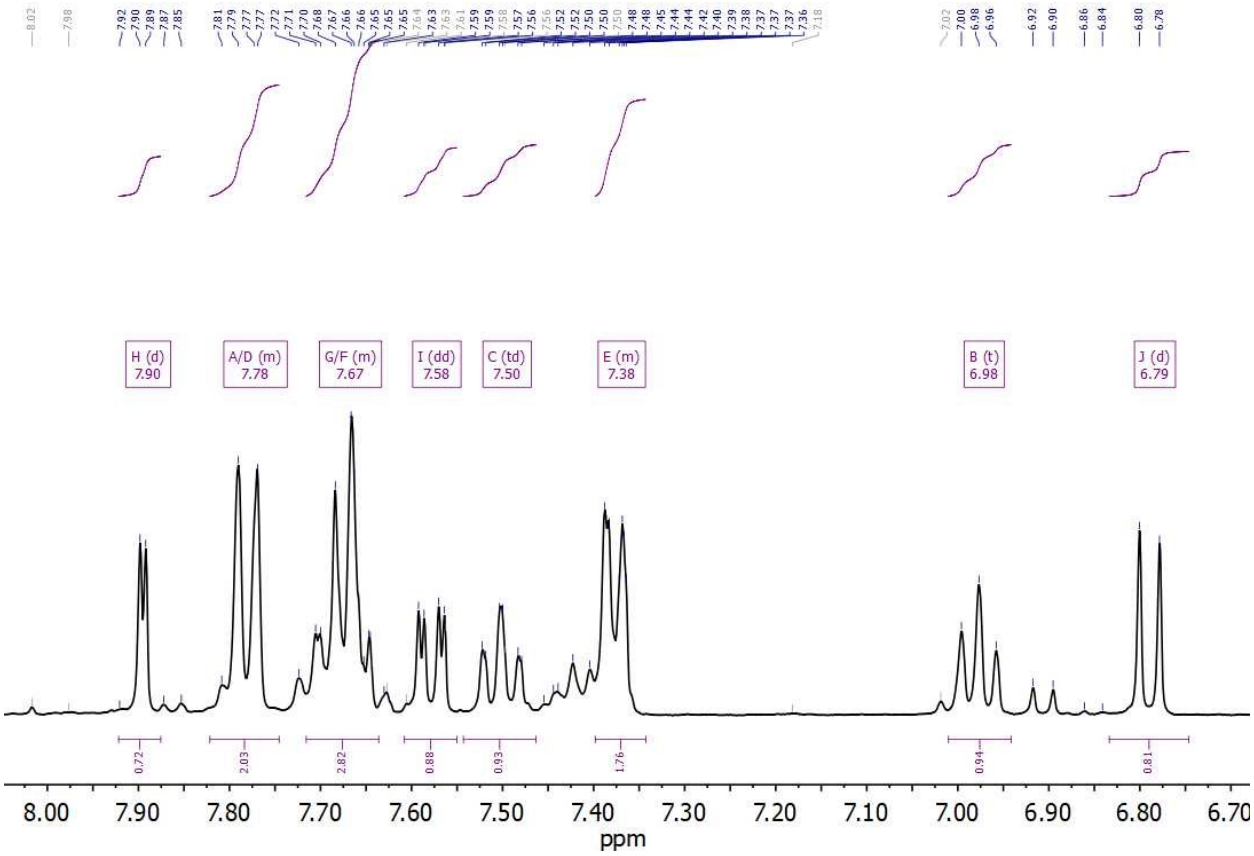

Figure 4.11: The ^{1}H NMR spectrum of the aromatic region of Zincon^{2-} in D_2O at pH 9.09 (pD to 9.49). Proton assignments are given in the multiplet box. ^{1}H NMR (400 MHz, Deuterium Oxide) δ 7.90 (d, *J* = 2.5 Hz, 1H), 7.82 – 7.75 (m, 2H), 7.72 – 7.64 (m, 3H), 7.58 (dd, *J* = 8.8, 2.4 Hz, 1H), 7.50 (td, *J* = 8.0, 1.6 Hz, 1H), 7.40 – 7.34 (m, 2H), 6.98 (t, *J* = 7.6 Hz, 1H), 6.79 (d, *J* = 8.8 Hz, 1H). There are some impurities, even though commercial grade.

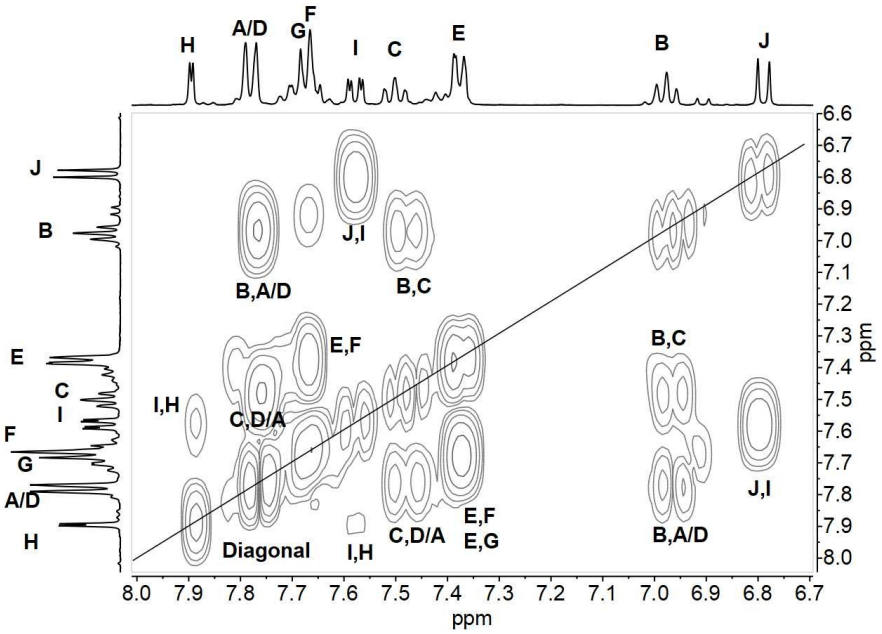

Figure 4.12: A $^{1}H^{1}H$ COSY NMR plot of the aromatic region of Zincon^{2-} in D_2O at pH 9.09 (pD 9.49). Cross-peaks are indicated by proton correlations next to the cross-peak, and the diagonal is labeled (solid black line).

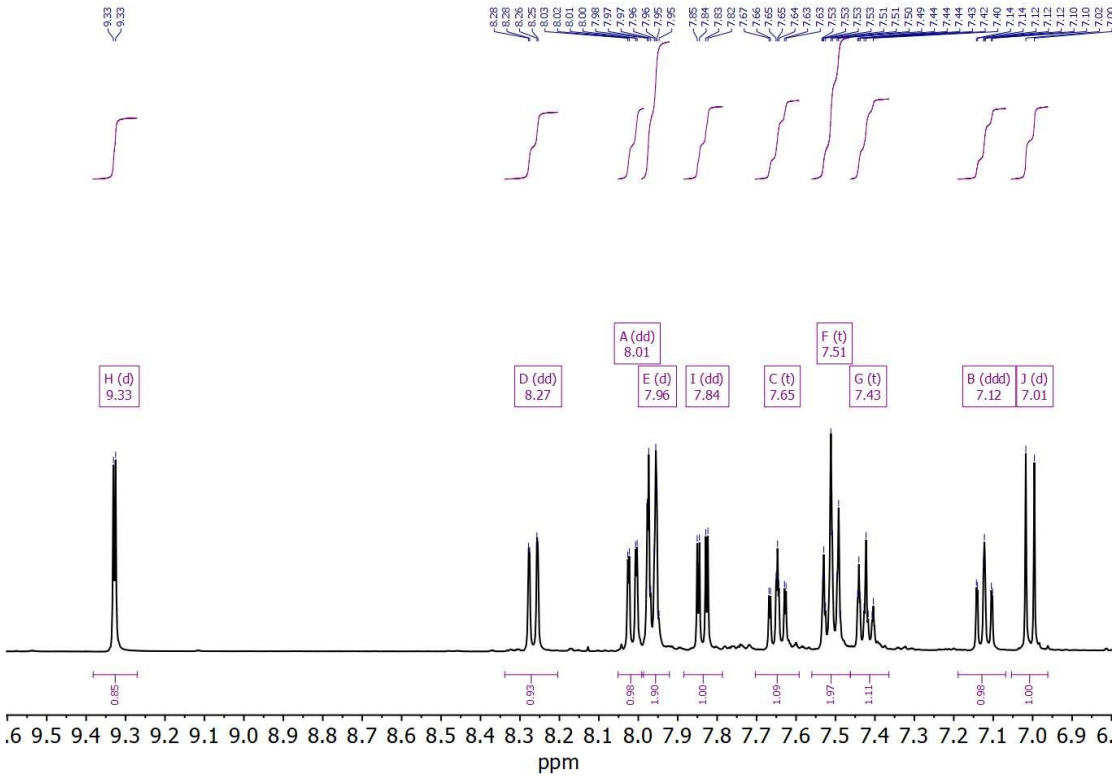

Figure 4.13: The ^{1}H NMR spectrum of the aromatic region of Zincon^{1-} in d_6-acetone with 7.7% D_2O. Proton assignments are given in the multiplet box. ^{1}H NMR (400 MHz, Acetone-d_6) δ 9.33 (d, J = 2.2 Hz, 1H), 8.27 (dd, J = 8.5, 1.1 Hz, 1H), 8.01 (dd, J = 8.0, 1.6 Hz, 1H), 7.96 (d, 2H), 7.84 (dd, J = 8.6, 2.2 Hz, 1H), 7.65 (t, J = 8.6, 7.2, 1.6 Hz, 1H), 7.51 (t, 2H), 7.43 (t, 1H), 7.12 (ddd, J = 8.2, 7.2, 1.2 Hz, 1H), 7.01 (d, J = 8.6 Hz, 1H).

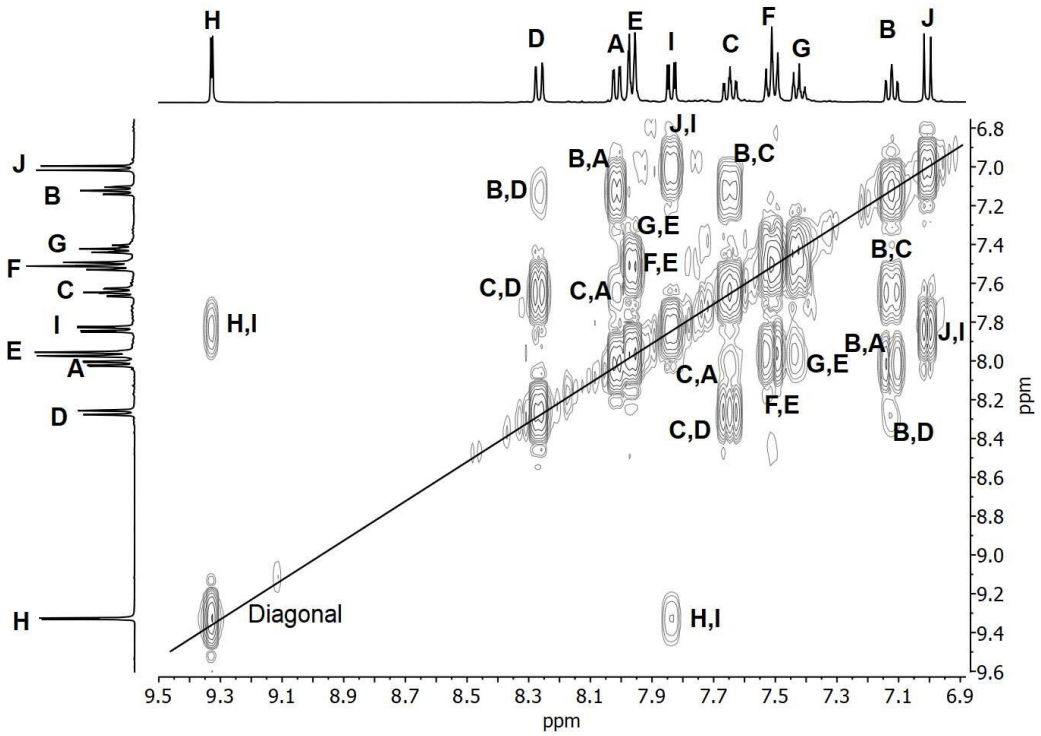

Figure 4.14: A $^{1}H^{1}H$ COSY plot of the aromatic region of Zincon^{1-} in d_6-acetone with 7.7% D_2O. Cross-peaks are indicated by proton correlations next to the signal, and the diagonal is labeled (solid black line).

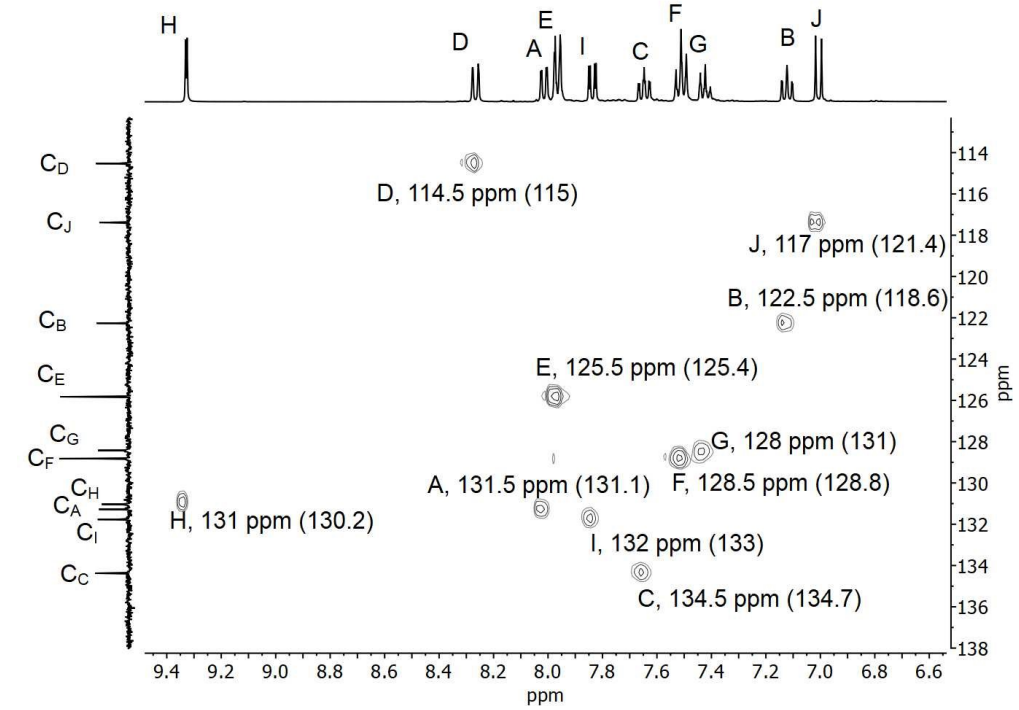

Figure 4.15: A ^{1}H ^{13}C HSQC plot of the aromatic region of Zincon^{1-} in d_6 acetone with 7.7% D_20. The signals are given by the proton assignments and the corresponding carbon atom with each proton. The given chemical shift is the value on the vertical axis, and the value in parenthesis is the estimated carbon chemical shift derived from ChemDraw relative to TMS.

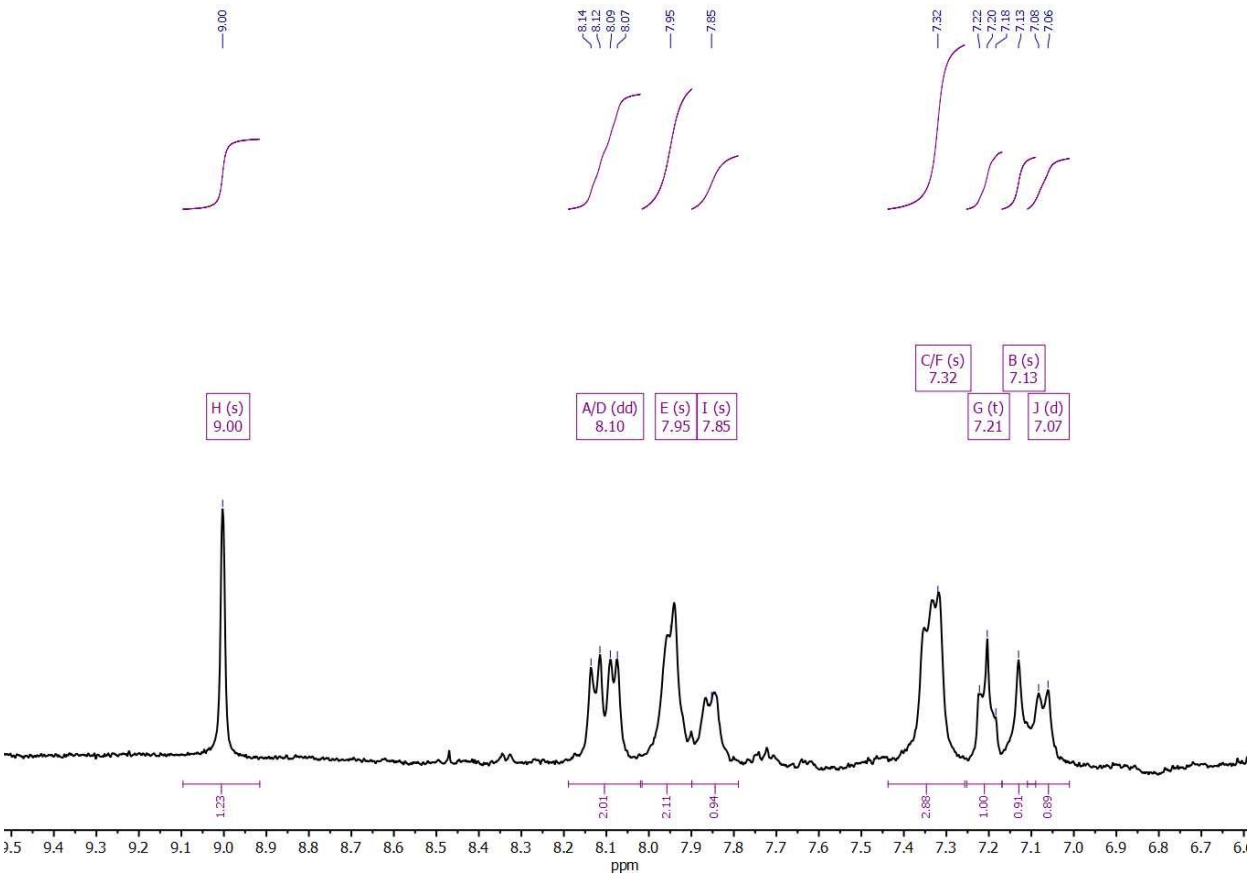

Figure 4.16: The ^{1}H NMR spectrum of the aromatic region of Zincon^{2-} in a reverse micelle, w_0 = 20, 0.75 M AOT, with a pH 9.10 (pD 9.50). Proton assignments are given in the multiplet box. ^{1}H NMR (400 MHz, Deuterium Oxide) δ 9.00 (s, 1H), 8.10 (dd, *J* = 17.3, 7.5 Hz, 2H), 7.95 (s, 2H), 7.85 (s, 1H), 7.32 (s, 3H), 7.21 (t, *J* = 7.3 Hz, 1H), 7.13 (s, 1H), 7.07 (d, *J* = 8.9 Hz, 1H).

4.4.2.2 The NMR analysis of [Zn(Zincon)]$^{2-}$ in aqueous buffer and reverse micelle chemical environments.

Unlike free Zincon^{2-}, the ^{1}H NMR spectrum of [Zn(Zincon)]$^{2-}$ complex, shown in **Figure 4.17**, reveals the significant similarity between aqueous and reverse micelle environments. The proton assignments were determined from 1D ^{1}H NMR integration, splitting, and 2D ^{1}H^{1}H COSY cross-peaks, see **Figures 4.18** (^{1}H NMR in D_2O), **4.19** (^{1}H^{1}H COSY in D_2O) and **4.20** (^{1}H NMR in w_0 = 20 reverse micelles, 0.75 M AOT). The chemical shift range of [Zn(Zincon)]$^{2-}$ in reverse micelles is 6.92 – 8.37 ppm, which is almost the same for the aqueous spectrum, 6.92 – 8.30 ppm. The hydrogens chemical shift order is the same in each environment; only slight Δ ppm were observed, **Table 4.3**. Peaks associated with hydrogens J and I on phenyl ring 3 have identical peak positions and no change in ppm, while H experiences only a slight downfield shift of Δ ppm = 0.07, **Table 4.3**. These observations indicate phenyl ring 3 is associated with the

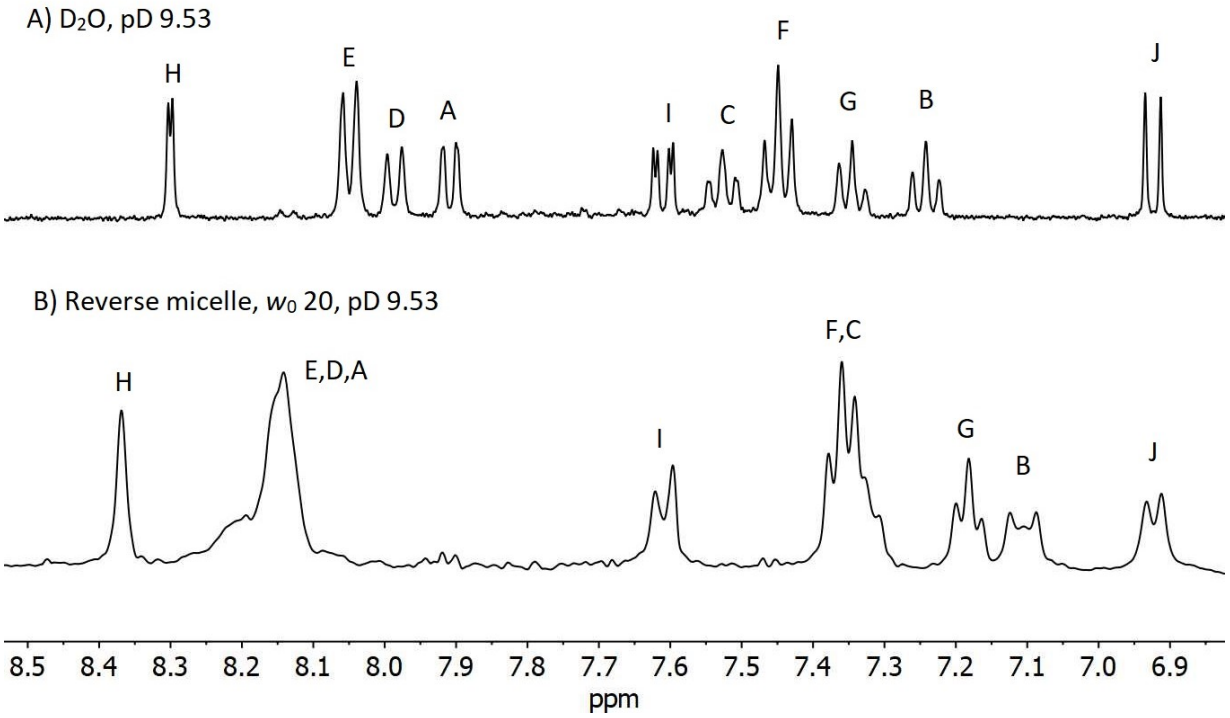

Figure 4.17: The stacked ^{1}H NMR spectra of $[Zn(Zincon)]^{2-}$ in A) D_2O pD 9.53 and B) w_0 = 20 reverse micelle (0.75 M AOT, pD 9.53). The aromatic hydrogens are labeled as assigned in **Figure 4.9**.

bulk water pool. The aromatic hydrogens from the phenyl rings of 1 and 3 also experienced a slight upfield or downfield shifting, which would indicate an association or interaction with the interface, but not to the extent of the $Zincon^{2-}$ as previously discussed. These chemical shifts suggest that the $[Zn(Zincon)]^{2-}$ complex is not entirely embedded in the interface; it most likely sits in the interfacial water layer, with phenyl ring 3 pointed toward the water pool. Although the UV-vis absorption spectrum of $[Zn(Zincon)]^{2-}$ does not display a significant peak shift, the changes to the shorter wavelength shoulder peak shape could indicate some interaction with the interface. The line broadening in the $[Zn(Zincon)]^{2-}$ NMR reverse micelle spectrum is not as severe as the $Zincon^{2-}$ spectrum; however, it is still present. This indicated that the reverse micelle environment hinders $[Zn(Zincon)]^{2-}$ tumbling less than it does the free $Zincon^{2-}$, which inferred less interaction with the interface. The peaks for the aromatic hydrogens on the phenyl rings 1 and 3 are the most affected as the signals are coalesced and broadened, due to these two phenyl rings being situated towards the interface. These observations indicate that the $[Zn(Zincon)]^{2-}$ species is likely interacting less with the interface/Stern layer and have more interactions with the water pool than $Zincon^{2-}$ does.

Table 4.3: Chemical shifts and differences of $[Zn(Zincon)]^{2-}$ aromatic protons in aqueous and reverse micelle environments. The change in proton chemical shift, Δ ppm, is the reverse micelle – aqueous chemical shift. A downfield shift is a positive number, while an upfield shift is a negative number.

Proton, H_i	Aqueous ppm	Reverse micelle ppm	Δ ppm
A	7.91	8.15	0.24
B	7.24	7.11	-0.13
C	7.53	7.34	-0.19
D	7.99	8.15	0.16
E	8.05	8.15	0.1
F	7.45	7.36	-0.09
G	7.35	7.18	-0.17
H	8.3	8.37	0.07
I	7.61	7.61	0
J	6.92	6.92	0

Perhaps most notable are the differences between the location we interpret for free $Zincon^{2-}$ and the $[Zn(Zincon)]^{2-}$. Despite both species carrying the same doubly negative charge, neither $Zincon^{2-}$ nor $[Zn(Zincon)]^{2-}$ resides entirely in the bulk-like reverse micelle water pool. Indeed, other studies by our group have shown that doubly deprotonated aromatic acid species can interact with negatively charged interfaces and reside deep within the interface.[43] The $[Zn(Zincon)]^{2-}$ reverse micelle NMR spectra share more spectral similarities to the aqueous environment than do the free $Zincon^{2-}$ spectra. It is possible that the molecular geometry plays a role in the location sampled by $Zincon^{2-}$ and $[Zn(Zincon)]^{2-}$. As Zn^{2+} is coordinated in a square planar geometry when complexed to $Zincon^{2-}$ this may impede the ability of the complex to penetrate the surfactant tail region as it becomes much less flexible than a free $Zincon^{2-}$ molecule. The $Zincon^{2-}$ internal rotations are not fixed and can sample the more organic portions of the interface as it can move and rotate to fill spaces between AOT tails. UV-vis and NMR spectra indicate that the free $Zincon^{2-}$ is embedded deep into the interface while the $[Zn(Zincon)]^{2-}$ only slightly interacts with the interface.

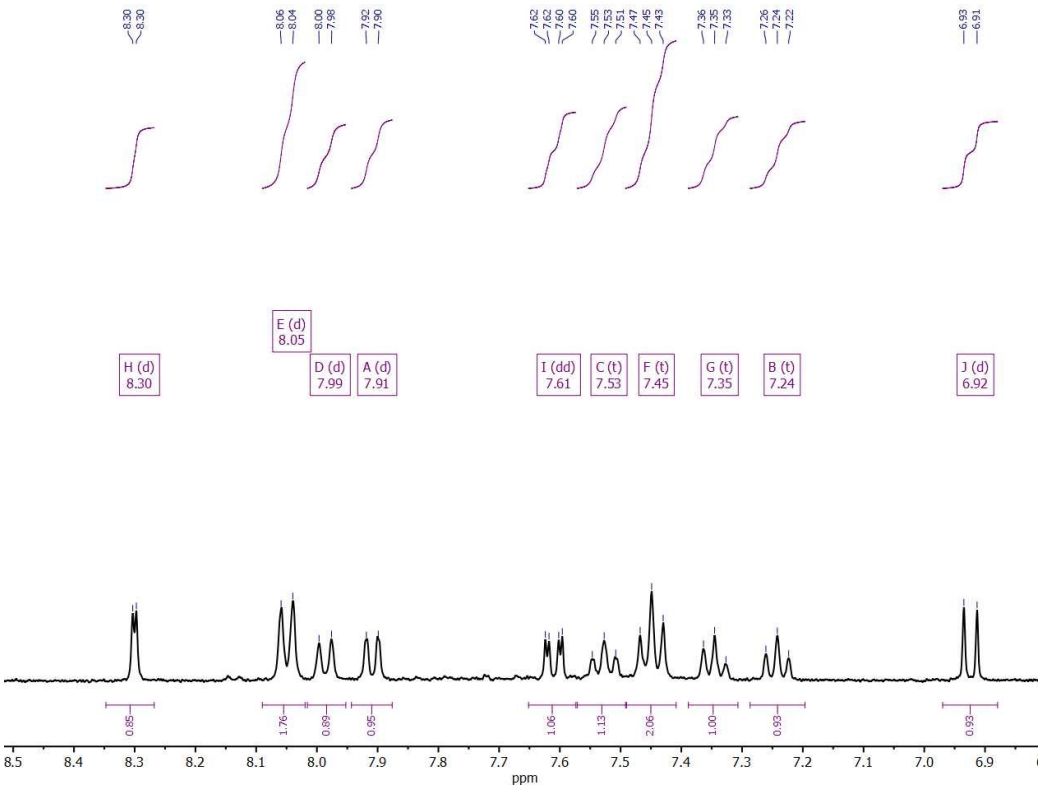

Figure 4.18: The ^{1}H NMR of the aromatic region spectrum of $[Zn(Zincon)]^{2-}$ in D_2O at pH to 9.13 (pD 9.53). Proton assignments are given in the multiplet box. ^{1}H NMR (400 MHz, Deuterium Oxide) δ 8.30 (d, *J* = 2.4 Hz, 1H), 8.05 (d, *J* = 7.8 Hz, 2H), 7.99 (d, *J* = 8.2 Hz, 1H), 7.91 (d, *J* = 7.9 Hz, 1H), 7.61 (dd, *J* = 8.8, 2.4 Hz, 1H), 7.53 (t, *J* = 7.7 Hz, 1H), 7.45 (t, *J* = 7.6 Hz, 2H), 7.35 (t, *J* = 7.4 Hz, 1H), 7.24 (t, *J* = 7.5 Hz, 1H), 6.92 (d, *J* = 8.7 Hz, 1H).

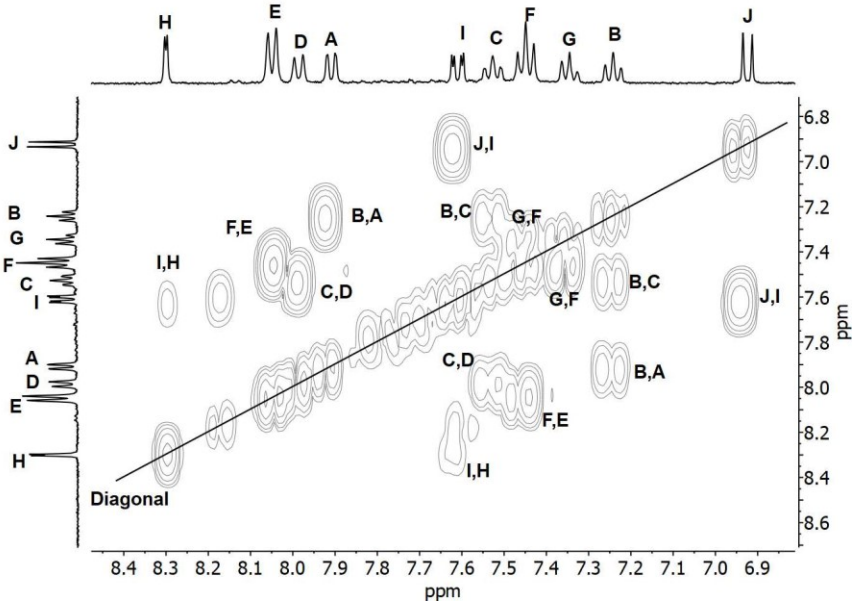

Figure 4.19: The $^{1}H^{1}H$ COSY NMR of the aromatic region of $[Zn(Zincon)]^{2-}$ in D_2O at pH 9.13 (pD 9.53). Cross peaks are indicated with proton correlations next to the cross-peak, and the diagonal is labeled (solid black line).

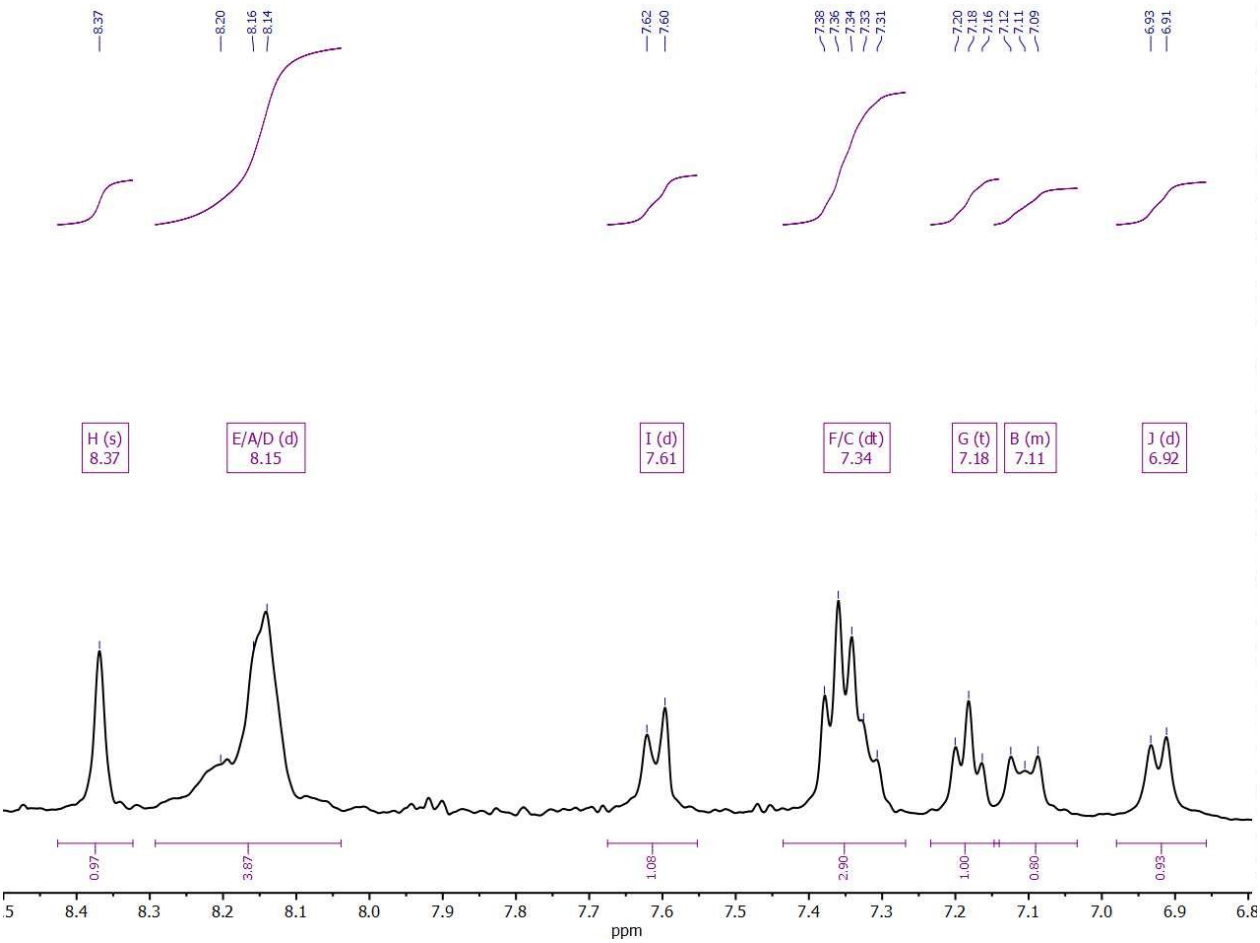

Figure 4.20: The ^{1}H NMR spectrum of the aromatic region for [Zn(Zincon)]$^{2-}$ in reverse micelles, w_0 = 20, 0.75 M AOT, with a pH 9.13 (pD 9.53). Proton assignments are given in the multiplet box. ^{1}H NMR (400 MHz, Deuterium Oxide) δ 8.37 (s, 1H), 8.15 (d, *J* = 7.4 Hz, 4H), 7.61 (d, *J* = 9.9 Hz, 1H), 7.34 (dt, *J* = 13.9, 7.5 Hz, 3H), 7.18 (t, *J* = 7.4 Hz, 1H), 7.15 – 7.03 (m, 1H), 6.92 (d, *J* = 8.6 Hz, 1H).

4.4.2.3 The NMR analysis of [Zn(Zincon)]$^{2-}$ coordination geometry.

The [Zn(Zincon)]$^{2-}$ coordination geometry can be confirmed by these aqueous NMR spectra and interpretation of the aromatic proton shifting from the unbound to bound states. For a Zn^{2+} and Cu^{2+} indicator that is commercially available, no crystal structure or NMR confirming the coordination has been found in the literature for Zincon^{2-}. The lack of more information is astounding, considering the first report of this ligand in the literature is from the 1950s.[55] Spectroscopic data in the form of the chemical shifts of aromatic hydrogen atoms on the phenyl rings 1-3 obtained in an aqueous solution of the unbound Zincon^{2-} (**Figure 4.11**) and [Zn(Zincon)]$^{2-}$ complex (**Figure 4.18**) can indicate coordinate geometry because of coordination

induced downfield shifts.[58-59] Specifically, all the aromatic hydrogens of the $[Zn(Zincon)]^{2-}$ complex experience a downfield shift as compared to the unbound ligand except F and G on phenyl ring 2, **Table 4.4**. Hydrogens F and G are the least affected by the Zn^{2+} coordination because they are furthest from the proposed ligand coordination sites, resulting in small upfield shifts. Hydrogen E on the same ring experiences the largest shift due to the proximity to the delocalization to the two nitrogen atoms coordinating to the Zn^{2+}.

Table 4.4: The chemical shifts and differences of $Zincon^{2-}$ and $[Zn(Zincon)]^{2-}$ aromatic protons in D_20. The difference in ppm is calculated as Δ ppm = $[Zn(Zincon)]^{2-}$ ppm – $Zincon^{2-}$ ppm, where a downfield shift is a positive number while an upfield shift is a negative number.

Proton, H_i	$Zincon^{2-}$, ppm	$[Zn(Zincon)]^{2-}$, ppm	Δ ppm
A	7.78	7.91	0.13
B	6.98	7.24	0.26
C	7.50	7.53	0.03
D	7.78	7.99	0.21
E	7.38	8.05	0.67
F	7.67	7.45	-0.22
G	7.68	7.35	-0.33
H	7.90	8.30	0.40
I	7.58	7.61	0.03
J	6.79	6.92	0.13

4.4.2.4 The analysis of aromatic chemical shifts in the ^1H NMR spectra of $Zincon^{2-}$ and $[Zn(Zincon)]^{2-}$ in aqueous solution confirm isomer content.

There are some impurities in the $Zincon^{2-}$ and $[Zn(Zincon)]^{2-}$ ^1H NMR spectra, especially the aqueous solutions. Through integration analysis using the MestReNova resolution booster tool, we have estimated that the percent of these extra proton signals do not exceed 15% of the total aromatic integration region for $Zincon^{2-}$ and 5.96% for $[Zn(Zincon)]^{2-}$ in the aqueous ^1H NMR spectra. These percentages would indicate that these extra signals arise from isomers. The lower percent value in the $[Zn(Zincon)]^{2-}$ suggested an isomer in which the Zn^{2+} binding is less favored. We attempted to separate possible Zincon isomers by preparatory TLC plates but were unsuccessful.

4.4.3 Photolysis experiments that generate light-induced Zn^{2+} bursts at the nanoscale in reverse micelles

With the absorption and NMR spectroscopy interpretation, the three species exhibit different partitioning as envisioned in the cartoon schematic given in **Figure 4.21**. The $Zincon^{2-}$ partitions deep in the interface, the $[Zn(Zincon)]^{2-}$ partitions into the interfacial water/Stern layer, and the $[Zn(NTAdeCage)]^{1-}$ partitions into the water pool. The locations of each species are important to understand and interpret the results of the photolysis experiments. The series of UV-vis absorption spectra of $[Zn(NTAdeCage)]^{1-}$ and $Zincon^{2-}$ following exposure to increasing photolysis radiation in reverse micelles (panel a) and bulk aqueous buffered solution (panel b) are shown in **Figure 4.22**. The decreasing intensity in the 250 – 350 nm spectral range in both panels reflects the conversion of $[Zn(NTAdeCage)]^{1-}$ to its photolysis products, as well as the conversion of $Zincon^{2-}$ to $[Zn\text{-}Zincon]^{2-}$. The $Zincon^{2-}$ peak decreased with exposure as Zn^{2+} are generated from the photolysis reaction. An isosbestic point at 600 nm (reverse micelle) or 545 nm (aqueous buffered solution) indicates a clean 1:1 conversion of $Zincon^{2-}$ to $[Zn(Zincon)]^{2-}$. In reverse micelles, the $Zincon^{2-}$ peak wavelength maximum appears to shift toward longer wavelengths as the photolysis progresses. We can accurately simulate the observed shift in weighted averages of the individual $Zincon^{2-}$ and $[Zn(Zincon)]^{2-}$ spectra. Thus, we attribute the apparent shift as due to the overlapping of the $Zincon^{2-}$ peak with the short-wavelength $[Zn(Zincon)]^{2-}$ spectral feature, **Figure 4.2b**. There is some loss of the $Zincon^{2-}$ absorbance with laser exposure, but little loss of $[Zn(Zincon)]^{2-}$, **Figure 4.23**, suggesting slight photobleaching of the ligand.

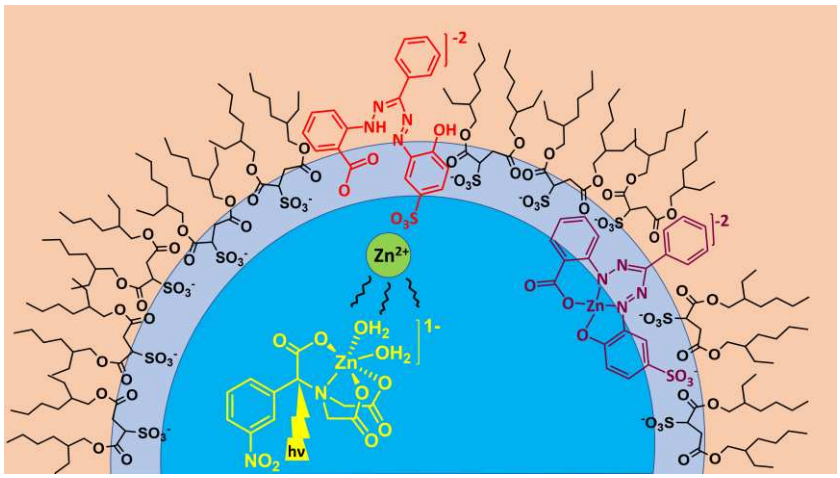

Figure 4.21: Cartoon representing the interpreted reverse micelle partitioning of the three species $Zincon^{2-}$ (red), $[Zn(NTAdeCage)]^{1-}$ (yellow), and $[Zn(Zincon)]^{2-}$ (purple).

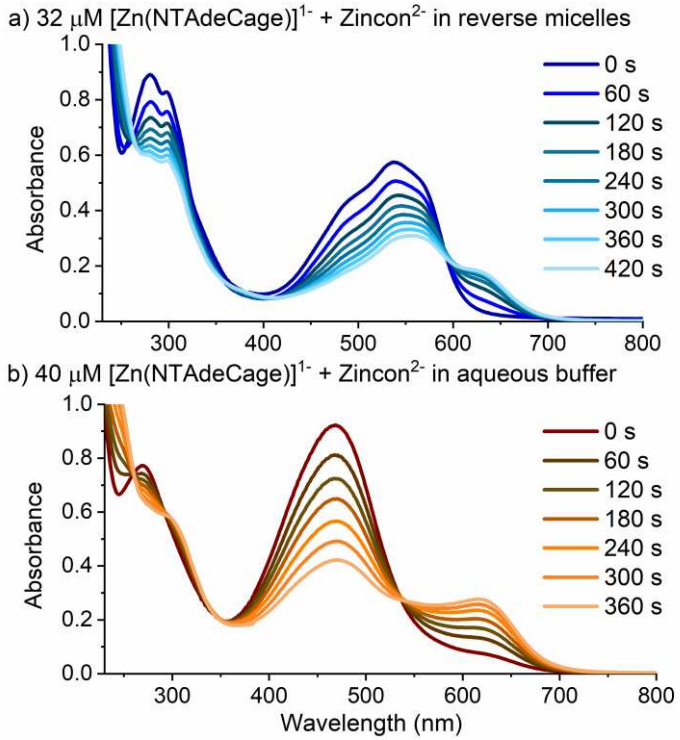

Figure 4.22: UV-vis absorption spectra marking the progressive photolysis of $[Zn(NTAdeCage)]^{1-}$ and $Zincon^{2-}$ in 40 mM HEPES at pH 7.40 within AOT-isooctane (0.02 M AOT) reverse micelles of w_0 = 30 (a) or in 40 mM HEPES at pH 7.40 (b). The average power of the laser was 133 mW per pulse with a frequency of 20 Hz, set at 355 nm.

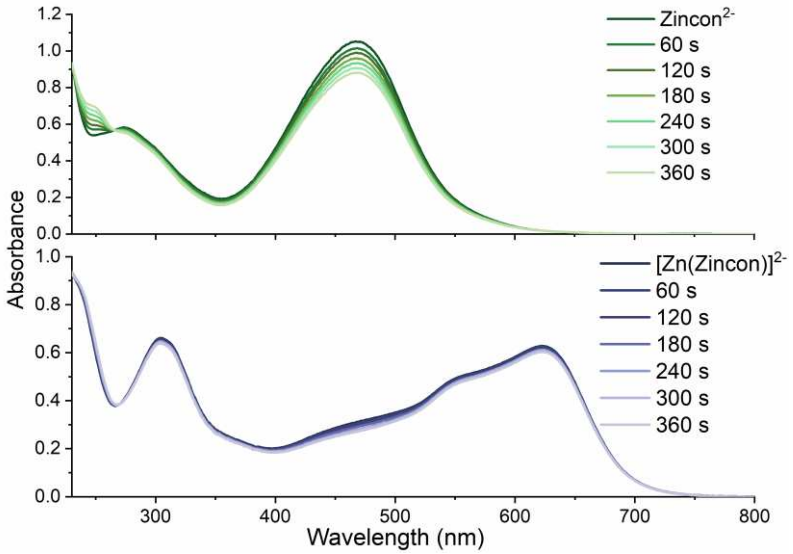

Figure 4.23: The results of laser photolysis conditions on samples in the absence of $NTAdeCage^{3-}$. *Top* 40 μM aqueous buffered $Zincon^{2-}$; *Bottom* 40 μM aqueous buffered $[Zn(Zincon)]^{2-}$. The photolysis radiation leads to a slight degradation of each species from the laser alone, which is less pronounced for the $[Zn(Zincon)]^{2-}$ complex. About a 0.15 absorbance decrease is observed in the $Zincon^{2-}$ over the entire photolysis period with only a 0.04 decrease for the $[Zn(Zincon)]^{2-}$ complex.

The nanoscale proportion of the reverse micelle places the [Zn(NTAdeCage)]$^{1-}$ and Zincon^{2-} closer together than they would be in bulk aqueous buffer. Specifically, a w_0 = 30 reverse micelle has a hydrodynamic radius of ~50 Å, including the Stern layer and the water pool.[48] At a micromolar concentration in bulk aqueous buffer, the average distance between the Zn^{2+} and a Zincon^{2-} molecule is 100's of nanometers, far greater than the distance in a reverse micelle and would imply a lower reaction efficiency as the two species would encounter each other less. However, in the presence of an interface and confined to the nanoscale, Zincon^{2-} partitions into the interface while the photocage partitions into the water pool. Thus, released Zn^{2+} cations must diffuse across a highly heterogeneous interface with a barrier of a high concentration of hydrated sodium cations to reach the Zincon^{2-}. Alternatively, Zincon^{2-} must diffuse out of the interface to bind Zn^{2+}, which is not thermodynamically favorable.

We expected that confining [Zn(NTAdeCage)]$^{1-}$ and Zincon^{2-} in the reverse micelle environment would lead to efficient capture of the released Zn^{2+}. Our observations show the opposite effect, most apparent when we compare the normalized Zincon^{2-} absorbance versus total energy added, **Figure 4.24**. **Equation 4.1** defines the total exposure energy, $E_{exposure}$ *(J)*, from exposure time in seconds, $t_{exposure}$, laser repetition rate, r_{laser}, (20 pulses/s), and laser power, P_{laser} (~133 mW). By comparing the slopes, the reduction in Zincon^{2-} absorbance is approximately 1.4 times more efficient in aqueous buffered solution

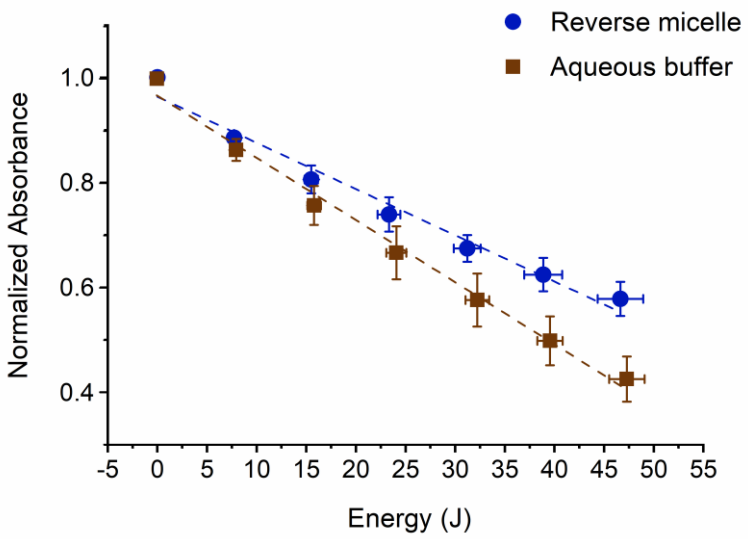

Figure 4.24: The normalized Zincon^{2-} absorbance as a function of exposure energy in aqueous buffered solution (brown square) and reverse micelles (blue circle). Error bars indicate absorbance of two replicates, and the lines are unweighted linear fits to data. The slopes of the aqueous buffered solution were -11.9 (± 0.5) x 10^{-3} J^{-1} and reverse micelles were -8.8 (± 0.6) x 10^{-3} J^{-1}.

than in reverse micelles. The interfacial location of Zincon^{2-} in the reverse micelle diminishes its ability to capture the Zn^{2+} by about 25%. If the chelating ligand remains in the water pool with the photocage, we expect a more efficient capture of the freed cation. Thus simple confinement on the nanoscale may not dictate observed kinetics, and species partitioning must be considered.

(**Eq. 4.1**) $$E_{exposure}\ (J) = t_{exposure} * r_{laser} * P_{laser}$$

4.5 Conclusions

We attempted to measure the ion binding by nanosecond transient absorption spectroscopy[60], but the absorbance changes were too small for us to detect. We believe the low photolysis efficiency of the photocage may not generate a large enough burst of Zn^{2+}. We expect that using a photocage with a larger quantum yield and metal ion sensitive fluorophores with emission spectroscopy will enhance the ability to measure kinetics.[61-62] We have used similar types of signal dampening to measure the kinetic constants of Cu^{2+} transfer in small peptide complexes found in blood using tryptophan fluorescence quenching.[63]

These results demonstrate an effective method to monitor metal ion coordination reactions at the nanoscale by controlled Zn^{2+} release through irradiation of a photocage. Association with the reverse micelle interface reduces the reactivity of Zincon^{2-} to coordinate Zn^{2+} by 25% and demonstrates that the confinement impacts the reaction due to partitioning exhibited by the different species.[46-47] The proof-of-concept methodology presented here can be optimized to measure metal ion coordination reactions with fast time-scale spectroscopy using a photocage with a sufficient quantum efficiency able to release a large burst of ions. This approach would benefit measurements where stopped-flow mixing methods are too slow to measure free ion complexation.

CHAPTER 4 REFERENCES

1. Beuning, C. N.; Barkley, N. E.; Basa, P. N.; Burdette, S. C.; Levinger, N. E.; Crans, D. C., Coordination Chemistry of a Controlled Burst of Zn^{2+} in Bulk Aqueous and Nanosized Water Droplets with a Zincon Chelator. *Inorg. Chem.* **2019,** *Published ASAP Dec. 6 2019* DOI: 10.1021/acs.inorgchem.9b02848.

2. Basa, P. N.; Antala, S.; Dempski, R. E.; Burdette, S. C., A Zinc(II) Photocage Based on a Decarboxylation Metal Ion Release Mechanism for Investigating Homeostasis and Biological Signaling. *Angew. Chem. Int. Ed.* **2015,** *54* (44), 13027-13031.

3. Kocyła, A.; Pomorski, A.; Krężel, A., Molar Absorption Coefficients and Stability Constants of Zincon Metal Complexes for Determination of Metal Ions and Bioinorganic Applications. *J. Inorg. Biochem.* **2017,** *176*, 53-65.

4. Säbel, C. E.; Neureuther, J. M.; Siemann, S., A Spectrophotometric Method for the Determination of Zinc, Copper, and Cobalt Ions in Metalloproteins Using Zincon. *Anal. Biochem.* **2010,** *397* (2), 218-226.

5. Levina, A.; Crans, D. C.; Lay, P. A., Speciation of Metal Drugs, Supplements and Toxins in Media and Bodily Fluids Controls in vitro Activities. *Coord. Chem. Rev.* **2017,** *352*, 473-498.

6. Maret, W., Metalloproteomics, Metalloproteomes, and the Annotation of Metalloproteins. *Metallomics* **2010,** *2* (2), 117-125.

7. Hasan, M. K.; Cheng, Y.; Kanwar, M. K.; Chu, X.-Y.; Ahammed, G. J.; Qi, Z.-Y., Responses of Plant Proteins to Heavy Metal Stress—A Review. *Frontiers in Plant Science* **2017,** *8* (1492).

8. Dean, K. M.; Qin, Y.; Palmer, A. E., Visualizing Metal Ions in Cells: An Overview of Analytical Techniques, Approaches, and Probes. *Biochim. Biophys. Acta, Mol. Cell Res.* **2012,** *1823* (9), 1406-1415.

9. Sigel, A. S., H. Sigel R. , *Interrelations Between Essential Metal Ions and Human Diseases*. Springer: Dordrecht, The Netherlands, 2013; Vol. 13, p 1-29, 229-286, 359-381, 389-409.

10. Haas, K. L.; Franz, K. J., Application of Metal Coordination Chemistry To Explore and Manipulate Cell Biology. *Chem. Rev.* **2009,** *109* (10), 4921-4960.

11. Kambe, T.; Tsuji, T.; Hashimoto, A.; Itsumura, N., The Physiological, Biochemical, and Molecular Roles of Zinc Transporters in Zinc Homeostasis and Metabolism. *Physiol. Rev.* **2015,** *95* (3), 749-784.

12. Krężel, A.; Maret, W., The Biological Inorganic Chemistry of Zinc Ions. *Arch. Biochem. Biophys.* **2016,** *611*, 3-19.

13. Maret, W., Zinc and Zinc Ions in Biological Systems. In *Encyclopedia of Metalloproteins*, Kretsinger, R. H.; Uversky, V. N.; Permyakov, E. A., Eds. Springer New York: New York, NY, 2013; pp 2396-2400.

14. Que, E. L.; Domaille, D. W.; Chang, C. J., Metals in Neurobiology: Probing Their Chemistry and Biology with Molecular Imaging. *Chem. Rev.* **2008,** *108* (5), 1517-1549.

15. Kepp, K. P., Alzheimer's Disease: How Metal Ions Define β-amyloid Function. *Coord. Chem. Rev.* **2017,** *351* (Supplement C), 127-159.

16. Kozlowski, H.; Janicka-Klos, A.; Brasun, J.; Gaggelli, E.; Valensin, D.; Valensin, G., Copper, Iron, and Zinc ions Homeostasis and Their Role in Neurodegenerative Disorders (Metal Uptake, Transport, Distribution and Regulation). *Coord. Chem. Rev.* **2009,** *253* (21), 2665-2685.

17. Que, E. L.; Bleher, R.; Duncan, F. E.; Kong, B. Y.; Gleber, S. C.; Vogt, S.; Chen, S.; Garwin, S. A.; Bayer, A. R.; Dravid, V. P.; Woodruff, T. K.; O'Halloran, T. V., Quantitative Mapping of Zinc Fluxes in the Mammalian Egg Reveals the Origin of Fertilization-induced Zinc Sparks. *Nat. Chem.* **2014,** *7*, 130.

18. Tapiero, H.; Tew, K. D., Trace Elements in Human Physiology and Pathology: Zinc and Metallothioneins. *Biomed. Pharmacother.* **2003,** *57* (9), 399-411.

19. Deibel, M. A.; Ehmann, W. D.; Markesbery, W. R., Copper, Iron, and Zinc Imbalances in Severely Degenerated Brain Regions in Alzheimer's Disease: Possible Relation to Oxidative Stress. *J. Neurol. Sci.* **1996,** *143* (1–2), 137-142.

20. Faller, P.; Hureau, C.; Berthoumieu, O., Role of Metal Ions in the Self-assembly of the Alzheimer's Amyloid-β Peptide. *Inorg. Chem.* **2013,** *52* (21), 12193-12206.

21. Kozlowski, H.; Luczkowski, M.; Remelli, M.; Valensin, D., Copper, Zinc and Iron in Neurodegenerative Diseases (Alzheimer's, Parkinson's and Prion Diseases). *Coord. Chem. Rev.* **2012,** *256* (19), 2129-2141.

22. Lovell, M. A.; Robertson, J. D.; Teesdale, W. J.; Campbell, J. L.; Markesbery, W. R., Copper, Iron and Zinc in Alzheimer's Disease Senile Plaques. *J. Neurol. Sci.* **1998,** *158* (1), 47-52.

23. Miura, T.; Suzuki, K.; Kohata, N.; Takeuchi, H., Metal Binding Modes of Alzheimer's Amyloid β-Peptide in Insoluble Aggregates and Soluble Complexes. *Biochemistry* **2000,** *39* (23), 7024-7031.

24. Jomova, K.; Vondrakova, D.; Lawson, M.; Valko, M., Metals, Oxidative Stress and Neurodegenerative Disorders. *Mol. Cell. Biochem.* **2010,** *345* (1), 91-104.

25. Cuajungco, M. P.; Lees, G. J., Zinc metabolism in the Brain: Relevance to Human Neurodegenerative Disorders. *Neurobiol. Dis.* **1997,** *4* (3-4), 137-169.

26. Kepp, K. P., Bioinorganic Chemistry of Alzheimer's Disease. *Chem. Rev.* **2012,** *112* (10), 5193-5239.

27. Alies, B.; Hureau, C.; Faller, P., The Role of Metal Ions in Amyloid Formation: General Principles from Model Peptides. *Metallomics* **2013,** *5* (3), 183-192.

28. Pedersen, J. T.; Hureau, C.; Hemmingsen, L.; Heegaard, N. H. H.; Østergaard, J.; Vašák, M.; Faller, P., Rapid Exchange of Metal between Zn7–Metallothionein-3 and Amyloid-β Peptide Promotes Amyloid-Related Structural Changes. *Biochemistry* **2012,** *51* (8), 1697-1706.

29. Yamasaki, S.; Sakata-Sogawa, K.; Hasegawa, A.; Suzuki, T.; Kabu, K.; Sato, E.; Kurosaki, T.; Yamashita, S.; Tokunaga, M.; Nishida, K.; Hirano, T., Zinc is a Novel Intracellular Second Messenger. *J. Cell Biol.* **2007,** *177* (4), 637-645.

30. Kiss, T.; Odani, A., Demonstration of the Importance of Metal Ion Speciation in Bioactive Systems. *Bull. Chem. Soc. Jpn.* **2007,** *80* (9), 1691-1702.

31. Rubino, J. T.; Franz, K. J., Coordination Chemistry of Copper Proteins: How Nature Handles a Toxic Cargo for Essential Function. *J. Inorg. Biochem.* **2012,** *107* (1), 129-143.

32. Shafaat, O. S.; Winkler, J. R.; Gray, H. B.; Dougherty, D. A., Photoactivation of an Acid-Sensitive Ion Channel Associated with Vision and Pain. *Chembiochem* **2016,** *17* (14), 1323-1327.

33. Rimmerman, D.; Leshchev, D.; Hsu, D. J.; Hong, J.; Abraham, B.; Henning, R.; Kosheleva, I.; Chen, L. X., Probing Cytochrome c Folding Transitions upon Phototriggered Environmental Perturbations Using Time-Resolved X-ray Scattering. *J. Phys. Chem. B* **2018,** *122* (20), 5218-5224.

34. Donten, M. L.; Hassan, S.; Popp, A.; Halter, J.; Hauser, K.; Hamm, P., pH-Jump Induced Leucine Zipper Folding beyond the Diffusion Limit. *J. Phys. Chem. B* **2015,** *119* (4), 1425-1432.

35. Franz, K. J.; Metzler-Nolte, N., Introduction: Metals in Medicine. *Chem. Rev.* **2019,** *119* (2), 727-729.

36. Vijayakumar, V.; Samal, S. K.; Mohanty, S.; Nayak, S. K., Recent Advancements in Biopolymer and Metal Nanoparticle-based Materials in Diabetic Wound Healing Management. *Int. J. Biol. Macromol.* **2019,** *122*, 137-148.

37. Chiarante, N.; García Vior, M. C.; Awruch, J.; Marino, J.; Roguin, L. P., Phototoxic Action of a Zinc(II) Phthalocyanine Encapsulated into Poloxamine Polymeric Micelles in 2D and 3D Colon Carcinoma Cell Cultures. *J. Photochem. Photobiol. B, Biol.* **2017,** *170*, 140-151.

38. Fanti, M.; Mancin, F.; Tecilla, P.; Tonellato, U., Ester Cleavage Catalysis in Reversed Micelles by Cu(II) Complexes of Hydroxy-Functionalized Ligands. *Langmuir* **2000,** *16* (26), 10115-10122.

39. Crans, D. C.; Rithner, C. D.; Baruah, B.; Gourley, B. L.; Levinger, N. E., Molecular Probe Location in Reverse Micelles Determined by NMR Dipolar Interactions. *J. Am. Chem. Soc.* **2006,** *128* (13), 4437-4445.

40. Milanesio, M. E.; Alvarez, M. G.; Bertolotti, S. G.; Durantini, E. N., Photophysical Characterization and Photodynamic Activity of Metallo 5-(4-(trimethylammonium)phenyl)-10,15,20-tris(2,4,6-trimethoxyphenyl)porphyrin in Homogeneous and Biomimetic Media. *Photochem. Photobiol. Sci.* **2008,** *7* (8), 963-972.

41. Sedgwick, M.; Cole, R. L.; Rithner, C. D.; Crans, D. C.; Levinger, N. E., Correlating Proton Transfer Dynamics To Probe Location in Confined Environments. *J. Am. Chem. Soc.* **2012,** *134* (29), 11904-11907.

42. Samart, N.; Beuning, C. N.; Haller, K. J.; Rithner, C. D.; Crans, D. C., Interaction of a Biguanide Compound with Membrane Model Interface Systems: Probing the Properties of Antimalaria and Antidiabetic Compounds. *Langmuir* **2014,** *30* (29), 8697-8706.

43. Crans, D. C.; Trujillo, A. M.; Bonetti, S.; Rithner, C. D.; Baruah, B.; Levinger, N. E., Penetration of Negatively Charged Lipid Interfaces by the Doubly Deprotonated Dipicolinate. *J. Org. Chem.* **2008,** *73* (24), 9633-9640.

44. Koehn, J. T.; Beuning, C. N.; Peters, B. J.; Dellinger, S. K.; Van Cleave, C.; Crick, D. C.; Crans, D. C., Investigating Substrate Analogues for Mycobacterial MenJ: Truncated and Partially Saturated Menaquinones. *Biochemistry* **2019,** *58* (12), 1596 - 1615.

45. Biasutti, M. A.; Abuin, E. B.; Silber, J. J.; Correa, N. M.; Lissi, E. A., Kinetics of Reactions Catalyzed by Enzymes in Solutions of Surfactants. *Adv. Colloid Interface Sci.* **2008,** *136* (1), 1-24.

46. Johnson, M. D.; Lorenz, B. B.; Wilkins, P. C.; Lemons, B. G.; Baruah, B.; Lamborn, N.; Stahla, M.; Chatterjee, P. B.; Richens, D. T.; Crans, D. C., Switching Off Electron Transfer Reactions in Confined Media: Reduction of Co(dipic)(2) (-) and Co(edta) (-) by Hexacyanoferrate(II). *Inorg. Chem.* **2012,** *51* (5), 2757-2765.

47. Borunda, T.; Myers, A. J.; Mary Fisher, J.; Crans, D. C.; Johnson, M. D., Confinement Effects on Chemical Equilibria: Pentacyano(Pyrazine)Ferrate(II) Stability Changes within Nanosized Droplets of Water. *Molecules* **2018,** *23* (4), 858.

48. Maitra, A., Determination of Size Parameters of Water-Aerosol OT-oil Reverse Micelles from their Nuclear Magnetic Resonance Data. *J. Phys. Chem.* **1984,** *88* (21), 5122-5125.

49. Stahla, M. L.; Baruah, B.; James, D. M.; Johnson, M. D.; Levinger, N. E.; Crans, D. C., 1H NMR Studies of Aerosol-OT Reverse Micelles with Alkali and Magnesium Counterions: Preparation and Analysis of MAOTs. *Langmuir* **2008,** *24* (12), 6027-6035.

50. Eastoe, J.; Robinson, B. H.; Heenan, R. K., Water-in-oil Microemulsions Formed by Ammonium and Tetrapropylammonium Salts of Aerosol OT. *Langmuir* **1993,** *9* (11), 2820-2824.

51. Biotechnology, S. C. Zincon sodium salt. https://www.scbt.com/scbt/product/zincon-sodium-salt-56484-13-0 (accessed July 13, 2018).

52. Säbel, C. E.; Neureuther, J. M.; Siemann, S., A spectrophotometric method for the determination of zinc, copper, and cobalt ions in metalloproteins using Zincon. *Analytical Biochemistry* **2010,** *397* (2), 218-226.

53. Baruah, B.; Roden, J. M.; Sedgwick, M.; Correa, N. M.; Crans, D. C.; Levinger, N. E., When Is Water Not Water? Exploring Water Confined in Large Reverse Micelles Using a Highly Charged Inorganic Molecular Probe. *J. Am. Chem. Soc.* **2006,** *128* (39), 12758-12765.

54. Glasoe, P. K.; Long, F. A., Use of Glass Electrodes to Measure Acidities in Deuterium Oxide1,2. *The Journal of Physical Chemistry* **1960,** *64* (1), 188-190.

55. Rush, R. M.; Yoe, J. H., Colorimetric Determination of Zinc and Copper with 2-Carboxy-2´-hydroxy-5´-sulfoformazylbenzene. *Analytical Chemistry* **1954,** *26* (8), 1345-1347.

56. Peters, B. J.; Van Cleave, C.; Haase, A. A.; Hough, J. P. B.; Giffen-Kent, K. A.; Cardiff, G. M.; Sostarecz, A. G.; Crick, D. C.; Crans, D. C., Structure Dependence of Pyridine and Benzene Derivatives on Interactions with Model Membranes. *Langmuir* **2018,** *34* (30), 8939-8951.

57. Vermathen, M.; Stiles, P.; Bachofer, S. J.; Simonis, U., Investigations of Monofluoro-Substituted Benzoates at the Tetradecyltrimethylammonium Micellar Interface. *Langmuir* **2002,** *18* (4), 1030-1042.

58. Crans, D. C.; Shin, P. K., Characterization of Vanadium(V) Complexes in Aqueous Solutions: Ethanolamine- and Glycine-Derived Complexes. *Journal of the American Chemical Society* **1994,** *116* (4), 1305-1315.

59. Crans, D. C.; Chen, H.; Anderson, O. P.; Miller, M. M., Vanadium(V)-protein model studies: solid-state and solution structure. *Journal of the American Chemical Society* **1993,** *115* (15), 6769-6776.

60. Ashbrook, L. N.; Elliott, C. M., Dye-Sensitized Solar Cell Studies of a Donor-Appended Bis(2,9-dimethyl-1,10-phenanthroline) Cu(I) Dye Paired with a Cobalt-Based Mediator. *J. Phys. Chem. C* **2013,** *117* (8), 3853-3864.

61. Domaille, D. W.; Que, E. L.; Chang, C. J., Synthetic Fluorescent Sensors for Studying the Cell Biology of Metals. *Nat. Chem. Biol.* **2008,** *4* (3), 168-175.

62. Lee, M. H.; Kim, J. S.; Sessler, J. L., Small Molecule-based Ratiometric Fluorescence Probes for Cations, Anions, and Biomolecules. *Chem. Soc. Rev.* **2015,** *44* (13), 4185-4191.

63. Beuning, C. N.; Mestre-Voegtlé, B.; Faller, P.; Hureau, C.; Crans, D. C., Measurement of Interpeptidic Cu(II) Exchange Rate Constants by Static Fluorescence Quenching of Tryptophan. *Inorg. Chem.* **2018,** *57* (9), 4791-4794.

PART 2) THE ELECTROCHEMISTRY OF TRUNCATED MENAQUINONE ELECTRON TRANSPORTERS WITH SATURATED ISOPRENE SIDE CHAINS IMPORTANT IN TUBERCULOSIS

CHAPTER 5: REDOX POTENTIALS OF TRUNCATED MENAQUINONE ANALOGS IN APROTIC SOLVENTS ARE SENSITIVE TO SATURATION IN THE ISOPRENE SIDE CHAIN[1]

5.1 Summary

Menaquinone (MK) analogs with regiospecific partial saturation in their isoprenyl side chain, such as MK-9(II-H_2), are found in many types of bacteria, including pathogenic *Mycobacterium tuberculosis* and function as electron transport lipids cycling between quinone and quinol forms within the electron transport system. While the function of MK is well established, the role of regiospecific partial saturation in the isoprenyl side chain on MK remains unclear and may be related to the redox function. We performed cyclic voltammetry on a series of truncated MK analogs with partially saturated, fully saturated, and unsaturated isoprene side chains in three aprotic solvents (acetonitrile, dimethyl sulfoxide, and pyridine) and their redox potentials and diffusion coefficients are reported herein. Most notably, the partially saturated MK-2(II-H_2) and MK-3(II-H_2) analogs were easier to reduce (more positive potentials), while the fully saturated MKs were among the hardest to reduce (more negative potentials), and most unsaturated MK analogs were in the mid-range of potentials measured. Principal component analysis performed on the measured redox potentials shows that the degree of double bond saturation in the isoprenyl side chain was the primary variable in the observed redox potential differences for truncated MK analogs. Absorption spectroelectrochemistry was performed on the truncated MK analogs to observe semiquinone intermediates. In the spectroelectrochemistry, small bathochromic red-shifts in wavelength were detected for the quinoid absorption bands between the unsaturated/partially saturated and fully saturated analogs in acetonitrile and dimethyl sulfoxide, which seems to be an effect from the first isoprene unit saturation. These studies give insight into why partially saturated MKs are found as the primary electron transporter in many bacteria.

[1] Beuning, C. N.; Koehn, J. T.; Crick, D. C.; Crans, D. C., Redox Potentials of Truncated Menaquinone Analogs in Aprotic Solvents are Sensitive to Saturation in the Isoprene Side Chain. **2020,** *Submitted*.

5.2 Introduction to menaquinones, their redox processes, and importance in tuberculosis

Menaquinones (MK) are a class of membrane-bound 1,4-naphthoquinone electron transport lipids (lipoquinones), which function in respiration and are essential to generate proton motive force (PMF) through membranes in bacteria.[2-13] In humans, ubiquinone (UQ), which is structurally similar to MK, is the major mitochondrial electron-transporting lipoquinone.[2] In humans, MK-4, also known as Vitamin K_2, is an essential co-factor for blood coagulation and MKs have other functions in bone and cardiovascular health[14], while in plant life phylloquinones (e.g., Vitamin K_1) are essential in photosynthesis.[2, 5, 15] In bacteria, PMF is generated by the reduction of lipoquinones by electron-donating membrane-bound enzymes such as dehydrogenases, hydrogenases, and oxidoreductases, while the subsequent oxidation is carried out by electron-accepting membrane-bound enzymes such as oxidases (aerobic respiration), reductases (anaerobic respiration), or some cytochromes, **Figure 5.1**.[2-3, 7] This redox cycle of quinone (Q) and hydroquinone species (QH_2) in bacteria generates PMF, which is used in ATP synthesis, producing cellular energy and is critical for sustained life.

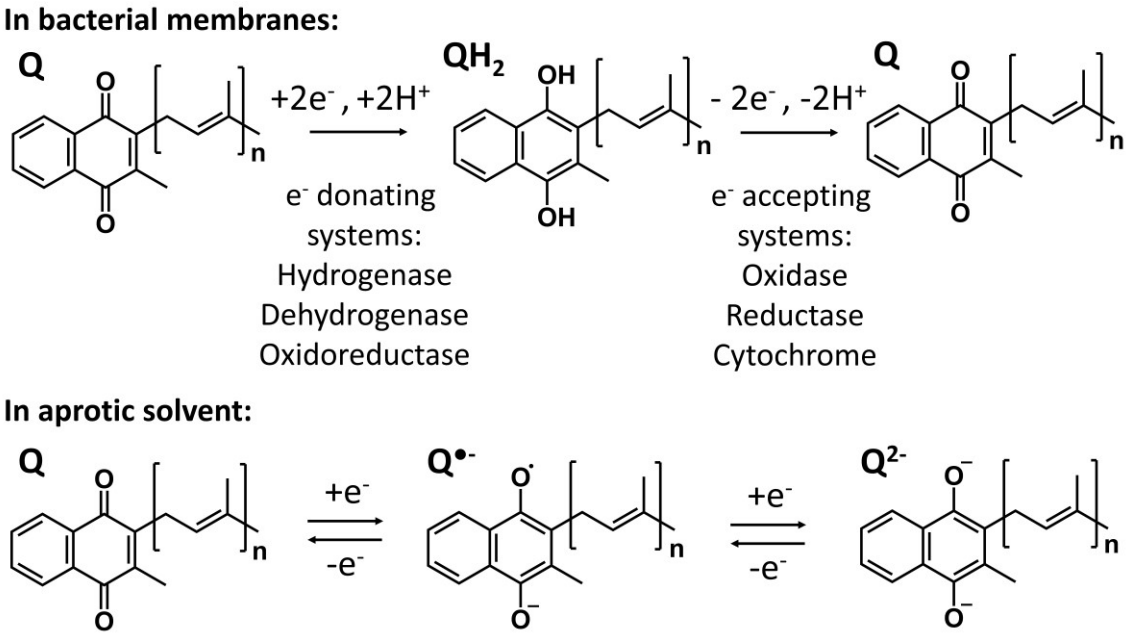

Figure 5.1: The reduction of a MK-*n* analog within bacterial membrane-bound enzymes versus aprotic solvent. In bacteria, the quinone is reduced by the actions of e^- donating membrane-bound enzyme systems to the hydroquinone (QH_2) and then oxidized by e^- accepting membrane-bound enzyme systems to the quinone (Q), where both electrons are simultaneously added or removed. Depending on the MK analog, double bonds may or may not be present in all of the isoprenyl units in the side chain; see **Figure 5.2** for all MK-*n* structures used in this study.

The reduction of the quinone in aprotic media such as acetonitrile (MeCN), dimethyl sulfoxide (DMSO), or pyridine follows a different path than in aqueous solution, creating a radical semiquinone ($Q^{\bullet-}$) and dianion (Q^{2-}) when an external potential is applied.[4, 6, 16-26] There are examples of stable semiquinone species having biological activity with receptor sites in QH_2-reductases; however, the most common reduced form in biological systems is the quinol.[27-29] Due to the hydrophobicity of many quinones, often studies of quinone redox potentials in aqueous solution have been estimated by modeling calculations or by solvating the quinones in lipid bilayers or films, or mixed organic-water solvent systems with acidic proton donors.[29-35] Therefore, quinone redox chemistry is often studied in aprotic solvents, where discrete differences in redox potentials can be reproducibly measured. Importantly, these solvents more closely mimic the hydrophobic region of the lipid bilayer where lipoquinones reside and allow for comparison in hydrophobic environments.

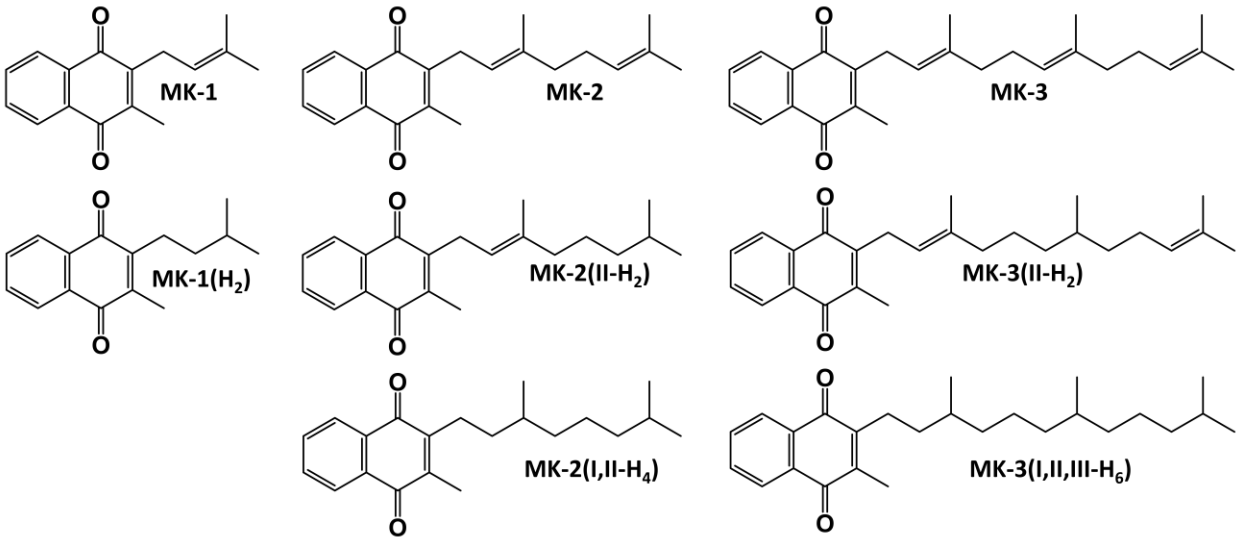

Figure 5.2: The structures of all truncated MK-*n* analogs examined in this work; MK-1, MK-1(H_2), MK-2, MK-2(II-H_2), MK-2(I,II-H_4), MK-3, MK-3(II-H_2), and MK-3(I,II,III-H_6). These structures do not show the solution dependent conformational folding that can be exhibited by the longer chained analogs, which we have previously reported for MK-2.[36]

Considerable research has been performed to elucidate the redox mechanisms, functions, roles, and redox potential differences among the varying types of lipoquinones (e.g., UQ, MK, phylloquinone); as well redox potential differences that arise from substitutions made on the ring moiety, across varying biological and synthetic sources, in aqueous buffered solutions, aprotic solvents, and mixed

aprotic/aqueous systems.[2, 4-6, 16-18, 20, 22-25, 29-30, 32, 34, 36-44] It is known that the hydrophobicity of the isoprene side chain helps to anchor the MK in the membrane and to help lateral diffusion.[12, 45-46] One study showed that in UQ-2 analogs with a fully saturated side chain and partial saturation at the first isoprene unit increased binding affinity to bovine complex 1 compared to the unsaturated or partial second isoprene saturation.[45] Thus, saturation in the isoprene side chain may have more significant roles than just quinone mobility. The regiospecific partial saturation of the second isoprene unit on the isoprenyl side chain has been reported for the MK pools for many bacteria, including the *Mycobacterium*, *Corynebacterium*, *Halobacterium*, and *Brevibacterium* families, although less information is available on their formation.[2, 13, 47-51] In *Mycobacterium tuberculosis* (*M. tuberculosis*), the oxidoreductase MenJ is responsible for the regiospecific isoprene saturation converting MK-9 to MK-9(II-H_2).[3, 8] Removal of the genes responsible for the expression of this enzyme resulted in a three-fold decrease in electron transport efficiency in growth media, while in host mouse macrophages, was found to be essential for the survival of the bacteria.[3] In some archaea, fully saturated MK analogs are suggested to have a role in membrane stability under harsh environments such as high salinity or extreme pH, and many examples of fully saturated lipoquinones have been reported.[47-48, 52-55]

Much is known regarding the composition of the MK pool in bacteria and archaea, which has been used for taxon classification.[2, 12-13, 55-56] It is not clear why saturated lipoquinone derivatives are conserved across all of these bacterial families but could be related to its electron transport functions. We recently reported on the observed differences in redox potential between MK-1 and MK-1(H_2), and we observed a conserved 20 mV difference in the same three solvents.[40] These studies showed there were significant differences in the reactivity of the quinones based on changes in side chain isoprene saturation, which warranted a systematic analysis of isoprene unit saturation of truncated MK analogs. To this end, we have synthesized various truncated MK-*n* analogs with partial saturation, full saturation, and unsaturated isoprenyl side chains, **Figure 5.2**.[57]

In this work, the electrochemistry of these hydrophobic compounds was characterized in three aprotic solvents (MeCN, DMSO, and pyridine) by cyclic voltammetry (CV). The MK redox reaction was monitored by absorption spectroelectrochemistry in MeCN and DMSO to characterize the redox progress from quinone to the semiquinone reaction intermediate, as well as the dianion. We hypothesize that the

extent of saturation in the isoprene side chain directly affects the redox potentials of the truncated MK-*n* analogs with partial and full saturation in the isoprene side chain. A systematic statistical analysis is used to determine if the electrochemical redox potential differences are significantly confident which arise from the type and extent of saturation in the isoprene side chain. This investigation is an important to step to understand why partial and full saturated isoprene side chains in MKs are observed in pathogenic bacteria such as *M. tuberculosis*.

5.3 Experimental methods

5.3.1 Materials

All MK-*n* analogs analyzed were synthesized, and the procedures for the synthesis of the MK-*n* analogs are previously reported by Dr. Jordan T. Koehn (MK-3 was reported in the paper this chapter was created from).[1, 36, 40, 57] All MK-*n* molecular masses, physical appearances, and weighed masses used in the CV are listed in **Table 5.1**. The supporting electrolyte was tetrabutylammonium perchlorate (TBAP, Sigma Aldrich, ≥99.0%) and was used as purchased without any additional purification. The internal standard for the cyclic voltammetry was ferrocene (Fc, Sigma). Silver nitrate ($AgNO_3$, Sigma Aldrich) was used for the Ag^+/Ag reference electrode. Organic solvents used included, acetonitrile (MeCN), dimethyl sulfoxide (DMSO), and pyridine were purchased from Sigma Aldrich and dried under argon on a Solv-Tek alumina drying column to remove water, as previously reported.[40] Glassware was dried in the oven (>130

Table 5.1: Molecular mass and physical appearances of MK-*n* analogs, masses weighed for each run used in the determination of diffusion coefficients. All masses were dissolved in 5.00 mL of 0.1 M TBAP with 2 mM Fc, to give concentrations near 2 mM.

MK-*n*	MW (g/mol)	Physical Appearance*	MeCN Runs 1, 2, 3 (mg)	DMSO Runs 1, 2, 3 (mg)	Pyridine Runs 1, 2, 3 (mg)
MK-1	240.3	Oil	3.0, 3.5, 4.0	2.9, 3.0, 2.8	2.8, 9.2, 2.7
MK-1(H_2)	242.32	Powder	3.2, 2.9, 2.9	4.5, 4.5, 4.3	3.5, 4.9, 3.0
MK-2	308.42	Powder	3.2, 4.5, 3.9	3.3, 4.2, 4.0	4.0, 3.2, 4.5
MK-2(I,II-H_4)	312.45	Oil	5.6, 5.6, 9.3	9.5, 5.1, 4.8	4.9, 3.4, 5.9
MK-2(II-H_2)	310.44	Oil	3.1, 3.1, 3.2	3.2, 3.2, 3.1	3.1, 3.1, 3.2
MK-3	376.54	Oil	5.8, 4.3, 4.0	7.5, 5.1, 7.1	5.4, 5.2, 4.5
MK-3(I,II,III-H_6)	382.59	Powder	3.8, 3.8, 3.9	3.8, 3.9, 4.0	3.9, 3.8, 3.9
MK-3(II-H_2)	378.56	Oil	3.8, 3.8, 3.8	3.7, 3.8, 3.8	3.1, 3.1, 3.2

* Most analogs had a yellow to orange color (some even slightly red) but once dissolved in solvent all were yellow in color.

°C) and cooled under vacuum and put under anhydrous/inert atmosphere before the addition of solvent to the receiving vessel. Solvents were used fresh from the drying column and were analyzed to make sure the ferrocene and shorter isoprenyl side chain length MK-1 and MK-2 redox potentials were the same compared to in solvents dried over activated molecular sieves, as we previously reported.[36, 40] Ultra-high purity argon gas was purchased from Airgas.

5.3.2 Electrochemistry methods, instrumentation, and analysis

5.3.2.1 Cyclic voltammetry electrodes

A classical three-electrode system was used with a glassy carbon working electrode (BASi MF2012, 3 mm, area of 0.707 cm^2), a platinum wire auxiliary electrode (BASi MW1032), and a non-aqueous Ag^+/Ag reference electrode (BASi MW1085) with 0.1 M TBAP as the electrolyte. The redox potentials are reported as half-wave potentials, **Eq.1.12**, $E_{1/2}$, where E_{pc} and E_{pa} are cathodic and anodic peak potentials. For all electrochemistry performed in this work, half-wave potentials are referenced to the internal standard of ferrocene, whose half-wave potential is set to zero (Fc^+/Fc $E_{1/2}$ = 0 V). The Fc^+/Fc CV peaks are well resolved from the MK peaks, which allowed for direct comparison of potentials across different solvents. Electrodes were cleaned after each set of three measurements and manually inspected between runs to ensure no buildup accumulated on the glassy carbon electrode. The glassy carbon electrode was polished with water and alumina in a figure-eight motion after each CV was recorded, then rinsed with ethanol and then dried by evaporation with a stream of Ar (g). Both Pt and Ag wires were cleaned by polishing with 600 grit sandpaper and rinsed with ethanol, which was then evaporated under a stream of Ar (g). The Ag^+/Ag electrode was constructed by using the same solvent as the MK-*n* solution with 0.10 M TBAP and 0.010M $AgNO_3$ to eliminate any liquid junction potentials. The Fc^+/Fc redox potentials were within experimental error (ones of mV) in all three solvents across all runs in that solvent, as previously reported.[36, 40]

5.3.2.2 Instrumentation and software

All electrochemical data was performed on either a CHI 750D potentiostat or Pine Research WaveDriver 20 bipotentiostat (Model AFP2). The scan rate for all samples was 100 mV/s and was performed in the direction from -2.00 V to 1.00 V to -2.00 V vs Ag^+/Ag (some may have been run in the opposite direction starting at 1.00 V). The CVs were graphed using Origin2019b student version. Microsoft

Excel 2016 was used for mathematical analysis and subtraction of internal standard Fc^+/Fc $E_{1/2}$ redox potential from experimental MK data to set the potential axis versus ferrocene.

5.3.2.3 Sample preparation

The MK-*n* concentrations were approximately 2 mM for CV experiments. Experimental solutions were created by weighing out the MK-*n* (**Table 5.1**) then 5.00 mL of 2 mM Fc in 0.1 M TBAP was added by a graduated cylinder. All electrodes equilibrated to each MK-*n* solution for at least 5 minutes while Ar (g) was bubbled through to de-solvate any dissolved O_2 (g). All sample preparation and electrochemical analysis were performed in a hood system, especially when working with pyridine.

5.3.2.4 Diffusion coefficient analysis

The diffusion coefficient, D_o, can be determined from the Randles-Sevcik equation, **Eq. 1.15**, where the constant 2.69 x 10^5 is determined by Faraday's constant, temperature, and the gas constant at STP, i_p is peak current measured, n is the number of electrons in the redox process, C_O^* is the bulk concentration of species, A is the area of the working electrode, and v is the scan rate. Cathodic peak current passed was manually measured from printed CVs using a ruler and converted to amps (A) using an A/cm tick marks ratio. The double-layer capacitance was easily observed and subtracted by drawing a tangential line on the approach to the CV peak in the direction of the scan. The i_p was then drawn as a vertical line down from the peak current maximum to the tangential line and measured in cm. Since masses of the MK-*n* analogs were weighed in mg quantities, the diffusion coefficients are restricted to reporting two significant figures. Any outliers were determined and excluded by Grubb's tests if the value was G = 1.15 or greater.[58] The i_p values for both cathodic (i_{pc}) and anodic (i_{pa}) peak current passed were also used to determine reversibility by **Eq. 1.14** in which all CV peaks showed peak ratios that approached unity, which indicates a reversible redox process. To determine the number of electrons involved in each redox process **Eq. 1.17** is used, and all the MKs studied had n = 1 electron for both $Q/Q^{\bullet-}$ and $Q^{\bullet-}/Q^{2-}$ redox processes.

5.3.3 Absorption spectroelectrochemistry methods

5.3.3.1 Pine Research Honeycomb spectroelectrochemical cell cuvette

To perform the spectroelectrochemistry, we used the platinum Honeycomb spectroelectrochemical cuvette/electrode system created by Pine Research with the WaveDriver20 bipotentiostat. This electrode has both the working and counter electrodes directly on the plate. The reference electrode used was a low-profile non-aqueous Ag^+/Ag in each solvent, just as in the CV electrochemistry. Pyridine was not a suitable solvent for absorption spectroscopy due to its limited solvent window in the low UV region; therefore, the spectroelectrochemistry absorption spectra were only measured in MeCN and DMSO. The cuvette is quartz and has a thin layer path-length of 1.7 mm, where the electrode plate fits snuggly. The honeycomb design allows the light to pass through the solution and helps to quickly equilibrate the solution to the applied potential. All MK concentrations were kept below 0.5 mM due to the smaller path-length. Ferrocene was not used in the absorption spectroscopy. The AfterMath software program from Pine Research was used to perform the spectroelectrochemical measurements, which controls both the potentiostat and the absorption instrumentation. The spectroelectrochemical absorption spectra were graphed in Origin2019b (student version).

5.3.3.2 Avantes optics for UV-vis absorption spectroscopy

Avantes optics were used for the absorption spectroscopy. AvaLight DHc dual deuterium-halogen lamps were used as light sources for spectroscopy in the 200 – 2500 nm range and an AvaSpec-2048 was used as the detector. The cuvette holder was attached to the light source and the detector by fiber optic cables. **Table 5.2** lists the potentials used in the measurement of absorption spectra, which were the cathodic peak potentials versus Ag^+/Ag reference electrode in each solvent. Equilibration times of 60 s were used between potential steps, a boxcar width of 5, and an average of 100 scans per spectrum capture. Blank solutions were reference captured with ambient light, while the solvent and electrode plate was in the cuvette. This reference spectrum was automatically subtracted from the absorption spectra acquired by the AfterMath software program.

Table 5.2: Cathodic peak potentials used for spectroelectrochemical absorption spectroscopy measurements ($E_{cathodic}$ vs Ag^+/Ag) for each redox process $Q/Q^{\bullet-}$ and $Q^{\bullet-}/Q^{2-}$.

MK-*n*	Solvent	E_{pc1} $Q/Q^{\bullet-}$, V vs Ag^+/Ag	E_{pc2} $Q^{\bullet-}/Q^{2-}$, V vs Ag^+/Ag
MK-1	MeCN	-1.102	-1.749
	DMSO	-0.927	-1.713
MK-1(H_2)	MeCN	-1.107	-1.767
	DMSO	-0.929	-1.745
MK-2	MeCN	-1.091	-1.750
	DMSO	-0.929	-1.635
MK-2(I,II-H_4)	MeCN	-1.121	-1.761
	DMSO	-0.939	-1.727
MK-2(II-H_2)	MeCN	-1.091	-1.736
	DMSO	-0.931	-1.725
MK-3	MeCN	-1.111	-1.743
	DMSO	-0.933	-1.709
MK-3(I,II,III-H_6)	MeCN	-1.101	-1.734
	DMSO	-0.950	-1.743
MK-3(II-H_2)	MeCN	-1.089	-1.740
	DMSO	-0.939	-1.726

5.3.4 Statistical analysis of MK-n redox potentials

5.3.4.1 Principal component analysis

A matrix of unaveraged half-wave redox potentials, **Table 5.3**, for each solvent and each MK-*n* analog was generated and then analyzed by the principal component analysis (PCA) in Origin Pro 2019b (student version). The multivariate analysis was performed on this matrix, and the subsequent eigenvalues graphed as PC 1 as the x-axis and PC 2 as the y-axis. The PC 1 percentage of variance was determined to be 88.61%, while PC 2 was 6.30%, and the other variables were less than 2.43 %, each totaling the remaining 5%, **Table 5.4,** including the PCA Scree plot, **Figure 5.3**.

Table 5.3: PCA matrix of all measured half-wave potentials ($Q/Q^{\bullet-}$) versus Fc^+/Fc in each solvent for each MK-*n* analog.

	MeCN			DMSO			Pyridine		
	$E_{1/2}$, V	$E_{1/2}$, V	$E_{1/2}$, V	$E_{1/2}$, V	$E_{1/2}$, V	$E_{1/2}$, V	$E_{1/2}$, V	$E_{1/2}$, V	$E_{1/2}$, V
MK-*n*	Run 1	Run 2	Run 3	Run 1	Run 2	Run 3	Run 1	Run 2	Run 3
MK-1	-1.226	-1.225	-1.230	-1.160	-1.156	-1.158	-1.318	-1.318	-1.320
MK-1(H_2)	-1.240	-1.255	-1.247	-1.178	-1.179	-1.181	-1.343	-1.342	-1.343
MK-2	-1.228	-1.228	-1.233	-1.155	-1.154	-1.156	-1.332	-1.330	-1.330
MK-2(I,II-H_4)	-1.259	-1.251	-1.253	-1.178	-1.178	-1.179	-1.342	-1.342	-1.348
MK-2(II-H_2)	-1.223	-1.227	-1.225	-1.157	-1.156	-1.155	-1.310	-1.315	-1.313
MK-3	-1.233	-1.225	-1.230	-1.161	-1.164	-1.159	-1.328	-1.328	-1.332
MK-3(I,II,III-H_6)	-1.243	-1.240	-1.258	-1.183	-1.178	-1.176	-1.332	-1.332	-1.338
MK-3(II-H_2)	-1.220	-1.221	-1.223	-1.158	-1.158	-1.157	-1.320	-1.315	-1.316

Table 5.4: The principal component analysis eigenvalues of the correlation matrix, percentage of variance, and cumulative percentage as determined by OriginPro 2019b software.

PC X	Eigenvalue	Percentage of Variance	Cumulative
PC 1	7.9747	88.61%	88.61%
PC 2	0.56727	6.30%	94.91%
PC 3	0.21827	2.43%	97.34%
PC 4	0.13111	1.46%	98.79%
PC 5	0.08254	0.92%	99.71%
PC 6	0.02277	0.25%	99.96%
PC 7	0.00333	0.04%	100.00%

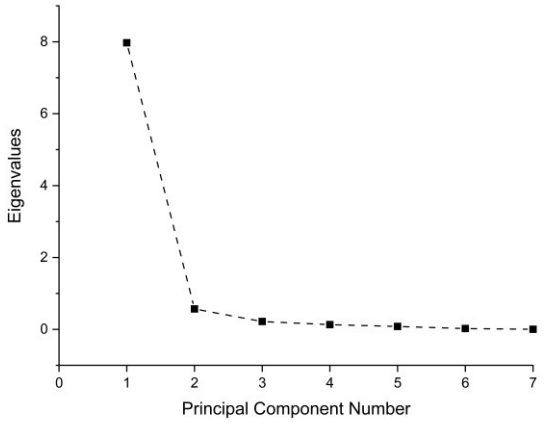

Figure 5.3: The Scree plot from the PCA performed on the redox potential matrix. The Scree plot shows there should be one major principal component (PC 1) and a second less significant component (PC 2), with an additional 5 with very low to no statistical significance.

5.3.4.2 Student's t tests

Statistical analysis using Student's *t* tests of MK-*n* half-wave potentials were performed in Microsoft Excel 2016. Standard deviations and 95% confidence intervals used in the statistical analysis of half-wave redox potentials and are listed below in section *5.4.1* in **Table 5.5**. Student's *t* tests were performed to determine if two averaged MK-*n* $E_{1/2}$ were statistically different or not using $t_{calculated}$, **Eq. 5** and calculated the degrees of freedom (*dof*) for t_{table}, **Eq. 6**.[58] Depending on the *dof* calculated, the highest confidence interval where $t_{calculated} > t_{table}$ are reported for the following comparisons: for MK-*n* of the same value of *n* across different solvents **Tables 5.6** or degree of saturation **Table 5.8**, and when compared across different values of *n*, **Table 5.9**, see section *5.4.2*. Two- or one-tailed *p*-values were determined using values corresponding to the confidence intervals and GraphPad free software.

(**Eq. 5.1**) $t_{calculated} = \frac{|\bar{x}_1 - \bar{x}_2|}{\sqrt{s_1^2/n_1 + s_2^2/n_2}}$ (**Eq. 5.2**) $dof = \frac{\left(s_1^2/n_1 + s_2^2/n_2\right)^2}{\frac{(s_1^2/n_1)^2}{(n_1-1)} + \frac{(s_2^2/n_2)^2}{(n_2-1)}}$

The hydroquinone (QH_2) species, **Figure 5.1**, is kinetically favored in the presence of water, acidic protons, or Lewis acid/base donors. Upon reduction, the two quinoid carbonyl oxygens will become hydrated simultaneously, which results in a single two-electron redox process.[17] As the amount of inherent water content or presence of acidic protons increases in an aprotic solvent, the $Q^{\bullet-}/Q^{2-}$ redox process will shift to more positive potentials until finally merging onto the $Q/Q^{\bullet-}$ redox process, which is not affected by water content.[17] Statistical analysis presented in this work utilizes the first redox process, $Q/Q^{\bullet-}$ as it is unaffected by inherent water content, even though all solvents used in this work were rigorously dried, used fresh, and under an Argon atmosphere to minimize the effects of water.

5.4 Results and discussion

5.4.1 Cyclic voltammetry and redox potentials

Electrochemical analysis of each MK-*n* analog in the presence of Fc was performed in MeCN, DMSO, or pyridine, where the CVs are given in **Figure 5.4**. In these CVs, three distinct reversible peaks are observed, see MK-1 in pyridine for labeling, first-row second panel, **Figure 5.4**. The right peak is the internal standard of ferrocene, whose potential is set to 0 V, so all MK-*n* half-wave potentials in different solvents can be directly compared versus Fc^+/Fc couple. The middle peak is the first one-electron reduction of the quinone to the semiquinone, $Q/Q^{\bullet-}$ **Figure 5.1**. The left peak is the second one-electron reduction of the semiquinone to the dianion, $Q^{\bullet-}/Q^{2-}$ **Figure 5.1**. The peak current passed by the semiquinone reduction is always smaller than that of the quinone due to the repulsion of the negatively charged semiquinone from the diffusion layer of the working electrode.[17] All half-wave potentials for each redox process were determined by **Eq. 1.12**, referenced to an internal standard of Fc^+/Fc, and are listed in **Table 5.5** with their standard deviations and 95% confidence levels (CL). For all MK-*n* analogs of the same value *n*, whether saturated or unsaturated, the quinone redox potentials were statistically different at 99% confidence or higher when comparing across different solvent environment (MeCN vs DMSO, etc.), **Table 5.6**. Most of the MK semiquinone redox processes are above 95% confidence. These observed redox potential

differences for MK arises from the changes in dielectric constants (relative polarities) of the three solvents, where MeCN (36.64) and DMSO (47) are similar, while pyridine (12.3) is significantly dissimilar.

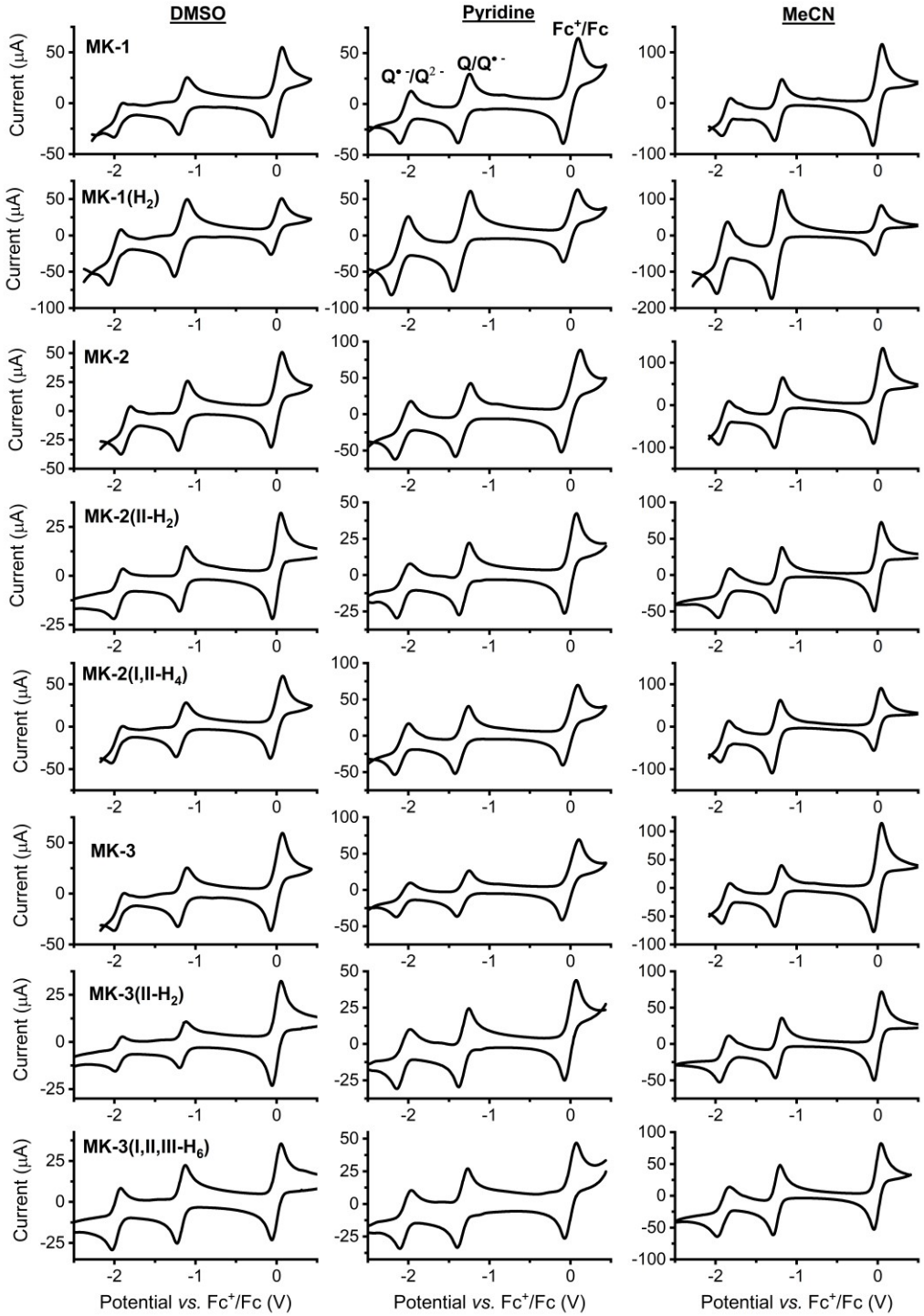

Figure 5.4: The CVs of MK-*n* analogs in MeCN, DMSO, and pyridine. Concentrations of MK-*n* and Fc are near 2 mM (see **Table 5.1** for details), *v* = 100 mV/s, at ambient room temperature, and under Argon atmosphere. Fc internal standard $E_{1/2}$ set to 0 V vs Ag^+/Ag in reference electrode.

Table 5.5: Average $E_{1/2}$ vs Fc^+/Fc for each MK-*n* with standard deviations (σ) and 95% CL. Standard deviations were used in statistical analysis calculations, while reported $E_{1/2}$ are given at 95% confidence level (*t* = 4.303, *n* = 3 replicates) at a scan rate of 100 mV/s, under Ar (g), and at ambient room temperature. Numbers in parentheses indicate where the CL is not significant.

MK-*n*	Solvent	$E_{1/2}$ $Q/Q^{\bullet-}$ vs Fc^+/Fc (V)	σ (V)	CL 95% (V)	$E_{1/2}$ $Q^{\bullet-}/Q^{2-}$ vs Fc^+/Fc (V)	σ (V)	CL 95% (V)
MK-1	MeCN	-1.227	0.002	0.006	-1.88(2)	0.014	0.034
MK-1(H_2)		-1.24(7)	0.007	0.019	-1.91(2)	0.009	0.023
MK-2		-1.230	0.003	0.006	-1.90(2)	0.012	0.031
MK-2(I,II-H_4)		-1.25(4)	0.004	0.011	-1.89(2)	0.010	0.024
MK-2(II-H_2)		-1.225	0.002	0.005	-1.89(0)	0.011	0.028
MK-3		-1.229	0.004	0.009	-1.87(0)	0.016	0.041
MK-3(I,II,III-H_6)		-1.24(7)	0.010	0.024	-1.89(3)	0.008	0.019
MK-3(II-H_2)		-1.221	0.001	0.003	-1.89(8)	0.011	0.028
MK-1	DMSO	-1.158	0.002	0.004	-1.94(9)	0.006	0.014
MK-1(H_2)		-1.179	0.002	0.004	-1.995	0.001	0.002
MK-2		-1.155	0.001	0.003	-1.86(3)	0.008	0.021
MK-2(I,II-H_4)		-1.178	0.0001	0.0002	-1.97(2)	0.005	0.013
MK-2(II-H_2)		-1.156	0.001	0.003	-1.951	0.002	0.005
MK-3		-1.161	0.002	0.005	-1.943	0.003	0.006
MK-3(I,II,III-H_6)		-1.179	0.004	0.009	-1.97(6)	0.004	0.010
MK-3(II-H_2)		-1.158	0.001	0.001	-1.949	0.002	0.006
MK-1	Pyridine	-1.319	0.001	0.002	-2.03(7)	0.005	0.013
MK-1(H_2)		-1.343	0.001	0.002	-2.10(9)	0.005	0.012
MK-2		-1.331	0.001	0.003	-2.075	0.003	0.008
MK-2(I,II-H_4)		-1.344	0.004	0.009	-2.082	0.003	0.009
MK-2(II-H_2)		-1.313	0.003	0.006	-2.063	0.003	0.007
MK-3		-1.329	0.002	0.005	-2.066	0.001	0.002
MK-3(I,II,III-H_6)		-1.334	0.003	0.008	-2.04(0)	0.009	0.022
MK-3(II-H_2)		-1.317	0.003	0.006	-2.04(9)	0.010	0.024

Table 5.6: Student's *t* tests of measured redox process $E_{1/2}$ vs Fc^+/Fc of MK-*n* based on differences in the solvent environment. Values are given at the highest % confidence level determined for that comparison. The *p*-values given are based on the highest % confidence level.

MK-*n*	Solvent 1	Solvent 2	Highest % CL $E_{1/2}$ $Q/Q^{\bullet-}$ vs Fc^+/Fc	p (2-tail)	Highest % CL $E_{1/2}$ $Q^{\bullet-}/Q^{2-}$ vs Fc^+/Fc	p (2-tail)
MK-1	MeCN	DMSO	99.9	0.001	99	0.01
	DMSO	Pyridine	99.9	0.001	99.9	0.001
	MeCN	Pyridine	99.9	0.001	99.9	0.001
MK-1(H_2)	MeCN	DMSO	99	0.01	99	0.01
	DMSO	Pyridine	99.9	0.001	99.9	0.001
	MeCN	Pyridine	99	0.01	99.9	0.001
MK-2	MeCN	DMSO	99.9	0.001	98	0.02
	DMSO	Pyridine	99.9	0.001	99.9	0.001
	MeCN	Pyridine	99.9	0.001	99.8	0.002
MK-2(I,II-H_4)	MeCN	DMSO	99.8	0.002	99.8	0.002
	DMSO	Pyridine	99.9	0.001	99.9	0.001
	MeCN	Pyridine	99.9	0.001	99.9	0.001
MK-2(II-H_2)	MeCN	DMSO	99.9	0.001	98	0.02
	DMSO	Pyridine	99.9	0.001	99.9	0.001
	MeCN	Pyridine	99.9	0.001	99.8	0.002
MK-3	MeCN	DMSO	99.9	0.001	98	0.02
	DMSO	Pyridine	99.9	0.001	99.9	0.001
	MeCN	Pyridine	99.9	0.001	99	0.01
MK-3(I,II,III-H_6)	MeCN	DMSO	99.8	0.002	99.9	0.001
	DMSO	Pyridine	99.9	0.001	99.8	0.002
	MeCN	Pyridine	99	0.01	99.9	0.001
MK-3(II-H_2)	MeCN	DMSO	99.9	0.001	98	0.02
	DMSO	Pyridine	99.9	0.001	99	0.01
	MeCN	Pyridine	99.9	0.001	99.9	0.001

Some trends can be visualized when the averaged half-wave potentials of the $Q/Q^{\bullet-}$ redox process in **Table 5.5** are plotted against solvent, **Figure 5.5**. Most notably are the absolute differences in the redox potentials of the MK-*n* analogs with partially and fully saturated isoprenyl side chains. The partially saturated MK-2(II-H_2) and MK-3(II-H_2) analogs were among the more easily reducible (more positive potentials) MK-*n* analogs as compared to their fully saturated counterparts, MK-2(I,II-H_4) and MK-3(I,II,III-H_6), which are all the hardest to reduce (more negative potentials). This trend is conserved across all solvents tested. A 20 - 30 mV potential difference is observed between the partially saturated versus fully saturated MK analogs, **Table 5.7**. Similarly, we observed a 17 - 24 mV difference between the unsaturated MK-1, MK-2, and MK-

3 analogs and their fully saturated counterparts MK-1(H_2), MK-2(I,II-H_4), and MK-3(I,II,III-H_6) in MeCN and DMSO, **Table 5.7**. However, in pyridine, these differences were much smaller in the MK-2 (13.2 mV) and MK-3 comparisons (4.7 mV). Only small 1.1 – 8.2 mV redox potential differences were observed between the unsaturated versus the partially saturated MK analogs in MeCN and DMSO but were larger for pyridine (12.7, 17.7 mV) **Table 5.7**. The differences seen in pyridine versus the MeCN and DMSO are probably due to the differences in their dielectric constants, where MeCN and DMSO have similar dielectric constants.

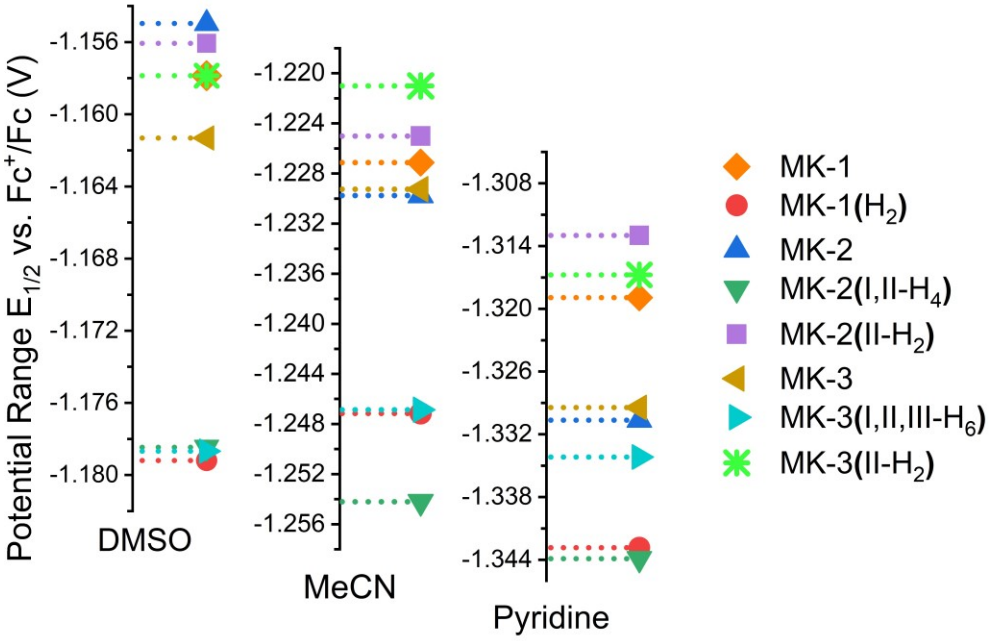

Figure 5.5: All MK-*n* averaged $E_{1/2}$ vs Fc^+/Fc of the $Q/Q^{\bullet-}$ redox process compared by the solvent used. Measured potential ranges on the y-axis are different for each solvent but are aligned with the MK analog with the most positive potential at the top while the MK analog with the most negative is at the bottom. Along the x-axis, the solvents are arranged from the most positive potential range to the most negative potential range. The range in DMSO was -1.156 V to -1.180V, in MeCN was -1.220 V to -1.256 V, and in pyridine was -1.306V to -1.344 V. Potentials are averaged values, *n* = 3, a scan rate of 100 mV/s, at ambient room temperature, and under Ar (g) atmosphere.

Table 5.7: The absolute change in the redox potential of $Q/Q^{\bullet-}$ $\Delta E_{1/2}$ vs Fc^+/Fc (mV) between unsaturated, partially saturated, and fully saturated isoprenyl side chain of the same MK-*n* analog.

MK-*n* (1)	MK-*n* (2)	MeCN $\Delta E_{1/2}$, (mV)	DMSO $\Delta E_{1/2}$, (mV)	Pyridine $\Delta E_{1/2}$, (mV)
MK-1	MK-1(H_2)	20.0	21.3	23.9
MK-2	MK-2(I,II-H_4)	24.5	23.5	13.2
MK-3	MK-3(I,II,III-H_6)	17.6	17.4	4.7
MK-2	MK-2(II-H_2)	4.9	1.1	17.7
MK-3	MK-3(II-H_2)	8.2	3.5	12.7
MK-2(II-H_2)	MK-2(I,II-H_4)	29.4	22.4	30.9
MK-3(II-H_2)	MK-3(I,II,III-H_6)	25.8	20.8	17.4

These observations show that saturation of the first isoprene unit of the quinone in the fully saturated analogs requires more energy for the reduction, which generated more negative redox potentials compared to the partially saturated or unsaturated MK analogs. This effect is observed even though the saturation is several carbons away from the quinoid moiety. Accordingly, some non-covalent interactions may be inferred. Conversely, when only the second isoprene unit is saturated, the quinone is easier to reduce, resulting in more positive redox potentials, as compared to their fully saturated MK counterparts. The alkene on the second isoprene unit is several carbons away from the quinoid moiety, and one possible explanation is a through-space interaction of the isoprenyl side chain with the naphthoquinone. Indeed, MKs with longer chain lengths can fold over the quinone moiety, which we have previously reported for MK-2.[36] Since there is no conjugation within the isoprene side chain, this appears to be a viable explanation. The energy minimum structures of MK-2 in DMSO and MeCN are in a folded conformation, where the second isoprene unit folds over the ring system.[36] Preliminary data with MK-3 also show folding. Thus, the conformation of the isoprenyl side chain over the naphthoquinone moiety is accessible for the longer side chain MK analogs, and this interaction with the quinoid appears to influence the redox potentials.

The synthesis of MK-2(II-H_2) generated both *cis* and *trans* isomers. Most biological MKs have a *trans* configuration, but there are examples of *cis* isomers in bacteria such as *Mycobacterium phlei* and *Bacillus subtilis*.[2] The *trans*-MK isomers are essential to restoring oxidative phosphorylation when photoinactivation of quinones in bacteria was performed.[2] During the synthesis of MK-2(II-H_2), we were able to obtain two mixtures of the isoprenologs based on different combinations of fractions collected during column chromatography purification of the geometric isomers. Specifically, we obtained *cis*:*trans* ratios of 1:2.2 and 1:2.7; and were able to isolate the pure *trans*-MK isomer for electrochemical analysis, see supporting information section 4, for details on the purification protocol.[57] Measuring the redox potentials in the two different isomer ratios, yielded no significant difference in redox potentials in each solvent. In MeCN, the redox potentials of the 1:2.2 and 1:2.7 *cis*:*trans* isomer ratios were -1.225 and -1.223 V vs Fc^+/Fc, respectively, while in DMSO and pyridine were identical. For the purified *trans* isomer of MK-2(II-H_2), the potential in MeCN was -1.222 V vs Fc^+/Fc. These results suggest that the isomerism in the isoprenyl side chain at the first isoprene unit does not result in differences in redox potentials observed for MK-2(II-H_2).

5.4.2 Statistical comparisons with Student's t tests and principal component analysis

Principal component analysis (PCA) was used to visualize what structural properties influence the redox potentials for these MK analogs. The PCA was performed with the matrix consisting of the unaveraged Q/Q$^{\bullet-}$ redox potentials for each MK-*n* in each solvent, **Figure 5.6, Table 5.3.** The MK-*n* analogs cluster in the PCA by how their structural properties affected the measured redox potentials with PC 1 having the most influence and PC 2 having less influence. For the MK analogs studied, the extent of isoprenyl side chain saturation (percentage of variance – 88.61%) influenced PC 1. The variable which influences PC 2 (percentage of variance – 6.30%) is less clear but may be due to a combination of saturation and chain length.

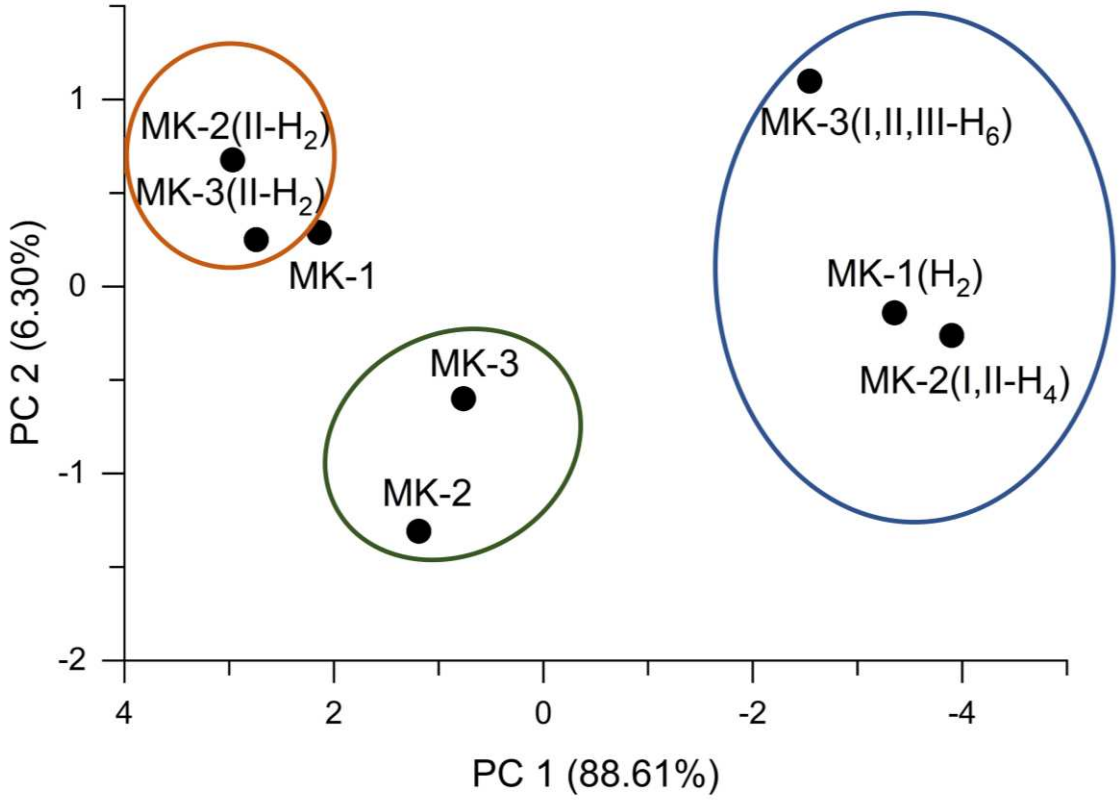

Figure 5.6: PCA from a matrix of all measured Q/Q$^{\bullet-}$ redox potentials of each MK-*n* analog in each solvent examined. Circles are drawn around the different saturation type, where the partially saturated MK-*n* analogs are in an orange circle, unsaturated analogs are in a green circle (except MK-1), and fully saturated analogs are in a blue circle.

The variability in PC 1 is based on either partial or full isoprenyl side chain saturation for truncated MK analogs. The partially saturated MK analogs cluster together to the left of PC 1, the fully saturated MK analogs cluster together to the right of PC 1, and the unsaturated MK analogs cluster together between them except for MK-1. The MK-1 analog clusters closer to the partially saturated MK analogs on PC 1, which would indicate MK-1, with only one isoprene unit, behaves differently than the other unsaturated MK analogs. As compared to the other unsaturated MK analogs, MK-1 had relatively more positive potentials in each solvent. MK-1 is distinct from the other unsaturated analogs as it is too short to fold over the naphthoquinone.[40]

When the unsaturated MK-1, MK-2, and MK-3 analogs were compared to their fully saturated counterparts MK-1(H_2), MK-2(I,II-H_4), and MK-3(I,II,III-H_6), by Student's *t* tests, the redox potentials are statistically different at 95% confidence or higher except for MK-3 vs MK-3(I,II,III-H_6) in MeCN (90%) and pyridine (80%), **Table 5.8**. When the partially saturated MK-2(II-H_2) and MK-3(II-H_2) analogs were compared to the fully saturated counterparts MK-2(I,II-H_4) and MK-3(I,II,III-H_6), the redox potentials are statistically different at the 99% confidence level or higher except for MK-3(II-H_2) vs MK-3(I,II,III-H_6) in MeCN, which was at 95%. These results agree with our hypothesis that saturation in the isoprenyl side chain on MK influences the redox potential, as we observe in the plots in **Figure 5.5** and the PCA in **Figure 5.6**. It appears that the largest contribution to the redox potential differences in the fully saturated analogs is due to the saturation of the first isoprene unit on the side chain. The partially saturated versus unsaturated MK analogs had lower significance in DMSO for MK-2 vs MK-2(II-H_2) at 60%, and for MK-3 vs MK-3(II-H_2) at 80 %, but both comparisons were 90% in MeCN and greater than 99% in pyridine. Generally, the differences in redox potential between the partially saturated and the unsaturated of the same MK-*n* in the same solvent were less than 8 mV (except in pyridine) and were more significantly different in MeCN and pyridine than in DMSO, **Table 5.7, Table 5.8**. These observations indicate that the effect of partial saturation at the second isoprene unit on MKs lessens the energy burden required to reduce the quinone that makes them easier to reduce when compared to the unsaturated or fully saturated counterparts.

Table 5.8: Highest confidence level based on Student's *t* tests of the differences of $Q/Q^{\bullet-}$ $E_{1/2}$ vs Fc^{+}/Fc based on the extent saturation of the isoprene chain for the same MK-*n* length in the same solvent environment. Those comparisons which are not statistically significant at greater than 90% are greyed out.

MK-*n* (1)	MK-*n* (2)	Solvent	Highest % CL	p (2-tail)
MK-1	MK-1(H_2)	MeCN	95	0.05
		DMSO	99.9	0.001
		Pyridine	99.9	0.001
MK-2	MK-2(I,II-H_4)	MeCN	99	0.01
		DMSO	99.8	0.002
		Pyridine	95	0.05
MK-2	MK-2(II-H_2)	MeCN	90	0.1
		DMSO	60	0.4
		Pyridine	99.8	0.002
MK-2(I,II-H_4)	MK-2(II-H_2)	MeCN	99.8	0.002
		DMSO	99.9	0.001
		Pyridine	99.8	0.002
MK-3	MK-3(I,II,III-H_6)	MeCN	90	0.1
		DMSO	99	0.01
		Pyridine	80	0.2
MK-3	MK-3(II-H_2)	MeCN	90	0.1
		DMSO	80	0.2
		Pyridine	99	0.01
MK-3(I,II,III-H_6)	MK-3(II-H_2)	MeCN	95	0.05
		DMSO	99	0.01
		Pyridine	99.8	0.002

The PC 2 seems to be influenced by both the extent of saturation, and isoprene side chain length across all the MK analogs examined. Therefore, using Student's *t* tests, we compared the MK-*n* analogs of different values of *n* with either the same or different type of saturation in the side chain, **Table 5.9**. When comparing MKs of the same type, (e.g. fully saturated, partially saturated, or unsaturated), there was less statistical confidence that the two measured redox potential values are different. For example, the fully saturated MK-1(H_2) vs MK-2(I,II-H_4) had no confidence of being different in any solvent, while MK-1(H_2) vs MK-3(I,II,III-H_6) were only statistically different in pyridine (95%), and MK-2(I,II-H_4) vs MK-3(I,II,III-H_6) were not statistically different in DMSO only (MeCN and pyridine were both 95%). Similarly, when comparing the two partially saturated analogs, MK-2(II-H_2) vs MK-3(II-H_2), the highest confidence was 90% in MeCN and DMSO, with only 80% in pyridine. Lastly, when the unsaturated MK analogs were compared, MK-1 vs MK-2 or MK-3, they had low confidences in MeCN, but 90% in DMSO and 99% in pyridine, while MK-2 vs MK-3 were only statistically different in DMSO. Conversely, when the different types of saturation (fully saturated, partially saturated, or unsaturated) are compared across different MK-*n* isoprene chain lengths,

the confidence these measurements have different redox potentials were overall much more significant, with most comparisons at greater than 90%. For example, in all solvents studied, MK-1 vs MK-2(I,II-H_4) were all statistically different at 99% or greater. Similarly, we observed significant differences in redox potentials in the following comparisons (all solvents); MK-1 vs MK-3(I,II,III-H_6) were > 90%, MK-1(H_2) vs MK-2 were > 90%, MK-2 vs MK-3(II-H_2) were > 95%, and MK-3 vs MK-2(I,II-H_4) were > 99%, **Table 5.9**. Therefore, most of the variability in PC 2 comes from the differences that arise from when both side chain length and different saturation types are considered.

Table 5.9: Highest confidence level based on Student's *t* tests of the differences of $Q/Q^{\bullet-}$ $E_{1/2}$ vs Fc^+/Fc based on differences in length and saturation of isoprene chain in the same solvent environment. Those comparisons which are not statistically significant at greater than 90% are greyed out.

MK-*n* (1)	MK-*n* (2)	MeCN Highest CL %	DMSO Highest CL %	Pyridine Highest CL %
MK-1	MK-2	70	90	99.9
	MK-2(I,II-H_4)	99	99.8	99
	MK-2(II-H_2)	70	80	95
	MK-3	50	90	99
	MK-3(I,II,III-H_6)	90	99	98
	MK-3(II-H_2)	95	0	70
MK-1(H_2)	MK-2	90	99.9	99.9
	MK-2(I,II-H_4)	70	0	0
	MK-2(II-H_2)	95	99.9	99
	MK-3	95	99.9	99.8
	MK-3(I,II,III-H_6)	0	0	95
	MK-3(II-H_2)	95	99.9	99
MK-2	MK-3	0	95	50
	MK-3(I,II,III-H_6)	90	99.8	70
	MK-3(II-H_2)	98	95	99
MK-2(I,II-H_4)	MK-3	99.9	99	99
	MK-3(I,II,III-H_6)	95	0	95
	MK-3(II-H_2)	80	99.9	99.9
MK-2(II-H_2)	MK-3	80	95	99.9
	MK-3(I,II,III-H_6)	90	99	99.9
	MK-3(II-H_2)	90	90	80

Through our statistical analysis, we conclude that the isoprene saturation type is the defining variable in our measured redox potentials of truncated MK analogs when compared against the same or differing chain lengths. The reducibility of the quinone is directly affected by the fully saturated MK analogs, requiring much more energy to be reduced, while the partially saturated MK analogs were among the easiest to reduce. Although the differences in redox potentials observed in these truncated MKs are

relatively small, they may be significant in a non-biological context as well. There are many industrial applications of quinones reported in the last decade, including quinone functionalized hybrid materials used as conducting films, electrode materials, electrochemical sensors for NADH, or as replacements for traditional battery electrolytes in flow cells.[59-65] The electrochemical reversibility of quinones and their ability to polymerize with organic and inorganic frameworks allows for their use in energy storage.[59-61, 64] Application of quinones in flow batteries and lithium batteries reduces the presence of toxic metal ions and represents an alternative cathode material. [62-63] Therefore, a complete understanding of how structural differences in the quinone isoprenyl side chain can affect their redox potentials is relevant in both biological and industrial settings.

5.4.3 Diffusion coefficients

As the CVs of all MK-*n* analogs tested were completely reversible, the double layer charge was visible, and the concentrations of MK-*n* were known (see **Table 5.1**), we could estimate the diffusion coefficients from their CVs as calculated by the Randles-Sevcik equation, **Eq. 1.15**. Each MK-*n* redox process was found to be a one-electron reduction, as determined by **Eq. 1.17**. The diffusion coefficients are listed in **Table 5.10**, with 90% confidence. We found that the diffusion coefficients are an order of magnitude larger in MeCN than in the other two solvents, but were on the order of 10^{-7} to 10^{-8} cm^2/s. These diffusion coefficients indicate that the approach of the MK-*n* analogs to the electrode surface are slow due to their size, bulkiness, and different solvation. These values do have large confidence intervals due to some outliers identified by Grubb's tests and were generally quite large in pyridine.

Table 5.10: Diffusion coefficient constants of the oxidized MK-*n* species, values are given at 90% confidence.

MK-*n*	MeCN D_o (cm^2/s)	DMSO D_o (cm^2/s)	Pyridine D_o (cm^2/s)
MK-1	1.2 ± (0.4) x 10^{-7}	2.1 ± (0.5) x 10^{-8}	4 ± (6) x 10^{-8}
MK-1(H_2)	6.6 ± (1.4) x 10^{-7}	4.2 ± (1.9) x 10^{-8}	1.8 ± (1.4) x 10^{-7}
MK-2	3.7 ± (1.6) x 10^{-7}	3.7 ± (1.7) x 10^{-8}	7 ± (6) x 10^{-8}
MK-2(I,II-H_4)	1.1 ± (0.1) x 10^{-7}	1.9 ± (0.6) x 10^{-8}	8 ± (2) x 10^{-8}
MK-2(II-H_2)	1.9 ± (0.4) x 10^{-7}	1.6 ± (0.1) x 10^{-8}	4.0 ± (0.8) x 10^{-8}
MK-3	1.2 ± (0.5) x 10^{-7}	1.2 ± (0.2) x 10^{-8}	3 ± (2) x 10^{-8}
MK-3(I,II,III-H_6)	2.1 ± (0.4) x 10^{-7}	2.3 ± (0.7) x 10^{-8}	4.6 ± (0.8) x 10^{-8}
MK-3(II-H_2)	1.3 ± (0.5) x 10^{-7}	9 ± (4) x 10^{-8}	5 ± (4) x 10^{-8}

Our studies provide information on the movement of truncated MK analogs in an organic environment. Experimental diffusion coefficients for some UQs within lipid bilayers range from 10^{-6} to 10^{-9} cm^2/s, in which this large range is dependent on the method used to determine the constant.[66] Our experimental diffusion coefficients for MKs in organic solvents are within the range of reported diffusion coefficients found in lipid bilayers for UQs. For the case of UQ-10, one such study found that for a folded conformation versus a flat-extended conformation, the diffusion coefficients were on the order of 10^{-6} and 10^{-7} cm^2/s, respectively.[67]

5.4.4 Absorption spectroelectrochemistry of MK-n analogs in MeCN and DMSO

To determine the changes in the spectroscopic signatures of the MK analogs based on the redox potential, we characterized the analogs in MeCN (**Figure 5.7**) and DMSO (**Figure 5.8**) using spectroelectrochemical absorption spectroscopy. The absorption spectra of oxidized species (black lines) shown in **Figures 5.7** and **5.8** are not under any applied potential. The quinone reduction $Q/Q^{\bullet-}$ (red lines) absorption spectra were taken at cathodic potentials $E_{pc\,1}$ vs Ag^+/Ag, **Table 5.2**. The semiquinone reduction $Q^{\bullet-}/Q^{2-}$ (blue lines) absorption spectra were taken at cathodic potentials $E_{pc\,2}$ vs Ag^+/Ag, **Table 5.2**.

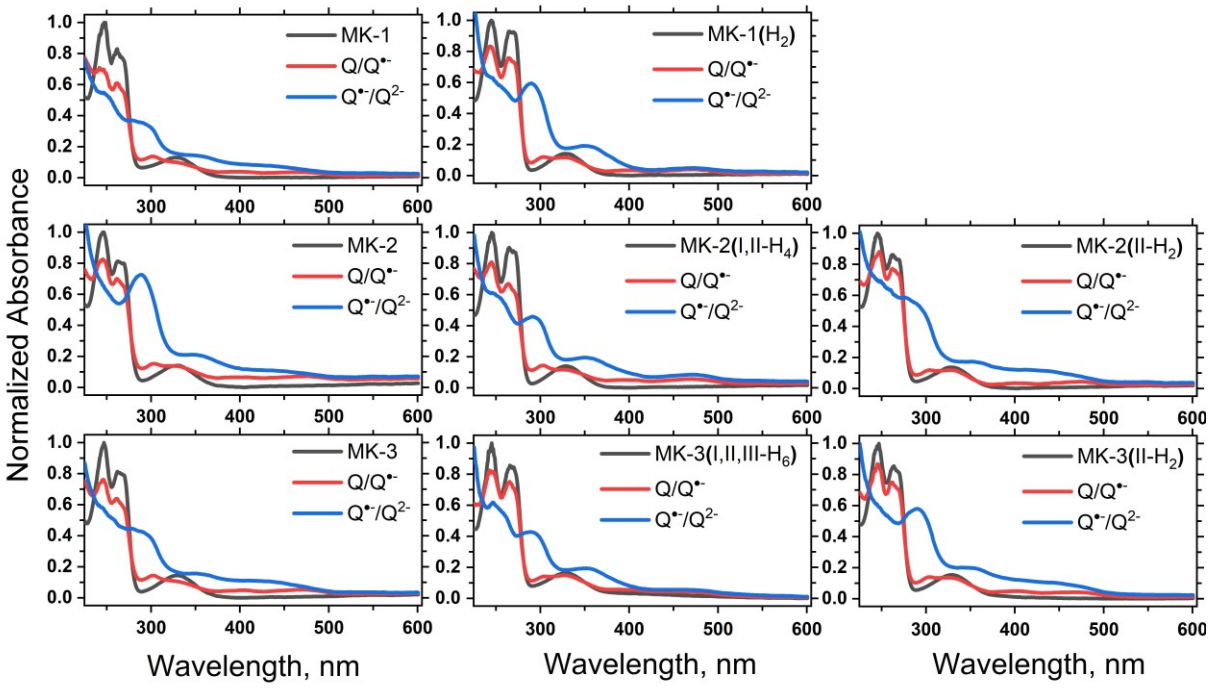

Figure 5.7: Spectroelectrochemical normalized absorption spectra of each MK-*n* analog in anhydrous MeCN.

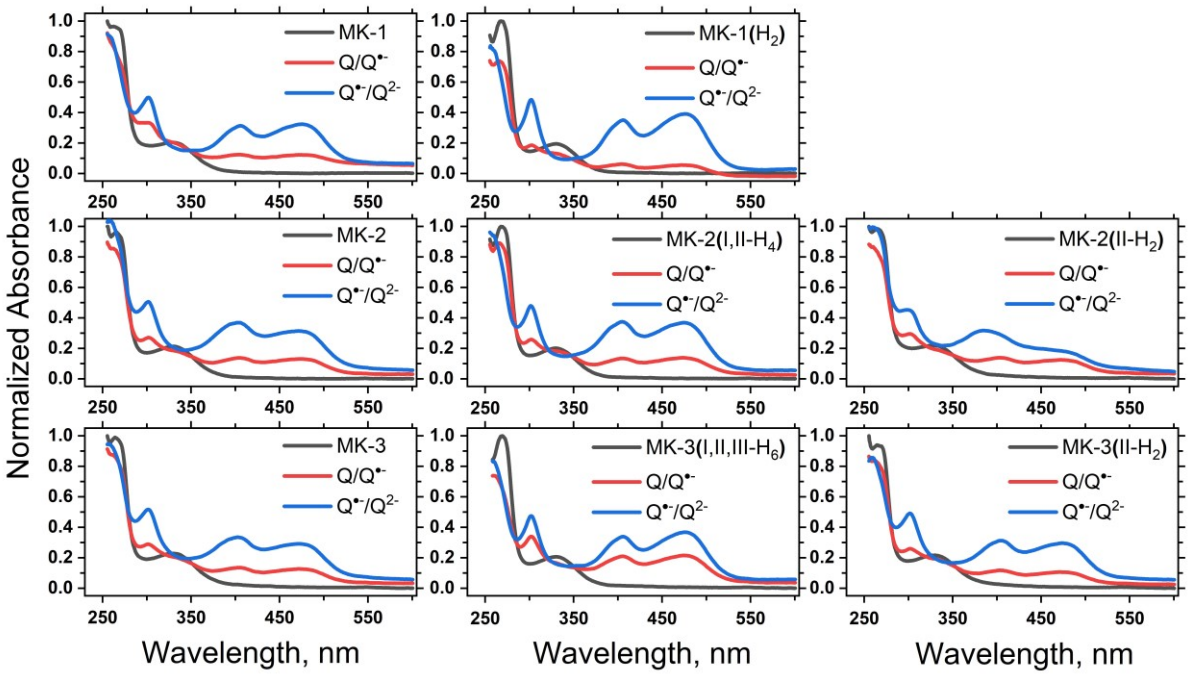

Figure 5.8: Spectroelectrochemical normalized absorption spectra of each MK-*n* analog in anhydrous DMSO.

Collectively, the MeCN spectroelectrochemistry of the MK analogs presented here appear very similar in their respective redox states, Q, $Q^{\bullet-}$, and Q^{2-}. The MK-*n* oxidized forms (black lines) have absorption peaks in the UV region observed near 250 and 265 nm, which are the strongly absorbing π-π* transitions of benzenoid and quinoid absorption (double peak character left is benzenoid, right is quinoid) respectively, while the peak at 332 nm is the weakly absorbing n-π* transition of the benzenoid.[2, 41, 68-69] Upon semiquinone and dianion reductions (red and blue lines respectively), new peaks form near 300, 350, and between 400-500 nm. As the aromaticity in the naphthoquinone is formed upon reduction to the semiquinone and dianion species, the benzenoid/quinoid peaks shift from their maxima at 250/265 nm to 300 nm and coalesce into one single peak. The n-π* transition shifts from 332 nm to 350 nm. An intramolecular charge transfer band appears near 400 – 500 nm when one of the quinoids becomes negatively charged and grows in intensity as the second is reduced (note this phenomenon is clearer in the DMSO spectra, see **Figure 5.8**). The intramolecular charge transfer of the quinoid anionic oxygen is a through bond effect from the increased conjugation of the naphthoquinone. Isosbestic points are seen in each set of MeCN spectra near 230 and 275 nm, which is the conversion of oxidized to reduced species.

In DMSO, the MK-*n* oxidized form benzenoid/quinoid π-π* transitions appear as a single peak near 270 nm and the benzenoid n-π* transition near 333 nm. Upon reduction, the benzenoid/quinoid π-π* transition peak shifts near 300 nm while the n-π* transition peak shifts near 400 nm. Unlike MeCN, the charge transfer from the reduced anionic oxygen was well resolved near 475 nm. An isosbestic point near 280 nm is the change from oxidized to reduced species, similar in MeCN. Detailed wavelength maxima of these spectra are listed in **Table 5.11**.

Table 5.11: Detailed absorption maximum wavelengths for MK-*n* analogs spectroelectrochemistry in MeCN and DMSO.

MK-*n*	MeCN $\lambda_{maximum}$ (nm)			DMSO $\lambda_{maximum}$ (nm)		
	Q	$Q/Q^{\bullet-}$	$Q^{\bullet-}/Q^{2-}$	Q	$Q/Q^{\bullet-}$	$Q^{\bullet-}/Q^{2-}$
MK-1	248, 262, 332	248, 262, 304, 401, 467	250, 300, 330-500 (broad)	266, 333	298, 405, 478	304, 407, 477
MK-1(H_2)	246, 268, 331	246, 267, 305, 332, 399, 472	299, 351, 473	271, 333	269, 304, 407, 475	303, 408, 479
MK-2	246, 266, 331	246, 263, 304, 329, 398, 475	291, 350, 436	267, 334	266, 304, 334, 406, 477	304, 405, 478
MK-2(I,II-H_4)	246, 268, 330	246, 265, 304, 327, 397, 471	249, 293, 352, 474	271, 332	269, 304, 334, 408, 475	303, 407, 476
MK-2(II-H_2)	246, 265, 332	249, 266, 306, 328, 403, 477	300, 353, 422 (broad)	267, 333	262, 304, 404, 475	301, 390, 476
MK-3	248, 265, 331	248, 263, 304, 404, 472	300, 351, 400 - 500 (broad)	267, 333	265, 304, 406, 476	304, 405, 476
MK-3(I,II,III-H_6)	245, 268, 332	248, 267, 305, 328, 392, 470	248, 292, 355, 470	271, 333	305, 408, 478	304, 408, 480
MK-3(II-H_2)	248, 265, 332	247, 264, 306, 327, 404, 471	292, 349, 443	268, 332	265, 303, 405, 476	302, 406, 477

Upon the first inspection of the absorption spectroscopy in both solvents, there seem to be no differences due to isoprenyl side chain saturation but only the redox state. The quinoid absorption bands range from 262-272 nm in various solvents, and small 2 – 10 nm bathorchromic red-shifts to longer wavelengths are observed upon saturation of the first isoprene unit.[2, 49] Indeed, when comparing the unsaturated MK-1, MK-2, and MK-3 analogs with their fully saturated counterparts MK-1(H_2), MK-2(I,II-H_4)

and MK-3(I,II,III-H_6), small bathochromic shifts between 2 to 6 nm were observed in their oxidized absorption spectra, **Table 5.12**. Similarly, these small 2 – 6 nm bathochromic shifts were also observed between the partially saturated analogs, MK-2(II-H_2) and MK-3(II-H_2), and their fully saturated counterparts, MK-2(I,II-H_4) and MK-3(I,II,III-H_6), **Table 5.12**. The relatively large redox potential changes observed based on full saturation of the isoprenyl side chain as compared to the partial/unsaturated MK analogs only resulted in very small shifts in the quinoid absorption peak. Other than these bathochromic wavelength shifts, we do not observe other changes in the spectroelectrochemistry due to the type of saturation or conformational folding. Using other more sensitive techniques such as fluorescence or infrared spectroelectrochemistry may elucidate these interactions but are not currently available to us.

Table 5.12: Quinoid absorption shifts of unsaturated versus fully saturated MK-*n* analogs.

MK-*n* Quinoid Absorption Shifts	MeCN λ, (nm)	DMSO λ, (nm)
MK-1 / MK-1(H_2)	262 / 268	266 / 271
MK-2 / MK-2(I,II-H_4)	266 / 268	267 / 271
MK-3 / MK-3(I,II,III-H_6)	265 / 268	267 / 271
MK-2(II-H_2) / MK-2(I,II-H_4)	265 / 268	267 / 271
MK-3(II-H_2) / MK-3(I,II,III-H_6)	265 / 268	268 / 271

5.5 Conclusion

The observations in this work support our hypothesis that the extent and placement of isoprene unit saturations in the side chain directly affects the redox potentials of the truncated MK-*n* analogs studied in aprotic solvents. The partially saturated MK-*n*(II-H_2) derivatives are observed in the available quinone pool for many bacterial families, including *Mycobacteria*, *Corynebacteria*, *Halobacteria*, and *Brevibacteria*. This includes the pathogenic *M. tuberculosis,* where the regiospecific partial saturation of MK-9 to MK-9(II-H_2) is carried out by the reductase, MenJ. Motivated by this observation, we pursued studies where a systematic statistical analysis approach was used to determine if there are electrochemical redox potential differences which arise from the extent and placement of saturation in the isoprene side chain.

We found that partial saturation of the second isoprene unit in truncated MK-*n* analogs generally resulted in more positive redox potentials compared to their unsaturated and fully saturated isoprenyl side chain counterparts, meaning they require less energy to reduce. The fully saturated MKs were the hardest to reduce, requiring much larger negative potentials and thus more energy than the partially or unsaturated MK analogs. The principal component analysis confirmed that the saturation type of the MK isoprenyl side chain was the defining variable in the redox potential differences analyzed. The statistical analyses and spectroelectrochemistry performed on these truncated MK analogs suggested that saturation of the first isoprene unit may influence redox potentials the most. Indeed, a lot of our observations in both the cyclic voltammetry, statistical analysis, and spectroelectrochemistry would agree that saturation of the first isoprene unit on MK does seem to influence the potentials the most and synthesis of analogs such as MK-2(I-H_2) and MK-3(I-H_2) are already being initiated in our lab to confirm these observations. These results are an important step toward understanding why the partial saturation of MK-9 to MK-9(II-H_2) is observed and conserved within pathogenic bacteria, including *M. tuberculosis*, which is responsible for the infection of one-third of the global human population and the death of ~1.3 million people annually.[70]

5.6 Unpublished work on the unsaturated MK-4, MK-7, and MK-9 analogs

The commercially available unsaturated analogs MK-4 (Sigma Aldrich), MK-7 (U.S. Pharmacopia, USP), and MK-9 (Santa Cruz Biotechnology, Inc.) were analyzed by the same methods described in this chapter. The following data were not included in the manuscript prepared for publication, as we wanted to focus on the characterization of the synthesized truncated forms of the MK-n analogs. These analogs are easier to incorporate into liposomes, for instance. A graduate student in the group, Kaitlin A. Doucette, has begun to measure the redox potentials of these analogs in liposomes, in preparation for studies with non-pathogenic *M. tuberculosis* lipid extracts. Similarly, their conformation in the liposome bilayer is to be investigated. The group is interested in measuring the redox potentials of MK-7(II-H_2) and MK-9(II-H_2) from possible synthetic routes, or more likely from purified non-pathogenic bacterial sources. Phylloquinone or MK-4 with the first isoprene unit saturated is also commercially available. As these studies continue with the Crans and Crick collaboration, these data will be published along with their partially saturated analogs.

The averaged $E_{1/2}$ vs Fc^+/Fc of each redox process of the unsaturated analogs MK-4, MK-7, and MK-9 are reported in **Table 5.13** with their standard deviations and 95% CL. The CVs of MK-4, MK-7, and MK-9 in all three solvents are given in **Figure 5.9** (concentrations are approximately 2 mM except MK-9, which is 0.5 mM). Note MK-9 was insoluble in DMSO. **Table 5.14** lists the diffusion coefficients, masses weighed, and spectroscopic cathodic peak potentials for each redox process for these analogs. The $E_{1/2}$ vs Fc^+/Fc for the $Q/Q^{\bullet-}$ processes can be added to the principal component analysis matrix. The added values for MK-4, MK-7, and MK-9 are given in **Table 5.15**. Note the values for MK-9 in DMSO are estimated from the trends observed in MeCN and pyridine. Otherwise, the PCA would not include MK-9. The PCA with all eleven analogs discussed in Chapter 5 is shown in **Figure 5.10**. A similar plot of averaged $E_{1/2}$ vs Fc^+/Fc of the first redox process compared against the solvent is with all eleven analogs is shown in **Figure 5.11.**

Table 5.13: The average $E_{1/2}$ $Q/Q^{\bullet-}$ and $Q^{\bullet-}/Q^{2-}$ vs Fc^+/Fc with standard deviations and 95% CL of MK-4, MK-7, and MK-9. Values in parentheses are not significant at 95%.

MK-*n*	Solvent	$E_{1/2}$ $Q/Q^{\bullet-}$ vs Fc^+/Fc (V)	σ (V)	95% (V)	$E_{1/2}$ $Q^{\bullet-}/Q^{2-}$ vs Fc^+/Fc (V)	σ (V)	95% (V)
MK-4	MeCN	-1.23(5)	0.007	0.018	-1.82(9)	0.029	0.073
MK-7		-1.24(1)	0.005	0.012	-1.90(0)	0.017	0.043
MK-9		-1.233	0.001	0.003	-1.83(1)	0.006	0.014
MK-4	DMSO	-1.160	0.001	0.002	-1.916	0.003	0.007
MK-7		-1.165	0.001	0.004	-1.962	0.003	0.007
MK-4	Pyridine	-1.32(7)	0.006	0.015	-2.02(0)	0.025	0.063
MK-7		-1.317	0.0002	0.0004	-2.04(1)	0.005	0.012
MK-9		-1.306	0.003	0.008	-1.96(9)	0.010	0.024

Table 5.14: The diffusion coefficients and masses weighed for MK-4, MK-7, and MK-9.

Value	Solvent	MK-4	MK-7	MK-9
D_o (cm^2/s)	MeCN	$1.5 \pm (0.4) \times 10^{-7}$	$5.5 \pm (1.0) \times 10^{-8}$	$3.7 \pm (0.3) \times 10^{-8}$
D_o (cm^2/s)	DMSO	$1.8 \pm (0.6) \times 10^{-8}$	$1.2 \pm (0.1) \times 10^{-8}$	----
D_o (cm^2/s)	Pyridine	$5.9 \pm (1.2) \times 10^{-8}$	$4.0 \pm (1.1) \times 10^{-8}$	$2.6 \pm (0.2) \times 10^{-8}$
Molecular Weight (g/mol)		444.66	649.02	785.23
Runs 1-3 (mg)	MeCN	5.0, 4.6, 4.2	6.1, 6.0, 6.4	1.3, 1.3, 1.3
Runs 1-3 (mg)	DMSO	4.4, 4.9, 4.6	5.6, 6.8, 6.0	Insoluble
Runs 1-3 (mg)	Pyridine	4.9, 4.4, 5.0	6.1, 3.2, 6.0	1.5, 1.5, 1.7

Table 5.15: The values added to the PCA matrix for MK-4, MK-7, and MK-9. The values for MK-9 in DMSO are estimates, based on the trends in the MK-7 and MK-9 in MeCN and pyridine.

MK-*n*	$E_{1/2}$ vs Fc^+/Fc (V) MeCN Run 1	$E_{1/2}$ vs Fc^+/Fc (V) MeCN Run 2	$E_{1/2}$ vs Fc^+/Fc (V) MeCN Run 3	$E_{1/2}$ vs Fc^+/Fc (V) DMSO Run 1	$E_{1/2}$ vs Fc^+/Fc (V) DMSO Run 2	$E_{1/2}$ vs Fc^+/Fc (V) DMSO Run 3	$E_{1/2}$ vs Fc^+/Fc (V) Pyridine Run 1	$E_{1/2}$ vs Fc^+/Fc (V) Pyridine Run 2	$E_{1/2}$ vs Fc^+/Fc (V) Pyridine Run 3
MK-4	-1.231	-1.230	-1.243	-1.159	-1.161	-1.159	-1.332	-1.328	-1.320
MK-7	-1.237	-1.247	-1.240	-1.165	-1.165	-1.163	-1.317	-1.317	-1.318
MK-9	-1.235	-1.233	-1.233	*-1.161*	*-1.160*	*-1.161*	-1.310	-1.305	-1.305

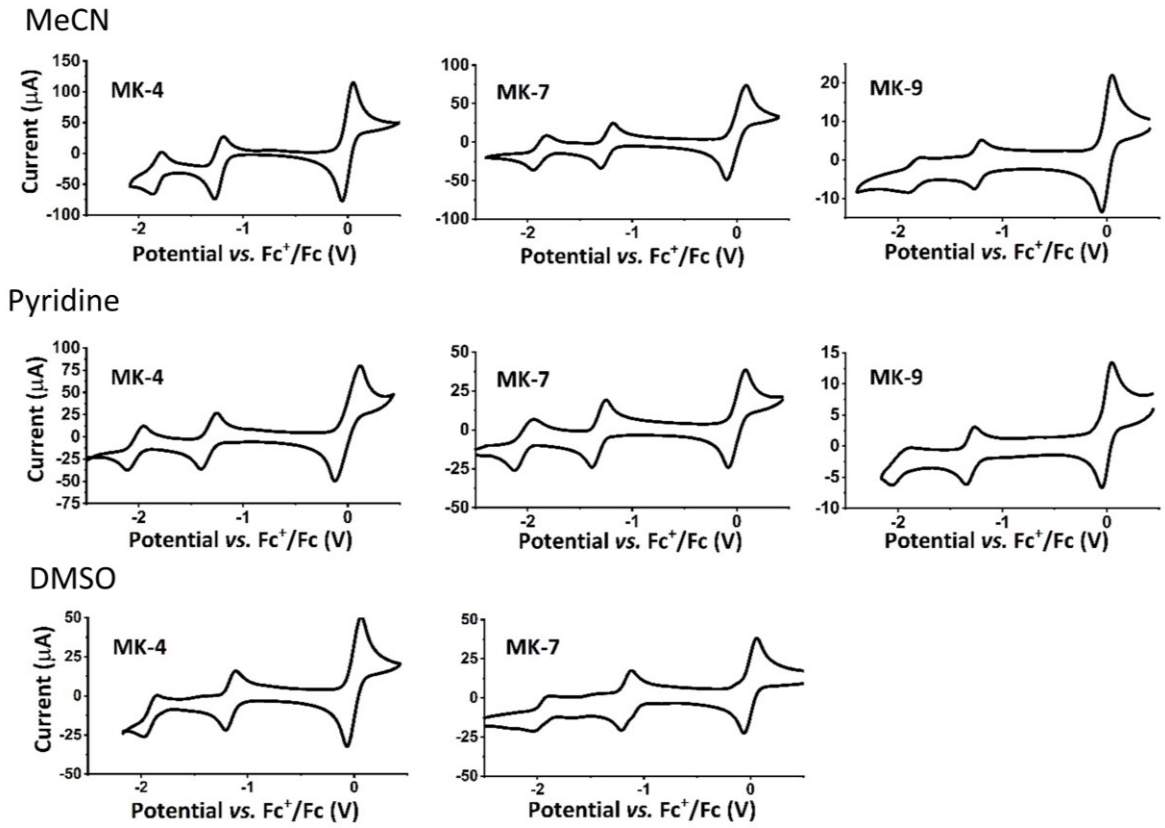

Figure 5.9: The CVs of MK-4, MK-7, and MK-9 in MeCN, DMSO, and pyridine. Samples are 2 mM in 0.1 M TBAP with 2 mM Fc except MK-9 which is 0.5 mM and 0.5 mM Fc. A scan rate of 100 mV/s was used at ambient room temperature.

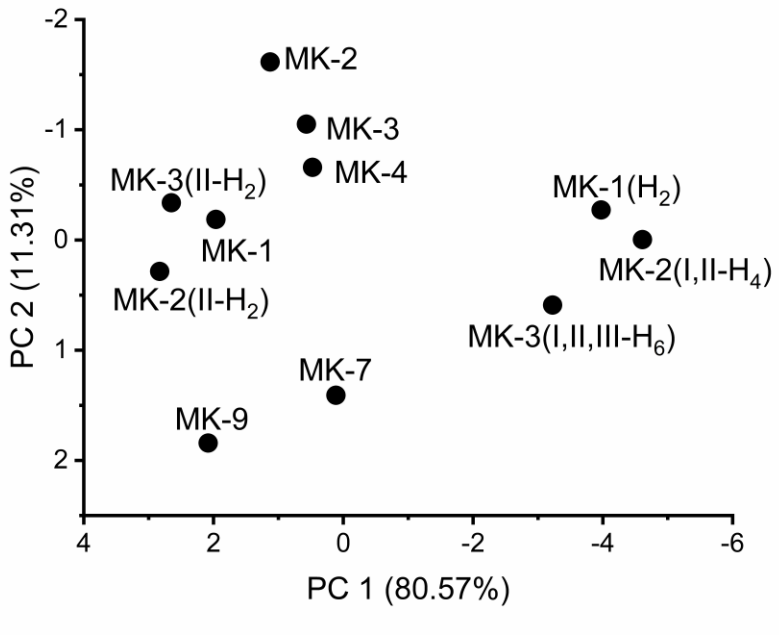

Figure 5.10: PCA with all 11 analogs analyzed.

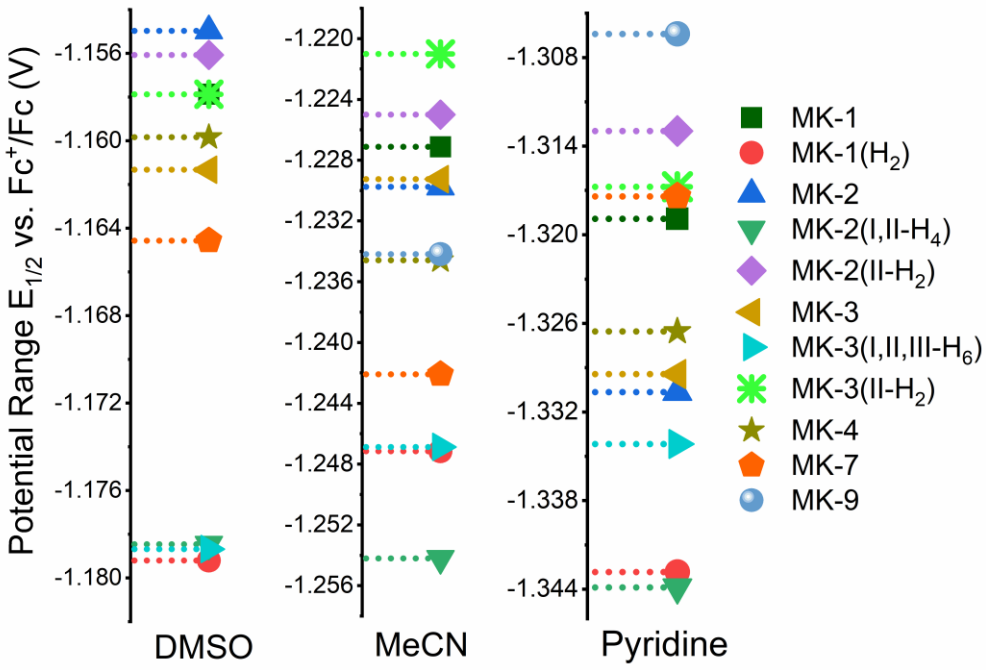

Figure 5.11: Plot of averaged $E_{1/2}$ of the first redox process all eleven analogs in each solvent, same as in **Figure 5.5** but with MK-4, MK-7, and MK-9 added.

In this expanded PCA, the same trends discussed above are still observed, and the most variability comes from the type of saturation in the isoprene tail, **Figure 5.10**. For the new analogs added, the MK-4 analog seems to follow the trends of the other unsaturated MK-2 and MK-3 analogs and clusters next to them, **Figure 5.10**. The MK-7 seems to follow the same trend; that the longer the chain length, the more negative the potential, in the more polar solvents, DMSO and MeCN, but in the non-polar solvent pyridine has a much more positive potential than MK-3 and MK-4, **Figure 5.11**. Similarly, MK-9 in MeCN has a more positive redox potential than MK-4 and MK-7, **Figure 5.11**. Most interestingly, however, MK-9 has the most positive potential of any analog in pyridine, **Figure 5.11**. The position of MK-9 in the PCA in **Figure 5.10** would suggest that it is different than the other analogs. The longer side chain MK-9 has redox potentials that are relatively more positive compared to the shorter side chain unsaturated MK-*n* analogs in the most non-polar solvent, pyridine. As pyridine was the most non-polar solvent studied and differences in the solvent have been shown to affect the isoprenyl side chain folding[36], this could directly affect the reducibility of the quinone in a through space manner. One would expect that the long aliphatic chain of lipids in cell membranes would present a similar non-polar chemical environment and may favorably influence the folding of a similar non-polar isoprenyl side chain. I predict the beta-saturated MK-9(II-H_2) will likely have a more positive redox potential than any of these analogs studied so far, especially in pyridine and other non-polar solvents. I base this prediction on how the truncated MK-2(II-H_2) and MK-3(II-H_2) behaved as well as MK-9 in these solvents. This lessening burden on the energy required to reduce the quinone may be the reason why these beta-saturated analogs are so well conserved in pathogenic bacteria.

The same statistical analyses were performed with these analogs. **Table 5.16** shows that all of the solvent comparisons of the same MK-n were greater than 99% confidence for the $Q/Q^{\bullet-}$ process and greater than 95% for the $Q^{\bullet-}/Q^{2-}$ process. The significances arise from the different dielectric constants between the solvents. **Table 5.17** shows the comparisons of different analogs in the same solvent environment. As we previously found, those comparisons which have very similar chain length and similar saturation type were less confident than when there was a differing saturation type. Similarly, when MK-4 was compared to MK-1, MK-2, MK-3, MK-7, and MK-9, the only comparisons that were different at 90% or higher were MK-2 and MK-7 in DMSO and MK-9 in pyridine. As MK-4 was an analog with a chain length in the middle of the ones examined, this is interesting that the redox potentials were so similar to all the others. However,

when MK-4 is compared to those analogs with saturations in their isoprene tails, more statistically significant differences are observed. For example, MK-2(I,II-H_4) is statistically different in all solvents at 99% or higher (except one is 95%) for MK-4, MK-7, and MK-9. Another observation is that very small chained analogs versus the long-chained analogs generally have significant differences, like MK-2 vs MK-9 in pyridine, or MK-1 vs MK-9 in both solvents. So even in this expanded PCA, the effect of chain length is likely in combination with saturations in the isoprene side chain, as concluded in the previous sections. The significant differences that arise in one solvent but not another may be due to solvent-dependent conformations as through-space interactions from the folding of the side chain over the naphthoquinone on the electrochemical band gap energies would be more likely than through-bond effects, especially in the longer-chained analogs.

Table 5.16: Highest confidence from Student's *t* tests of MK-4, MK-7, and MK-9 in different solvent environments.

MK-*n*	Solvent 1	Solvent 2	Highest % CL $E_{1/2}$ $Q/Q^{\bullet-}$ vs Fc^+/Fc	p (2-tail)	Highest % CL $E_{1/2}$ $Q^{\bullet-}/Q^{2-}$ vs Fc^+/Fc	p (2-tail)
MK-4	MeCN	DMSO	99	0.01	95	0.05
	DMSO	Pyridine	99.9	0.001	98	0.02
	MeCN	Pyridine	99.9	0.001	99.8	0.002
MK-7	MeCN	DMSO	99.8	0.002	95	0.05
	DMSO	Pyridine	99.9	0.001	99.9	0.001
	MeCN	Pyridine	99.8	0.002	99	0.01
MK-9	MeCN	Pyridine	99.9	0.001	99.9	0.001

Table 5.17: Highest confidence from Student's *t* tests of all analogs compared to MK-4, MK-7, and MK-9 in the same solvent environment. Confidences under 90% are greyed out.

MK-*n* (1)	MK-*n* (2)	MeCN Highest CL %	DMSO Highest CL %	Pyridine Highest CL %
MK-1	MK-4	70	80	80
	MK-7	95	98	80
	MK-9	95	---	98
MK-1(H_2)	MK-4	80	99.9	95
	MK-7	60	99.9	99.9
	MK-9	90	---	99.9
MK-2	MK-4	60	98	60
	MK-7	95	99.8	99
	MK-9	80	---	99.8
MK-2(I,II-H_4)	MK-4	99	99.9	95
	MK-7	99	99	99
	MK-9	95	---	99
MK-2(II-H_2)	MK-4	80	98	95
	MK-7	98	99.8	90
	MK-9	99	---	50
MK-3	MK-4	60	60	0
	MK-7	95	80	99
	MK-9	70	---	99
MK-3(I,II,III-H_6)	MK-4	80	98	80
	MK-7	50	99	98
	MK-9	80	---	99
MK-3(II-H_2)	MK-4	90	95	90
	MK-7	95	99	0
	MK-9	99.9	---	70
MK-4	MK-7	70	98	80
	MK-9	0	---	90
MK-7	MK-9	80	---	99.8

CHAPTER 5 REFERENCES

1. Beuning, C. N.; Koehn, J. T.; Crick, D. C.; Crans, D. C., Redox Potentials of Truncated Menaquinone Analogs in Aprotic Solvents are Sensitive to Saturation in the Isoprene Side Chain. **2020,** *Submitted*.

2. Dunphy, P. J.; Brodie, A. F., The Structure and Function of Quinones in Respiratory Metabolism. In *Methods in Enzymology*, Academic Press: 1971; Vol. 18, pp 407-461.

3. Upadhyay, A.; Fontes, F. L.; Gonzalez-Juarrero, M.; McNeil, M. R.; Crans, D. C.; Jackson, M.; Crick, D. C., Partial Saturation of Menaquinone in Mycobacterium tuberculosis: Function and Essentiality of a Novel Reductase, MenJ. *ACS Cent. Sci.* **2015,** *1* (6), 292-302.

4. Guin, P. S.; Das, S.; Mandal, P. C., Electrochemical Reduction of Quinones in Different Media: A Review. *Int. J. Electrochem.* **2011,** *2011*, 22.

5. Dryhurst, G., Kadish, K. M., Scheller, F., Renneberg, R., *Biological Electrochemistry*. Academic Press: New York, 1982.

6. Crane, F. L.; Low, H., Quinones in Energy-Coupling Systems. *Physiol. Rev.* **1966,** *46* (4), 662-695.

7. Cook, G. M.; Hards, K.; Dunn, E.; Heikal, A.; Nakatani, Y.; Greening, C.; Crick, D. C.; Fontes, F. L.; Pethe, K.; Hasenoehrl, E.; Berney, M., Oxidative Phosphorylation as a Target Space for Tuberculosis: Success, Caution, and Future Directions. *Microbiol. Spectrum* **2017,** *5* (3), 10.1128/microbiolspec.TBTB2-0014-2016.

8. Upadhyay, A.; Kumar, S.; Rooker, S. A.; Koehn, J. T.; Crans, D. C.; McNeil, M. R.; Lott, J. S.; Crick, D. C., Mycobacterial MenJ: An Oxidoreductase Involved in Menaquinone Biosynthesis. *ACS Chem. Biol.* **2018,** *13* (9), 2498-2507.

9. Bentley, R., Biosynthesis of Vitamin-K and Other Natural Naphthoquinones. *Pure and Appl. Chem.* **1975,** *41* (1-2), 47-68.

10. Fujimoto, N.; Kosaka, T.; Yamada, M., *Menaquinone as Well as Ubiquinone as a Crucial Component in the Escherichia coli Respiratory Chain.* InTech: 2012; p 444.

11. Nowicka, B.; Kruk, J., Occurrence, Biosynthesis and Function of Isoprenoid Quinones. *Biochim. Biophys. Acta* **2010,** *1797*, 1587-1605.

12. Hauska, G.; Hurt, E., 1 - Pool Function Behavior and Mobility of Isoprenoid Quinones. In *Function of Quinones in Energy Conserving Systems*, Trumpower, B. L., Ed. Academic Press: 1982; pp 87-110.

13. Collins, M. D.; Jones, D., Distribution of Isoprenoid Quinone Structural Types in Bacteria and Their Taxonomic Implication. *Microbiol. rev.* **1981,** *45* (2), 316-354.

14. Beulens, J. W. J.; Booth, S. L.; van den Heuvel, E. G. H. M.; Stoecklin, E.; Baka, A.; Vermeer, C., The Role of Menaquinones (Vitamin K2) in Human Health. *Br. J. Nutr.* **2013,** *110* (8), 1357-1368.

15. van der Est, A., Electron Transfer Involving Phylloquinone in Photosystem I. In *Photosystem I. Advances in Photosynthesis and Respiration*, Golbeck, J. H., Ed. Springer, Dordrecht: 2006; Vol. 24.

16. Prince, R. C.; Leslie Dutton, P.; Malcolm Bruce, J., Electrochemistry of Ubiquinones. *FEBS Letters* **1983,** *160* (1), 273-276.

17. Wawzonek, S.; Berkey, R.; Blaha, E. W.; Runner, M. E., Polarographic Studies in Acetonitrile and Dimethylformamide: III . Behavior of Quinones and Hydroquinones. *J. Electrochem. Soc.* **1956,** *103* (8), 456-459.

18. Kolthoff, I. M.; Reddy, T. B., Polarography and Voltammetry in Dimethylsulfoxide. *J. Electrochem. Soc.* **1961,** *108* (10), 980-985.

19. Peover, M. E., A Polarographic Investigation into the Redox Behaviour of Quinones: the Roles of Electron Affinity and Solvent. *J. Chem. Soc.* **1962,** (0), 4540-4549.

20. Turner, W. R.; Elving, P. J., Electrochemical Behavior of the Quinone-Hydroquinone System in Pyridine. *J. Electrochem. Soc.* **1965,** *112* (12), 1215-1217.

21. Brodsky, A. E.; Gordienko, L. L.; Degtiarev, L. S., Cathodic Reduction of Some Aromatic Compounds to Free Anion-Radicals. *Electrochim. Acta* **1968,** *13* (5), 1095-1100.

22. Eggins, B. R.; Chambers, J. Q., Electrochemical Oxidation of Hydroquinone in Acetonitrile. *J. Chem. Soc. D* **1969,** (5), 232-233.

23. Eggins, B. R., Interpretation of Electrochemical Reduction and Oxidation Waves of Quinone-Hydroquinone System in Acetonitrile. *J. Chem. Soc. D* **1969,** (21), 1267-1268.

24. Jaworski, J. S.; Leniewska, E.; Kalinowski, M. K., Solvent Effect on the Redox Potential of Quinone-Semiquinone Systems. *J. Electroanal. Chem. Interfacial Electrochem.* **1979,** *105* (2), 329-334.

25. Hart, J. P.; Shearer, M. J.; McCarthy, P. T.; Rahim, S., Voltammetric Behaviour of Phylloquinone (Vitamin K1) at a Glassy-Carbon Electrode and Determination of the Vitamin in Plasma using High-Performance Liquid Chromatography with Electrochemical Detection. *Analyst* **1984,** *109* (4), 477-481.

26. Batanero, B.; Saez, R.; Barba, F., Electroreduction of Quinones Under Aprotic Conditions. *Electrochim. Acta* **2009,** *54* (21), 4872-4879.

27. De Vries, S.; Berden, J. A.; Slater, E. C., 6 - Function and Properties of a Semiquinone Anion Located in the QH2: Cytochrome c Oxidoreductase Segment of the Respiratory Chain. In *Function of Quinones in Energy Conserving Systems*, Trumpower, B. L., Ed. Academic Press: 1982; pp 235-246.

28. Ohnishi, T.; Salerno, J. C.; Blum, H., 7 - Ubisemiquinones in Electron-Transfer Systems of Mitochondria. In *Function of Quinones in Energy Conserving Systems*, Trumpower, B. L., Ed. Academic Press: 1982; pp 247-261.

29. Swallow, A. J., 3 - Physical Chemistry of Semiquinones. In *Function of Quinones in Energy Conserving Systems*, Trumpower, B. L., Ed. Academic Press: 1982; pp 59-72.

30. Kishi, S.; Saito, K.; Kato, Y.; Ishikita, H., Redox Potentials of Ubiquinone, Menaquinone, Phylloquinone, and Plastoquinone in Aqueous Solution. *Photosynth. Res.* **2017,** *134* (2), 193-200.

31. Marchal, D.; Boireau, W.; Laval, J. M.; Moiroux, J.; Bourdillon, C., An Electrochemical Approach of the Redox Behavior of Water Insoluble Ubiquinones or Plastoquinones Incorporated in Supported Phospholipid Layers. *Biophys. J.* **1997,** *72* (6), 2679-2687.

32. Shim, Y.-B.; Park, S.-M., Spectroelectrochemical Studies of p-Benzoquinone Reduction in Aqueous Media. *J. Electroanal. Chem.* **1997,** *425* (1), 201-207.

33. Khan, M. S.; Khan, Z. H., Ab Initio and Semiempirical Study of Structure and Electronic Spectra of Hydroxy Substituted Naphthoquinones. *Spectrochim. Acta, Part A* **2005,** *61* (4), 777-790.

34. Bailey, S. I.; Ritchie, I. M., A Cyclic Voltammetric Study of the Aqueous Electrochemistry of Some Quinones. *Electrochim. Acta* **1985,** *30* (1), 3-12.

35. Pekmez, K.; Can, M.; Yildiz, A., Electrochemistry in Aprotic Solvents Containing Anhydrous Perchloric Acid: Electroreduction Behavior of Quinones. *Electrochim. Acta* **1993,** *38* (4), 607-611.

36. Koehn, J. T.; Magallanes, E. S.; Peters, B. J.; Beuning, C. N.; Haase, A. A.; Zhu, M. J.; Rithner, C. D.; Crick, D. C.; Crans, D. C., A Synthetic Isoprenoid Lipoquinone, Menaquinone-2, Adopts a Folded Conformation in Solution and at a Model Membrane Interface. *J. Org. Chem.* **2018,** *83* (1), 275-288.

37. Aguilar-Martínez, M.; Macías-Ruvalcaba, N. A.; Bautista-Martínez, J. A.; Gómez, M.; González, F. J.; González, I., Review: Hydrogen Bond and Protonation as Modifying Factors of the Quinone Reactivity. *Curr. Org. Chem.* **2004,** *8*, 1721-1738.

38. Asahi, Y., Polarographic Studies of Pharmaceuticals. I - Polarography of Naphthoquinone Derivatives. *YAKUGAKU ZASSHI* **1956,** *76* (4), 365-369.

39. Dron, P. I.; Ramešová, Š.; Holloran, N. P.; Pospíšil, L.; Michl, J., Redox Behavior of 2,3-Diamino-1,4-naphthoquinone and its N-Alkylated Derivatives. *Electroanalysis* **2016,** *28* (11), 2855-2860.

40. Koehn, J. T.; Beuning, C. N.; Peters, B. J.; Dellinger, S. K.; Van Cleave, C.; Crick, D. C.; Crans, D. C., Investigating Substrate Analogues for Mycobacterial MenJ: Truncated and Partially Saturated Menaquinones. *Biochemistry* **2019,** *58* (12), 1596 - 1615.

41. Ma, W.; Zhou, H.; Ying, Y.-L.; Li, D.-W.; Chen, G.-R.; Long, Y.-T.; Chen, H.-Y., *In Situ Spectroeletrochemistry and Cytotoxic Activities of Natural Ubiquinone Analogues*. 2011; Vol. 67, p 5990-6000.

42. Monks, T. J.; Hanzlik, R. P.; Cohen, G. M.; Ross, D.; Graham, D. G., Quinone Chemistry and Toxicity. *Toxicol. Appl. Pharmacol* **1992,** *112* (1), 2-16.

43. Morrison, L. E.; Schelhorn, J. E.; Cotton, T. M.; Bering, C. L.; Loach, P. A., 2 - Electrochemical and Spectral Properties of Ubiquinone and Synthetic Analogs: Relevance to Bacterial Photosynthesis. In *Function of Quinones in Energy Conserving Systems*, Trumpower, B. L., Ed. Academic Press: 1982; pp 35-58.

44. Prince, R. C.; Gunner, M. R.; Dutton, P. L., 1 - Quinones of Value to Electron-Transfer Studies: Oxidation–Reduction Potentials of the First Reduction Step in an Aprotic Solvent. In *Function of Quinones in Energy Conserving Systems*, Trumpower, B. L., Ed. Academic Press: 1982; pp 29-33.

45. Sakamoto, K.; Miyoshi, H.; Ohshima, M.; Kuwabara, K.; Kano, K.; Akagi, T.; Mogi, T.; Iwamura, H., Role of the Isoprenyl Tail of Ubiquinone in Reaction with Respiratory Enzymes: Studies with Bovine Heart Mitochondrial Complex I and Escherichia coli bo-Type Ubiquinol Oxidase. *Biochemistry* **1998,** *37* (43), 15106-15113.

46. Schneider, H.; Lemasters, J. J.; Hackenbrock, C. R., 3 - Lateral Diffusion of Ubiquinone in Mitochondrial Electron Transfer. In *Function of Quinones in Energy Conserving Systems*, Trumpower, B. L., Ed. Academic Press: 1982; pp 125-139.

47. Ogawa, T.; Isobe, K.; Mori, T.; Asakawa, S.; Yoshimura, T.; Hemmi, H., A Novel Geranylgeranyl Reductase from the Methanogenic Archaeon Methanosarcina Acetivorans Displays Unique Regiospecificity. *FEBS J.* **2014,** *281* (14), 3165-3176.

48. Bang, C.; Schmitz, R. A., Archaea Associated with Human Surfaces: Not to be Underestimated. *FEMS Microbiol. Rev.* **2015,** *39* (5), 631-648.

49. Gale, P. H.; Arison, B. H.; Trenner, N. R.; Page, A. C.; Folkers, K.; Brodie, A. F., Characterization of Vitamin K9(H) from Mycobacterium phlei. *Biochemistry* **1963,** *2* (1), 200-203.

50. Azerad, R.; Cyrot, M.-O.; Lederer, E., Structure of the Dihydromenaquinone-9 of Mycobacterium phlei. *Biochem. Biophys. Res. Commun.* **1967,** *27* (2), 249-252.

51. Azerad, R.; Cyrot-Pelletier, M.-O., Structure and Configuration of the Polyprenoid Side Chain of Dihydromenaquinones from Myco- and Corynebacteria. *Biochim.* **1973,** *55* (5), 591-603.

52. Tindall, B. J.; Stetter, K. O.; Collins, M. D., A Novel, Fully Saturated Menaquinone from the Thermophilic, Sulphate-reducing Archaebacterium Archaeoglobus fulgidus. *Microbiology* **1989,** *135* (3), 693-696.

53. Tindall, B. J.; Wray, V.; Huber, R.; Collins, M. D., A Novel, Fully Saturated Cyclic Menaquinone in the Archaebacterium Pyrobaculum organotrophum. *Syst. Appl. Microbiol.* **1991,** *14* (3), 218-221.

54. da Costa, M. S.; Albuquerque, L.; Nobre, M. F.; Wait, R., The Extraction and Identification of Respiratory Lipoquinones of Prokaryotes and Their Use in Taxonomy. In *Methods in Microbiology, Vol 38: Taxonomy of Prokaryotes*, Rainey, F.; Oren, A., Eds. Elsevier Academic Press Inc: San Diego, 2011; Vol. 38, pp 197-206.

55. Elling, F.; Becker, K.; Könneke, M.; Schröder, J.; Kellermann, M.; Thomm, M.; Hinrichs, K.-U., *Respiratory Quinones in Archaea: Phylogenetic Distribution and Application as Biomarkers in the Marine Environment*. 2015; Vol. 18.

56. Collins, M. D.; Pirouz, T.; Goodfellow, M.; Minnikin, D. E., Distribution Of Menaquinones In Actinomycetes and Corynebacteria *J. Gen. Microbiol.* **1977,** *100* (JUN), 221-230.

57. Koehn, J. T.; Crick, D. C.; Crans, D. C., Synthesis and Characterization of Partially and Fully Saturated Menaquinone Derivatives. *ACS Omega* **2018,** *3* (11), 14889-14901.

58. Harris, D. C., *Quantitative Chemical Analysis*. 8th ed.; W.H. Freeman and Company: USA, 2010.

59. Ahmad, A.; Meng, Q.; Melhi, S.; Mao, L.; Zhang, M.; Han, B.-H.; Lu, K.; Wei, Z., A Hierarchically Porous Hypercrosslinked and Novel Quinone based Stable Organic Polymer Electrode for Lithium-Ion Batteries. *Electrochim. Acta* **2017,** *255*, 145-152.

60. Son, E. J.; Kim, J. H.; Kim, K.; Park, C. B., Quinone and its derivatives for energy harvesting and storage materials. *Journal of Materials Chemistry A* **2016,** *4* (29), 11179-11202.

61. Sterby, M.; Emanuelsson, R.; Huang, X.; Gogoll, A.; Strømme, M.; Sjödin, M., Characterization of PEDOT-Quinone Conducting Redox Polymers for Water Based Secondary Batteries. *Electrochim. Acta* **2017,** *235*, 356-364.

62. Zhang, S.; Li, X.; Chu, D., An Organic Electroactive Material for Flow Batteries. *Electrochim. Acta* **2016,** *190*, 737-743.

63. Zhang, Y.; Murtaza, I.; Liu, D.; Tan, R.; Zhu, Y.; Meng, H., Understanding the Mechanism of Improvement in Practical Specific Capacity using Halogen Substituted Anthraquinones as Cathode Materials in Lithium Batteries. *Electrochim. Acta* **2017,** *224*, 622-627.

64. Dongmo, S.; Witt, J.; Wittstock, G., Electropolymerization of Quinone-polymers onto Grafted Quinone Monolayers: A Route Towards Non-passivating, Catalytically Active Film. *Electrochim. Acta* **2015,** *155*, 474-482.

65. Rębiś, T.; Sobczak, A.; Wierzchowski, M.; Frankiewicz, A.; Tężyk, A.; Milczarek, G., An Approach for Electrochemical Functionalization of Carbon Nanotubes/1-amino-9,10-anthraquinone Electrode with Catechol Derivatives for the Development of NADH Sensors. *Electrochim. Acta* **2018,** *260*, 703-715.

66. Galassi, V. V.; Arantes, G. M., Partition, Orientation and Mobility of Ubiquinones in a Lipid Bilayer. *Biochim. Biophys. Acta-Bioenerg.* **2015,** *1847* (12), 1560-1573.

67. Di Bernardo, S.; Fato, R.; Casadio, R.; Fariselli, P.; Lenaz, G., A High Diffusion Coefficient for Coenzyme Q10 Might be Related to a Folded Structure. *FEBS Letters* **1998,** *426* (1), 77-80.

68. Carlone, G. M.; Anet, F. A. L., Detection of Menaquinone-6 and a Novel Methyl-substituted Menaquinone-6 in Campylobacter jejuni and Campylobacter fetus subsp. fetus. *Microbiology* **1983,** *129* (11), 3385-3393.

69. Petrucci, R.; Marrosu, G.; Astolfi, P.; Lupidi, G.; Greci, L., Cyclic Voltammetry, Spectroelectrochemistry and Electron Spin Resonance as Combined Tools to Study Thymoquinone in Aprotic Medium. *Electrochim. Acta* **2012,** *60*, 230-238.

70. Glaziou, P.; Sismanidis, C.; Floyd, K.; Raviglione, M., Global Epidemiology of Tuberculosis. *Cold Spring Harbor Perspect. Med.* **2015,** *5*, a017798.

CHAPTER 6: FUTURE PERSPECTIVES

First, I would like to bring attention to the importance of collaborative work, which is realized in this dissertation. The ability to work with others from both our own institutions, our own country, and from another country is required to tackle tough research questions and is important to the advancement of chemistry. In working together, we can figure out how to combat disease and create innovative technology. We have made great strides in the method development to measure and understand very specific disease mechanisms associated with AD and TB. The works performed in this dissertation are important steps to the overall goals we first set out to achieve in the characterization of disease mechanisms in AD and TB, but much more work needs to be done in each respective field. In the following paragraphs I have discussed the necessary experiments that I believe should be performed in the future to advance our knowledge of each field.

While tryptophan fluorescence quenching has been used to determine Cu(II) binding sites in peptides for quite some time, using it to determine interpeptidic Cu(II) exchange was a new methodology we were able to provide. We were able to successfully quantify the rate constants in exchanges of small peptide complexes and motifs found in the blood. Then we were able to modify and extend that methodology to work with soluble amyloid complexes with the same small tryptophan peptides. For the interpeptidic Cu(II) exchange in amyloid peptides, extension into the full-length Aβ peptide is the next step. However, these peptides are much harder to work with, especially due to their hydrophobicity and propensity to aggregate. Special care must be employed to work with these peptides. For example, there are special treatments to remove pre-aggregates and following protocols for incubation to induce specific aggregation mechanisms to create oligomers, aggregates, or fibrils, all of which can have very different structures. Therefore, these experiments are inherently more difficult than the ones described in Chapter 3, where aggregation mechanisms were not observed. The addition of tryptophan or synthesized Cu(II)/Zn(II) sensitive fluorophores into the sequence will be expensive. Even the native Aβ peptide is thousands of dollars for milligram quantities. Therefore, I suggest these experiments with the caveat that it will likely require grant funding for this research to be performed.

Full-length Aβ peptide isoforms will need substitutions within the metal-binding domain that are sensitive to Cu(II) and Zn(II) to further study interpeptidic metal ion exchange in Aβ peptides. The Ala2 residue would be a very reasonable location for this substitution. The most logical substitutions are Trp2 or another type of Cu(II) or Zn(II) sensitive fluorophore that is attached to an amino acid base. At the very least, a Trp2 replacement would be able to measure the interpeptidic exchange between native Cu($A\beta_{1-40}$) or Cu($A\beta_{1-42}$) complex. This Trp2 replacement should be easy to incorporate and wouldn't be quite as expensive as using Cu(II) sensitive fluorophore. However, in order to measure Zn(II) interpeptidic exchange, these types of synthetic residues will have to be purchased since it cannot quench tryptophan fluorescence. With the full-length Aβ peptide, the effect of aggregation mechanisms and fibril formation on the interpeptidic Cu(II) exchange rate constants can be determined. This is probably the most important goal, as these aggregates and fibrils are where the Cu(II) and Zn(II) are localized and stored in senile plaques. There may be mechanisms that we do not know, that stabilize these metal ions when embedded within the plaques, despite the use of drugs like strong chelators or other peptides. Observing these interpeptidic exchanges within liposomes or reverse micelles could give insight into how a cellular scale can alter the kinetics. We know the synaptic cleft space is on the nanoscale. Therefore, the development of a method to measure kinetics in nanoscale models like reverse micelles is important. As we observed in Chapter 4, the effect of nanoconfinement and the partitioning of species into a membrane can affect observed metal ion coordination reactions. Therefore, these experiments should be performed once the interpeptidic Cu(II) exchange between two Aβ peptides is finally measured.

The initial binding dynamics of Cu(II) and Zn(II) to the Aβ peptide should also be tested using fast time-scale spectroscopy with metal ion photocages able to release the metal ions in bursts with temporal control through irradiation. By creating isoforms that have had residues changed near key binding sites with specific sensitive fluorophores, which have different spectroscopic signatures, the initial binding can be determined. For example, if one fluorophore emits at 360 nm and is exchanged for the N-terminus residue while another emits at 450 nm and is exchanged for the Ala2 residue, then if the initial binding is at the N-terminus, we would observe quenching only at 360 nm. Similarly, fluorophores that enhance signal upon binding could also be employed. Importantly, these fluorophores must be non-coordinating, so that the metal ion complexation is the same in the isoform used to study the initial binding dynamics. In any case,

as these metal ion coordination reactions are so fast, we only know the finalized coordination sphere, but not the initial dynamics. The experiments performed in Chapter 4 were the first steps to the realization of this type of research.

In the menaquinone research, there is still a lot to be done. The research described in Chapter 5 was the first discussion in the ample MK literature of how a regiospecific saturation of the isoprenyl side chain affected quinone its redox potentials. Most notably, partial saturation of the second (beta) isoprene unit generally leads to an easier to reduce quinone. Until now, there has been no mention of this in the literature. However, these beta-saturated MKs are highly conserved in many pathogenic bacteria. So why is that; why do these bacteria have enzymes whose sole purpose is to saturate the beta isoprene unit? We believe it is because it has a beneficial effect of requiring less energy to reduce the quinone, as our studies have indicated. Full saturation of the isoprenyl side chain of these MK analogs produced the most negative potentials in each aprotic solvent, which meant they were much harder to reduce than the other analogs. However, we still need to synthesize MK analogs with partial saturation at the first isoprene unit to confirm that it is not just an effect of the first isoprene saturation. Indeed, a lot of our observations in both the CV, statistical analysis and PCA, and spectroelectrochemistry would agree that saturation of the first isoprene unit does seem to influence the potentials the most and synthesis of analogs such as MK-2(I-H_2) and MK-3(I-H_2) are already being initiated in our lab to confirm if that is the case.

Isolation and purification of MK-9(II-H_2) from non-pathogenic *M. tuberculosis* sources should be carried out in the future as this analog is the most biologically relevant. Similarly, synthesis of other MK-*n* analogs with longer chain lengths between $n = 4 – 9$ need to be analyzed with partial and full saturation and compared to their unsaturated counterparts. However, these syntheses are not trivial, it is extremely difficult to couple the longer isoprene tails to the naphthoquinone, and often have very low yields. Other analogs like MK-6(II-H_2), MK-7(II-H_2), and MK-8(II-H_2) could be purified from many different bacterial sources, but that alone would be a large undertaking.

A similar systematic principal component analysis should be performed on the beta-saturated, fully saturated, alpha-saturated, and unsaturated analogs of MK-*n* with $n = 1 – 9$. This would mean there would need to be a total of 36 analogs created, 11 of which I have already been analyzed by electrochemistry

methods and described in Chapter 5. As most of these analogs are not commercially available, this means we are just scratching the surface of this research, as many of them would need to be synthesized. A large systematic statistical analysis would give an overall view of what structural components affect the MK redox potentials and, ultimately, their reactivity the most. While our initial studies do indicate that partial beta-saturated analogs are easier to reduce, we need more than just two analogs to confirm our hypothesis. It would be very interesting to see how the longer chained beta-saturated analogs compared to their shorter chained counterparts in terms of the ease of reducibility of the quinone. I believe that the MK-9(II-H_2) analog will have one of the most positive potentials of all the analogs. Especially since its unsaturated analog, MK-9 was so fascinatingly different than the other unsaturated analogs we were able to study, including MK-1, MK-2, MK-3, MK-4, and MK-7. This may have to do with the conformations these molecules are able to take in different environments, but more studies need to be performed to confirm the hypothesis that conformation affects redox potential.

Lastly, Kaitlin Doucette in the Crans group has worked extensively with liposomes and MKs and has been able to successfully incorporate the *n* = 1 – 3 MK-*n* analogs in liposomes made with phosphatidylcholine. Under my guidance, I was able to teach her how to perform and analyze the electrochemistry on these liposomes. The extension of my electrochemical methodology is already being used in our lab on the instrumentation that I helped procure using the NSF grant funds for our MK project. This collaboration produced a novel way to study these electron transporters in more biological media, which will undoubtedly help the Crans group to understand and extend our initial findings in aprotic media to more biologically relevant systems. While this research is currently ongoing, I will be a co-author on this work. This project also has the potential to discover the differences in the conformation of the MK structure in a lipid bilayer and their possible effects on redox potential. This would have to be done through 2D NMR techniques such as NOESY (nuclear Overhauser effect spectroscopy), which can show proton correlations on the isoprene tail having with those on the naphthoquinone.

APPENDIX A: CONTRIBUTIONS TO THE CO-AUTHORED PAPER ENTITLED "INTERACTION OF A BIGUANIDE COMPOUND WITH MEMBRANE MODEL INTERFACE SYSTEMS: PROBING THE PROPERTIES OF ANTIMALARIAL AND ANTIDIABETIC COMPOUNDS"[1]

A.1 Statement of contributions

The contributions I made to this paper were concerned with the preparation and interpretation of the 2D $^1H^1H$ NOESY NMR spectroscopy of the 1-phenylbiguanide (PBG) within reverse micelles (RMs). The following areas are only where I scientifically contributed to the paper. Figure numbers have been changed for clarity. There is a section of unpublished work associated with this content.

A.2 Experimental method contributions

A.2.1 Preparation of Aqueous Stock Solutions of 1-Phenylbiguanide (PBG)

The 100 mM PBG (0.886 g, 5.00 mmol) stock solution was prepared in deuterium oxide, D_2O (10 mL), in a volumetric flask. The solution was stirred until it was clear, and the pH of the suspension was adjusted using DCl and NaOD when needed. The pH of the solutions was measured at 25 °C on an Orion 720A+ pH meter, and these readings were converted to pD by the formula pD = pH + 0.4[2], and adjusted values are reported in this article.

A.2.2 Preparation of the 2D $^1H^1H$ NMR NOESY Sample in an AOT Reverse Micelle Solution with PBG

A w_0 = 10 sample of PBG in AOT/2,2,4- trimethylpentane was prepared with 100 mM PBG in D_2O solution with pD = 7.07 using NaOD and DCl to adjust the pH, where pD = pH + 0.4. The samples were slightly heated in a water bath up to 60 °C in order to dissolve precipitated PBG during the titration at this neutral pH. Purified AOT was used to make a 750 mM AOT solution in 2,2,4-trimethylpentane. Once the aqueous PBG and AOT in 2,2,4- trimethylpentane were mixed, the suspension was vortex mixed until the solution became transparent.

[1] Samart, N.; Beuning, C. N.; Haller, K. J.; Rithner, C. D.; Crans, D. C., Interaction of a Biguanide Compound with Membrane Model Interface Systems: Probing the Properties of Antimalaria and Antidiabetic Compounds. *Langmuir* **2014,** *30* (29), 8697-8706

A.2.3 2D NOESY NMR Spectroscopy

$^1H^1H$ NOESY NMR experiments were performed on a 400 MHz Agilent Inova NMR spectrometer. The NOESY data were acquired with a 4500 Hz window for protons in t2 and t1. The NOESY mixing time was 200 ms, and 32 transients were acquired per increment. The total recycle time between transients was 1.85 s. The data set consisted of 1332 complex points in t2 by 200 complex points in t1 using States-TPPI. Cosine-squared weighting functions were matched to the time domain in both t1 and t2, and the time domains were zero-filled prior to the Fourier transform. The final resolution was 2.2 Hz/pt in F2 and 8.8 Hz/pt in F1. Data processing was done using the Agilent VNMRJ-3.2D software.

A.3 Results and discussion contributions: 1-Phenylbiguanide (PBG) in an AOT RM 2D NOESY Study

To further characterize the interactions of PBG with AOT/2,2,4-trimethylpentane in this model membrane system, we employed 2D NMR NOESY to investigate the location of the drug in the RM system.[3-5] The structures of PBG and AOT are given in **Figure A.1**. Specifically, we characterized the interaction of the solution of 100 mM PBG at neutral pH (pD = 7.07) in 750 mM AOT using 2D ^1H NOESY. Since the NOESY spectra shown in **Figure A.2** are for studies carried out on samples prepared from a solution of PBG at neutral pH, the Ha signal was found to be different from those shown at w_0 = 10 at basic or acidic pH. This effect will be investigated at a later time but suffice it to say that for the series at basic pH, corresponding line broadening was observed at the lower w_0 values.

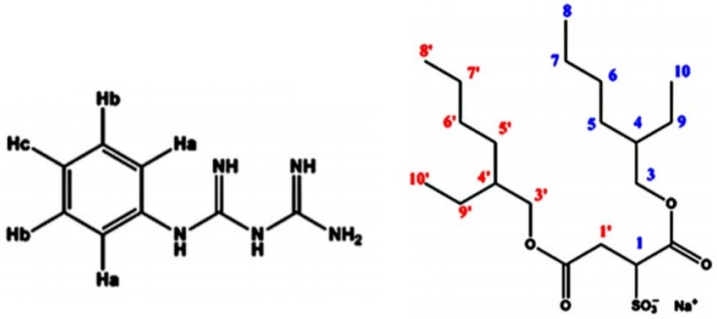

Figure A.1: Structure of 1-phenylbiguanide (left) and AOT (right) and their aromatic proton assignments for NMR analysis.

As shown in **Figure A.2**, the partial 2D spectrum in the F2 frame is a close-up of phenyl protons Ha (2H, 7.57 ppm), Hb (2H, 7.32 ppm), and Hc (1H, 7.06 ppm) along with a broad H peak, which is the N−H signal (6.82 ppm) in PBG. The F1 frame is the full spectrum including a HOD peak (1H, 4.60 ppm), a

broad and large peak of 2,2,4-trimethylpentane at 1.01 ppm, and especially the side-arm-chain methylene protons of AOT, which show an overlapping signal in AOT (4H, 1.41 ppm, 9,9′ as labeled in **Figure A.1**). The diagonal (solid line) is present to emphasize the two different scales of the sides on the 2D spectrum. As expected, there are intense cross-peaks between Ha and Hb as well as between Hb and Hc from PBG, and these signals demonstrate that the protons are near each other. A weaker cross-peak between Ha and Hc was also observed. The cross-peak between Ha and Hc is weak in comparison to the cross-peak for Ha and Hb, indicating that these protons are not as close.

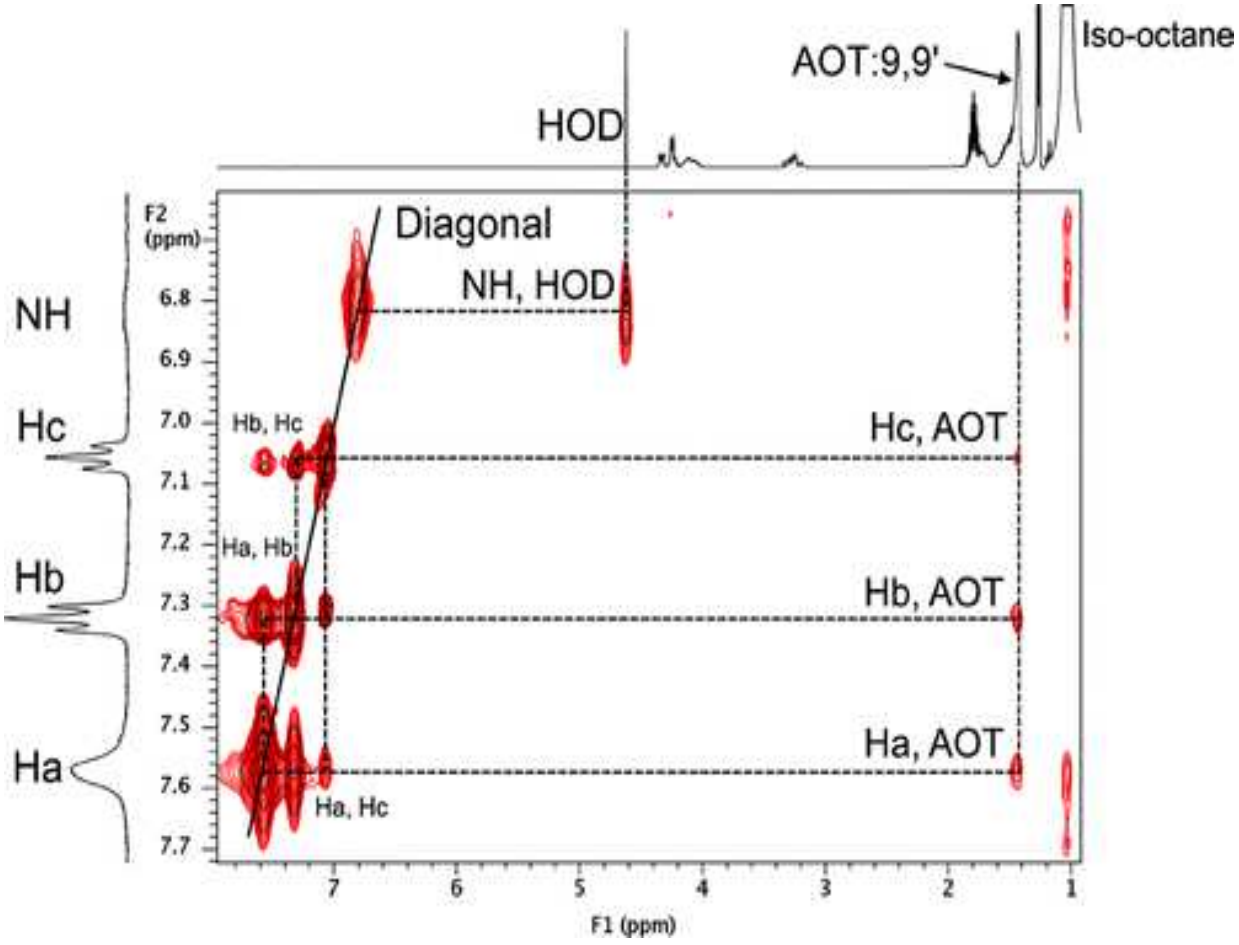

Figure A.2: Partial ^{1}H NMR NOESY spectrum of 100 mM PBG at pD (= pH + 0.4) 7.07 in 750 mM AOT. The spectrum was recorded at 400 MHz using the parameters detailed in the Experimental Section. The F2 or y-axis is enlarged for the phenyl and nitrogen protons in PBG, and the F1 or x-axis is the full spectrum. The diagonal is the solid line, and prominent cross-peaks are shown as dotted lines along with their respective hydrogen interactions.

The intense cross-peaks of Ha and Hb, as well as those of Hb and Hc, show that these protons are close together, which is expected. Phenyl protons Ha, Hb, and Hc all have weak cross-peaks with the 9,9′-methylene protons of AOT. Prominent cross-peaks between the PBG and signals in AOT are indicated by dashed lines. The Hb and Ha protons can interact with the 9,9′-methylene protons in the backbone of the AOT tails; this peak is at approximately 1.41 ppm on AOT. As shown in **Figure A.2**, the weak cross-peak with the 9,9′-methylene AOT protons with Ha and Hb indicates the positioning of the molecule in the interface; Hc will interact less with these methylene protons. The lack of a cross-peak of Ha, Hb, and Hc with the HOD signal at approximately 4.60 ppm shows that the phenyl group is less likely to interact with the water pool. Presumably, the phenyl group protons are mainly interacting with the AOT methylene protons since there is a defined cross-peak with AOT. Thus, this portion of the PBG is nestled high in the interface of the RMs.

Finally, an intense cross-peak to the NH signal was observed and traced to HOD. As seen in **Figure A.1,** PBG has multiple NH groups, and their signal is very broad, which is an indication that the relaxation times (t1 and t2) are very short and different from those of the phenyl protons. However, in the 2D spectrum, we see a very intense NH signal along the diagonal and an intense cross-peak with HOD, indicating a close association between the NH protons and the HOD protons in the water pool. Although it is possible that some water molecules could penetrate the interface, the interaction observed between the NH and HOD protons is very strong, suggesting that this interaction of HOD and NH protons is only expected if these groups are in or very near the water pool. The lack of an NH cross-peak with any AOT protons also suggested that this part of the PBG is nestled inside the water pool.

Since the 2D NOESY studies suggested that part of the PBG molecule resides in the water pool, we carried out preliminary differential FTIR studies confirming that PBG affects the H bonding in the water pool of the RMs.[6] These studies characterized AOT/2,2,4-trimethylpentane RMs by comparing spectra in the absence and presence of 5% HOD. Differential FTIR spectra were recorded for RM samples with 100% H_2O and RMs containing 5% HOD at pH ~7.0 and 10 and 100 mM PBG in AOT RMs with w_0 = 10. These spectra were then subtracted to produce the resulting spectrum of OD stretching. Preliminary differential FTIR spectra confirmed the conclusion obtained by NMR spectroscopy studies that part of the PBG resides in the AOT RM water pool, as expected for an amphiphilic molecule.

In conclusion, PBG interacts both with the hydrophobic and hydrophilic parts of the interface as well as HOD in the water pool. This study shows an example of a probe that extends into both the interface and the water pool. NMR spectroscopy results show that the chemical shift for the phenyl protons in PBG changes, which is consistent with penetration into the interface.

The NOESY experiments furthermore show that the NH groups on the biguanide interact, consistent with the PBG molecule residing at the interface and extending deep into the hydrophobic part as well as in the water pool at the same time. The preliminary IR spectroscopy results show that the biguanide group in PBG significantly affects the hydrogen bonding present among the water molecules in the water pool. These results are consistent with the model illustrated in **Figure A.3**.

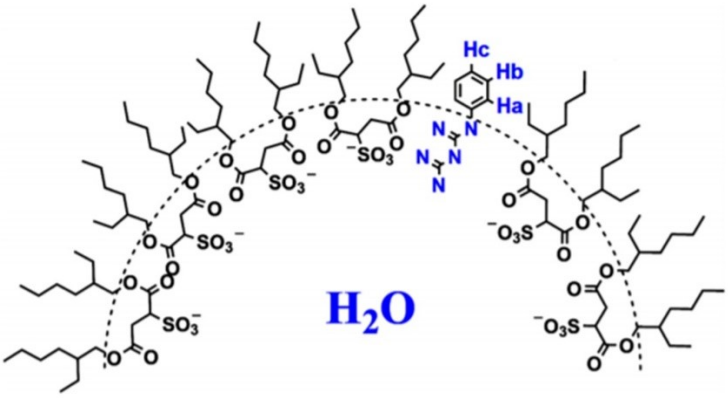

Figure A.3: Cartoon illustrating the suggested location of 1-phenylbiguanide in the AOT reverse micelle. H_2O is actually D_2O within the reverse micelle water pool.

A.4 Unpublished work using a small volume percent of deuterated cyclohexane within 2,2,4-trimethylpentane as the NMR deuterium lock instead of D_2O to enable the use of H_2O in the reverse micelle water pool.

We were interested in using water and not heavy water within the reverse micelles to study peptide kinetics and mechanisms associated with the Aβ peptide. This is because D_2O has been found to stabilize proteins and can affect folding, commonly referred to as the deuterium isotope effect.[7] Since deuterium can exchange with hydrogen easily, the R-D bond is much stronger than an R-H bond. Proteins that are susceptible to misfolding and metal chelation may not act chemically similar in a deuterium rich environment

as compared to an aqueous one.[7] Specifically, deprotonation mechanisms that are important for Cu(II) or Zn(II) coordination to peptides may be significantly harder if deuterium is bound instead of hydrogen. Some of the amino acid side chains and the amide backbone protons can exchange with deuterium and then would not be able to deprotonate to allow for metal binding. Thus, using D_2O in the water pool would not be suitable for 2D NOESY NMR studies of protein mechanisms like those described.

One way to avoid isotope exchange would be to use H_2O in the water pool and not D_2O, but this requires an alternate deuterium lock for the NMR magnet. The use of d_{12}cyclohexane as the organic solvent would be a good alternative. However, cyclohexane RMs tend to be smaller in size than those in 2,2,4-trimethylpentane (isooctane).[8] Unfortunately, larger RM sizes do not form in cyclohexane, and in order for Aβ peptides to fit, a larger RM size is needed. Some simulation studies done in RMs of $A\beta_{16-22}$ used $w_o = 6$ for a 7 residue peptide.[9] Therefore, a $w_0 = 20 – 30$ RM size would be needed for $A\beta_{1-16}$, for example. A small volume percent of d_{12}cyclohexane in isooctane solvent should not alter the AOT RM self-assembly as it should stay in the organic phase and is a suitable deuterium source to lock the NMR. By only using between 1- 5 % of d_{12}cyclohexane to the AOT/isooctane solution, we can lock the NMR and not affect the overall self-assembly of the AOT molecules with the isooctane solvent. The number of AOT molecules that aggregate is known for each w_0 size; therefore, it also determines its radius. The HOD or H_2O chemical shift peak is very sensitive to its environment, especially at small w_0 size, where the water pool is less bulk like.[10-11] Previous studies showed that the HOD peak shifts upfield from the bulk aqueous solution chemical shift since the environment of the water is changing drastically.[11] If these chemical shifts are the same in RMs prepared in both ways, then the self-assembly of these RMs is likely not affected.

First, ^{1}H NMR studies of small RM sizes, $w_o = 0$, 1, 3, and 5 with 1%, 2.5%, and 5% (v/v) d_{12}cyclohexane were performed to consider if the presence of d_{12}cyclohexane significantly altered the H_2O peak chemical shift (HOD in D_2O pools), **Figure A.4**. Previous studies done with AOT showed that the HOD peak of D_2O water pools had a chemical shift of 3.63, 3.88, and 4.23 ppm for w_o of 0, 1, and 5, respectively, **Table A.1**.[10] For d_{12}cyclohexane in 1%, 2.5% and 5% (v/v) systems of AOT/isooctane/H_2O the chemical shift of H_2O for w_o of 0, 1, and 5 were all approximately 3.63, 3.77, and 4.19 ppm, respectively, **Table A.1**. Slight variations in the chemical shift were observed. The most changed shift was $w_o = 1$ with a 0.11 ppm difference. The other w_o sizes were consistent with the literature values.[8] The water peak shift is most

affected in small RM sizes, and as the RM grows in size, the water pool becomes more bulk-like.[11] Thus, if there were any errors in the addition of this small amount of water (w_o = 1) into the RM sample preparation, for instance, from a poorly calibrated pipette, it would have large effects on the chemical shift. Since these values are consistently about 0.11 ppm difference across the three different w_o sizes, it is likely that there is a difference in the addition of water compared to previous studies. Since RM size is based on the number of water molecules added to the sample, and there is no variability in the change in chemical shift, I believe this is a pipette measurement error, resulting in a slightly different sized RM. Since all shifts are relatively close to the literature values, this would indicate that the water chemical environment is very nearly the same with or without the added d_{12}cyclohexane and thus the RMs are being formed.

Table A.1: ^{1}HNMR studies of H_2O chemical shift (ppm) change due to environmental changes from NaAOT RM size and d_{12}cyclohexane volume as compared to known literature values of HOD.

w_o	Known HOD ppm, NaAOT RMs	1% (v/v) d_{12}cyclohexane, H_2O ppm	2.5% (v/v) d_{12}cyclohexane, H_2O ppm	5.0% (v/v) d_{12}cyclohexane, H_2O ppm
0	3.63	3.63	3.63	3.63
1	3.88	3.75	3.77	3.77
3	---	4.02	4.02	4.02
5	4.23	4.19	4.19	4.20

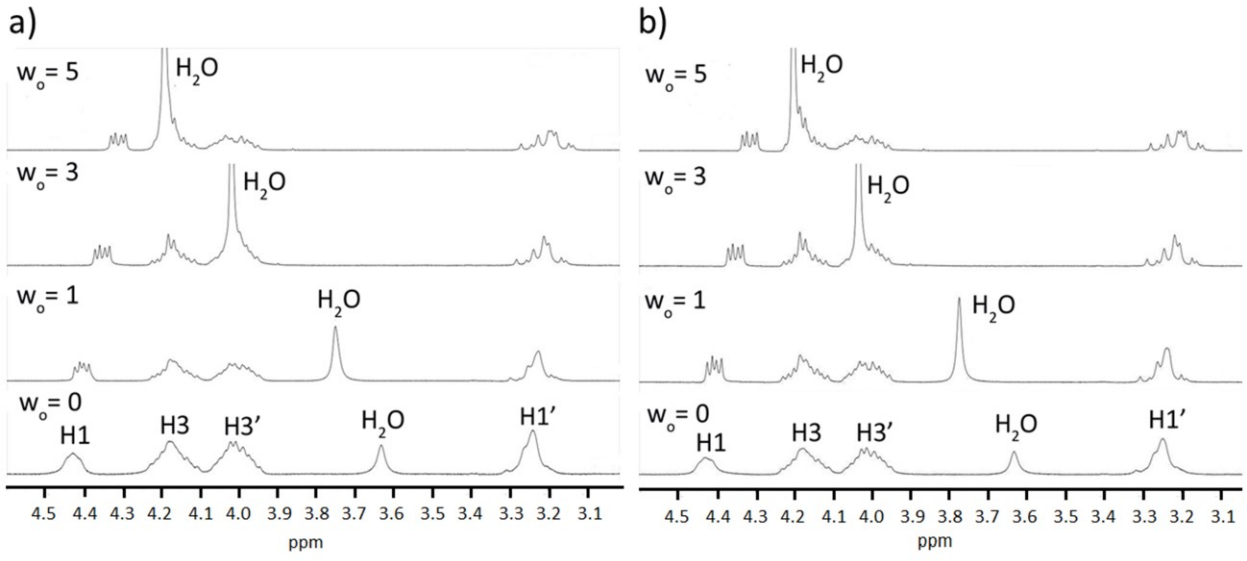

Figure A.4: The ^{1}HNMR spectra of AOT/isooctane/H_2O with a) 1 % (v/v) and b) 5 % (v/v) d_{12}cyclohexane. Performed on a 400 MHz Aligent Inova NMR, 256 scans, at 25°C.

The next question to answer would be how much d_{12}cyclohexane is needed to lock the NMR. As seen in **Figure A.4** and listed in **Table A.1**, the 1%, 2.5%, and 5% (v/v) d_{12}cyclohexane resulted in almost identical H_2O chemical shifts for the respective w_o sizes. This would indicate that a 1% (v/v) volume can lock the NMR and not interfere with the self-assembly of the RMs.

Figure A.2 shows the previous ^{1}H NOESY NMR spectrum of PBG in a w_0 = 10 RM but in D_2O at a pD of 7.07. The N-H peak was not observed in this spectrum due to isotope exchange but had an intense cross-peak of N-H with HOD was observed. Using this method with H_2O in the water pool, isotope exchange with deuterium is not observed, and a broad N-H peak is seen in the 1D ^{1}HNMR, **Figure A.5**. This broadness is expected as the relaxation time of N-H protons is much longer than C-H protons and thus does not have time to relax back down before being excited again.

As previously interpreted from **Figure A.2**, the internal references of the Ha, Hb, and Hc protons are also observed in the spectra shown in **Figure A.5**. These protons are near in space for NOE transfer and thus will show cross-peaks with one another. They have distinct similarities in intensity, as previously stated. Where the closest protons Ha-Hb and Hb-Hc have very intense cross-peaks, while the Ha-Hc cross-peak intensity is weaker. Also, as previously observed, they have distinct similarities in intensity with their AOT 9, 9' cross-peaks. The intense NH-H_2O is also familiar and expected, as the majority of the biguanide moiety should sit within the water pool. The intensity of the H_2O peak is expected and can be dampened using the NMR software. But this was not necessary for the proof-of-concept studies performed here.

This leaves the two new cross-peaks not observed previously. The NH-AOT and the Ha-H_2O cross-peaks are new observations in the cyclohexane addition. It is likely that the PBG can move within the interface, meaning that it is not statically anchored, and some RMs may have PBG molecules that have deeper interfacial or water pool penetration than others. This means that N-H protons closest to the phenyl ring can come into range of the AOT protons. Similarly, since Ha is close to the biguanide moiety, it can come into the range of some of the water protons. Why, then, are these interactions not observed with the D_2O pool? One reason could be that the small amount of HOD found when pure D_2O is used as the polar phase does not penetrate the interface like normal water can or is not in a large enough concentration to produce an NOE transfer.

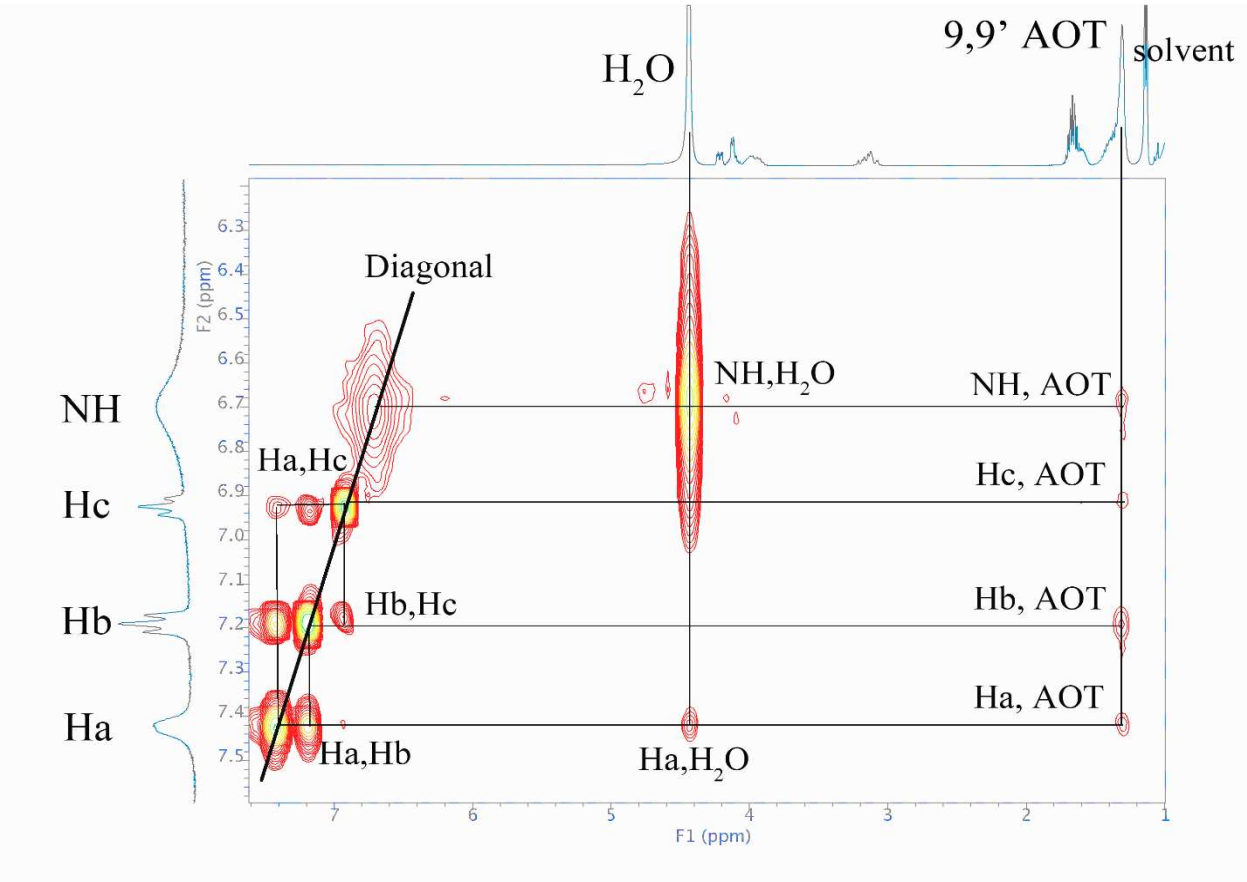

Figure A.5: The 2D ^{1}H NOESY plot of 0.08 M PBG, pH = 7.03, w_0 = 10 in 0.75 M AOT in isooctane, and 5 % (v/v) d_{12}cyclohexane. The diagonal and cross-peaks are identified. Note the solvent is isooctane. No Hc-H_2O peak exists as no overlap of signals can be distinguished, and no underlying signal is seen under the water cross-peak. The experiment was performed with the same parameters as in **Figure A.2**.

In summary, this method verified that PBG resides embedded into the interface of the RM just as our published work described, as envisioned in **Figure A.3**. The phenyl ring embeds into the AOT part of the interface, and the protonated biguanide moiety penetrates the water pool. Thes studies show the addition of d_{12}cyclohexane does not alter the expected spectra of this known system or the self-assembly of the RMs. In fact, using the deuterated cyclohexane gives a better descriptive picture of this dynamic system because the use of deuterium oxide is not needed. The effects of isotope exchange are not observed, and discrete observations such as the two NOE transfer that were not previously observed were clear in the RMs with H_2O water pools.

APPENDIX A REFERENCES

1. Samart, N.; Beuning, C. N.; Haller, K. J.; Rithner, C. D.; Crans, D. C., Interaction of a Biguanide Compound with Membrane Model Interface Systems: Probing the Properties of Antimalaria and Antidiabetic Compounds. *Langmuir* **2014,** *30* (29), 8697-8706.

2. Glasoe, P. K.; Long, F. A., Use of Glass Electrodes to Measure Acidities in Deuterium Oxide 1,2. *The Journal of Physical Chemistry* **1960,** *64* (1), 188-190.

3. Chen, J.; van Praag, H. M.; Gardner, E. L., Activation of 5-HT3 Receptor by 1-phenylbiguanide Increases Dopamine Release in the Rat Nucleus Accumbens. *Brain Research* **1991,** *543* (2), 354-357.

4. Crans, D. C.; Trujillo, A. M.; Bonetti, S.; Rithner, C. D.; Baruah, B.; Levinger, N. E., Penetration of Negatively Charged Lipid Interfaces by the Doubly Deprotonated Dipicolinate. *J. Org. Chem.* **2008,** *73* (24), 9633-9640.

5. Sedgwick, M.; Cole, R. L.; Rithner, C. D.; Crans, D. C.; Levinger, N. E., Correlating Proton Transfer Dynamics To Probe Location in Confined Environments. *J. Am. Chem. Soc.* **2012,** *134* (29), 11904-11907.

6. Moilanen, D. E.; Levinger, N. E.; Spry, D. B.; Fayer, M. D., Confinement or the Nature of the Interface? Dynamics of Nanoscopic Water. *J. Am. Chem. Soc.* **2007,** *129* (46), 14311-14318.

7. Kushner, D. J.; Baker, A.; Dunstall, T. G., Pharmacological uses and perspectives of heavy water and deuterated compounds. *Canadian Journal of Physiology and Pharmacology* **1999,** *77* (2), 79-88.

8. Maitra, A., Determination of size parameters of water-Aerosol OT-oil reverse micelles from their nuclear magnetic resonance data. *The Journal of Physical Chemistry* **1984,** *88* (21), 5122-5125.

9. Martinez, A. V.; Małolepsza, E.; Rivera, E.; Lu, Q.; Straub, J. E., Exploring the role of hydration and confinement in the aggregation of amyloidogenic peptides Aβ16−22 and Sup357−13 in AOT reverse micelles. *The Journal of Chemical Physics* **2014,** *141* (22), 22D530.

10. Stahla, M. L.; Baruah, B.; James, D. M.; Johnson, M. D.; Levinger, N. E.; Crans, D. C., 1H NMR Studies of Aerosol-OT Reverse Micelles with Alkali and Magnesium Counterions: Preparation and Analysis of MAOTs. *Langmuir* **2008,** *24* (12), 6027-6035.

11. Baruah, B.; Roden, J. M.; Sedgwick, M.; Correa, N. M.; Crans, D. C.; Levinger, N. E., When Is Water Not Water? Exploring Water Confined in Large Reverse Micelles Using a Highly Charged Inorganic Molecular Probe. *J. Am. Chem. Soc.* **2006,** *128* (39), 12758-12765.

APPENDIX B: CONTRIBUTIONS TO THE CO-AUTHORED PAPER ENTITLED "A SYNTHETIC ISOPRENOID LIPOQUINONE, MENAQUINONE-2, ADOPTS A FOLDED CONFORMATION IN SOLUTION AND AT A MODEL MEMBRANE INTERFACE"[1]

B.1 Statement of contributions

My contributions to this manuscript included the electrochemical analysis of the MK-2 in the aprotic solvents. The MK-2 redox potentials were also included in the Chapter 5 analysis. Figure numbers have been changed for clarity. Figure B.1 and Table B.1 were originally in the supporting information.

B.2 Experimental contributions

All electrochemistry was performed on a CHI 750D potentiostat. For the cyclic voltammetry (CV), a classical three-electrode system was used with a scan rate of 100 mV/s at 22 °C. The working electrode was a glassy carbon electrode (BASi MF2012, 3 mm), and the counter electrode was a platinum wire electrode (BASi MW1032). The Ag^+/Ag reference electrode (BASi MW1085) was constructed by inserting a Ag wire into a freshly prepared solution of organic solvent (CH_3CN, DMSO, or pyridine) with 0.1 M TBAP and 0.01 M $AgNO_3$.

B.3 Results and discussion contributions: Electrochemistry of MK-2 in Different Solvents

Our interest in these systems relates to the fact that the redox potential of MK is important in shuttling electrons between protein complexes. Although the focus of this manuscript has been on the conformations of these compounds, we are particularly interested in redox properties because we are aiming to investigate the function of these systems as well. For MKs to carry out this process, MKs must associate with the transmembrane proteins involved in the electron-transfer processes.[2] The electron-transfer processes all take place within or near the membrane interface with two one-electron reduction processes sequentially forming the radical anion (semiquinone) and then the dianion.[3-5] Even though there have been many reports in the literature on the redox potentials of MK derivatives, the origin of these changes is not well understood.[3-5] These processes are particularly poorly understood when the quinones

[1] Koehn, J. T.; Magallanes, E. S.; Peters, B. J.; Beuning, C. N.; Haase, A. A.; Zhu, M. J.; Rithner, C. D.; Crick, D. C.; Crans, D. C., A Synthetic Isoprenoid Lipoquinone, Menaquinone-2, Adopts a Folded Conformation in Solution and at a Model Membrane Interface. *J. Org. Chem.* **2018,** *83* (1), 275-288.

are present in a hydrophobic molecule that is entirely or partly located in the membrane of a biological system. Although it is premature to correlate conformation with redox potential, we are seeking systematic information where redox potentials and conformations are known (i.e., within different organic solvents) and the electrochemical data on this system becomes an important frame of reference because the conformational analysis has been carried out. We hypothesized that the redox potential of MK-2 will vary based on the organic solvent environment.

Although this hypothesis would be anticipated to be confirmed, it is important to measure how and if the magnitude of the redox potential changes as the solvent environment changes because the function of MK-2 is tied to the redox potentials. Initially, redox studies were planned to be carried out in DMSO, acetonitrile, and benzene; however, because of the low solubility of all of the electrolytes examined in benzene, benzene was replaced with pyridine as a representative aromatic solvent.[6] The electrolyte tetrabutylammonium perchlorate (TBAP) was chosen because 1D ^{1}H NMR studies showed that the addition of TBAP to MK-2 solutions (solvents: d_6-DMSO, d_5-pyridine, d_3-acetonitrile) did not affect the observed chemical shifts of the MK-2 protons, and thus no evidence for artifacts due to ion-pairing would be observed (see Supporting Information – section B.4 for further description of the electrochemical analysis, and see **Figure B.4** for MK-2/TBAP NMR studies).

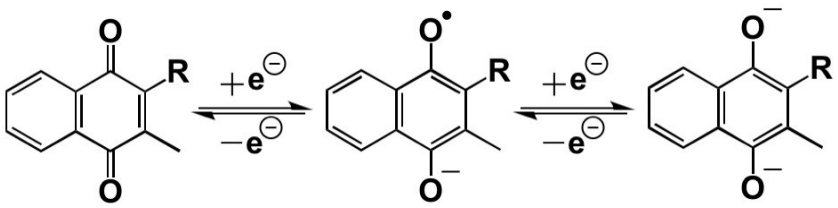

Figure B.1: Illustration of the one electron reduction of the quinone (Q) to the semiquinone radical anion ($Q^{\bullet-}$) and the second one electron reduction to the dianion (Q^{2-}). The R is n = 2 isoprene units.

MK-2's first electrochemical potential is the one-electron reduction of the quinone to semiquinone ($Q/Q^{\bullet-}$), and the second is the one-electron reduction of the semiquinone to the dianion ($Q^{\bullet-}/Q^{2-}$), **Figure B.1**.[3-5] The cyclic voltammogram's (CVs) of MK-2 and an internal standard of ferrocene (Fc^{+}/Fc) in three organic solvents are shown in **Figure B.2**. The $Q/Q^{\bullet-}$ $E_{1/2}$ vs Fc^{+}/Fc for MK-2 in DMSO, CH_3CN, and pyridine were measured to be −1.155 (±0.001) V, −1.230 (±0.003) V, and −1.331 (±0.001) V, respectively, **Table B.1**. As shown in **Figure B.2**, we included the Fc^{+}/Fc reference in the data presented. These results are

consistent with $Q/Q^{\bullet-}$ $E_{1/2}$ vs Fc^+/Fc values given for 1,4-naphthoquinone.[3, 7] The values determined experimentally for $Q^{\bullet-}/Q^{2-}$ $E_{1/2}$ vs Fc^+/Fc for MK-2 in DMSO, CH_3CN, and pyridine were measured to be −1.863 (±0.008) V, −1.902 (±0.012) V, and −2.075 (±0.003) V, respectively (**Table B.1**). In **Figure B.3**, the half-wave potentials are plotted, showing the trend that both redox processes are more readily reduced in DMSO than CH_3CN or pyridine similar to the trend observed in literature for 1,4-naphthoquinone potentials.[7]

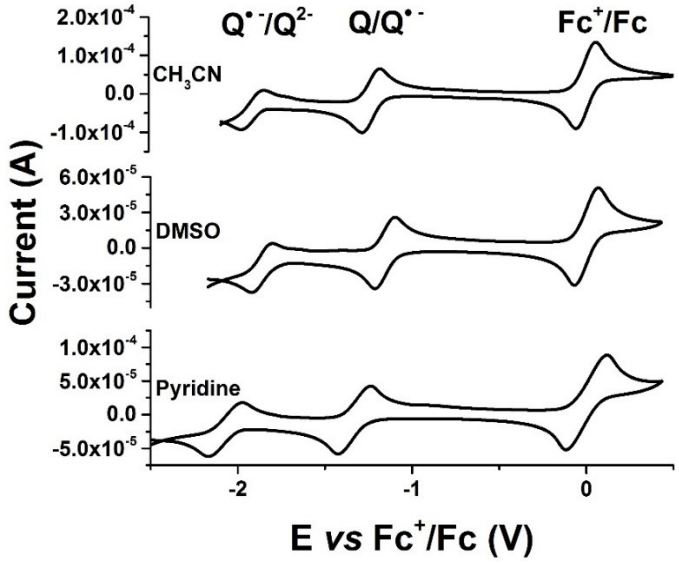

Figure B.2: Three representative CVs of 2 mM MK-2 in CH_3CN, DMSO, and pyridine. The potentials are referenced to the Fc^+/Fc couple (2 mM) determined in each solvent. From left to right, redox processes are $Q^{\bullet-}/Q^{2-}$, $Q/Q^{\bullet-}$, and Fc^+/Fc. Each sample has 0.1 M TBAP and was degassed with argon gas for 10 min at ambient room temperature before spectra were recorded. Current sweeps are in the anodic direction from −2 V to 1 V and back to −2 V. A 100 mV scan rate was used.

Table B.1: Averaged half-wave potentials of MK-2 in organic solvents. The $E_{1/2}$ potential measurements were done in triplicate. A Student's *t* test analysis determined that the $E_{1/2}$ of $Q/Q^{\bullet-}$ and $Q^{\bullet-}/Q^{2-}$ are statistically different in each solvent. All comparisons were at $p<0.0001$ except the $Q^{\bullet-}/Q^{2-}$ CH_3CN vs DMSO which was, $p<0.01$.

Solvent	$Q/Q^{\bullet-}$ $E_{1/2}$ V vs Fc^+/Fc	$Q^{\bullet-}/Q^{2-}$ $E_{1/2}$ V vs Fc^+/Fc
CH_3CN	-1.230 ± 0.003	-1.902 ± 0.012
DMSO	-1.155 ± 0.001	-1.863 ± 0.008
Pyridine	-1.331 ± 0.001	-2.075 ± 0.003

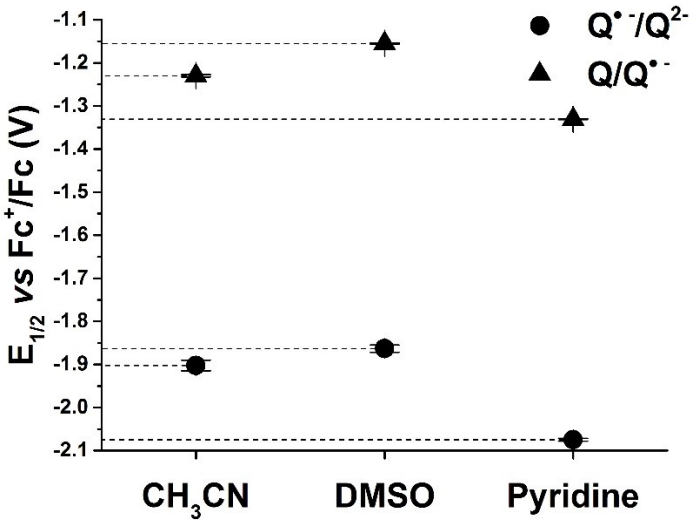

Figure B.3. Measured $E_{1/2}$ (vs Fc^+/Fc in V) of MK-2 $Q/Q^{\bullet-}$ and $Q^{\bullet-}/Q^{2-}$ redox processes vs solvent. Added lines show the distinction between each solvent for each redox process. Each solvent was run in triplicate with error bars shown. Student's *t* test indicated the half wave potentials of each redox process are significantly different in each solvent ($p < 0.01$ for $Q^{\bullet-}/Q^{2-}$ CH_3CN-DMSO and $p < 0.0001$ for all other comparisons).

In summary, during the first electrochemical process producing the semiquinone, MK-2 has the most positive potential in DMSO and the most negative potential in pyridine, showing MK-2 is slightly more reducible in DMSO than pyridine or CH_3CN. The observation of different redox potentials between organic solvents supports the second hypothesis that the redox potential of MK-2 is influenced by the specific organic solvent, where a contributing factor to the observed changes is due to the differences between the dielectric constant of each solvent. The different organic solvents influence the observed redox potential of MK-2, and from the 2D NMR studies on the conformation of MK-2, slight differences in conformation were observed, which may suggest that a combination of solvent effect and conformational differences of MK-2 may affect the redox potential.

B.4 Supporting information contributions

B.4.1 Electrochemistry experimental methods

Instrumentation and electrode preparations. All electrochemistry was performed on a CHI 750D potentiostat. For the cyclic voltammetry (CV), a classical three-electrode system was used with a scan rate of 100 mV/s at 22 °C in an air-conditioned. The glassy carbon working electrode (BASi MF2012, 3 mm) was lightly polished between runs with alumina powder then rinsed with water and ethanol. The platinum

wire counter electrode (BASi MW1032) was gently polished between runs with 600 grit sandpaper. The Ag^+/Ag reference electrode (BASi MW1085) was constructed by using the Ag wire gently polished with 600 grit sandpaper inserted into a freshly prepared solution of organic solvent (CH_3CN, DMSO, or pyridine) with 0.1 M tetrabutylammonium perchlorate (TBAP) and 0.01 M $AgNO_3$ as has been reported for other studies with quinones.[8]

Experimental procedures. Electrochemistry measurements were carried out in organic solvents (dried over molecular sieves) and are often done using a reference redox system to standardize the measurements.[9-10] Ferrocene (Fc) oxidation potential varies little between solvents and is used as a standard. To document this process, we show the redox wave for the Fc^+/Fc couple in our CV. Before the CV spectra were recorded, the reference electrode equilibrated in the 2 mM MK-2 with 2 mM Fc in the same organic solvent for 10 minutes with bubbling argon gas to degas any O_2. All half-wave potentials recorded were referenced to the Fc^+/Fc couple in the respective solvent, this was achieved by subtracting the Fc^+/Fc couple from calculated half wave potentials. After drying the solvent of water, the Fc^+/Fc couple against the Ag^+/Ag couple in CH_3CN, DMSO and pyridine was measured in quadruplicate and the Fc^+/Fc half-wave potential versus Ag^+/Ag couple in CH_3CN was 0.080 ± 0.006 V in DMSO 0.171 ± 0.002 V and in pyridine 0.563 ± 0.003 V. We determined that the presence of Fc did not alter any redox potentials of MK-2 by running CVs in the presence and absence of Fc. Current sweeps begin in the anodic direction and run from -2V to a minimum of 1V and back to -2V even though the sweeps shown in Figure 5 are only shown to about 0.5V.

Analysis. The half wave potentials were calculated using **Eq. 1.12,** where E_{pc} and E_{pa} are the cathodic and anodic peak potentials, respectively. The i_{pc} and i_{pa} were measured manually with a ruler on the CVs in cm to determine reversibility as all ratios approached unity, see **Table B.2**. The number of electrons in each process was determined using **Eqs. 1.16** and **1.17**, where ΔE_p is the difference between cathodic and anodic peak potentials and where x is the adjustment factor for the Ohmic drop that can be seen in low conductivity solvents and was determined by setting the internal standard ferrocene number of electrons as n=1 as the ΔE_p in non-aqueous solvents can differ from 0.059 V for one electron. The two-tailed p-values of the $E_{1/2}$ comparisons in each solvent for each redox process were determined using the mean, standard deviations, and triplicate measurements with the software program GraphPad.

Table B.2. Peak current ratios i_{pc}/i_{pa} and number of electrons (*n*) of MK-2 $Q/Q^{\bullet-}$ and $Q^{\bullet-}/Q^{2-}$ redox processes.

Process	Solvent	i_{pc}/i_{pa}	*n*
$Q/ Q^{\bullet-}$	ACN	0.9	1
	DMSO	1	1
	Pyridine	0.9	1
$Q^{\bullet-}/Q^{2-}$	ACN	0.9	1
	DMSO	0.8	1
	Pyridine	0.9	1

B.4.2 1D ^{1}H NMR spectra of MK-2 with the electrolyte TBAP

^{1}H NMR spectra of MK-2 with and without electrolyte (TBAP) were recorded to investigate if the electrolyte was associating with the MK-2 derivative and impact the electrochemical potential. TBAP was chosen because the addition of TBAP to MK-2 solutions in each solvent did not affect the observed chemical shifts of the MK-2 protons, and thus no evidence for ion-pairing was found (see **Figure B.4**). Samples prepared with and without TBAP (0.1 M) in either d_6-DMSO, d_3-acetonitrile, or d_5-pyridine with ~15 mg of MK-2. This was done to determine if the presence of 0.1 M TBAP affected the observed chemical shifts of protons in MK-2.

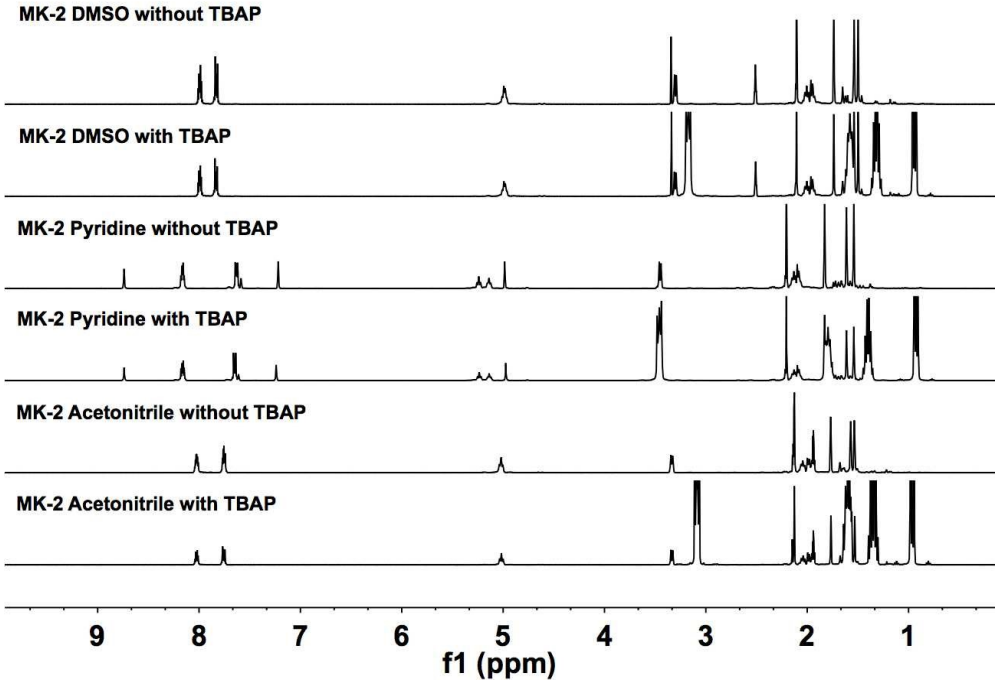

Figure B.4: 1D ^{1}H NMR (400 MHz) spectra of MK-2 with and without TBAP (0.1 M) at room temperature in d_6-DMSO, d_5-pyridine, d_3-acetonitrile. The spectra were referenced by internal TMS at 0.00 ppm.

B.4.3 Electrochemical results, interpretation, and discussion

The electrochemistry of MK-2 in three different organic solvents (DMSO, CH_3CN, and pyridine) was examined to determine if the organic solvent environment affected the redox potential of MK-2. Experiments to measure the reduction reaction of MK-2 in benzene were unsuccessful due to the electrolyte's low solubility in benzene and, therefore, low conductivity in this benzene.[11] Pyridine was chosen as a suitable replacement for benzene because it is aromatic and has similar properties. 1D ^{1}H NMR studies of MK-2 were carried out in solvents with and without the electrolyte present, to define the best conditions to carry out the redox chemistry. The electrolyte tetrabutylammonium perchlorate (TBAP) was chosen because the addition of TBAP to MK-2 solutions in each solvent did not affect the observed chemical shifts of the MK-2 protons and thus no evidence for ion-pairing was found (see above and **Figure B.4**).

MK-2's first electrochemical potential is the one-electron reduction of the quinone to semiquinone ($Q/Q^{\bullet-}$) and the second is the one-electron reduction of the semiquinone to the dianion ($Q^{\bullet-}/Q^{2-}$), **Figure B.1**.[3-5] The cyclic voltammogram's (CV's) of MK-2 in each solvent are shown in **Figure B.2**. The Fc^+/Fc couple $E_{1/2}$ is set to zero as all potentials were referenced to the internal standard. The $Q/Q^{\bullet-}$ peak current is larger than that of the $Q^{\bullet-}/Q^{2-}$, which has been attributed to the repulsion of the semiquinone from the diffusion layer of the working electrode.[12] The lower concentration of semiquinone at the electrode surface results in lower current produced, as shown by the Nernstian equation.

There can be various problems associated with the electrochemical measurements of quinones in organic solvents that can influence the half-wave potential observed. The major issues that are negligible for the system we used include: inter- and intra-molecular hydrogen bonding from solvent or hydroxyl groups on the quinone, ion-pair formation from Lewis acid cations of the electrolyte or from pyridinium ions, the working electrode adhesion of hydroquinone (QH), and from interactions of MK-2 with the internal standard.[3-5, 7, 12-17] The water or acidic proton content greatly impacts the electrochemical potential of the semiquinone $Q^{\bullet-}/Q^{2-}$ process, while the quinone $Q/Q^{\bullet-}$ process is unaffected.[3-5, 12, 16] As the solvent's water or acidic proton concentration increases, the concentration of hydroquinone increases. This shifts the observed semiquinone half-wave potential to more positive potentials until only one two-electron wave is observed.[4-5, 12, 16] Therefore, the greater standard deviations in the $Q^{\bullet-}/Q^{2-}$ half-wave potentials are

consistent with the inherent water in the solvent even after distillation and drying over activated molecular sieves.

The values determined for MK-2 in each solvent agree with the literature values of substituted 1,4-naphthoquinones. The literature values for the 1,4-naphthoquinone in DMSO, CH_3CN, and pyridine are $Q/Q^{\bullet-}$ $E_{1/2}$ vs Fc^+/Fc of -1.06V, -1.08V, and -1.19 V, respectively.[7] The addition of a methyl substituent lowers the $Q/Q^{\bullet-}$ $E_{1/2}$ by ~70 mV while the addition of an isoprenyl unit lowers it by an additional 50-60 mV.[7] In **Figure B.3**, the half-wave potentials are plotted showing the trend that the $Q/Q^{\bullet-}$ reduction is easier in DMSO than CH_3CN or pyridine. This trend is also observed in the 1,4-naphthoquinone potentials for the $Q/Q^{\bullet-}$ process in the three solvents.[7] In summary, a clear solvent effect (contributing factor is the change in the solvent's dielectric constant) on redox potential is demonstrated with MK-2.

APPENDIX B REFERENCES

1. Koehn, J. T.; Magallanes, E. S.; Peters, B. J.; Beuning, C. N.; Haase, A. A.; Zhu, M. J.; Rithner, C. D.; Crick, D. C.; Crans, D. C., A Synthetic Isoprenoid Lipoquinone, Menaquinone-2, Adopts a Folded Conformation in Solution and at a Model Membrane Interface. *J. Org. Chem.* **2018,** *83* (1), 275-288.

2. Lancaster, C. R. D.; Haas, A. H.; Madej, M. G.; Mileni, M., Recent Progress on Obtaining Theoretical and Experimental Support for the "E-Pathway Hypothesis" of Coupled Transmembrane Electron and Proton Transfer in Dihaem-containing Quinol: Fumarate Reductase. *Biochim. Biophys. Acta-Bioenerg.* **2006,** *1757* (8), 988-995.

3. Prince, R. C.; Leslie Dutton, P.; Malcolm Bruce, J., Electrochemistry of Ubiquinones. *FEBS Letters* **1983,** *160* (1), 273-276.

4. Guin, P. S.; Das, S.; Mandal, P. C., Electrochemical Reduction of Quinones in Different Media: A Review. *Int. J. Electrochem.* **2011,** *2011*, 22.

5. Dryhurst, G., Kadish, K. M., Scheller, F., Renneberg, R., *Biological Electrochemistry*. Academic Press: New York, 1982.

6. Luder, W. F.; Kraus, P. B.; Kraus, C. A.; Fuoss, R. M., Properties of Electrolytic Solutions. XVII. The Conductance of Some Salts in Benzene and Dioxane. *Journal of the American Chemical Society* **1936,** *58* (2), 255-258.

7. Jaworski, J. S.; Leniewska, E.; Kalinowski, M. K., Solvent Effect on the Redox Potential of Quinone-Semiquinone Systems. *J. Electroanal. Chem. Interfacial Electrochem.* **1979,** *105* (2), 329-334.

8. Izutsu, K., Chapter 6: Reference Electrodes for Use in Nonaqueous Solution. In *Handbook of Reference Electrodes*, Inzelt, G.; Lewenstam, A.; Scholz, F., Eds. Springer: 2013; pp 145-188.

9. Gritzner, G.; Kuta, J., Recomendations on Reporting Electrode Potentials in Nonaqueous Solvents. *Pure and Appl. Chem.* **1984,** *56* (4), 461-466.

10. Gagne, R. R.; Koval, C. A.; Lisensky, G. C., Ferrocene as an Internal Standard for Electrochemical Measurements. *Inorg. Chem.* **1980,** *19*, 2854-2855.

11. Luder, W. F.; Kraus, P. B.; Kraus, C. A.; Fuoss, R. M., Properties of Electrolytic Solutions. XVII. The Conductance of Some Salts in Benzene and Dioxane. *J. Am. Chem. Soc.* **1936,** *58* (2), 255-258.

12. Wawzonek, S.; Berkey, R.; Blaha, E. W.; Runner, M. E., Polarographic Studies in Acetonitrile and Dimethylformamide: III . Behavior of Quinones and Hydroquinones. *J. Electroanal. Chem. Soc.* **1956,** *103* (8), 456-459.

13. Eggins, B. R.; Chambers, J. Q., Electrochemical Oxidation of Hydroquinone in Acetonitrile. *J. Chem. Soc. D* **1969,** (5), 232-233.

14. Fujinaga, T.; Izutsu, K.; Nomura, T., Effect of metal ions on the polarographic reduction of organic compounds in dipolar arrotic solvents. *J. Electroanal. Chem.* **1971,** *29* (1), 203-209.

15. Hart, J. P.; Shearer, M. J.; McCarthy, P. T.; Rahim, S., Voltammetric Behaviour of Phylloquinone (Vitamin K1) at a Glassy-Carbon Electrode and Determination of the Vitamin in Plasma using High-Performance Liquid Chromatography with Electrochemical Detection. *Analyst* **1984,** *109* (4), 477-481.

16. Kolthoff, I. M.; Reddy, T. B., Polarography and Voltammetry in Dimethylsulfoxide. *J. Electrochem. Soc.* **1961,** *108* (10), 980-985.
17. Turner, W. R.; Elving, P. J., Electrochemical Behavior of the Quinone-Hydroquinone System in Pyridine. *J. Electrochem. Soc.* **1965,** *112* (12), 1215-1217.

APPENDIX C: CONTRIBUTIONS TO THE CO-AUTHORED PAPER ENTITLED "INVESTIGATING SUBSTRATE ANALOGUES FOR MYCOBACTERIAL MENJ: TRUNCATED AND PARTIALLY SATURATED MENAQUINONES" [1]

C.1 Statement of contribution

I performed the electrochemical measurements, analysis, and interpretation in this manuscript. Figure and table numbers have been changed for clarity. Please see Chapter 5 and section B.2 for electrochemical methods as they are the same.

C.2 Results and discussion contributions: Reactivity of MK-1 and MK-1(H_2) in Different Organic Solvents: Electrochemistry.

To determine the effect of saturation of the MK isoprenyl side chain on the quinone redox potential, we used cyclic voltammetry to measure the redox potentials of MK-1 and MK-1(H_2). Both MK-1 and MK-1(H_2) have two reversible single electron redox processes, the first is the quinone to semiquinone ($Q/Q^{\bullet-}$) and the second is the semiquinone to the dianion ($Q^{\bullet-}/Q^{2-}$) (**Figure 5.1**). The half-wave potentials for each redox process $Q/Q^{\bullet-}$ and $Q^{\bullet-}/Q^{2-}$ in each solvent for MK-1 and MK-1(H_2) are listed in **Table 5.5**, and cyclic voltammograms (CVs) are shown in **Figure C.1** (also in Chapter 5, but this figure was in the published manuscript). The electrolyte, tetrabutylammonium perchlorate (TBAP), was chosen because of the excellent solubility in all organic solvents. Furthermore, the addition of TBAP to MK-1 solutions in each solvent did not affect the observed chemical shifts of the MK-1 hydrogens, and thus no evidence for ion-pairing or association was found (see **Figure C.2**). The water content of the solvents can affect the semiquinone $Q^{\bullet-}/Q^{2-}$ process as acidic hydrogens influence hydroquinone production, which results in potentials that approach the quinone $Q/Q^{\bullet-}$ half-wave potentials and therefore, we only compared the first redox process, $Q/Q^{\bullet-}$ in our analyses.[2-3] Thus, it was important that we carried out our electrochemical

[1] Koehn, J. T.; Beuning, C. N.; Peters, B. J.; Dellinger, S. K.; Van Cleave, C.; Crick, D. C.; Crans, D. C., Investigating Substrate Analogues for Mycobacterial MenJ: Truncated and Partially Saturated Menaquinones. *Biochemistry* **2019,** *58* (12), 1596 - 1615.

experiments in anhydrous aprotic organic solvents as this issue is then avoided, and organic solvents more closely resemble the native MK environment within a cellular membrane compared to aqueous solutions.

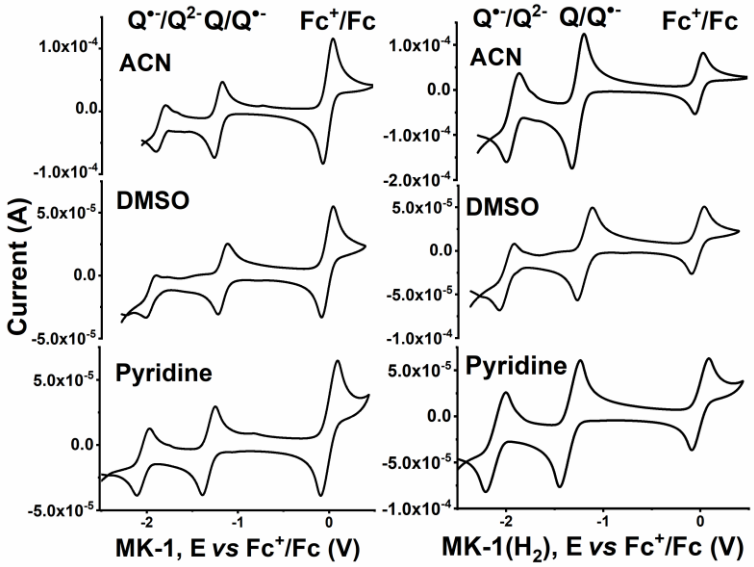

Figure C.1: Six cyclic voltammogram's (CVs) of 2 mM MK-1 and MK-1(H_2) in ACN, DMSO, and pyridine. The potentials are referenced to the Fc^+/Fc couple internal standard (2 mM) determined in each solvent. From left to right, redox processes are $Q^{\bullet-}/Q^{2-}$, $Q/Q^{\bullet-}$, and Fc^+/Fc. Each sample has 0.1 M TBAP and was degassed with argon gas for 10 min at ambient temperature before spectra were recorded. Current sweeps are in the anodic direction from -2V to 1V and back to -2V vs Ag/AgCl. A 100 mV/s scan rate was used.

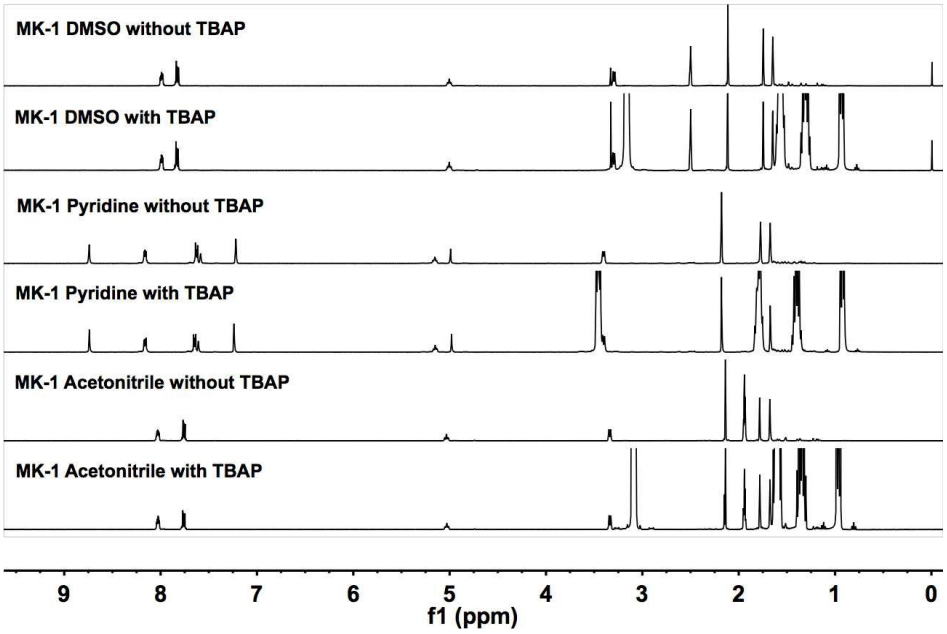

Figure C.2: 1D ^1H NMR (400 MHz) spectrum of MK-1 with and without electrolyte TBAP (0.1 M) at room temperature in d_6-DMSO, d_5-pyridine, and d_3-acetonitrile. The spectra were referenced to internal solvent peak as follows: d_6-DMSO = 2.50 ppm, d_5-pyridine = 8.74 ppm, and d_3-acetonitrile = 1.94 ppm.

As shown in **Figure C.1**, the ferrocene couple, Fc^+/Fc, was used as an internal reference standard so that the half-wave potentials are set to 0 V vs Fc^+/Fc. The $Q/Q^{\bullet-}$ $E_{1/2}$ vs Fc^+/Fc for MK-1 in ACN, DMSO, and pyridine were measured to be -1.227 (± 0.002) V, -1.158 (± 0.002) V, and -1.319 (± 0.001) V, respectively. The $Q/Q^{\bullet-}$ $E_{1/2}$ vs Fc^+/Fc for MK-1(H_2) in ACN, DMSO, and pyridine were measured to be -1.247 (± 0.007) V, -1.179 (± 0.002) V, and -1.343 (± 0.001) V, respectively. The results for the $Q/Q^{\bullet-}$ $E_{1/2}$ vs Fc^+/Fc values are near those reported for 1,4-naphthoquinone and those previously reported by our group for MK-2.[4-6] The $Q^{\bullet-}/Q^{2-}$ $E_{1/2}$ vs Fc^+/Fc for MK-1 in ACN, DMSO, and pyridine were measured to be -1.882 (± 0.014) V, -1.949 (± 0.006) V, and -2.037 (± 0.005) V, respectively. The $Q^{\bullet-}/Q^{2-}$ $E_{1/2}$ vs Fc^+/Fc for MK-1(H_2) in ACN, DMSO, and pyridine were measured to be -1.912 (± 0.009) V, -1.9947 (± 0.0008) V, and -2.109 (± 0.005) V, respectively. The measured quinone half-wave redox potential differences in these solvents are statistically significant as they are distinctly different from each other at high confidence intervals, see **Figure C.3** and caption.

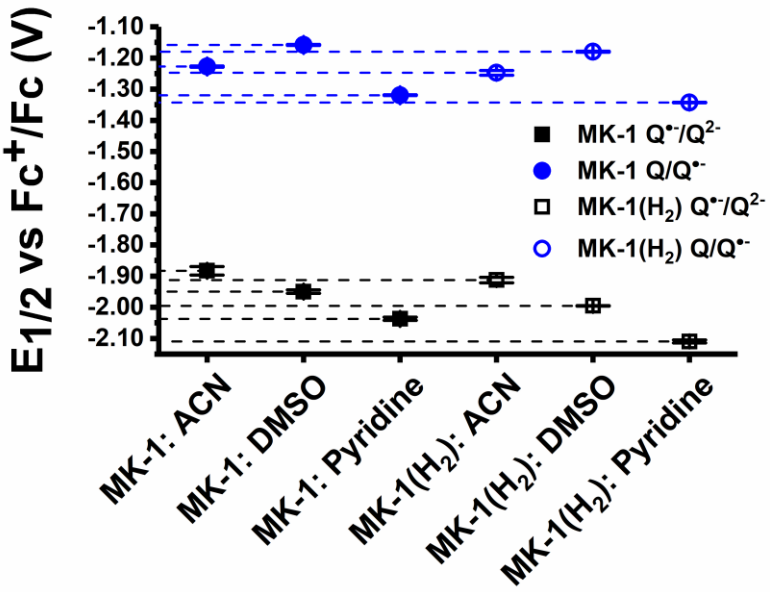

Figure C.3: Measured $E_{1/2}$ (vs Fc^+/Fc in V) of MK-1 and MK-1(H_2) $Q/Q^{\bullet-}$ and $Q^{\bullet-}/Q^{2-}$ redox process versus solvent. Each solvent was run in triplicate, with error bars shown. Added horizontal lines show the distinction between each solvent for each redox process. All solvent comparisons (ACN vs DMSO, etc.) for each redox process half-wave potential for MK-1 or MK-1(H_2) are statistically different with Student's *t* test confidence intervals of 99.9% ($p < 0.0001$) except the ACN vs DMSO $Q/Q^{\bullet-}$ of MK-1, which was 99.5% ($p < 0.0016$), (at four degrees of freedom). Comparisons between MK-1 vs MK-1(H_2) half-wave potentials of $Q/Q^{\bullet-}$ and $Q^{\bullet-}/Q^{2-}$ for each solvent were at the 99.9% ($p < 0.0001$) confidence level except for ACN, which were 98% ($p < 0.0089$) and 95% ($p < 0.0355$), respectively, (at four degrees of freedom).

The difference in millivolts between the unsaturated MK-1 vs the saturated MK-1(H_2) quinone redox potential in each solvent of the less variable $Q/Q^{\bullet-}$ process are of the same magnitude of ~20 mV with specific values of 20.033 (± 0.007) mV, 21.333 (± 0.002) mV, and 23.917 (± 0.001) mV for ACN, DMSO, and pyridine, respectively (**Figure C.3**). The $Q/Q^{\bullet-}$ process potentials are less variable as the presence of acidic hydrogens and/or water can create the hydroquinone species, which results in the $Q^{\bullet-}/Q^{2-}$ process coalesced onto the first redox potential. Our previous work on MK-2 demonstrated that the isoprenyl side chain folds over toward the naphthoquinone moiety and that the solvent environment can influence the preferred conformation.[6] The mixing of molecular orbitals (MOs) on the naphthoquinone moiety with the isoprenyl side chain may potentially result in different energies of the electrochemical bandgap (or HOMO to LUMO gap) needed to reduce the quinone carbonyl oxygen to an anionic oxygen radical. The electrochemical bandgap is suggestive of the potential observed or the energy required to reduce or oxidize an electrochemical process. This difference in the bandgap results in unique half-wave potentials as energy (*E*) and potential difference (*V*) are directly proportional, as evident by the electrostatic equation $E = VQ$ where *Q* is charge. The saturation or unsaturation of the isoprenyl side chain can, therefore, potentially influence these MOs and may alter the quinone redox potential in this manner. The semiquinone redox potential difference of ~20 mV between MK-1 and MK-1(H_2) could indicate the bandgap energy difference between the saturated and unsaturated double bond in the one unit isoprenyl side chain. However, the difference of ~20 mV is most likely due to an indirect effect manifested by a through-bond electronic change by the isoprenyl substituent on the quinone. An indirect substituent effect was used to explain a redox potential change for an N-aromatic substituent on a quinone.[7] The conformational differences of MK-1 between solvents were small, and the short isoprenyl side chain has limited spatial reach toward the naphthoquinone. If such an effect existed between conformation and redox potential, it might not be evident in the one isoprene unit system. However, suitable high-level computational calculations should be carried out to characterize the HOMO-LUMO gap of this system and determine the exact contributions to the observed ~20 mV difference.

We also observed a trend in the data of the potential difference for the $Q/Q^{\bullet-}$ process as compared by the solvent versus degree of saturation. For both MK-1 and MK-1(H_2), the potential difference of the $Q/Q^{\bullet-}$ process between ACN and DMSO is 69.250 (± 0.003) mV and 67.950 (± 0.008) mV, respectively.

The other solvent comparisons also have values that agree with each other. For MK-1 and MK-1(H_2), the potential difference of the $Q/Q^{\bullet-}$ process between DMSO and pyridine is 161.050 (± 0.002) mV and 163.633 (± 0.002) mV, respectively. Similarly, MK-1 and MK-1(H_2) have a potential difference of the $Q/Q^{\bullet-}$ process between ACN and pyridine is 91.800 (± 0.003) mV and 95.683 (± 0.008) mV, respectively. This conserved difference of the $Q/Q^{\bullet-}$ half-wave potentials between MK-1 vs MK-1(H_2) in each solvent may signify that how the isoprenyl side chain folds is truly solvent dependent and/or it may also suggest that the conformation of the short isoprenyl side chain (5 carbons) of MK-1 has little effect on the observed quinone redox potential in the one isoprene unit system.

In summary, both MK-1 and MK-1(H_2) during the first electrochemical process producing the semiquinone has the most positive potential in DMSO and the most negative potential in pyridine, demonstrating MK-1 or MK-1(H_2) is slightly more reducible in DMSO than ACN or pyridine. Most remarkably, the observation of a ~20 mV change in quinone $Q/Q^{\bullet-}$ $E_{1/2}$ between MK-1 and MK-1(H_2) supports our second hypothesis that saturation of the isoprenyl side chain of MK-1 affects the observed quinone redox potential. This is the first time that these subtle changes have been demonstrated in a quinone/MK system. The difference is presumably mainly due to a through-bond indirect effect, which results in an electronic perturbation of the quinone system upon saturation of the isoprenyl side chain. There was not a large difference between the MK-1 analog conformations. Therefore changes in the observed redox potentials are not likely due to conformational differences. However, a potential correlation should be investigated using the appropriate fully unsaturated and partially saturated MK-2 analogs in combination with computational methods to determine if conformational folding of the second isoprene unit can alter the quinone redox potential in MK analogs with unsaturated vs partially saturated isoprenyl side chain.

APPENDIX C REFERENCES

1. Koehn, J. T.; Beuning, C. N.; Peters, B. J.; Dellinger, S. K.; Van Cleave, C.; Crick, D. C.; Crans, D. C., Investigating Substrate Analogues for Mycobacterial MenJ: Truncated and Partially Saturated Menaquinones. *Biochemistry* **2019,** *58* (12), 1596 - 1615.

2. Dryhurst, G., Kadish, K. M., Scheller, F., Renneberg, R. , *Biological Eletrochemistry.* Academic Press: New York, 1982.

3. Wawzonek, S.; Berkey, R.; Blaha, E. W.; Runner, M. E., Polarographic Studies in Acetonitrile and Dimethylformamide: III. Behavior of Quinones and Hydroquinones. *J. Electroanal. Chem. Soc.* **1956,** *103* (8), 456-459.

4. Jaworski, J. S.; Leniewska, E.; Kalinowski, M. K., Solvent Effect on the Redox Potential of Quinone-semiquinone Systems. *J. Electroanal. Chem.* **1979,** *105* (2), 329-334.

5. Prince, R. C.; Leslie Dutton, P.; Malcolm Bruce, J., Electrochemistry of Ubiquinones. *FEBS Lett.* **1983,** *160* (1), 273-276.

6. Koehn, J. T.; Magallanes, E. S.; Peters, B. J.; Beuning, C. N.; Haase, A. A.; Zhu, M. J.; Rithner, C. D.; Crick, D. C.; Crans, D. C., A Synthetic Isoprenoid Lipoquinone, Menaquinone-2, Adopts a Folded Conformation in Solution and at a Model Membrane Interface. *J. Org. Chem.* **2018,** *83*, 275-288.

7. Aguilar-Martínez, M.; Macías-Ruvalcaba, N. A.; Bautista-Martínez, J. A.; Gómez, M.; González, F. J.; González, I., Review: Hydrogen Bond and Protonation as Modifying Factors of the Quinone Reactivity. *Curr. Org. Chem.* **2004,** *8*, 1721-1738.

APPENDIX D: UNPUBLISHED CONTRIBUTIONS TO THE CYCLIC VOLTAMMETRY AND SPECTROELECTROCHEMICAL METHOD DEVELOPMENT AND DATA INTERPRETATION OF VANADIUM(V) CATECHOL SCHIFF BASE COMPOUNDS

D.1 Statement of contributions

Jordan T. Koehn, of the Crans lab, synthesized a series of vanadium (V) catechol Schiff base compounds denoted as VO(HSHED)(cat), with varying electron-donating or withdrawing substitutions on the catechol ligand as potential anti-cancer agents.[1] He then performed their ^{51}V NMR spectroscopy. My undergraduate Molly Hartman and I performed the cyclic voltammetry and spectroelectrochemistry on the series of six different compounds in acetonitrile. These experiments were done to confirm some of the observations in the previous work performed in the group and to see if we could relate ^{51}V NMR chemical shift to the redox potential of the complex. This work will be written for publication by Dr. Crans.

D.2 Background

The Crans group synthesized a series of VO(HSHED)(cat) complexes, as shown in **Figure D.1**. The innocent ligand is the HSHED (N-(salicylideneaminato)-N'-(2-hydroxyethyl)ethylenediamine) while the catechol is non-innocent, and its substituents are either electron-donating or -withdrawing. The Crans group previously determined there is a linear relationship between the solution and solid-state ^{51}V NMR chemical shift, δ, of some of these non-innocent V(V) catechol complexes.[2] Through this NMR analysis they determined that the HOMO-LUMO gap increased for the catechol electron-donating group substitutions and the ^{51}V δ shifts upfield. The HOMO-LUMO gap decreased for the catechol electron-withdrawing group substitutions and the ^{51}V δ shifts downfield.

A study performed in 1992 on a large series of similar mono-oxovanadium (V) catecholate compounds showed that the magnitude of the shielding of the ^{51}V atom was linearly proportional to the inverse of the ligand-to-metal charge transfer band (LMCT) energy.[3] Since the optical and electrical band gaps are essentially the same, then the electrochemical properties of these compounds should be correlated to its ^{51}V NMR chemical shift, and one of the measurements should be able to predict the other.

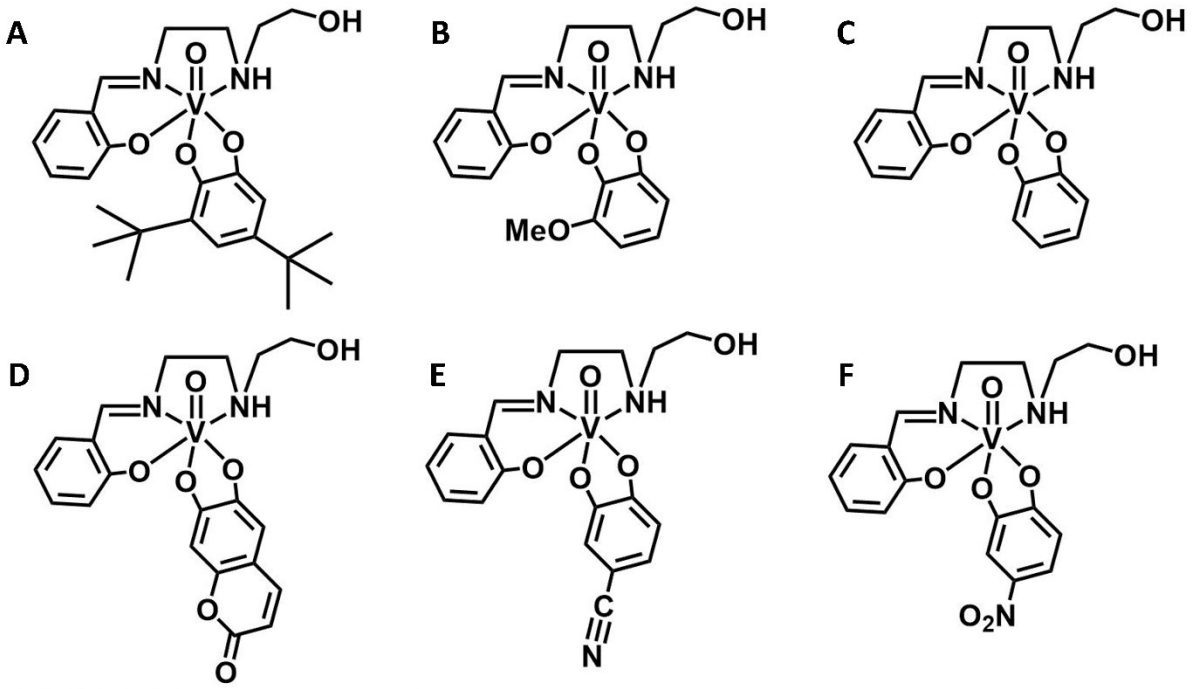

Figure D.1: Structures of the $V^{V}O$(HSHED)(cat) complexes are listed from the most electron-donating (A) to the most electron-withdrawing (F). Catechol ligands include A) 3,5-ditertbutyl catechol – DTBC; B) 3-methoxy catechol – 3-MeOC; C) catechol – cat; D) coumarin catechol – CC; E) 4-nitrile catechol – 4-CNC; F) 4-nitro catechol – 4-NOC.

D.3 Electrochemical and spectroelectrochemical methods and instrumentation

For the cyclic voltammetry a classical three-electrode system, as described in Chapter 1 section 1.6, was used with a glassy carbon working electrode (BASi MF2012, 3 mm, area of 0.707 cm^2), a platinum wire auxiliary electrode (BASi MW1032), and a non-aqueous 0.01 M Ag^+/Ag reference electrode (BASi MW1085). Analyte and reference electrode solutions were created with 0.1 M TBAP (tetrabutylammonium perchlorate) as the electrolyte and studied at a scan rate of 100 mV/s. 2 mM ferrocene was added as the internal standard. Acetonitrile was used dry as previously described in Chapter 5. VO(HSHED)(cat) complexes were studied at approximately 2 mM. A Pine Research WaveDriver 20 bipotentiostat was used to take all cyclic voltammetry data. For spectroelectrochemistry, the Pine Research Honeycomb plate and Avantes optics were used as described in Chapter 1, section 1.7. The concentrations of the vanadium complexes were about 0.5 mM for spectroelectrochemical studies and had no ferrocene in them.

D.4 Results and discussion

The cyclic voltammograms of all six complexes are given in **Figure D.2**. The ferrocene potential has been set to 0 V, as described in Chapter 5. The half-wave potentials, $E_{1/2}$, of each complex were determined from these cyclic voltammograms, in triplicate, from their clearly reversible peaks between -0.5 to -1.0 V vs Fc^+/Fc, **Table D.1**. The number of electrons in each V(V) redox process is one, going from V(V) to V(IV), and their peak current ratios approach unity. These half-wave potentials were then graphed versus their ^{51}V NMR chemical shifts in acetonitrile, and a linear relationship is observed, **Figure D.3**. Their diffusion coefficients could also be determined and are given in **Table D.1** at the 90% confidence (a greater number of measurements is needed to reduce error in these values).

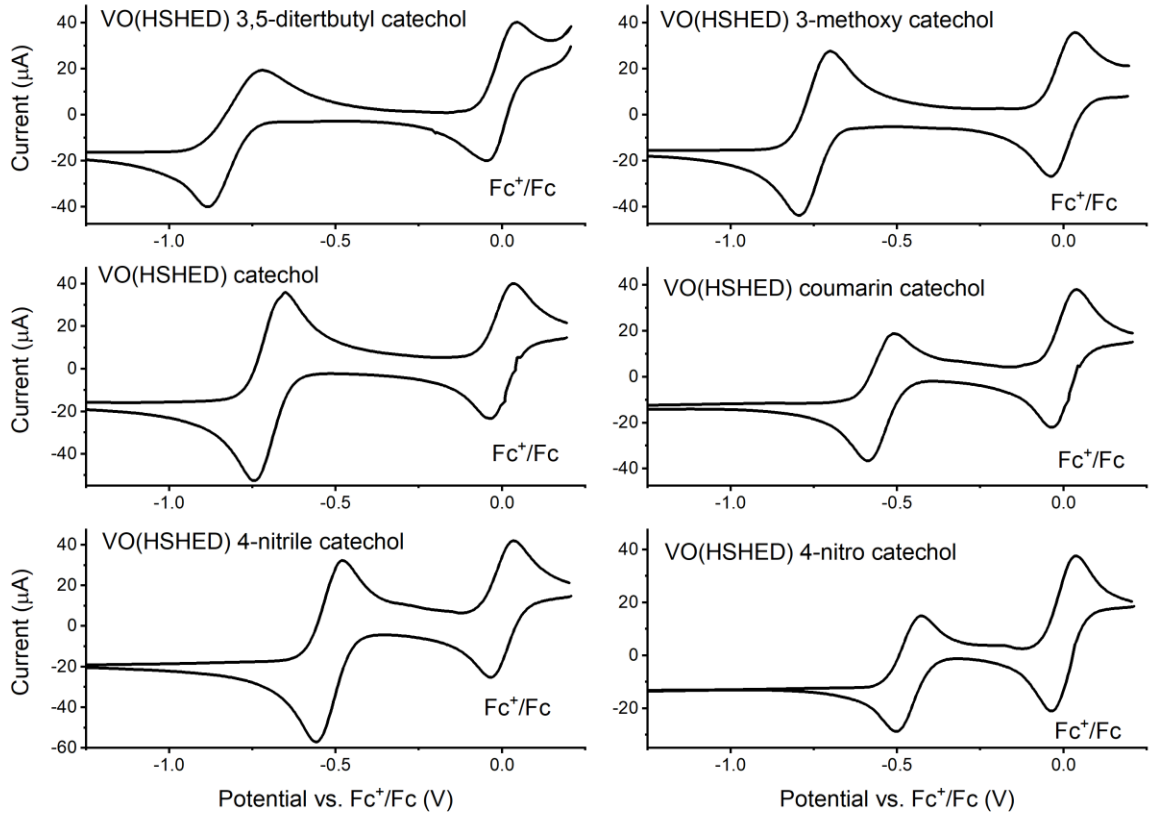

Figure D.2: The cyclic voltammograms of the VO(HSHED)(cat) complexes in acetonitrile with 0.1 M TBAP and 2 mM Fc^+/Fc at STP (ambient room temperature), under argon gas, and at a scan rate of 100 mV/s.

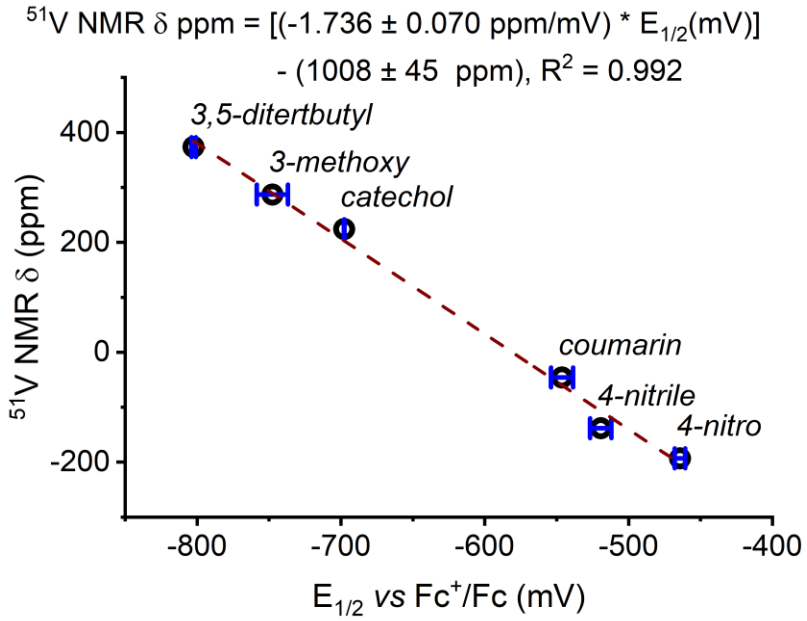

Figure D.3: The solution ^{51}V NMR chemical shift, δ (ppm) of the VO(HSHED)(cat) complexes versus their half-wave potentials, $E_{1/2}$ vs Fc^+/Fc in mV in acetonitrile.

Table D.1: Half-wave potentials and diffusion coefficients of the VO(HSHED)(cat) complexes in acetonitrile at 90% confidence. Diffusion coefficients are limited to two significant figures due to ones of mg on a balance with tenths of mg measurement capability. Those measurements with increased confidence are listed in parentheses.

VO(HSHED)	$E_{1/2}$ vs Fc^+/Fc (mV)	D_O (cm^2s^{-1}) at 90% CL
3,5-ditertbutyl	- 802 ± 1	6.6 (± 1.8) x 10^{-8}
3-methoxy	- 748 ± 11	1.2 (± 0.2) x 10^{-7} (98%)
coumarin	- 546 ± 8	6.6 (± 2.2) x 10^{-8}
catechol	- 698 ± 0.2	2.1 (± 1.7) x 10^{-7}
4-nitro	- 464 ± 4	5.8 (± 0.8) x 10^{-8}
4-nitrile	- 519 ± 7	1.5 (± 0.02) x 10^{-7} (98%)

As hypothesized, a correlation between the chemical shift ^{51}V NMR δ and the redox potential $E_{1/2}$ is observed. A direct linear relationship can be determined for the ^{51}V NMR δ in acetonitrile for a measured $E_{1/2}$ in mV, **Eq. D.1**. The more electron-donating substituents on the catechol produce more negative redox potentials, and their δ move upfield of the catechol base. The more electron-withdrawing substituents on the catechol produce more positive redox potentials and their δ move downfield of the catechol base. The relationship between the paramagnetic shielding component of δ in vanadium(V) compounds and their LMCT ΔE was discussed in the 1992 paper, and here we see direct relationship. The paramagnetic

shielding component is affected by the electronic structure of the vanadium and the bound ligands. As the electrons are being donated to the V, the redox process becomes more difficult to perform as the atom becomes highly shielded. Conversely, as electrons are being withdrawn from the V, the redox process becomes easier to perform as the atom becomes de-shielded. These effects are then observed in the ^{51}V NMR chemical shift as the magnetic field generated by the electron-donating/withdrawing affect the applied magnetic field in different magnitudes.

$$(\textbf{Eq D.1})\ 51V\ \delta\ (ppm) = -1.736\ E_{\frac{1}{2}} - 1008$$

The spectroelectrochemistry of the VO(HSHED)(cat) complexes in acetonitrile were also performed and are shown in **Figure D.4**. The 400 -560 nm (a 182 nm range) is the LMCT band of the V-catechol, while the 800 nm range is the LMCT of the V-HSHED (varies less only a 76 nm range), see **Table D.2** for all wavelength maxima. The UV region is from the aromatic rings and is very intense. However, we were more interested in examining the LMCT peaks. The LMCT HOMO-LUMO gaps were determined to be larger for electron-withdrawing with shorter λ_{maxima} and smaller for electron-donating with longer λ_{maxima}. These conclusions confirm the group's previous work with solid-state and solution ^{51}V NMR studies.

Table D.2: The absorption spectroscopy maximum wavelengths of LMCT bands of VO(HSHED)(cat) complexes in acetonitrile.

Type	Catechol	LMCT V-catechol λ, nm	LMCT V-HSHED λ, nm	Color 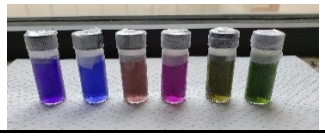
e^- donate	DTBC	549	864	Dark Blue
e^- donate	3-MeOC	561	829	Indigo
e^- donate	cat	526	872	Brown-Red
e^- withdraw	CC	517	870	Plum
e^- withdraw	4-CNC	475	814	Army Green
e^- withdraw	4-NOC	379	796	Grass Green

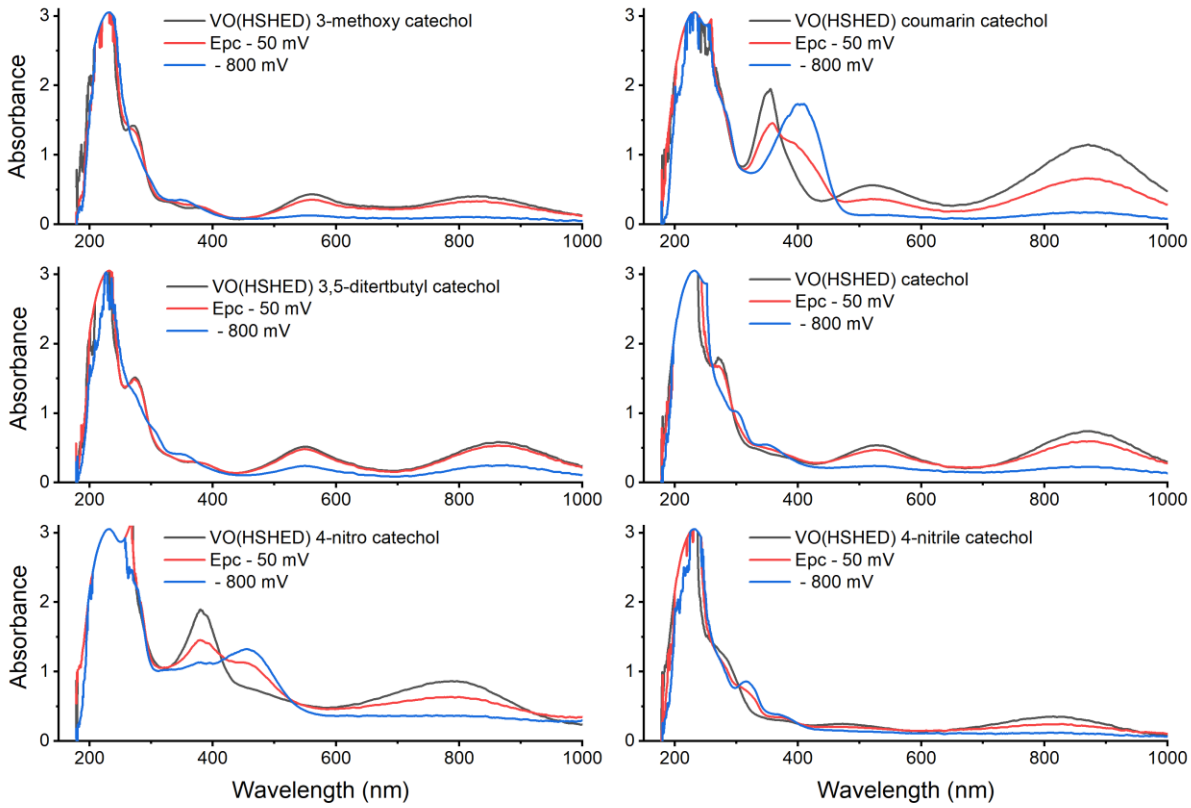

Figure D.4: The spectroelectrochemical spectra of the VO(HSHED)catechol complexes in acetonitrile. The black lines are oxidized forms, under no applied potential. The red lines are -50 mV of their cathodic peak potential, E_{pc}, while the blue lines are at a reducing potential quite negative of all complex's $E_{1/2}$, -800 mV vs Ag^{+}/Ag.

D.5 Conclusions and future experiments

This linear relationship is a novel correlation between the NMR and the electrochemistry of vanadium compounds. The ability to predict either physical value from another is an important characterization tool, especially if one of the spectroscopies is not available. There is much more research to perform in this area, including analysis in different solvents to see if the correlation is conserved. Similarly, changes to the innocent ligand or alternative substituents on the catechol could be investigated.

APPENDIX D REFERENCES

1. Crans, D. C.; Koehn, J. T.; Petry, S. M.; Glover, C. M.; Wijetunga, A.; Kaur, R.; Levina, A.; Lay, P. A., Hydrophobicity May Enhance Membrane Affinity and Anti-cancer Effects of Schiff Base Vanadium(v) Catecholate Complexes. *Dalton Trans.* **2019,** *48* (19), 6383-6395.

2. Chatterjee, P. B.; Goncharov-Zapata, O.; Quinn, L. L.; Hou, G. J.; Hamaed, H.; Schurko, R. W.; Polenova, T.; Crans, D. C., Characterization of Noninnocent Metal Complexes Using Solid-State NMR Spectroscopy: o-Dioxolene Vanadium Complexes. *Inorg. Chem.* **2011,** *50* (20), 9794-9803.

3. Cornman, C. R.; Colpas, G. J.; Hoeschele, J. D.; Kampf, J.; Pecoraro, V. L., Implications For The Spectroscopic Assignment of Vanadium Biomolecules - Structural and Spectroscopic Characterizatin of Monooxovanadium (V) Complexes Containing Catecholate AND Hydroximate Based Noninnocent Ligands. *J. Am. Chem. Soc.* **1992,** *114* (25), 9925-9933.